Imperial College London

Imperial College London

Department of Chemical Engineering

Hybrid Nuclear-Solar Power

Abdullah A. Al Kindi

Supervised by Professor Christos N. Markides

A thesis submitted for the degree of

Doctor of Philosophy

August 2023


بِسْمِ ٱللَّهِ ٱلرَّحْمَٰنِ ٱلرَّحِيمِ

Dedication

To my parents, my wife, and my beautiful daughter Alia.

Statement of Originality

I hereby certify that, to the best of my knowledge, the content of this thesis is original and the results of my own work. All of the assistance I received and the sources I used have been properly acknowledged.

Abdullah A. Al Kindi

August 2023

Copyright Declaration

Abstract

Nuclear and solar power, in the form of concentrated solar power (CSP), play a significant role in achieving the ambitious global targets of reducing greenhouse emissions and guaranteeing security of energy supply. However, both power generation technologies still require further development to realise their full potential, especially in terms of attaining economic load following operations and higher thermal efficiencies. Therefore, the aim of this research is to investigate and thermo-economically evaluate the available options of upgrading the flexibility and enhancing the thermal efficiency of nuclear and solar power generation technologies (i.e., through the integration with thermal energy storage (TES) and by hybridising both power generation technologies) while providing reasonable economic returns.

The thesis starts with describing the development and validation of several thermodynamic and economic computational models and the formulation of the whole-energy system model. The formulated models are utilised to perform several thermo-economic studies in the field of flexible nuclear and solar power, and to quantify the economic benefits that could result from enhancing the flexibility of nuclear power plants from the whole-energy system perspective. The studies conducted in this research are: (i) a thermo-economic assessment of extending the conventional TES system in direct steam generation (DSG) CSP plants; (ii) a thermo-economic evaluation of upgrading the flexibility of nuclear power plants by the integration with TES and secondary power generation systems; (iii) an investigation of the role of added flexibility in future low-carbon electricity systems; and (iv) a design and operation analysis of a hybrid nuclear-solar power plant.

The most common TES option in DSC CSP plants is steam accumulation. This conventional option is constrained by temperature and pressure limits, leading to lower efficiency operations during TES discharging mode. Therefore, the option of integrating steam accumulators with sensible-heat storage in concrete to provide higher-temperature superheated steam is thermo-economically investigated in this research, taking an operational DSG CSP plant as a case study. The results show that the integrated concrete-steam TES (extended) option delivers 58% more electricity with a 13% enhancement in thermal efficiency during TES discharging mode, compared to the conventional steam accumulation (existing) configuration. With an estimated additional investment of $4.2M, the projected levelised cost of electricity (LCOE) and the net

present value (NPV) for the considered DSG CSP plant with the extended TES option are respectively 6% lower and 73% higher than those of the existing TES option.

The option of upgrading the flexibility of nuclear power plants through the integration with TES and secondary power generation systems is investigated for two conventional nuclear reactors, a 670-MW_{el} advanced gas-cooled reactor (AGR) and a 1610-MW_{el} European pressurised reactor (EPR). In both investigated case studies, the reactors are assumed to continuously operate at full rated thermal power, while load following operations are conducted through the integrated TES tanks and secondary power generators. Based on the designed TES and secondary power generation systems, the AGR-based configuration can modulate the power output between 406 MW_{el} and 822 MW_{el}, while the EPR-based configuration can operate flexibly between 806 MW_{el} and 2130 MW_{el}. The economic analysis results demonstrate that the economics of added flexibility are highly dependent on: (i) the size of the TES and the secondary power generation systems; (ii) the number of TES charge/discharge cycles per day; and (iii) the ratio and difference between off-peak and peak electricity prices.

Replacing conventional EPR-based nuclear power plants with added flexibility ones is found to generate whole-system cost savings between \$30.4M/yr and \$111M/yr. At an estimated cost of added flexibility of \$53.4M/yr, the proposed flexibility upgrades appear to be economically justified with net system economic benefits ranging from \$5.0M/yr and \$39.5M/yr for the examined low-carbon scenarios, provided that the number of flexible nuclear plants in the system is small.

The concept of hybridising a small modular reactor (SMR) with a solar-tower CSP integrated with two-tank molten salt TES system, with the aim of achieving economically enhanced load following operations and higher thermal efficiency levels, is also thermo-economically investigated in this research. The integration of both technologies is achieved by adding a solar-powered superheater and a reheater to a standalone SMR. The obtained results demonstrate that hybridising nuclear and solar can offer a great amount of flexibility (i.e., between 50% and 100% of nominal load of 131 MW_{el}) with the SMR continuously operated at full rated thermal power output. Furthermore, the designed hybrid power plant is able to operate at higher temperatures due to the addition of the solar superheater, resulting in a 15% increase of thermal efficiency compared to nuclear-only power plant. Moreover, the calculated specific investment cost and the LCOE of the designed hybrid power plant are respectively 5410 \$/kW_{el} and 77 \$/MWh_{el}, which are 2% and 4% lower than those calculated for the nuclear-only power plant.

Acknowledgments

I would like to express my deepest appreciation and sincere gratitude to my supervisor, Professor Christos N. Markides, for giving me the opportunity to pursue my PhD in the Clean Energy Processes (CEP) Laboratory and for his continuous support during my PhD study. His steady and constant guidance, invaluable advice, logical thinking, and immense knowledge have helped me not only improving my research skills but also encouraged me throughout my PhD journey. I will always be grateful for being lucky to be supervised by such a great and compassionate supervisor.

I would like to acknowledge the Government of the Sultanate of Oman for their financial support, which made it possible for me to reach this far in terms of knowledge, research skills and academic achievements. I would also like to express my sincere gratitude and deepest appreciation to my colleagues in the Foreign Ministry and the Embassy of the Sultanate of Oman in London for their continuous support and encouragement during my PhD journey.

I would like to thank my colleagues and trusted friends, the members of the Clean Energy Processes (CEP) Laboratory, Andreas Olympios, Jian Song, Marco Antonio Pantaleo, Matthias Mersch, Michael Simpson, Paul Sapin and Tarik Al Kharusi, for their support, encouragement and fun times. They will be friends for life. I am also thankful for all other previous and current CEP Laboratory members: Abdullah, Ahmed, Andrew, Asmaa, Benedict, Chandan, Dauda, Diego, Erdem, Gan, Hannah, Ivan, James, Jingyuan, Joy, Kai, Konstantin, Mohammed A., Mohammed M., Niccolo, Oyeniyi, Ray, Sara, Solomos, Surya, Victor, Yao, Yongliang and Zihao who were there for encouragement and enjoyable times. I would also like to extend my special thanks to Professor Goran Strbac, and Marko Aunedi for their research collaboration and for their high-level research input and advice.

Finally, and most importantly, my deepest gratitude and heartfelt appreciation goes to my wonderful and wise parents Abbas and Kamla, my lovely wife Sara, my beautiful daughter Alia, who was born during this journey, and my amazing brother and sisters Faisal, Kinda, Reem, Bushra and Ameera. They all have always shown endless encouragement, positivity, support and boundless, unconditional love not only during my PhD journey, but throughout my entire life.

Table of Contents

List of Publications

To date these are the publications that have been presented to the public domain in relation to the research presented in this thesis.

Journal articles

- Aunedi M, **Al Kindi AA**, Pantaleo AM, Markides CN, Strbac G. System-driven design of flexible nuclear power plant configurations with thermal energy storage. Energy Conversion and Management 2023;291:117257.
- **Al Kindi AA**, Sapin P, Pantaleo AM, Wang K, Markides CN. Thermo-economic analysis of steam accumulation and solid thermal energy storage system in direct steam generation concentrated solar power plants. Energy Conversion and Management 2022;274:116222.
- **Al Kindi AA**, Aunedi M, Pantaleo AM, Strbac G, Markides CN. Thermo-economic assessment of flexible nuclear power plants in future low-carbon electricity systems: Role of thermal energy storage. Energy Conversion and Management 2022;258:115484.
- Romanos P, **Al Kindi AA**, Pantaleo AM, Markides CN. Flexible nuclear plants with thermal energy storage and secondary power cycles: Virtual power plant integration in a UK energy system case study. e-Prime – Advances in Electrical Engineering, Electronics and Energy 2022;2:100027.

Peer-reviewed conference papers

- Aunedi M, **Al Kindi AA**, Pantaleo AM, Markides CN, Strbac G. System-driven design of flexible nuclear power plant configurations with thermal energy storage. The 17th Conference on Sustainable Development of Energy, Water and Environmental Systems (SDEWES) 2022. 6-10 November 2022. Paphos, Cyprus.
- **Al Kindi AA**, Aunedi M, Pantaleo AM, Strbac G, Markides CN. Thermo-economic assessment of flexible nuclear power plants in the UK's future low-carbon electricity system: role of thermal energy storage. The 16th Conference on Sustainable Development of Energy, Water and Environmental Systems (SDEWES) 2021. 10-15 October 2021. Dubrovnik, Croatia. **(Received the Best Paper Award in the conference).**

- **Al Kindi AA**, Pantaleo AM, Wang K, Markides CN. Optimal system configuration and operation strategies of flexible hybrid nuclear-solar power plants. The 33rd International conference on Efficiency, Cost, Optimisation, Simulation and Environmental Impact of Energy Systems (ECOS) 2020. 29 June - 3 July 2020. Osaka, Japan.
- **Al Kindi AA**, Pantaleo AM, Wang K, Markides CN. Thermodynamic assessment of steam-accumulation thermal energy storage in concentrating solar power plants. International Conference on Applied Energy 2019. 12-15 August 2019. Västerås, Sweden.

List of Figures

List of Tables

Nomenclature

Acronyms

AGR	advanced gas-cooled reactor	LP	low pressure
AOP	average off-peak price	LPT	low-pressure turbine
BECCS	bioenergy with carbon capture and storage	LWR	light water reactor
BESS	battery energy storage system	NIV	net imbalance volume
BM	balancing market	NPP	nuclear power plant
BWR	boiling water reactor	NPV	net present value
CCGT	combined cycle gas turbine	NRC	Nuclear Regulatory Commission
CCS	carbon capture and storage	O&M	operation and maintenance
CFWH	closed feedwater heater	OCGT	open cycle gas turbine
CHP	combined heat and power	OPEX	operating expenditure
CSP	concentrated solar power	ORC	organic Rankine cycle
DNI	direct normal irradiance	PCM	phase change material
DSG	direct steam generation	PD	price difference
DSR	demand side response	PPA	power purchase agreement
EdF	Electricite de France	PSRC	primary steam Rankine cycle
EMS	energy management system	PV	photovoltaic
EPR	European pressurised reactor	PWR	pressurised water reactor
FFR	fast frequency response	RH	reheater
FWH	feedwater heater	RMSE	root mean square error
HP	high pressure	SA	steam accumulator
HPT	high-pressure turbine	SG	steam generator
HTF	heat transfer fluid	SIC	specific investment cost
IAEA	International Atomic Energy Agency	SM	solar multiple
IEA	International Energy Agency	SMR	small modular reactor
IPT	intermediate-pressure turbine	SSRC	secondary steam Rankine cycle
IRENA	International Renewable Energy Agency	TES	thermal energy storage
IRR	internal rate of return	TSO	transmission system operator
LAES	liquid air energy storage	VVP	virtual power plant
LCOE	levelised cost of electricity	WeSIM	whole-electricity system investment model
LCOS	levelised cost of storage	WFR	water filling ratio

Symbols

A	area (m^2)	C	cost (currency)
Bi	Biot number (-)	c_p	specific heat – constant pressure (J/kg K)
c	specific heat (J/kg K)	CP	capacity payment (currency)

d	thickness (m)	NPV	net present value (currency)
D	diameter (m)	Nu	Nusselt number (-)
DE	discharged electricity (Wh)	P	pressure (Pa)
e	absolute tube roughness (m)	Pr	Prandtl number (-)
E	electricity (Wh)	PR	pressure ratio (-)
EP	electricity price (currency/Wh)	q	heat flux (W/m^2)
f	friction factor (-)	Q	heat (J)
F	factor (-)	$\dot{Q}$	heat power (W)
g	acceleration of gravity (m/s^2)	r	discount rate (%)
G	mass flux (kg/m^2 s)	R	radius (m)
h	specific enthalpy (J/kg)	Re	Reynolds number (-)
H	enthalpy (J) / height (m)	s	specific entropy (J/kg K)
$\dot{H}$	rate of enthalpy (W)	S	entropy (J/K)
i	number of items (-)	$\dot{S}$	rate of entropy (W/K)
I	cost index (-) / revenues (currency)	SIC	specific investment cost (currency/W)
IRR	internal rate of return (%)	t	time (s)
j	spatial node (-)	T	temperature (°C)
J	dimensionless velocity (-)	u	specific internal energy (J/kg)
k	thermal conductivity (W/m K)	U	unit price (currency)
K	correction factor (-)	v	velocity (m/s)
K_{e0}	efficiency parameter (-)	V	volume (m^3)
K_{v0}	velocity parameter (-)	$\dot{V}$	volumetric flowrate (m^3/s)
L	length (m)	W	work (J) / width (m)
$LCOE$	levelised cost of electricity (currency/Wh)	$\dot{W}$	power (W)
$LCOS$	levelised cost of storage (currency/Wh)	WFR	water filling ratio (-)
m	mass (kg)	x	quality (-)
$\dot{m}$	mass flowrate (kg/s)	$\dot{x}$	local dryness factor (-)
n	time step (-) / lifetime (years)	z	axial length (m)
N	number of units (-)	Z	Shah's correlation parameter (-)

Greek symbols

α	heat transfer coefficient (W/m^2 K)	Λ	Nusselt film height (m)
β	boundary constant (-)	μ	dynamic viscosity (kg/m s)
γ	boundary constant (-)	ν	specific volume (m^3/kg)
Δ	change between two values (-)	ξ	absorptivity (-)
ε	error (-)	ρ	density (kg/m^3)
ϵ	emissivity (-)	σ	Stefan-Boltzmann constant (W/m^2 K^4)
η	efficiency (-)	τ	total time (s)/ shear stress (N/m^2)
θ	approach angle (rad) / temperature (°C)	φ	flow coefficient (m^2)
λ	turbine positive constant (-)	ω	shaft rotational speed (rad/s)

Subscript/superscript

1 to 40	number of flow stream
′	saturated liquid
″	saturated vapour
a	ambient
A	analysis/present year
ava	availability
axial	axial
b	blade / base
B	base year
BM	bare module
c	calculated / capital
C	concrete mixture
CB	concrete block
CFWH	closed feed water heater
Ch	charging
CiP	circulation pump
CL	cold leg (stream)
cond	condenser
conv	convection
CP	condensate pump
crit	critical
CT	cooling tower / cold tank
Cyc	power generation cycle
d	dead-state
D	design
day	day
Dch	discharging
DE	deaerator
e	effective
E	electrical
EMS	energy management system
evp	evaporator
exp	experimental
f	fluid
F	foundation / fixed / film
FN	flexible nuclear
FP	feedwater pump
fuel	fuel
fus	fusion
gb	gear box
gen	generator
h	hydraulic
hel	heliostat
HFWH	high-pressure feedwater heater
HL	hot leg (stream)
HNS	hybrid nuclear solar
HPT	high-pressure turbine
HT	hot tank
HTF	teat transfer fluid
HX	heat exchanger
i	inner
I&C	instruments and control
IHX	internal heat exchanger
in	inlet
Ins	insulation
irr	irradiance
is	isentropic
L	liquid
La	laminar
LFWH	low-pressure feedwater heater
LM	logarithmic mean
Lo	all liquid
loss	loss
LPT	low-pressure turbine
m	melting
M	material
max	maximum
min	minimum
MS	molten salt
net	net
NO	nuclear only
nom	nominal
NR	nuclear reactor
Nu	Nusselt
num	numerical
o	outer
O&M	operation and maintenance
OD	off-design
ORC	organic Rankine cycle
out	outlet

p	provided from data / purchase
P	pressure / pump
P&S	platform and steel
P&V	piping and valves
P1	Part 1
P2	Part 2
P3	Part 3
P4	Part 4
PC	phase change
PGB	power generation block
Ph	film free-surface
PL	platform and ladders / part load
PP	power plant
pp	pinch point
PSRC	primary steam Rankine cycle
PV	pressure vessel
r	rough
R	reduced
rad	radiation
radial	radial
rec	receiver
RH	reheater
RMS	root mean square
s	solid / surface
SA	steam accumulator
sat	saturation
SE	turbine side extraction
SF	solar field
SG	steam generator
Sh	Shah
SH	superheater
SM	solar multiple
SP	single phase
spr	superheater
SSRC	secondary steam Rankine cycle
ST	solar tower
T	turbine
TES	thermal energy storage
tm	tube material
total	total
tow	tower
TP	two-phase / turbo-pump / turbine part
TS	turbine stage
TT	thermal tank
TT-1	Thermal Tank 1
TT-2	Thermal Tank 2
TT-3	Thermal Tank 3
Tu	turbulent
tubes	tubes
TV	throttling valve
Ü	superheated
V	vapour / variable
vap	vaporisation
view	view
w	wall
wf	working fluid

N.B.: Other symbols are defined in the text where they are first used. Where appropriate, lower-case symbols refer to specific quantities and upper-case symbols to extensive quantities.

Chapter 1

Introduction

1.1. Context and motivation

Providing sustainable, affordable, and clean energy for the increasing global energy demand is a challenge that requires an intensive international community collaboration. The governmental climate efforts have expanded dramatically since the 2015 Paris Agreement on climate change and many countries have already selected pathways to shifting from fossil fuel-based energy sources to rely more on carbon free sources, such as renewables and nuclear energy [1]. For example, the UK has initiated the Climate Change Act with the aim of reducing greenhouse gas emissions by 100% compared to 1990 levels by 2050 [2,3]. Figure 1.1 shows the total electricity generated in the UK by source from 1990 to 2021 [4]. The chart clearly indicates that renewables have been replacing fossil fuel sources, especially coal, in the last 10 years in order to meet the target of net-zero greenhouse emissions set by the UK government. However, there is a need to make significant efforts to meet this target, as more than 40% of total generated electricity in 2021 were generated using fossil-fuel based energy sources. Moreover, the nuclear share is almost constant during the last 20 years, indicating that nuclear is still significant in securing low-carbon electricity.

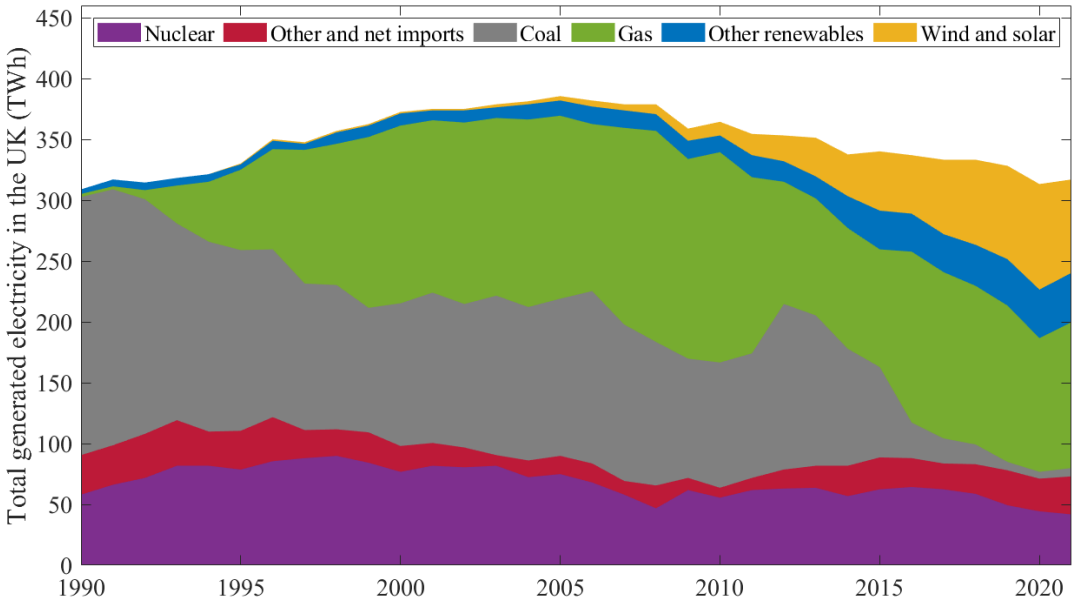

Figure 1.1. Electricity generation by source in the UK (from 1990 to 2021) [4].

Nuclear power is considered a carbon-free source of energy which is widely utilised around the world. Nuclear power plants (NPP) are commonly operated to meet the baseload demand of electricity due to their high reliability, high capital costs, and relatively low variable costs. Although nuclear power is an attractive option for the decarbonisation process, it is still not highly favoured by some governments due to challenges including high capital costs, long construction times, relatively low thermal efficiencies as well as limited and uneconomic load following operations [5].

Nevertheless, the global interest in nuclear power has recently increased due to international actions, which confirms the importance of energy security without the reliance on other countries. Nuclear power can play an important role for ensuring energy security in electricity systems with high shares of variable renewable sources. Its importance has come into focus in light of the recent Ukraine-Russia conflict, with several European countries recognising the need to secure domestic energy production with reduced dependence on energy imports. For example, France, which relies heavily on nuclear power that provides 70% of its electricity, announced in early 2022 plans to construct six new nuclear reactors [6]. France also considers building a further eight reactors in the future to secure its energy supply and reduce reliance on other countries [6]. Security of supply represents one of the main reasons why the UK is also considering future investments in nuclear power [7], in addition to the need to achieve the target of net-zero greenhouse gas emissions by 2050. Future UK government investment plans envisage expanding current nuclear capacity by four times in 2050, from 6 GW_{el} to 24 GW_{el} [8].

To tackle challenges such as high capital cost and long construction times of current nuclear reactors, the nuclear industry is shifting towards designing small modular reactors (SMRs), which are smaller, simpler, standardised, and safer type of nuclear reactors. Through the standardisation and modularisation concept, SMRs are expected to offer better upfront capital cost affordability and shorter construction times, compared to the conventional NPPs [9]. Most NPPs, especially light water reactors (LWRs) have thermal efficiencies ranging between 30% and 36%, which are relatively low compared to the other conventional power plants. For example, coal and oil power plants have thermal efficiencies up to 46%. Furthermore, combined cycle gas turbines have the highest thermal efficiency which can reach a level of more than 56% [10]. The relatively low cycle efficiency levels in LWRs are because of the operation temperature constraint, usually below 350 °C, due to the need of having liquid water in the reactor core for cooling purposes. Thus, achieving higher thermal efficiency levels, above 36%,

is a challenge in LWRs, but it can be tackled, to some degree, through the integration with other higher temperature heat sources such as biomass and solar power [10–12].

NPPs with load following capabilities are currently desired, especially with the increasing penetration of renewables in the electricity grids. Although new NPPs, including SMRs, are designed with better power variation capabilities, it is still more economical to operate nuclear units at full rated thermal power due to their low variable costs and higher profits from electricity sales, thus, quicker return of initial investments. Flexible and economical operation of NPPs can be achieved through the integration with thermal energy storage (TES) systems as proposed and investigated by several studies [13–18]. These studies suggest storing heat during off-peak demand periods and then discharging the stored heat either to the primary or the secondary power generation cycle systems during peak demand periods, which is usually accompanied by high electricity prices. Another option of achieving a more flexible power output is hybridising nuclear with other thermal power sources (i.e., solar power) [11,12,19–21]. This integration allows the nuclear reactor to operate at full rated thermal power while load following operations are achieved by adjusting the amount of heat provided from the other heat source.

Solar energy, in the form of concentrated solar power (CSP), is rapidly growing due to its abilities of providing high temperature thermal power, which can be utilised in several energy applications. However, the main disadvantage of CSP plants is their high dependence on weather conditions. This drawback can be resolved, to some degree, through the integration with TES systems, which can store solar heat for a period of time (i.e., commonly between 2 and 15 hours) to generate power during low or no sunlight times [22]. Still, the storage period might not be sufficient to secure energy supply during longer periods of unfavourable weather conditions (i.e., a cloudy week). Therefore, it is important to investigate the available options of increasing the reliability and the capacity factor of CSP plants. One option to achieve this is through the integration with other reliable and carbon-free source of energy such as nuclear power [23,24].

The use of TES technologies is nowadays common practice in some large-scale thermal power generation applications such as CSP plants. There is a wide range of TES technologies, which can be classified in terms of storage mechanism as: (i) sensible, (ii) latent, also known as phase change material (PCM), and (iii) thermochemical [25]. There is a growing demand for TES, as reported in a recent study by the International Renewable Energy Agency

(IRENA) [26] that predicts that the global market for TES could triple in size by 2030, with an increase from 234 GWh_{th} of installed capacity in 2019 to over 800 GWh_{th} within a decade. The role of TES technologies in systems with high renewable penetrations becomes even more prominent when considering renewable technologies such as CSP. This is evident in Ref. [27] which analyses different European scenarios with very high renewable penetrations and discusses the economic and technical issues. The advantages of the application of TES over batteries in combination with large-scale thermal power plants were also highlighted in Ref. [28]. According to that analysis, the use of TES in combination with conventional power plants allows to economically support variable renewables at larger capacity and for longer discharging hours than current battery storage technologies or hydropower storage.

It is evident that both nuclear power and solar power, in the form of CSP, can play a significant role in achieving the ambitious global emission reduction targets due to their ability to provide zero carbon emission electricity. However, both technologies have some technical and economic constraints, and both still need extra research attention, especially in terms of power flexibility, thermodynamic efficiency, and affordability.

1.2. Aim and objectives

Increased flexibility and thermal efficiency of large-scale carbon-free thermal power plants, including nuclear and concentrated solar power plants, can greatly aid in achieving low or net-zero carbon emission targets while navigating the energy trilemma of security, affordability and sustainability. Accurately accounting for the thermodynamic characteristics and costs of these two technologies, from a technology point of view as well as from a whole-energy system perspective, is crucial to assess the value of nuclear and solar power in future energy systems.

The overall aim of this research is the assessment of available options for upgrading the flexibility and enhancing the thermal efficiency of nuclear and concentrated solar power generation technologies (i.e., through the integration with thermal energy storage (TES) and by hybridising both power generation technologies) while providing reasonable economic returns. The use of the developed thermodynamic and economic models is the key to comprehensively analyse and investigate the potential benefits of the considered power generation and TES technologies. Furthermore, utilising the formulated models with the objective of evaluating the

upgrade, in terms of power flexibility and thermal efficiency, of currently operating nuclear and concentrated solar power plants is beneficial for making energy related decisions.

To achieve the overall aim of this research, several thermodynamic and economic computational models related to nuclear and concentrated solar power generation as well as TES technologies will be used to address the following objectives:

- To assess and investigate the potential thermodynamic and economic advantages of extending a TES system of an operating direct steam generation concentrated solar power plant.
- To evaluate and explore the available options of upgrading the flexibility of the current and future fleet of UK's nuclear power plants.
- To quantify the potential of achieving economic benefits, from a technology and a whole-electricity system perspectives, of upgrading the flexibility of nuclear power plants through the integration with TES and secondary power generation cycle systems.
- To design a hybrid nuclear-solar power plant integrated with TES system based in a specific geographical location, and to assess the degree of added flexibility and enhanced thermal efficiency as well as the economic benefits that could results from the hybridisation concept.

Detailed research gaps and questions will be clearly identified and defined in the last section of the background and literature review chapter (Chapter 2).

1.3. Thesis structure

Chapter 2 provides some background information and comprehensive literature review on the investigated technologies. In particular, Chapter 2 contains: (i) information on nuclear power plants (i.e., conventional and small modular reactors); (ii) background and discussion on current load following operations of the conventional nuclear reactors; (iii) general information and current status of CSP technologies; (iv) information on TES technologies including discussion of their importance in current electricity systems; and (v) explanation and literature review on hybridising nuclear power with renewables and specifically with solar power. The identified research gaps from the conducted literature review and the defined research questions are listed in the last section of Chapter 2 (Section 2.8).

In Chapter 3, the developed thermodynamic and economic models alongside with the collected data in this research are presented and discussed. The first section of Chapter 3 presents the

collected data on the investigated nuclear reactors. Then, the basis of the thermodynamic model for the considered CSP technology is discussed. After that, the formulation and the validation of a range of TES technologies models (steam accumulators, solid heat storage, two-tank molten salt) is presented and discussed. The chapter continues with presenting the modelling procedure of power generation cycles systems and defining the thermodynamic performance indicators that are used in this research. The component costing methods and the formulation of economic models alongside with an overview of economic performance indicators that are used throughout this research are also presented in Chapter 3. Lastly, the formulation and the main assumptions of the whole-electricity system model are listed and discussed.

The thermodynamic and economic assessments of extending a conventional steam-accumulation TES system through the addition of solid (i.e., concrete) heat storage blocks taking an operating direct steam generation (DSG) CSP power plant as a case study are presented and discussed in Chapter 4. The case study covered in Chapter 4 includes performance of parametric analysis to determine the most cost-effective size of the concrete blocks. Moreover, the thermodynamic characteristic of operating both steam-accumulation TES systems (i.e., with and without concrete) are also compared for different direct normal irradiance (DNI) profile inputs. The chapter ends with investigating the economic performance of both compared TES systems for a range of electricity prices.

Chapter 5 involves an assessment of the thermodynamics and the economics of upgrading the flexibility of the current fleet of UK's nuclear power plants (advance gas-cooled reactor (AGR)) through the integration with TES tanks and secondary power generation cycle systems. The study contains: (i) a thermodynamic analysis of three different TES system charging mechanisms; (ii) a design and performance analysis of phase change material thermal (PCM) TES tanks; and (iii) a design and parametric optimisation of secondary organic Rankine cycle (ORC) based power generation systems. Lastly, a comprehensive economic analysis to evaluate the profitability of the upgraded flexibility based on recent UK's wholesale electricity prices is presented and discussed.

In Chapter 6, a combined thermodynamic and economic analysis, from a whole-electricity system perspective, of upgrading the flexibility of power plant (European pressurised reactor (EPR)) through the integration with PCM-based TES tanks and steam Rankine cycle based secondary power generators is presented. The study in Chapter 6 involves: (i) a detailed thermodynamic

modelling and optimisation framework to identify the optimal operating conditions of the primary steam Rankine cycle system, and (ii) the design of modular TES and secondary steam Rankine cycle systems. Chapter 6 ends with a comprehensive analysis and quantification (i.e., for different electricity system scenarios) of the anticipated whole-electricity system economic benefits that could be gained from upgrading the flexibility of the considered nuclear power plant.

In Chapter 7, the design and operation of a hybrid nuclear-solar power plant integrated with two-tank molten salt TES system is presented. The study includes: (i) a cost-based design optimisation of a nuclear-only and hybrid nuclear-solar power plant configurations including the consideration of off-design performance of power generation block components during part-load operations; (ii) a parametric optimisation to size the solar field components and the integrated TES system taking a city in the Sultanate of Oman as a potential location; and (iii) a thermodynamic and economic comparison for the considered power plants for a set of economic parameters and a range of electricity prices.

The summary of main research findings and conclusions, the key research outputs, and the future work recommendations are all presented and discussed in Chapter 8.

Chapter 2

Background and literature review

2.1. Nuclear power plants

Nuclear power, which is carbon-free, reliable, and affordable energy source, plays an important role in providing low-carbon and sustainable power. Nuclear power is the use of nuclear reactions, either fission or fusion, that release a vast amount of energy to generate electricity or heat for other applications. Nuclear power plants (NPP) have been commercially available for electricity generation since the beginning of 1950s. Today, about 11% of the world's electricity is generated by about 450 NPPs [29]. The most common operating NPPs, about 82% of total NPPs, are light water reactors (LWRs), which are classified as either pressurised water reactors (PWRs) or boiling water reactors (BWRs) [29]. LWRs use ordinary water as neutron moderator and coolant. Other types of NPPs are: (i) gas-cooled reactors, which uses graphite as moderator and carbon dioxide as primary coolant, (ii) pressurised heavy water reactors, using heavy water (D_2O) as moderator and coolant, (iii) molten salt reactors, using graphite as moderator and fluoride based molten salt as coolant [30].

NPPs are mostly considered as a baseload electricity source due to their high reliability, high capital costs, and relatively low marginal cost (i.e., operation, maintenance, and fuel) [31]. However, with the development of cost competitive renewables such as wind and solar, NPPs started to compete with renewables in providing the baseload electricity demand [32]. This competition has forced the nuclear industry to develop innovative, more advanced, and potentially cheaper NPPs. These new technologies include small modular reactors (SMR) and advanced modular reactors (AMR).

2.1.1. Small modular reactors

Most of the current fleet of NPPs around the world are approaching the end of their operating lifetime. Therefore, the electricity share provided by these reactors must be replaced either by using nuclear or other energy sources. For example, half of the current NPPs fleet in the UK will retire by 2025 [33]. One viable option for replacement is the consideration of SMRs, which are a smaller, simpler, standardised, and safer type of nuclear reactors. SMRs are

designed to generate electric power up to 300 MW_{el} and can be deployable as a single unit or multi-unit system. The most important feature of SMRs is their modularity, meaning that their components and systems can be fabricated in factories and then shipped and installed at different sites [34]. Through this modularisation concept, SMRs are expected to offer better upfront capital cost affordability and shorter construction times, compared to the conventional NPPs [9]. The SMR technology is selected for the nuclear part in the proposed hybrid nuclear-solar power in Chapter 7 for two main reasons. The first is their comparable power output level to most CSP plants (in the range of 20-300 MW_{el}). The second reason is the growing interest of deploying SMRs due to their expected flexibility and affordability.

There is a wide range of SMR designs, which can be categorised in terms of their coolant type, power range, or temperature range. According to the latest status of SMRs report published by the International Atomic Energy Agency (IAEA), there are over 50 SMR concepts and designs with different types of coolant, neutron spectrum adopted, output power, and operating temperature range [9]. Figure 2.1 illustrates the existing SMR designs and concepts in terms of reactor type, electrical power output, and reactor core outlet temperature.

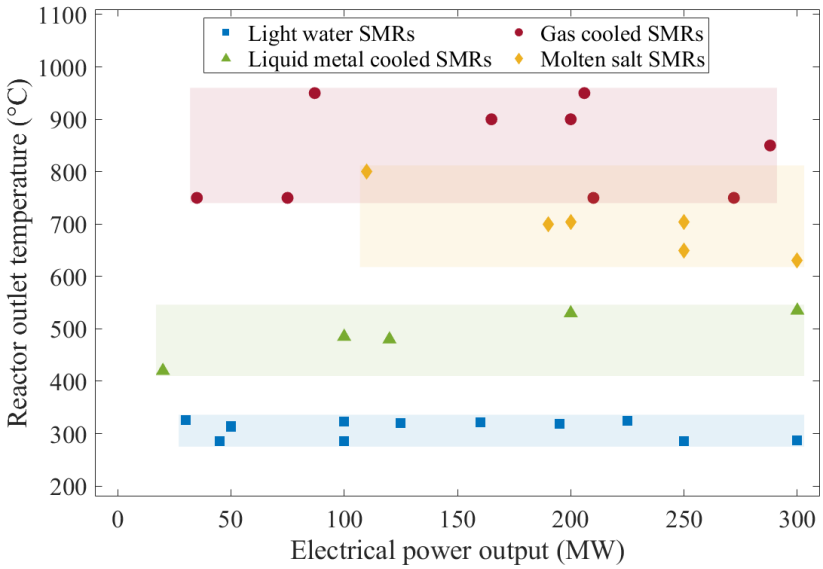

Figure 2.1. Classification of SMR designs in terms of reactor type, electrical power, and core outlet temperature [35,36].

SMRs are designed with a core outlet temperature in the range of 270-950 °C depending on the coolant type [9]. The operating temperature of LWRs based SMRs are between 250-340 °C. This relatively low temperature range is because of the size and the material constraints of the reactor

pressure vessel, which is usually optimised based on the operating conditions of LWRs as well as costs. For both types of LWRs, BWRs and PWRs, the presence of liquid water around the reactor core is necessary for neutron moderation and control. Therefore, the maximum operating temperature and pressure of LWRs is the critical point of water (T_{cr}= 374 °C and P_{cr} = 22.06 MPa).

There are other reactor designs that have much higher core outlet temperature, such as liquid metal-cooled reactors, molten salt-cooled reactors, and gas-cooled reactors. The latter can reach temperatures as high as 950 °C. The high temperature range of these reactors is a result of using other types of materials for neutron moderation such as graphite or Beryllium [37]. In this research, particularly in Chapter 7, LWR-type SMR design is selected for the proposed hybrid nuclear-solar power plant as it is the most operating reactor type as well as the possibility of achieving enhanced cycle efficiency (i.e., reaching temperature higher than 500 °C).

2.1.2. Power flexibility (load following and manoeuvring capabilities of current nuclear power plants)

Load following is varying the power output of a power plant to meet the fluctuating hourly and daily electricity demand. Load following is usually performed by fossil-fuel power plants because of their relativity high variable costs (i.e., fuel costs). In the case of NPPs, it is always preferred to operate them as baseload units at their full rated thermal power output. The main reason for that is purely economic since NPPs have the lowest variable costs (about 12% of the generation cost), especially when compared to the conventional fossil-fuel power plants (about 70-80% of the generation cost) [38]. Moreover, load following operations creates a loss in total revenues by selling lower amount of electricity, which prolongs the recovery of the NPPs capital investment [39]. However, there are some situations in which load following operations of NPPs becomes essential. These situations are when nuclear has a large share in the energy mix, (e.g., France), and when there is high penetration of renewables in the electricity grid (e.g., Germany and UK). Because of these reasons, modern NPPs, including SMRs, are designed with some degree of load following capabilities, but they are limited and not as flexible as those of fossil fuel power plants.

The load following in NPPs is achieved by varying the amount of fuel being burnt [31]. Table 2.1 summarises the control regimes of load following operations in modern LWRs, and the same control techniques are expected to be followed in LWRs type SMRs.

Fast control of reactor thermal power in PWRs and BWRs is achieved by using control rods, which are the most widely used mechanism to control the reactor. However, the approach of control rods is undesirable for large power variation since they deform the core axial power distribution. Moreover, it also affects the axial distribution of ^{135}Xe, which is a very strong neutron absorber [40]. Slow control in PWRs is usually performed by injecting boric acid (strong neutron absorbent) since it takes longer times than control rods to absorb neutrons. Furthermore, the uniform dissolving of boric acid does not affect the axial power distribution [31].

Table 2.1. Power control regimes of LWRs [31].

Power control method		**PWR**	**BWR**
Thermal power control (reactor core)	Fast control	Rod control (above 50% of P_{NPP})	Revolution speed control of reactor circulation pumps (70-100% P_{NPP}) basically $\Delta P_{\mathrm{NPP}}/t \leq 10\%\ P_{\mathrm{NPP}}$/s
	Slow control	Boric acid / de-ionised water injection (below 50% P_{NPP})	Rod control (also, below 70% P_{N}) $\Delta P_{\mathrm{NPP}}/t \leq 10\%\ P_{\mathrm{NPP}}$/min
Power control (turbines)		Turbine valve control, Steam pressure control (T_{coolant} = constant)	Turbine valve control (P_{core} = constant)

There are three important physical effects that limit the feasibility of power variations in LWRs which are, counter reactions, fission product poisoning, and fuel burn up. Furthermore, high temperature and power variations lead to thermo-mechanical stress on the power plant components, which increases maintenance costs and might reduce the lifespan of the reactor [39].

Persson et al. [41] conducted a comprehensive review of the experience with load-following NPPs in France, Germany, Sweden and the USA, as well as of the technical aspects of output changes in NPPs, focusing on the capability of nuclear power plants to complement the fluctuating power supply from renewables in Sweden. A similar study was conducted for nuclear power plants in Germany by Ludwig et al. [42]. Both studies investigate the possibilities of using nuclear power plants, either in Sweden or Germany, for flexible load-following power generation with minimum loads down to 50-65%, concluding that improved flexibility (ranges and rates) are possible with suitable changes such as optimised fuel management, optimised control of manoeuvring and predictive operating strategies [41,42].

Unlike coal-fired plants that can be modulated to some extent according to the demand, nuclear power plants are more suitable for delivering “baseload” electrical power in what is not

conventionally considered flexible generation. Yet, even in this case, flexibility is highly desirable, and efforts have been underway to increase generation flexibility. Modern Generation III (and its evolution, Gen. III+) nuclear reactors are capable of a certain degree of flexibility and load-following operations, with transmission system operators (TSOs) able to define the minimum requirements of such reactors [32,40,43]. The European utility standards require that nuclear power plants are capable of (at least) daily load-cycling operation between 50% and 100% of their nominal capacity, with a rate of change of generation output of 3-5% of nominal capacity per minute [40].

Although new reactor designs and SMRs are expected to have more load flexibility, it is still more economical to run them at full load to maximise their profitability. Thus, due to the challenging physical effects and limitations of reactor control during load following operations and due to the better economical return of always running the nuclear reactor at full rated power, it is more favourable to load follow using other techniques. These techniques include storing excess heat in thermal energy storage (TES) media as proposed by Alameri et al. [17] and Frick et al. [44], using excess power for cogeneration (i.e., algae-biofuel and desalination) as proposed by Locatelli et al. [39], or combine nuclear with solar power and TES system. The first and the last options are investigated in this research.

2.2. Concentrated solar power

Concentrated solar power is a technology that uses mirrors and lenses to reflect and concentrate a large area of solar irradiation onto a small area (i.e., solar receivers) in order to collect high-temperature heat. The collected high-temperature heat is then transferred to a heat transfer fluid (HTF) (e.g., water, air, molten salt and oil) and then used directly or indirectly (through TES system) either to power a turbine and generate electricity or to deliver heat for thermochemical and industrial processes [45]. There are three main types of CSP technologies, illustrated in Figure 2.2, that are commercially available and already installed in several countries. These technologies are: (i) parabolic trough; (ii) solar tower; and (iii) linear Fresnel [46]. The technology behind each CSP type is discussed in Sections 2.2.1 to 2.2.3. Parabolic dish collectors, another CSP technology, are not used anymore due to their higher costs and lower energy storage capabilities [47].

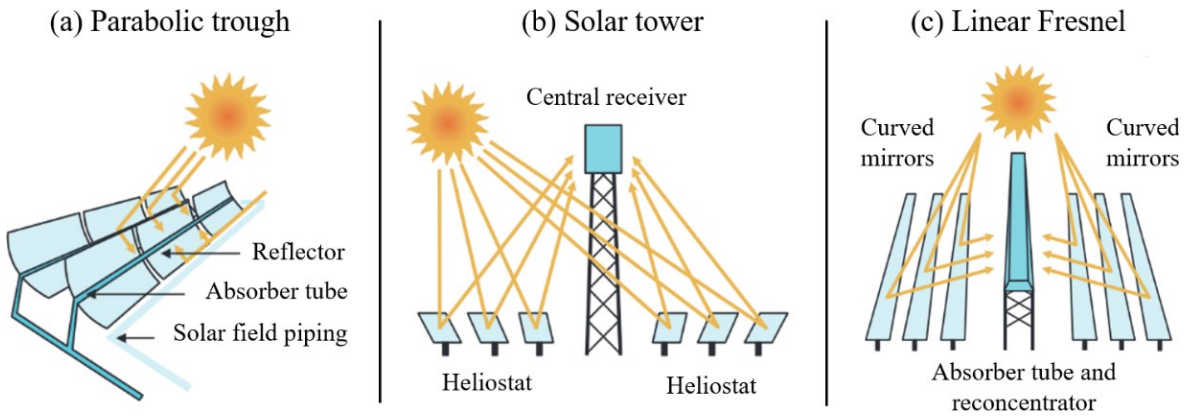

Figure 2.2. CSP solar field types: (a) parabolic trough, (b) solar tower and (c) linear Fresnel [46].

Figure 2.3 shows the breakdown of the global CSP plant capacity by technology type in 2023; Figure 2.3 (a) represents operational CSP plants, while Figure 2.3 (b) covers the CSP plants that are under construction. The presented data were collected from the US National Renewable Energy Laboratory (NREL) website [48]. The current fleet of CSP plants have a total nominal capacity of 6.37 GW_{el}. 75% of this power capacity is generated using parabolic trough technology while the rest, 25%, is generated by either solar tower or linear Fresnel technology. The CSP plants that are under construction are expected to provide an extra capacity of 1.17 GW_{el}, mostly by parabolic trough technology. Therefore, by the end of 2024, the total electrical capacity of installed CSP can reach to 7.54 GW_{el}.

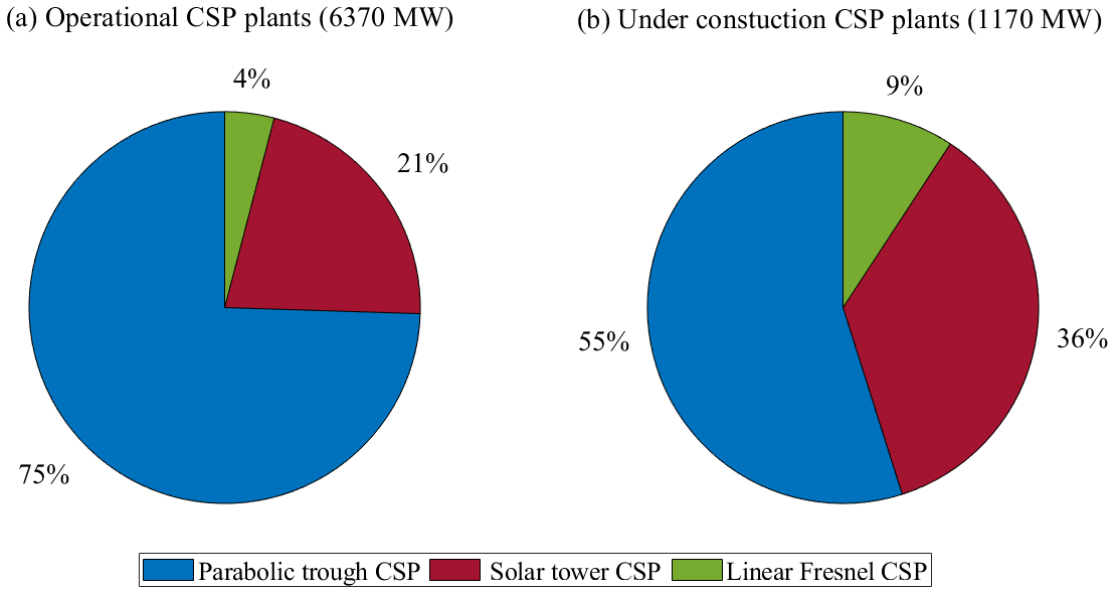

Figure 2.3. Global CSP plant generation capacity by type in 2023, (a) represents operational CSP plants and (b) represents CSP plants under construction.

The temperature and the electrical power output ranges of a number of installed CSP plant with different CSP technologies are shown in Figure 2.4. The temperature range spans from 180 °C to 575 °C, with the highest achieved in solar tower and linear Fresnel technologies due to the ability of attaining higher concentration ratios. The electrical power capacity can reach up to 250 MW_{el}, but most of CSP have power capacities of 150 MW_{el} or less. The CSP size constraint is mainly due to the need of having massive land areas to reach higher capacities.

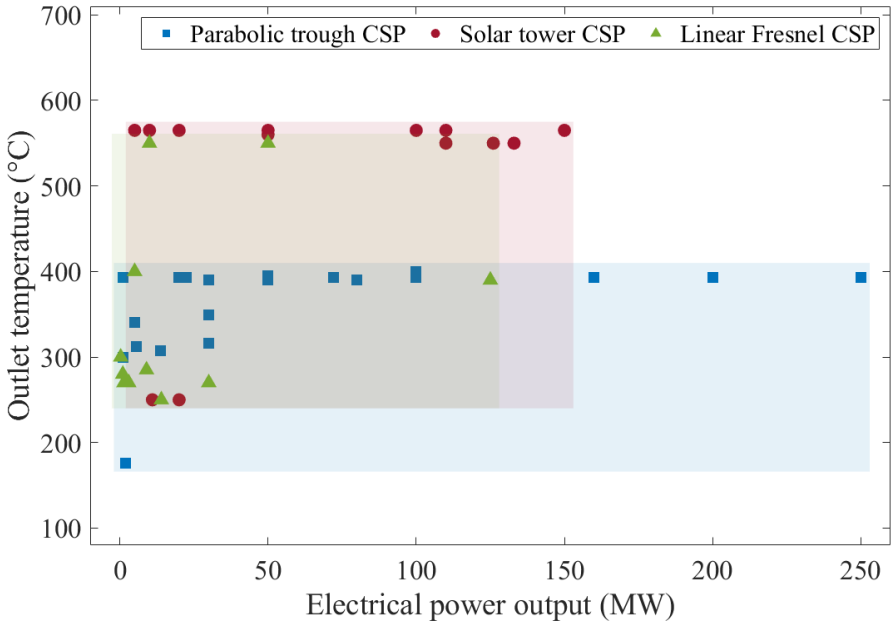

Figure 2.4. CSP plants in terms of technology, electrical power output, and outlet temperature.

2.2.1. Parabolic trough

Parabolic trough CSP consists of a line of rotating reflectors (i.e., mirrors) that are parabolically shaped to reflect and focus sunrays onto an absorber tube that is installed in the focal line of the parabola. The HTF, which is circulating through the absorber tube, gets heated and then used directly or indirectly to generate electricity through power generation cycle system, like in most conventional power plants [47]. The direct method is when the HTF is also the working fluid of the power cycle. This is the case in direct steam generation (DSG) CSP, in which water/steam gets heated and is then used to drive a turbine. In contrast, the indirect method has two separate fluids, HTF and working fluid. The collected heat is transferred between the two fluids using an extra heat exchanger. The most common types of HTF in parabolic trough are synthetic oil, molten salt, and water, and the operating temperature is between 180-420 °C [49]. More details about the performance and the operating parameters of this technology are provided in Section 2.2.4.

2.2.2. Solar tower

The solar tower technology operates by focusing sunlight rays using special sunlight tracking mirrors (i.e., heliostats) onto a receiver at the top of the solar tower. The concentrated solar heat is transferred to the HTF flowing inside the receivers, commonly molten salt or water/steam, which is then used directly or indirectly for power generation, as in parabolic trough CSPs [50]. Solar towers are a growing technology, as indicated in Figure 2.3, due to their ability to reach high temperature levels (up to 650 °C) [47–49]. Such high temperatures are desirable since it has a significant effect in increasing the cycle thermal efficiency. More details about the performance and the operating parameters of this technology are discussed and listed in Section 2.2.4.

2.2.3. Linear Fresnel

The working principle of linear Fresnel CSPs is a combination of parabolic trough and solar tower CSPs. Slightly curved or flat small mirrors, which are usually arranged in long parallel lines, reflect direct sunlight into along absorber tube topped with a second concentrator. Like in parabolic trough CSPs, the HTF gets heated and used for power generation. Linear Fresnel is still a new CSP technology and might compete with the other technologies due to its lower installation costs [47]. The most common types of HTF in linear Fresnel CSP are synthetic oil, molten salt, and water, and the operating temperature is between 250-550 °C [49]. More details about the performance and the operating parameters of this technology are provided in the following section.

2.2.4. Current status of CSP technologies

The main characteristics and the operation parameters of the discussed CSP technologies as well as compatible TES systems are summarised in Table 2.2. The power capacity of CSP plants range from 10 to 260 MW_{el}, which is comparable to SMRs power range. Moreover, the operating temperature range of the current CSP plants is in the range of 250-575 °C. This temperature range makes it applicable to use CSP for different steam heating process (i.e., preheating, evaporating, superheating, and reheating) in the proposed hybrid nuclear-solar power plant. Moreover, there is some ongoing research on designing high temperature solar receivers that would potentially increase the current maximum HTF temperature (to above 1000 °C) [51] as well as using air and supercritical CO_2 as working fluid in the power generation cycle systems (Brayton cycles).

Table 2.2. List of main characteristics and operating parameters of the current and the future CSP technologies as well as compatible TES systems [47–49,51–54].

CSP technology type	Parabolic trough	Solar tower	Linear Fresnel
Plant capacity (MW_{el})	10 - 255	10 - 260	10 - 200
Collector concentration ratio	70 - 80 suns	>1000 suns	>60 suns
Operating temperature (°C)	290 - 550	250 - 650 (possible >1000)	250 - 555
Operating pressure (MPa)	10	10 - 16	5 - 7
Power cycle	- superheated steam Rankine	- superheater steam Rankine - s-CO_2 Brayton (demo)	- saturated /superheated steam Rankine - organic Rankine
Plant cycle efficiency (%)	35 - 38	38 - 42	28 - 35
Heat transfer fluid	- synthetic oil - water/steam (DSG) - molten salt (demo) - air (demo)	- water/steam - molten salt - S-CO_2 (demo) - air (demo)	- water-steam - molten salt - mineral oil
TES system	- direct 2-tank molten salt - indirect 2-tank molten salt - steam accumulator	- direct 2-tank molten salt - indirect 2-tank molten salt - steam accumulator	- direct 2-tank molten salt -indirect 2-tank molten salt - steam accumulator

2.3. Thermal energy storage

Thermal energy storage (TES) systems have been around for a long time, but the interest in storing energy has drastically increased recently because of the growing dependence of renewable sources. TES is designed to store energy in the form of heat that can be used later for power generation or domestic and industrial heating applications. The main objectives of using TES are to balance out the intermittency of renewable sources, to increase the annual capacity factor of power plants, and to improve the power plant's performance and its thermal reliability [55]. Any energy storage system can be described in terms of the following properties, which are defined by the International Renewable Energy Agency (IRENA) [56]:

- *Capacity*: the amount of energy stored in the medium and the size of the storage system
- *Power*: an indication of how fast energy stored can be discharged or charged.
- *Efficiency*: the ratio of energy provided to the energy stored. It accounts for all associated energy loss during storage and charging/discharging periods.
- *Storage period*: the time of energy storage (hours, days, or months for seasonal storage)

- *Charge and discharge time*: time needed for charging and discharging.
- *Cost*: capital and operation cost of energy storage system (currency/Wh_{th}).

These properties are usually considered and evaluated before selecting the most suitable and efficient TES system for the desired application.

There is a growing demand for TES, as reported in a recent study by the International Renewable Energy Agency (IRENA) [26] that predicts that the global market for TES could triple in size by 2030, with an increase from 234 GWh_{th} of installed capacity in 2019 to over 800 GWh_{th} within a decade. Recent research of Cardenas et al. [57] estimated the required heat storage capacity as the penetration of renewables increases, and the timescales in which energy is most efficiently stored. The paper studied the effect that the renewable penetration, allowable curtailment, storage capacity and efficiency have on the total cost of electricity in the UK scenario, concluding that the most needed flexibility service at high solar photovoltaic (PV) and wind energy penetration is the medium duration one, with 4 to 200 h discharge duration.

The role of TES in systems with high renewable penetration becomes even more prominent when considering renewable technologies such as concentrated solar power (CSP). This is evident in Gils et al. [27], who analyse different European scenarios with very high renewable penetrations and discuss the economic and technical issues. The advantages of the application of TES over batteries in combination with large-scale thermoelectric power plants were also highlighted by Ma et al. [28]. According to that analysis, the use of TES in combination with conventional power plants allows to economically support variable renewables at larger capacity and for longer discharging times than current battery storage technologies or hydropower storage.

TES technologies can be classified in terms of storage mechanism (sensible, latent, and thermochemical as illustrated in Figure 2.5) as reported in Ref. [25]. These storage mechanisms are described in the following sections.

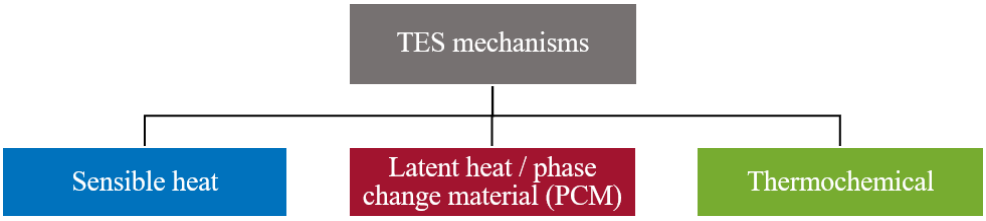

Figure 2.5. Classification of TES systems based on mechanism.

2.3.1. Sensible heat

Sensible heat is the simplest heat storage mechanism in which energy is stored by heating or cooling the storage medium without any phase change. It only utilises the temperature change (ΔT) and the medium's specific heat capacity (c_p) during the process of charging or discharging heat. The amount of stored heat, Q, can be expressed by:

$$Q = \int_{T_1}^{T_2} m\, c_\mathrm{p}\, \mathrm{d}T = m\, c_\mathrm{p}\, \Delta T \tag{2.1}$$

where m is the storage media mass, T_1 represent the initial temperature and T_2 the final temperature of the storage material

The storage media can be in the liquid state (e.g., water, oil, organic liquid, or molten salt), in the solid state (e.g., concrete, metal, rocks, fire bricks, etc) or in the gas state. The selection of the storage media highly depends on the operating temperature of the application and the average mass density and heat capacity of the storage media. For example, water is a good energy storage medium since it has a high specific heat capacity, and it is inexpensive. However, it not preferred to be used for high TES temperatures (T > 100 °C), as it would have to be pressurised in order to remain liquid, which incurs higher costs. Therefore, other TES media are usually considered for higher temperature applications such as oil, molten salts, and liquid metals [55]. Solid state media can operate at even higher temperatures (e.g., up to 1200 °C for magnesia fire bricks) and they usually have a higher average heat conductivity compared to liquids [25].

2.3.2. Latent heat

Latent heat TES, also known as phase change materials (PCMs), involves a phase change of the medium when heating or cooling. The phase change process is an isothermal process meaning that it takes place at the same temperature point. Such process is illustrated in Figure 2.6. For example, when a material reaches its melting temperature, it absorbs a specific amount of heat in order to physically change from solid to liquid. This amount of heat is called latent heat. The same concept works for vaporisation (liquid-to-vapor transition), and crystallisation (solid-to-solid transformation). Latent heat storage processes are usually associated with sensible heat storage processes, as a temperature change occurs before and after reaching the material's phase

change temperature [58]. The amount of latent heat and sensible heat stored in a material that undergoes a phase change process is expressed by:

$$Q = m\left(\int_{T_1}^{T_{PC}} c_p \, dT + \Delta h_{fus,vap} + \int_{T_{PC}}^{T_2} c_p \, dT\right) \tag{2.2}$$

where $\Delta h_{vap,fus}$ is the specific enthalpy of fusion or vaporisation and T_{PC} the phase change temperature (i.e., melting or evaporation temperature).

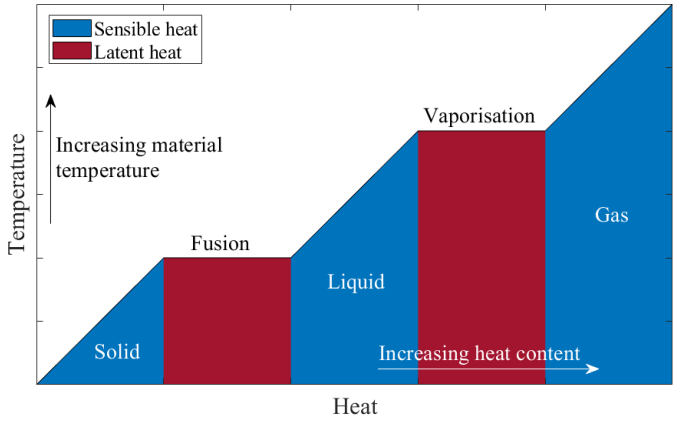

Figure 2.6. Materials temperature profile and formation with respect of supplied or extracted heat.

2.3.3. Thermochemical

Thermochemical energy storage involves a chemical compound that is able to store and release heat by reversible endothermic/exothermic chemical reaction process [55]. Figure 2.7 simply illustrates the concept of storing and discharging heat of in a thermochemical store [59].

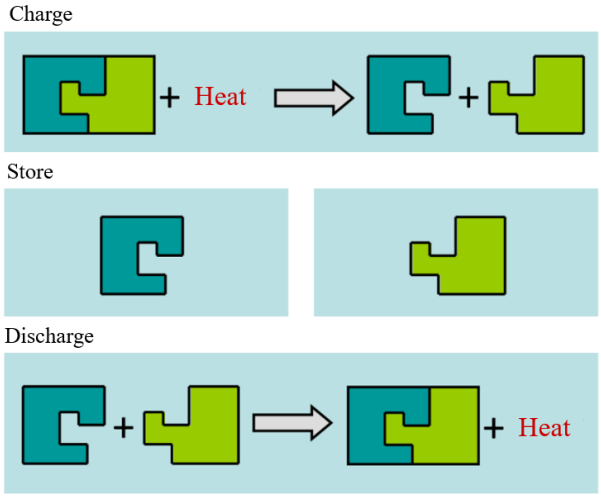

Figure 2.7. Illustration of thermochemical energy storage concept [59].

During a charging process, the energy consuming chemical reaction stores energy to form new chemical bonds. The stored energy is then released during a discharging process by undergoing a reversible chemical reaction where reactants go back to its initial state and bond structure.

2.4. Power generation cycles

The Rankine cycle is the dominant power cycle used in both CSP and nuclear power generation applications. The basic Rankine cycle consists of four main processes: compression (pumping) of the liquid working fluid to high pressure, isobaric heat addition (evaporation), expansion of the vapour to lower pressure through a turbine, and isobaric heat rejection and condensation back to the initial state. Basic Rankine cycles are usually upgraded to more complicated cycles for efficiency enhancements by following a Carnot engine efficiency concept. Some upgraded cycle configurations are superheated Rankine cycles, reheated Rankine cycles, and regenerative Rankine cycles. Most power plants adapt at least one of these efficiency enhancement methods to improve the overall thermal efficiency.

Candidate working fluids for Rankine cycle are water/steam and organic fluids. Steam, in subcritical conditions, is the most common working fluid in NPPs and CSP plants. Despite the superheating process and the existence of energy recovery devices such as feedwater heaters, the maximum thermal efficiencies of CSP facilities are in the range of 28-42%. Achieving higher thermal efficiency is a challenge due to certain turbine material concerns and issues that appear when steam temperature exceeds 627 °C [60]. Organic Rankine cycles (ORCs) are commonly used in medium-temperature and waste heat recovery applications. ORCs have thermal efficiencies in the range of 10-20% and can be combined as bottoming cycle with high temperature steam cycles for better heat recovery [60].

2.5. Direct steam generation concentrated solar power with TES

Direct steam generation (DSG) CSP is an option that uses water as HTF in the solar receivers and as working fluid in the thermodynamic power generation cycle [61]. The use of a single fluid offers a number of benefits such as: (i) no need of heat exchangers to transfer heat between the HTF and the working fluid, which is the case in most conventional CSP plants [62–64]; (ii) enhanced cycle thermal efficiency by achieving higher steam temperatures [62–64]; (iii) no

environmental risk of fire and leakage [64]; and (iv) lower investment and operation & maintenance costs due to the elimination of heat exchangers [64].

Most solar power plants are coupled with TES systems that store excess solar heat during daytime and discharge during night or during cloudy periods [55]. In DSG CSP plants, the typical TES options include: (i) direct steam accumulation; (ii) indirect sensible TES; and (iii) indirect latent TES [62]. Option (i) is considered as a direct method because the thermal energy is stored directly in the HTF. However, options (ii) and (iii) are indirect since thermal energy is stored in another storage medium such as a solid-state storage medium, a liquid-state storage medium, or PCMs [62].

Steam accumulation is the simplest TES technology for DSG as steam is directly stored in a storage pressure vessel, i.e., steam accumulator (SA), in form of pressurised saturated water [65]. Discharging from SAs usually takes place from the top part of the vessel as it is filled with saturated steam at the saturation pressure. Steam accumulation is commercially available and was implemented in several operating DSG power plants, such as the PS10 plant in Spain, and the Khi Solar One plant in South Africa [49]. A major disadvantage of steam accumulation is the relatively low temperature of the outlet saturated steam (i.e., a maximum temperature of 374 °C) when compared to the operating temperatures of DSG plants, which can reach up to 550 °C [66]. Reaching the maximum temperature of 374 °C is not a cost-effective option either as reaching this temperature in saturated conditions also means reaching the water critical pressure (22.1 MPa) and designing a pressure vessel that could withstand this high pressure requires expensive materials and/or larger and thicker, in terms of wall size, pressure vessels [66]. The low steam temperature decreases the cycle thermal efficiency and increases the risk of damaging steam turbines at part-load operating conditions [67]. Therefore, steam-accumulation TES systems are usually coupled with a superheater to increase the temperature of the discharged saturated steam (i.e., above the saturation temperature) before entering the steam turbine. The superheating process can be performed using: (i) another group of higher temperature and pressure SAs and a superheating heat exchanger; or (ii) higher temperature sensible or latent TES [65].

Prieto et al. [68] compared the thermodynamic and economic performances of the two aforementioned superheating options. Two tanks of molten salt are employed for the superheating process in the extended configuration. It was concluded that the conventional option is more feasible and more cost-effective than using the combination of SAs and molten-

salt tanks for energy storage, especially for storage durations of less than 6 h. It is mainly due to the added complexity, the high melting point, and high costs of molten-salt storage systems. Furthermore, Bai et al. [69] analysed the thermal characteristics of combining SAs with concrete as superheating storage media, proving the feasibility of this combination. However, the performance of this arrangement was not evaluated at the whole power plant level, and the thermodynamic and economic potential of this combination is not clear yet.

Moreover, several studies proposed and tested different sensible heat and latent TES options for DSG [49,63,70–74], but SAs were not an option in those TES configurations. For example, the use of PCM-based TES systems is suggested by Birnbaum et al. [63] as well as by Guédez et al. [74]. Both studies showed a potential increase of profitability and capacity factors of the studied DSG plants. Furthermore, a study performed by Li et al. [75] suggested the implementation of secondary organic and steam Rankine bottoming cycles to maximise the overall power output from heat stored in SAs. The study also suggested the use of extra low-pressure SA, in addition to the existing high-pressure SA. This extra SA increases the total storage capacity by 360% compared to having a high-pressure SA only. It was concluded that adding a secondary power generation system and a low-pressure SA improves the overall cost-effectiveness of the DSG plant.

There are many options for solid-state sensible TES to be considered in the steam accumulator-sensible TES system. These include concrete, cast iron, cast steel and silica fire bricks [76]. However, concrete has proven its capability of high-temperature heat storage (up to 550 °C), its ability to withstand large number of charging/discharging cycles, and its relatively low cost through testing [77–80]. The use of concrete for TES is already commercially available. It is used in the thermal battery technology developed by EnergyNest [81], proving the validity and applicability to utilise concrete for TES applications.

Nevertheless, none of the aforementioned previous research compared the thermodynamic performance and the economic returns of operating the two steam-accumulation options in a DSG CSP power plant. Moreover, these research studies did not evaluate the possibility of achieving enhanced cycle efficiency with the steam accumulator-solid heat TES option during the discharging phase, and did not compare the cost and the economic return of both options

2.6. Nuclear power generation with TES for increased flexibility

Combining nuclear reactors with TES systems for enhanced flexibility and increased revenues has been previously investigated in the literature [14–18,82–92]. For example, Carlson et al. [82] investigated the impact of integrating a PWR, Westinghouse AP1000, with TES tanks. The TES tanks are charged by diverting excess steam from the steam generator during low demand times. The tanks are discharged to the main nuclear-powered Rankine cycle system that includes turbines that can be operated at about 10% higher power output than the design point. Several TES materials such as concrete, silica and PCM were considered. It was concluded that such integration could potentially increase the capacity factor by up to 10% compared to operating the same power plant with a steam bypass option. Park et al. [83] performed a technoeconomic study on integrating a nuclear power plant with liquid air energy storage system (LAES). In that study, charging is performed by diverting steam from the nuclear-powered cycle to drive an external steam turbine driven compressor utilised for air compression in the LAES, while discharging is performed similar to conventional LAES systems. This nuclear-LAES integrated system resulted in increasing the capacity factor of the nuclear power plant by 3% and decreasing the LCOE of the LAES from 220 $/MWh_{el}$ (i.e., for standalone LAES) to 183 $/MWh_{el}$. Furthermore, Amuda et al. [15] explored the option of combining a currently operating a LWR based power plant (APR1400) with a packed-bed (i.e., crushed rocks) TES system. In the proposed configuration, which was selected based on an optimisation and exergy study performed by Kluba et al. [16], the TES is utilised to provide extra feedwater heating in the primary power generation cycle, which results in 135 MW_{el} of additional electrical power when the reactor is operated at full rated thermal capacity. This additional power can be supplied to the electricity grid during high demand to increase revenues. Other TES systems including molten-salt tanks [17], firebrick resistance-heated energy system [18], geothermal heat storage [84], cryogenic air energy storage [85] and hot rock storage [86] were also considered and discussed.

There are also several studies that considered the option of coupling nuclear reactors not only with TES systems but also with secondary power generators for extra peak power generation. Carlson et al. [87] conducted a thermodynamic analysis of coupling the AP1000 reactor with a TES system and secondary power generation cycle (steam Rankine cycle). Four different configurations based on the location of the TES system (i.e., where steam is diverted for charging

stream) and whether stored thermal energy is discharged using the primary or the secondary power generation cycle. It was found that the option where TES tanks are charged by heat from steam diverted after the moisture separator/reheater and then discharged using the optimised secondary power generation cycle gives the greatest thermodynamic performance compared to the other considered options. This charge/discharge option resulted in increasing the capacity factor of AP1000 by 15% compared to the bypass option that is generally used for baseload flexibility. Carlson et al. [88] also performed a parametric study investigating the thermodynamics and the cost performance of coupling the same reactor with a TES system and a secondary Rankine cycle system. Three configurations based on the TES charge/discharge mechanisms and duration were investigated, and two of these configurations could provide more than 1.5 times the nominal power output of 1050 MW_{el} due to the use of secondary power generators. Moreover, the integration of nuclear power plant with a cryogenic-based energy storage technology and secondary power generation unit was assessed by Li et al. [89]. The studied configuration showed the ability of generating a total net output power of 690 MW_{el} during peak times, which is 2.7 times the baseload power output of 250 MW_{el}.

In terms of economics, Forsberg [90] investigated the potential economic benefits of integrating LWRs with heat storage and an auxiliary fuel combustion heater. The combustion heater was added to assure a continuous peak electricity production, even when the stored heat in the TES system is fully depleted. It was concluded that the economics of this combination is dependent on three conditions: (i) the cost of heat storage need to be lower than the cost of electricity storage technologies, (ii) the cost of the nuclear reactor and the steam generators need to be higher than the costs of power generation cycle components, and (iii) low-cost boilers should provide assured peak-load capacity at lower costs than competing technologies such as combined cycle gas turbines (CCGTs). Furthermore, Carlson et al. [93] evaluated the profitability of operating such combination (with and without secondary generators) in deregulated US electricity grid. The study concluded that adding TES systems and secondary generators to nuclear reactors increases the total revenues by 3-8% and the internal rate of return (IRR) by 25-35%.

Another study performed by Borowiec et al. [94] focused on the potential economic benefits of running a 3.5 GW_{th} nuclear reactor coupled with a TES system in five different electricity markets in the USA. The study considered various market scenarios based on the shares of renewables (i.e., wind and solar) and several capacity prices. It was concluded that profitability can be

attained but it is highly dependent on: (i) the type of electricity markets; (ii) the share of renewables in the system; (iii) the size of installed capacity of nuclear and renewables; and (iv) the installation costs and the storage materials of the attached TES system. Moreover, Duan et al. [95] performed a stylised least-cost analysis of flexible nuclear power in decarbonised electricity systems while considering wind and solar resources worldwide. The study investigated the role of conventional and flexible nuclear power in 42 country-level electricity systems with carbon emission reduction constraints ranging from 50% to 100%. This study looked at different investment cost levels for nuclear plants and different wind power capacity factors. It was found that wind and solar generation provide the bulk of electricity in most of the studied regions with moderate carbon emission reduction targets (i.e., less than 80%) as this still allows some room for fossil-fuel generation sources in the electricity mix. However, the need for flexible nuclear, enabled through integration with TES, becomes critical with more stringent carbon emission constraints, as wind and solar cannot cost-effectively provide reliable power due to their intermittency and high cost of electricity storage.

All aforementioned research demonstrated the potential of flexible and profitable nuclear operation with the integration of TES, while keeping the reactor output at full rated power. However, integrating the current and future fleet of UK's reactors with TES systems and analysing their profitability were not considered. Moreover, the gained benefits, from the electricity system perspective, of replacing conventional NPPs with enhanced flexibility ones (integrated with TES systems and secondary generators) has not been thoroughly studied and quantified yet.

2.7. Hybrid power plants

A hybrid energy system, as defined by Ruth et al. [21], is a single facility which takes two or more energy resources as inputs and produces two or more outputs, with at least one being an energy commodity such as electricity or transportation fuel. The two or more energy resources are physically coupled to generate output by dynamically integrating energy and mass flows among their shared components. According to Peterseim et al. [96], hybrid systems can be classified, in terms of the number of shared components and equipment into three categories, light, medium, and strong hybrid synergies. Light hybrids share minimal plant infrastructure and the combined energy resources can operate separately. In medium hybrids, the two energy resources are physically connected and share major plant components such as turbines and condenser. However, the host

plant, which has all the major components, can operate separately without the need of the other energy resource. An example of a medium hybrid is combining CSP with a coal or a natural gas power plant, as in the Kuraymat power plant in Egypt [97]. In this hybrid power plant, CSP heat is used for preheating or superheating the working fluid to increase the amount of generated power. However, the CSP heat share is lower than 10% and the base natural gas power plant can operate without the CSP components. In strong hybrid power plants, the two or more energy resources are physically connected and share most of the major equipment, and the energy contribution of each is at least 30%. An example of strong hybrid is integrating solar with combined cycle gas turbines. This strong hybrid systems are already implemented in few North African countries [98–100]. In these solar-combined cycle gas turbine power plants, the solar component provides a significant amount of heat for the bottoming steam cycles, which increases the total power output and enhances the thermal-power conversion efficiency by several percentages.

2.7.1. Hybrid nuclear-renewable power plants

Numerous types of hybrid nuclear-renewable power designs were proposed and analysed. In most cases, renewable energy sources such as: wind, solar, hydroelectric, biomass, geothermal are combined with nuclear units. These hybrid system designs are implemented to utilise the total generated thermal energy in several application such as power generation, district heating, chemical processing, etc.

The overall aim of the hybridisation is to increase power variation flexibility, reduce greenhouse gas emissions, and get faster return of capital investment. Ruth et.al. [21] proposed combining nuclear plants, as SMRs, with various types of renewables such as wind, biomass, and CSP. The hybrid system was designed to offer flexible power operation while running the SMR at full load and using the excess heat to produce a second energy-intensive chemical product. Such combinations can potentially secure and deliver sustainable energy if installed in large numbers. Garcia et al. [19,20] dynamically analysed a hybrid nuclear-wind energy system in terms of operation flexibility and cost. The analysed hybrid system utilises heat produced from the nuclear reactor to balance fluctuating wind-generated electricity. The excess nuclear energy is used in a chemical plant complex. It was concluded that the hybrid system provides better grid flexibility and greater profitability. Suman [101] also reviewed the hybrid nuclear-renewables concept, analysing several combinations. The study highlighted that the integrated systems

would potentially overcome the drawbacks of both energy sources when coupled through informatics linkages and would also improve public perceptions of nuclear power [101]. Another energy hybridisation concept was developed by Papaioannou et al. [102], in which nuclear and wind are coupled for electricity generation, biomass processing, and hydrogen production. In this concept, nuclear unit operates at full load either to generate electricity or to supply heat for a biomass processing plant. The analysis concluded that the hybrid system would have better energy utilisation at lower costs compared to individual energy sources [102]. The abovementioned research covers the dynamic performance analysis, the overall optimal operations, and the costs of proposed hybrid energy systems. However, the thermodynamic aspects of the hybrid power plants were not intensely studied and analysed.

2.7.2. Hybrid nuclear-solar power plants

The concept of hybrid nuclear-solar power plant has been introduced and investigated in the literature [11,12,23,24,103–107]. A strong nuclear and solar hybridisation concept, named NuRenew energy park, was proposed by Petrovic [103]. NuRenew is a molten salt-based hybrid power plant, which consists of molten-salt cooled nuclear reactor, molten salt based CSP, and a molten salt TES system. The basic idea of NuRenew is collecting and storing heat in the TES unit using both nuclear and solar as heat resources. The stored heat is then used for different applications like power generation, high temperature industrial process, desalinations, etc. Such a highly integrated power plant would potentially increase the energy supply reliability and decrease the levelised cost of electricity (LCOE), compared to standalone NPP or CSP. The nuclear-solar hybridisation concept was introduced by Petrovic [103], but it was not thermodynamically analysed or investigated in detail.

A detailed thermodynamic study of a hybrid nuclear-solar power plant was performed by Popov et al. [11]. The study also compared the performance of a hybrid power plant to a standalone NPP and a standalone CSP. The analysed hybrid power plant consists of a CSP (solar tower type) and an SMR integrated with two molten-salt storage tanks. In this configuration, during the sunlight, the solar tower central receiver collects solar heat and transfer it to the heat transfer fluid (molten salt). The heated molten salt is then stored in large tanks at 565 °C. The total heat input in this configuration is 245 MW_{th} (in particular, 85 MW_{th} from solar and 160 MW_{th} from nuclear). The analysis was performed using the nominal operating conditions such as the amount of heat generated, steam mass flowrate, pressure and

temperature of the SMR unit. The high-temperature molten salt is utilised to superheat the saturated steam outflowing from the nuclear-powered steam generator from a temperature of 255 °C to 555 °C. The molten salt is also used to reheat the exhaust steam outflowing from the high-pressure turbine from a temperature of 327 °C to 555 °C. The analysis results show that the thermal cycle efficiency could be enhanced by 36%, from 27.5% to 37.5% and the amount of generated electricity could be increased by 109%, from 43.9 MW_{el} to 91.8 MW_{el}.

Popov et al. [11] also performed an annual power simulation of the hybrid system to evaluate its capacity factor during low or no solar heat inputs. During those times, the capacity factor drops to about 32.0% while it can reach values as high as 97.6% during summer times (i.e., abundant sunlight). The low-capacity factor is caused by the decreased total solar heat input and by the reduced nuclear heat input (about 40% of nominal heat). In terms of cost, the study showed that there is a high potential of capital cost saving due to the shared operation of most power cycle components (i.e., steam turbine, feedwater heater, condenser) by both heat inputs. Moreover, the hybrid system generates more power which could result in a faster return of capital investment. A similar hybrid system was also investigated by Popov et al. [12], in which a parabolic trough type CSP integrated with molten salt TES system was combined with NuScale SMR. The same potential cycle efficiency enhancements and LCOE reductions were observed.

Son et al. [24] investigated the feasibility of combining micro modular reactor (MMR) with a solar tower CSP and molten salt TES system to run a supercritical CO_2 Brayton cycle-based power generation block. The overall aim of proposing this hybridisation concept was to reduce the CSP solar field area (i.e., more compact for small islands) and to increase the capacity factor and the electricity fulfilment ratio of the CSP plant. The study shows promising thermodynamic results which highlights that CSP can benefit from such integration in terms of smaller field size and higher capacity rations. Son et. al [23] extended their study previous study, Ref. [24], by redesigning the hybrid system based on optimising the solar to nuclear ratio and tracing the change in LCOE. The extended study also included sensitivity analyses with respect to five variables which are: nuclear to solar heat, ratio, DNI profiles, nuclear island cost, discount rate and electricity demand ratio. The authors have concluded that the hybrid system is cost competitive when compared to a standalone CSP plant and their study also showed that hybrid nuclear solar can be an option for isolated islands. However, both studies considered a micro scale reactor and CSP system (less than 25 MW_{el}), and the operation of such plant were not presented.

Zhao et al. [104] proposed a conceptual design of a hybrid nuclear-solar power system integrated with molten-salt packed-ped thermal energy TES system. The proposed configuration consists of a molten-salt SMR with a nominal thermal capacity of 125 MW_{th} and a solar tower CSP, in which both supply heat to in integrated TES tank. The other end of the TES tank is connected to a power generation block to provide on-demand power supply. The performed performance analysis concluded that such hybridisation concept can be considered as a reliable source of energy with high flexibility capabilities. Their study did not cover the cost and the economics of the hybrid system, nor the design and the operation of the power generation block.

The concept of hybrid nuclear-solar power is also investigated by Naserbegi et al. [105]. In his study, this concept was used for cogeneration of electricity and fresh water (i.e., desalination). The proposed configuration consists of an SMR (NuScale) that is utilised, as heat input, to evaporate the working fluid and a solar tower CSP field, which is utilised to superheat the working fluid and also to supply heat to the coupled desalination plant. The study concluded that adding the solar powered superheater can increase the gross electrical output by 48% (from 47 MW_{el} to 70 MW_{el}) and the cycle efficiency by 12% (from 27% to 30.2%) when compared to a standalone nuclear reactor. The study performed by Naserbegi et al. [105] supports the possibility of achieving enhanced thermodynamic performance with the hybridisation concept but it did not include comprehensive cost and economic analysis.

All the aforementioned studies highlight the potential thermo-economic benefits of the nuclear solar hybridisation concept that could deliver flexible power, to some degree, while operating the nuclear reactor at full rated thermal power to maximise revenues. However, the studies did not include any design of the most-effective power generation block size and did not optimise the operation of the hybrid power plant during part-load operations.

2.8. Summary of research gaps and research questions

Decarbonising the energy sector is a challenging task, especially with other challenges related to energy security and affordability. In this context, large-scale thermal power plants such as nuclear and solar energy can play a major role in reducing the current carbon emissions while providing reliable and flexible electricity. Based on the conducted literature review on nuclear power plants, CSP plants and TES technologies, there are four major research gaps that can be

highlighted and each one of them is used to develop a research question that should be answered, to some extent, in this thesis. The identified research gaps are the following:

- **Research Gap 1**: In DSG CSP plants, water/steam is usually utilised as a heat transfer fluid, a storage media and a working fluid for the power generation cycle system. However, storing steam in steam accumulators is limited and might not be the most economical and efficient TES system for DSG CSP plants. In this context, the combination of steam accumulators and sensible (hazard free) heat storage system might offer more efficient and cost-effective solution when compared to a standalone steam-accumulation TES system. However, such combination has not been comprehensively evaluated, both thermodynamically and economically, in previous studies. Also, this combination has never been compared to a standalone steam-accumulation TES system. Therefore, investigating such combination of TES systems is crucial to identify the potential benefits that could result from deploying such system in DSG CSP plants.
- **Research Gap 2**: Flexible nuclear power is becoming more relevant, especially in electrical power grids that have high penetration of fuel-free and variable renewable energy sources as they have the advantage in meeting the baseload demand. However, operating nuclear reactors in load following modes is not very economical due to their high capital costs. Thus, there is a need to investigate the options of enhancing the thermodynamics and the economic returns of operating nuclear reactors at load following modes. In this context, investigating the available options of upgrading the flexibility of the current UK's nuclear power plants fleet (mostly AGRs) is important, especially with the increasing share of renewables in the UK's grid. This analysis has not been discussed in the literature.
- **Research Gap 3**: As the UK is still considering government-supported models for investing in nuclear power projects as part of the overall effort to achieve the objective of net-zero greenhouse emissions by 2050 under the Climate Change Act [2,3]. It is crucial to know the limits and the available options of upgrading the flexibility of the future fleet of nuclear reactors, not only from a technology perspective, but also from a whole-energy system perspective. Therefore, identifying and quantifying the potential whole-energy system benefits of enhancing the flexibility of future nuclear reactors helps the decision makers, to some extent, to know how nuclear would compete and perform with other energy sources. All this content has not been captured in the literature and it would be beneficial to know the position of nuclear in future low-carbon electricity systems.

- **Research Gap 4**: The feasibility of hybridising nuclear with solar power and integrating them with a TES system has been investigated in the literature. The performed research shows that such hybridisation concept could enhance the flexibility and the efficiency of LWRs as well as increase the reliability and capacity factor of CSP plants. There is a need to comprehensively investigate the thermodynamics and economics of this concept, and to find the optimum size of the integrated TES system that is suitable for a specific location. Moreover, it is also useful to evaluate the deployment of such hybrid system in the Gulf countries as these countries have abundance of sun rays and they are considering to heavily investing in green hydrogen production in order to diversify their energy mix, as well as to boost their national income.

The four research questions developed from the identified research gaps are:

- **Research Question 1**: Should DSG CSP plants be integrated with a TES system that consists of steam accumulators only or the one that combines steam accumulators and solid heat storage units? What are the thermodynamic and economic benefits of both systems?
- **Research Question 2**: What are the available options of upgrading the flexibility of the current fleet of UK's reactors? Would it be economically attractive to proceed with such upgrade?
- **Research Question 3**: What are the available options of enhancing the flexibility of potential future fleet of UK's reactors? What are the whole-electricity system economic benefits that could be gained from proceeding with such flexibility upgrade?
- **Research Question 4**: To what extent is the hybrid nuclear-solar power plant is flexible? What are the thermodynamic and economic benefits that could be gained from such integration?

To answer these research questions, several modelling tools have been developed and many data sets were extracted from the literature, which are discussed in detail in Chapter 3. The listed research questions are considered in Chapters 4 to 7. In particular, Research Question 1 is exclusively considered in Chapter 4, where two steam-accumulation TES options are thermodynamically and economically compared taking a currently operational DSG CSP plant as a case study. The design and the thermodynamic analysis of the available option of enhancing the flexibility of the current and future fleets of UK's reactors, which answers Research Questions 2 and 3, are discussed in Chapter 5 and Chapter 6. The whole system benefits of added flexibility that is part of Research Question 3 is considered in Chapter 6. Finally, the design and the technoeconomic evaluation of deploying a hybrid nuclear-solar power plant, which answers Research Question 4, is investigated in Chapter 7 where a city in the Sultanate of Oman is selected as a case study.

Chapter 3
Methodology

The methodology used throughout this thesis is presented and discussed in this chapter. First, the collected data of the considered nuclear reactors and the modelling of the nuclear reactors as heat sources are presented in Section 3.1. The modelling procedure for the considered CSP technology (solar tower) alongside with the main assumptions and input data are presented and listed in Section 3.2. The solar tower model was used to estimate the hourly solar thermal power that is absorbed in the solar receiver for a given direct normal irradiance (DNI) profile.

The design procedures and the model descriptions of the considered TES systems are covered in Section 3.3. The modelled TES technologies include steam accumulators, solid heat storage and two-tank molten salt. The first two technologies are implemented in the case study discussed in Chapter 4, whereas the two-tank molten salt TES system model is implemented in the study covered in Chapter 7. The design procedure of the phase change material (PCM) thermal tanks that are used in Chapter 5 is presented in Appendix A.

The generic modelling procedure and the main assumptions of the different power generation cycle systems in this thesis are described in Section 3.4. The formulated power generation cycle system models are quasi-steady, and they were formulated based on the energy and mass balance equations. Moreover, the formulated cycle models take into consideration the off-design performance of the power generation cycle components during part-load operations, which is covered in Section 3.4.2. It should be noted that main power generation cycle model inputs and other specific assumptions of each designed power generation cycle system are listed and discussed in the first sections of the relevant chapter.

The costing methods used to estimate the capital costs and other costs of the designed power plants and TES systems in Chapter 4 and Chapter 7 are presented and discussed in Section 3.5. The key thermo-economic indicators used to compare the performance of the designed power plants are defined in Section 3.6. Lastly, the description and the formulation of the whole-electricity system investment model (WeSIM) used in Chapter 6 is covered in Section 3.7.

Unless specified, all thermodynamic and economic modelling tasks and simulations in this research were performed using MATLAB [108], and all water/steam and organic fluids thermodynamic properties were obtained from the National Institute of Standards and Technology (NIST) database using the REFPROP interface (more information in Ref. [109]).

3.1. Nuclear reactor data

All nuclear reactors in this thesis are modelled as continuous heat sources that supply the power generation cycles with heat to generate electricity. There are three main reactors that are investigated in this thesis, which are advanced gas-cooled reactor (AGR), European pressurised reactor (EPR), and NuScale. The first two reactors are large and conventional nuclear reactors. The AGR is already operated in the UK (i.e., 14 AGRs are currently under operation [110]), while the EPR will be soon operated in the UK (i.e., currently under construction at Hinkley Point C, and is also the choice for the potential future construction of Sizewell C [111]). The flexibility analyses of both reactors are presented in Chapter 5 and Chapter 6. The third reactor, which is NuScale, is involved in the design and analysis of the hybrid nuclear-solar power plant that is discussed in Chapter 7. The NuScale reactor was selected since its design is already approved and certified by the United States Nuclear Regulatory Commission (NRC) – first SMR approved by the NRC – and it is ready to get commercialised in the next few years [112]. The key thermodynamic parameters of the three reactors are listed in Table 3.1.

Table 3.1. Key operation parameters of investigated nuclear reactors and steam generators.

Parameter	**AGR [113]**	**EPR [114–116]**	**NuScale* [11,117–119]**
Reactor thermal power (MW_{th})	1570	4520	250
Steam generator inlet temperature (°C)	156	230	149
Steam generator outlet temperature (°C)	538	293	306
Steam generator inlet pressure (MPa)	21.8	8.3	3.8
Steam generator outlet pressure (MPa)	15.9	7.5	3.5

* *Listed parameters are for a single NuScale module.*

All of the abovementioned reactors are attached to steam generators, which is a heat exchanger that transfer the heat between the primary reactor fluid that flows into the reactor vessel and the working fluid of the power generation cycles. The listed parameters in Table 3.1 were used as inputs to calculate the cycle working fluid mass flowrate based on the following expression:

$$\dot{Q}_{\mathrm{SG}} = \dot{m}_{\mathrm{wf}} \left(h_{\mathrm{wf,out}} - h_{\mathrm{wf,in}}\right) \tag{3.1}$$

where $\dot{Q}_{\mathrm{SG}}$ is the rate of added heat in the steam generator, $\dot{m}_{\mathrm{wf}}$ the mass flowrate of the cycle working fluid and $h_{\mathrm{wf,in}}$ and $h_{\mathrm{wf,out}}$ the specific enthalpies of the working fluid at the steam generator inlet and outlet.

3.2. Concentrated solar power (solar tower model)

The design of solar tower receiver in Chapter 7 and its thermal power requirements are determined by calculating the required rate of heat addition by the power generation block, $\dot{Q}_{\mathrm{PGB,SF}}$, at full rated power. The calculations consider the heat losses during the charging and discharging processes of the TES system (i.e., expressed as $\eta_{\mathrm{TES,Ch}}$ and $\eta_{\mathrm{TES,Dch}}$). Moreover, the receiver, which is assumed to be external (i.e., tubular) type, should be designed in a way to continuously supply sufficient thermal power to operate the power generation cycle at full rated power, at least during the daytime and not only during the maximum irradiance during the day. This requirement is satisfied by considering a solar multiple factor, F_{SM}, during the design of the receiver. Considering the intermediate heat losses and the solar multiple factor, the required rate heat addition in the receiver was calculated from [120]:

$$\dot{Q}_{\mathrm{rec}} = F_{\mathrm{SM}} \frac{\dot{Q}_{\mathrm{PGB,SF}}}{\eta_{\mathrm{TES,Ch}}\, \eta_{\mathrm{TES,Dch}}} \tag{3.2}$$

It should be noted that there are heat losses in the receiver due to radiation, $\dot{Q}_{\mathrm{rec,rad,loss}}$, and convection, $\dot{Q}_{\mathrm{rec,conv,loss}}$, which were estimated using [120]:

$$\dot{Q}_{\mathrm{rec,rad,loss}} = \epsilon\, \sigma\, F_{\mathrm{view}}\, A_{\mathrm{rec}}\, T_{\mathrm{rec}}^{4} \tag{3.3}$$

$$\dot{Q}_{\mathrm{rec,conv,loss}} = F_{\mathrm{conv}}\, \alpha_{\mathrm{rec}}\, A_{\mathrm{rec}} \left(T_{\mathrm{rec}} - T_{\mathrm{a}}\right) \tag{3.4}$$

$$\dot{Q}_{\mathrm{rec,loss}} = \dot{Q}_{\mathrm{rec,rad,loss}} + \dot{Q}_{\mathrm{rec,conv,loss}} \tag{3.5}$$

where ϵ the receiver emissivity, σ the Stefan-Boltzmann constant, F_{view} the radiative view factor from the receiver to the surrounding, F_{conv} the convective heat loss multiplier, A_{rec} the receiver surface area, T_{rec} the receiver temperature, T_{a} the ambient temperature and α_{rec} the convective heat transfer coefficient between the receiver and the surroundings.

The receiver thermal power and the total heat losses can be linked to the heliostat field thermal power that is concentrated into the receiver, $\dot{Q}_{\mathrm{hel}}$, using the receiver absorptivity, ξ, as [120]:

$$\dot{Q}_{\text{rec}} = \xi\, \dot{Q}_{\text{hel}} - \dot{Q}_{\text{rec,loss}} \tag{3.6}$$

$$\dot{Q}_{\text{hel}} = q_{\text{irr}}\, A_{\text{hel}}\, \eta_{\text{hel}} \tag{3.7}$$

where q_{irr} is the DNI, A_{hel} the total heliostat felid area and η_{hel} the heliostat efficiency.

The key design parameters of the solar receiver and the heliostat felid are listed in Table 3.2. These parameters were mostly extracted from System Advisor Model (SAM) software, which was developed by the National Renewable Energy Laboratory (NREL) [121]. Selecting constant values is usually associated with some degree of uncertainty as some of these parameters are dependent on weather factors (e.g., shading, soiling, and wind speed) [121]. For example, the heliostat felid efficiency, η_{hel}, is usually obtained after considering multiple optical loss factors such as cosine losses, reflectivity losses, shading losses, spillage losses and atmospheric attenuation losses [120]. With considering all these factors, the average heliostat efficiency usually falls in the range of 60-70%. In this thesis, the lowest heliostat efficiency (60%) was assumed in the solar tower model in order to be more conservative [120]. The disadvantages of selecting constant (averaged) parameters includes lack of accuracy when obtaining instantaneous (i.e., hourly) results, especially if the actual values are significantly higher or lower than the averaged one. However, such inaccuracy can be neglected since most of the assumed parameters in Table 3.2 were utilised to estimate heat losses in the solar receiver, and the magnitude of these losses are very minor (i.e., ~3-4% of the total heat absorbed by the solar receiver).

Table 3.2. Key design parameters of the solar tower receiver [120–123].

Parameter	**Value**
Receiver emissivity, ϵ (-)	0.95
Stefan-Boltzmann constant, σ (W/m^2 K^4)	5.67×10^{-8}
Radiative view factor, F_{view} (-)	0.2
Convective heat loss multiplier, F_{conv} (-)	1
Receiver convective heat transfer coefficient, α_{rec} (W/m^2 K)	15
Ambient temperature, T_{amb} (°C)	25
Receiver absorptivity, ξ (-)	0.94
Design direct normal irradiance, q_{irr} (W/m^2)	600
Heliostat efficiency, η_{hel} (%)	60

The determination of the design receiver dimensions (height and diameter), the heliostat area, and the tower height in Chapter 7 were obtained using the optimisation-based optical simulation

in SAM software. Once all solar field design parameters were generated from SAM, the transient receiver thermal power output for the fluctuating DNI data during the day is then obtained using Equations (3.2)-(3.7). Moreover, the solar field design parameters (i.e., receiver area, heliostat area, and tower height) were also used to estimate the capital cost of the solar felid as discussed in Section 3.5.4. The design DNI in Chapter 7 was assumed to be 600 W/m^2, which is based on the average peak day point of the entire year for the selected location (Duqm, Sultanate of Oman - Latitude:19.65°, Longitude 57.62°).

3.3. Thermal energy storage models

This section covers the modelling procedure and the design aspect of the various TES technologies that are analysed in the thesis. The modelling of the steam accumulators and the solid heat storage units that are used in Chapter 4 are presented in Sections 3.3.1 and 3.3.2, respectively, while the two-tank molten salt TES system model (i.e., Chapter 7) is discussed in Section 3.3.3. The design of the PCM tanks presented in Chapter 5 is discussed in Appendix A.

3.3.1. Steam accumulator model

The prediction of the mass, pressure, and energy of the steam/water in the steam accumulators (SA) were performed using mass and the energy balance equations of the thermal equilibrium model developed by Stevanovic et al. [124]. The rate of water (liquid) and steam (vapour) mass change in the SA was calculated using:

$$\frac{\mathrm{d}m}{\mathrm{d}t} = \Delta\dot{m}_{\mathrm{V}} + \Delta\dot{m}_{\mathrm{L}} \tag{3.8}$$

$$\Delta\dot{m}_{\mathrm{V}} = \dot{m}_{\mathrm{V,in}} - \dot{m}_{\mathrm{V,out}} \tag{3.9}$$

$$\Delta\dot{m}_{\mathrm{L}} = \dot{m}_{\mathrm{L,in}} - \dot{m}_{\mathrm{L,out}} \tag{3.10}$$

The SA enthalpy variations were predicted using:

$$\frac{\mathrm{d}H}{\mathrm{d}t} = \Delta(\dot{m}h)_{\mathrm{V}} + \Delta(\dot{m}h)_{\mathrm{L}} + V\,\frac{\mathrm{d}P}{\mathrm{d}t} \tag{3.11}$$

$$\Delta(\dot{m}h)_{\mathrm{V}} = (\dot{m}h)_{\mathrm{V,in}} - (\dot{m}h)_{\mathrm{V,out}} \tag{3.12}$$

$$\Delta(\dot{m}h)_{\mathrm{L}} = (\dot{m}h)_{\mathrm{L,in}} - (\dot{m}h)_{\mathrm{L,out}} \tag{3.13}$$

To calculate the transient pressure and mass of steam in the SAs during charging and discharging modes, the following steps and equations were used:

1. The total enthalpy of the SA is represented by:

$$H = m\,h \tag{3.14}$$

2. Differentiating with respect of time:

$$\frac{\mathrm{d}H}{\mathrm{d}t} = h\frac{\mathrm{d}m}{\mathrm{d}t} + m\frac{\mathrm{d}h}{\mathrm{d}t} \tag{3.15}$$

3. The specific enthalpy can be calculated by:

$$h = h' + x\,\Delta h_{\mathrm{vap}} \tag{3.16}$$

where superscript ‘’’ stands for saturated liquid conditions.

4. Taking the derivative of the specific enthalpy:

$$\frac{\mathrm{d}h}{\mathrm{d}t} = \frac{\mathrm{d}h'}{\mathrm{d}t} + \Delta h_{\mathrm{vap}}\,\frac{\mathrm{d}x}{\mathrm{d}t} + x\,\frac{\mathrm{d}\Delta h_{\mathrm{vap}}}{\mathrm{d}t} \tag{3.17}$$

5. Rearranging and introducing rate of change of pressure $\mathrm{d}P/\mathrm{d}t$:

$$\frac{\mathrm{d}h}{\mathrm{d}t} = \left(\frac{\mathrm{d}h'}{\mathrm{d}P} + x\,\frac{\mathrm{d}\Delta h_{\mathrm{vap}}}{\mathrm{d}P}\right)\frac{\mathrm{d}P}{\mathrm{d}t} + \Delta h_{\mathrm{vap}}\,\frac{\mathrm{d}x}{\mathrm{d}t} \tag{3.18}$$

6. The steam quality, x, can be predicted by:

$$x = \frac{v - v'}{v'' - v'} \tag{3.19}$$

$$v = \frac{V}{m} \tag{3.20}$$

7. Taking the derivative of steam quality, x, and specific volume, v, with respect of time or pressure, and knowing that SA volume, V, is constant:

$$\frac{\mathrm{d}x}{\mathrm{d}t} = -\frac{1}{m}\,\frac{v}{v'' - v}\,\frac{\mathrm{d}m}{\mathrm{d}t} - \left(\frac{1}{v'' - v'}\,\frac{\mathrm{d}v'}{\mathrm{d}P} + \frac{v - v'}{(v'' - v')^2}\,\frac{\mathrm{d}(v'' - v')}{\mathrm{d}P}\right)\frac{\mathrm{d}P}{\mathrm{d}t} \tag{3.21}$$

8. Finally, the rate of change of SA pressure can be calculated by substituting Equations (3.14)-(3.21) into Equation (3.11) and rearranging:

$$\frac{\mathrm{d}P}{\mathrm{d}t} = \frac{\Delta(\dot{m}h)_{\mathrm{V}} + \Delta(\dot{m}h)_{\mathrm{L}} + \left(\dfrac{\Delta h_{\mathrm{vap}}\dfrac{V}{m}}{v'' - v'} - h\right)(\Delta\dot{m}_{\mathrm{V}} + \Delta\dot{m}_{\mathrm{L}})}{m\left(\dfrac{\mathrm{d}h'}{\mathrm{d}P} + \dfrac{\dfrac{V}{m} - v'}{v'' - v'}\,\dfrac{\mathrm{d}\Delta h_{\mathrm{vap}}}{\mathrm{d}P} - \dfrac{\Delta h_{\mathrm{vap}}}{v'' - v'} - \dfrac{\mathrm{d}v'}{\mathrm{d}P} - \Delta h_{\mathrm{vap}}\dfrac{\dfrac{V}{m} - v'}{(v'' - v')^2}\,\dfrac{\mathrm{d}(v'' - v')}{\mathrm{d}P}\right) - V} \tag{3.22}$$

Equations (3.8) and (3.22) were solved numerically using the Runge-Kutta method for specified initial values of SA water/steam mass and pressure. Moreover, the steam thermodynamic properties presented in Equation (3.22) are only a function of pressure. Therefore, their rates of change were calculated using the slope of the property between slightly higher and lower pressure points.

3.3.1.1. Validation of the steam accumulator model

The validation of the formulated SA model was conducted using a set of data for three different SA charging and discharging tests (i.e., Tests A, B and C) reported in Ref. [124]. Same initial conditions and same charging/discharging steam parameters, as listed in Table 3.3 and can be found in detail in Refs. [124,125], were used to validate the formulated model. The initial conditions included water filling ratios (WFR), which is defined as:

$$WFR = \frac{V_{\mathrm{L}}}{V_{\mathrm{V}} + V_{\mathrm{L}}} = \frac{V_{\mathrm{L}}}{V_{\mathrm{SA}}} \tag{3.23}$$

where V_{L} is the liquid volume, V_{V} the vapour volume and V_{SA} the volume of the SA.

Figure 3.1 shows the time varying: (a) steam inlet or outlet pressure; (b) steam inlet or outlet mass flowrate; and (c) steam inlet/outlet temperature of the three tests. The conditions of each test are:

- *Test A*: SA is charged with a varying pressure, mass flowrate, and temperature steam for 11 min and 40 s.
- *Test B*: SA is charged with steam at a constant mass flowrate of 10 kg/s, a constant pressure of 2.5 MPa, and a constant temperature of 225 °C for 4 min and 35 s.
- *Test C*: SA is discharged with a constant steam mass flowrate of 10 kg/s but at different discharging steam pressure and temperature that depends on the SA pressure for 4 min and 10 s.

Table 3.3. Initial conditions and main SA parameters for SA model validation.

Parameter	Test A	Test B	Test C
SA volume (m^3)	64	64	64
SA initial pressure (MPa)	3.4	2.5	5.0
SA initial WFR (-)	0.5	0.5	0.5
Charging/discharging mode	charging	charging	discharging

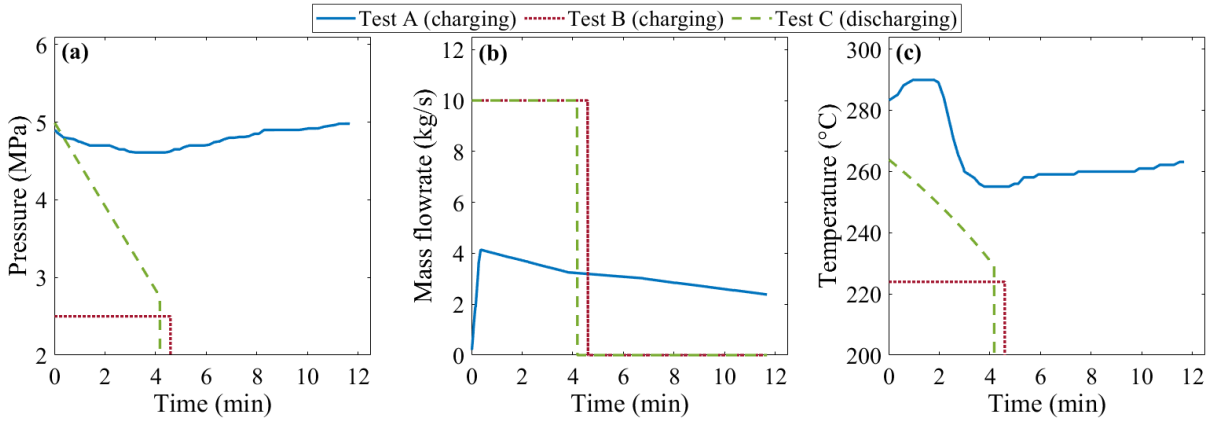

Figure 3.1. (a) SA inlet steam pressure for Test A and Test B alongside with outlet steam pressure for Test C, (b) SA inlet steam mass flowrate for Test A and Test B alongside with outlet steam mass flowrate for Test C, and (c) SA steam inlet temperature for Test A and Test B besides outlet steam temperature for Test C. All steam inlet conditions were digitally extracted from graphs and data provided in Ref. [124] and Ref. [125].

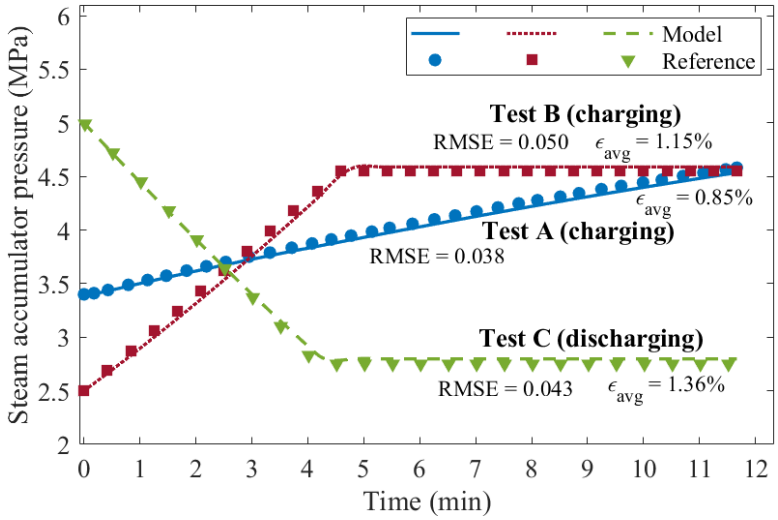

Figure 3.2. Comparison of the behaviour of the SA pressure between the model and Ref. [124] results for all tests. Tests A and B indicate the increase of SA pressure during steam charging while Test C shows the decrease of SA pressure during the discharge.

The calculated and the reference SA pressures for all tests are compared in Figure 3.2. The comparison shows that the formulated model is sufficiently accurate as the maximum RMSE is 0.05 and the maximum average relative error (ϵ_{avg}) is 1.4%. The small source of error could be a result of adopting a different way of calculating the rate of change of steam properties at different pressure points. Stevanovic et al. [124] state that the equilibrium model could have a

6% of estimation error when compared to non-equilibrium model, but both have same initial and final pressure points. However, the non-equilibrium model requires inner physical parameters and dimensions of the SA which is not available in the literature. Therefore, the equilibrium model was used in this thesis, specifically in Chapter 4.

3.3.2. Solid storage model

This section discusses the modelling aspect of the solid (concrete) heat storage of the case study presented in Chapter 4. Concrete was selected as the storage material because it has proven its compatibility of storing heat at high temperatures (up to 550 °C) and its comparatively cheaper price [77]. The schematic diagram of the proposed concrete blocks and the tube bundling is illustrated in Figure 3.3. In the study discussed in Chapter 4, each concrete block was assumed to be 10-m long and to have a square cross-section for easier installation and operation near the SAs, and each was assumed to comprise a number of tubes that are surrounded by concrete. The inner and outer diameters of each tube-solid element, D_i and D_o as shown in Figure 3.3, are equal to 2 cm and 8 cm [126,127]. The total size of the concrete blocks (i.e., width, height, length) was determined after performing a thermo-economic parametric study for different concrete block sizes (i.e., in terms of number of tubes and number of concrete blocks) in Section 4.6.1

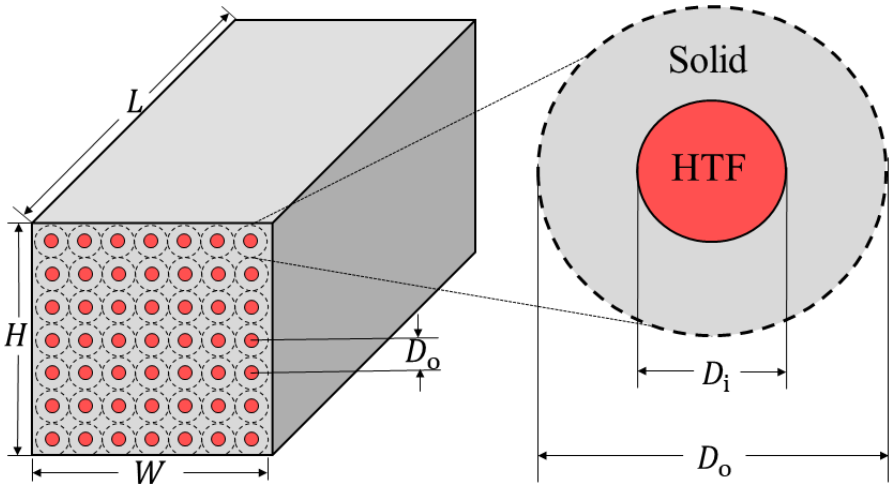

Figure 3.3. Simplified schematic diagram of a concrete storage block with in-line tube bundle arrangement. The right sketch shows the radial cross section of one HTF-solid (steam-concrete) element. The number of tubes does not reflect the actual number of tubes in the proposed design.

In this thesis, a transient energy and mass balance model for the solid storage was formulated based on the following assumptions:

- Conductive axial heat transfer within the fluid and between each solid element is very small compared to the radial heat transfer (i.e., $\dot{Q}_{\text{axial}} \ll \dot{Q}_{\text{radial}}$). The ratio of the maximum axial to the minimum radial heat transfer rates ($\dot{Q}_{\text{axial,max}}/\dot{Q}_{\text{radial,min}}$) is less than 0.5%. Thus, conductive axial heat transfer is neglected.
- The external surface of the concrete block is perfectly insulated (no heat loss to the environment).
- The transient radial heat conduction in the solid element is treated using a modified lumped capacitance method with an effective heat transfer coefficient (i.e., valid for large Biot numbers, up to 100) that accounts for the internal thermal gradient in the solid material [128,129].
- The tube between the solid and the fluid is very thin and made of a material that has a relatively high thermal conductivity (34-54 W/m K for carbon steel [130,131]), which is at least 15 times greater than the thermal conductivity of concrete (2.2 W/m K at 200 °C [132]). Based on the dimensions of the solid element and the tubes (thickness of 1 mm [129]), the calculated thermal resistance of the tube was observed to be less than 1% of that of the solid element. Therefore, the thermal resistance of the tube is neglected.
- Steam condensation is expected to occur during charging mode. Therefore, the two phases (vapour and liquid) are assumed to be in thermal, mechanical, and chemical equilibrium.
- Fluid flow is one dimensional (z-axis) and the velocity vector of each phase of the fluid (liquid and vapour) has one component only.
- Pressure drop of fluid in the tube is neglected when calculating fluid properties. However, a total pressure loss of 0.5 MPa throughout the concrete blocks is assumed.
- Temperature distribution in the solid is symmetrical about the axis.

Applying the listed assumptions and using the general energy and mass balance equations for unsteady-flow processes in Ref. [133], the final energy and mass balance equations for the fluid element can be written as:

$$\frac{\mathrm{d}(m_{\mathrm{f}} u_{\mathrm{f}})}{\mathrm{d}t} = \dot{m}_{\mathrm{f,in}}\, h_{\mathrm{f,in}} - \dot{m}_{\mathrm{f,out}}\, h_{\mathrm{f,out}} + \alpha_{\mathrm{e}}\, A_{\mathrm{w}}\, (T_{\mathrm{s}} - T_{\mathrm{f}}) \tag{3.24}$$

$$\frac{\mathrm{d}m_{\mathrm{f}}}{\mathrm{d}t} = \dot{m}_{\mathrm{f,in}} - \dot{m}_{\mathrm{f,out}} \tag{3.25}$$

$$A_{\mathrm{w}} = \pi\, D_{\mathrm{i}}\, \Delta z \tag{3.26}$$

$$m_{\mathrm{f}} = \rho_{\mathrm{f}}\, V_{\mathrm{f}} \tag{3.27}$$

$$V_{\mathrm{f}} = \frac{\pi}{4}\, D_{\mathrm{i}}^2\, \Delta z \tag{3.28}$$

where m_{f} and u_{f} are the mass and the specific internal energy of the fluid, respectively, $\dot{m}_{\mathrm{f}}$ the fluid mass flowrate, h_{f} the fluid specific enthalpy, α_{e} the effective heat transfer coefficient, A_{w} the tube surface area, D_{i} the tuber inner diameter, T_s the solid temperature, T_{f} the fluid temperature and V_{f} the volume of the fluid cell. It should be noted that the fluid mass in each cell is not constant as the fluid density in each cell varies, especially during condensation of fluid.

It should be noted that the fluid mass in each cell is not constant ($\mathrm{d}m_{\mathrm{f}}/\mathrm{d}t \neq 0$) as the fluid density in each cell varies, especially during condensation. The temporal change of fluid mass contained within the tube array of the concrete blocks is driven by steam condensation. The density difference between vapour steam and condensed liquid dictates that the mass must increase as liquid is accumulating in a fixed volume, which is captured by the mass balance in Equation (3.25).

The energy balance equation for the solid in each cell is:

$$m_{\mathrm{s}}\, c_{\mathrm{s}}\, \frac{\mathrm{d}T_{\mathrm{s}}}{\mathrm{d}t} = \alpha_{\mathrm{e}}\, A_{\mathrm{w}}\, (T_{\mathrm{f}} - T_{\mathrm{s}}) \tag{3.29}$$

$$m_{\mathrm{s}} = \rho_{\mathrm{s}}\, V_{\mathrm{s}} \tag{3.30}$$

$$V_{\mathrm{s}} = \frac{\pi}{4}\, (D_{\mathrm{o}}^2 - D_{\mathrm{i}}^2)\, \Delta z \tag{3.31}$$

where m_{s} is the solid mass, c_{s} the solid specific heat capacity, ρ_{s} the solid density and V_{s} the volume of the solid element. The solid mass in each cell was assumed to be constant as the solid density is almost constant for the considered temperature range.

The effective heat transfer coefficient in Equations (3.24) and (3.29) was calculated using Equation (3.32) that is proposed by Xu et al. [128] and Jian et al. [129]. This coefficient was derived by applying the lumped capacitance method and is valid for large (up to 100) Biot numbers, and for transient models. Based on a brief numerical analysis that is covered in detail in Section 3.3.2.1, the Biot number in the model is expected to fall between 0.80 and 88 depending on the HTF mass flowrate and the inner and outer diameters of the HTF-solid element.

$$\frac{1}{\alpha_{\mathrm{e}}} = \frac{1}{\alpha_{\mathrm{f}}} + \frac{1}{k_{\mathrm{s}}} \left(\frac{4\, R_{\mathrm{i}}\, R_{\mathrm{o}}^4\, \ln\left(\frac{R_{\mathrm{o}}}{R_{\mathrm{i}}}\right) - 3\, R_{\mathrm{i}}\, R_{\mathrm{o}}^4 + 4\, R_{\mathrm{i}}^3\, R_{\mathrm{o}}^2 - R_{\mathrm{i}}^5}{4\, (R_{\mathrm{o}}^2 - R_{\mathrm{i}}^2)^2} \right) \tag{3.32}$$

In Equation (3.32), α_{f} is the convective heat transfer coefficient of the fluid and calculated using Gnielinski's correlation for single-phase flows [134]:

$$\alpha_{\mathrm{SP}} = \frac{k_{\mathrm{f}}}{D_{\mathrm{h}}} \frac{\left(\frac{f}{8}\right)(Re - 1000)\,Pr}{1 + 12.7\left(\frac{f}{8}\right)^{0.5}(Pr^{0.67} - 1)} \tag{3.33}$$

$$Re = \frac{\rho\, v\, D_{\mathrm{h}}}{\mu} \tag{3.34}$$

$$Pr = \frac{c\,\mu}{k} \tag{3.35}$$

where k_{f} is the fluid thermal conductivity, Re the Reynolds number, Pr the Prandtl number and f the friction factor that was calculated using the following Colebrook-White correlation with an absolute tube roughness, e, equal to 0.04 mm for new carbon-steel tubes [135]:

$$\frac{1}{\sqrt{f}} = -2\log\left(\frac{e}{3.7\,D_{\mathrm{in}}} + \frac{2.51}{Re\,\sqrt{f}}\right) \tag{3.36}$$

For steam condensation, the fluid heat transfer coefficient was obtained using Shah's correlation for two-phase flows [136,137]:

$$\alpha_{\mathrm{TP}} = \begin{cases} \alpha_{\mathrm{Sh}} & J_{\mathrm{V}} \geq \beta \\ \alpha_{\mathrm{Sh}} + \alpha_{\mathrm{Nu}} & \gamma \leq J_{\mathrm{V}} < \beta \\ \alpha_{\mathrm{Nu}} & J_{\mathrm{V}} < \gamma \end{cases} \tag{3.37}$$

$$\alpha_{\mathrm{sh}} = \frac{k_{\mathrm{L}}}{D_{\mathrm{h}}}\, 0.023\, Re_{\mathrm{Lo}}^{0.8}\, Pr_{\mathrm{L}}^{0.4} \left(\frac{\mu_{\mathrm{L}}}{14\mu_{\mathrm{V}}}\right)^{(0.0058+0.557P_{\mathrm{R}})} \left(1 + \frac{3.8}{Z^{0.95}}\right) \tag{3.38}$$

$$\alpha_{\mathrm{Nu}} = \frac{k_{\mathrm{L}}}{D_{\mathrm{h}}}\, 1.32\, Re_{\mathrm{L}}^{-1/3} \left(\frac{\rho_{\mathrm{L}}\,(\rho_{\mathrm{L}} - \rho_{\mathrm{V}})\, g\, k_{\mathrm{L}}^3}{\mu_{\mathrm{L}}^2}\right)^{1/3} \tag{3.39}$$

$$J_{\mathrm{V}} = \frac{x\, G}{\left(g\, D_{\mathrm{h}}\, \rho_{\mathrm{V}}\,(\rho_{\mathrm{L}} - \rho_{\mathrm{V}})\right)^{0.5}} \tag{3.40}$$

$$Z = \left(\frac{1}{x} - 1\right)^{0.8} P_{\mathrm{R}}^{0.4} \tag{3.41}$$

$$P_{\mathrm{R}} = \frac{P_{\mathrm{sat}}}{P_{\mathrm{crit}}} \tag{3.42}$$

$$\beta = 0.98\,(Z + 0.263)^{-0.62} \tag{3.43}$$

$$\gamma = 0.95\,(1.254 + 2.27Z^{1.249})^{-1} \tag{3.44}$$

The transient energy and mass balance equations of the fluid and the solid elements were solved numerically using the finite difference method by discretising the total tube length, L, into small spatial segments, Δz, and the total time, τ, into small time steps, Δt. The spatial discretisation and the location of the nodes are illustrated in Figure 3.4. This set of equations were solved using the backward Euler method, as following:

$$\frac{(m_f u_f)_j^{n+1} - (m_f u_f)_j^n}{\Delta t} = (\dot{m}_f)_{j-1}^{n+1} (h_f)_{j-1}^{n+1} - (\dot{m}_f)_j^{n+1} (h_f)_j^{n+1} + (\alpha_e)_j^{n+1} A_w \left((T_s)_j^{n+1} - (T_f)_j^{n+1}\right) \quad (3.45)$$

$$\frac{(m_f)_j^{n+1} - (m_f)_j^n}{\Delta t} = (\dot{m}_f)_{j-1}^{n+1} - (\dot{m}_f)_j^{n+1} \quad (3.46)$$

$$m_s c_s \frac{(T_s)_j^{n+1} - (T_s)_j^n}{\Delta t} = (\alpha_e)_j^{n+1} A_w \left((T_f)_j^{n+1} - (T_s)_j^{n+1}\right) \quad (3.47)$$

where n is the time step index and j the spatial node.

The equations were solved using an iterative method and following the illustrated algorithm in Figure 3.5, with Δt = 1 s and Δz = 0.1 m (i.e., the selection of these time step and spatial node sizes is discussed later in this section). Moreover, the model assumed a homogenous starting point where the temperature of fluid in each spatial node was the same as the temperature of the solid and the initial conditions of each calculation step were determined based on previous time step [77].

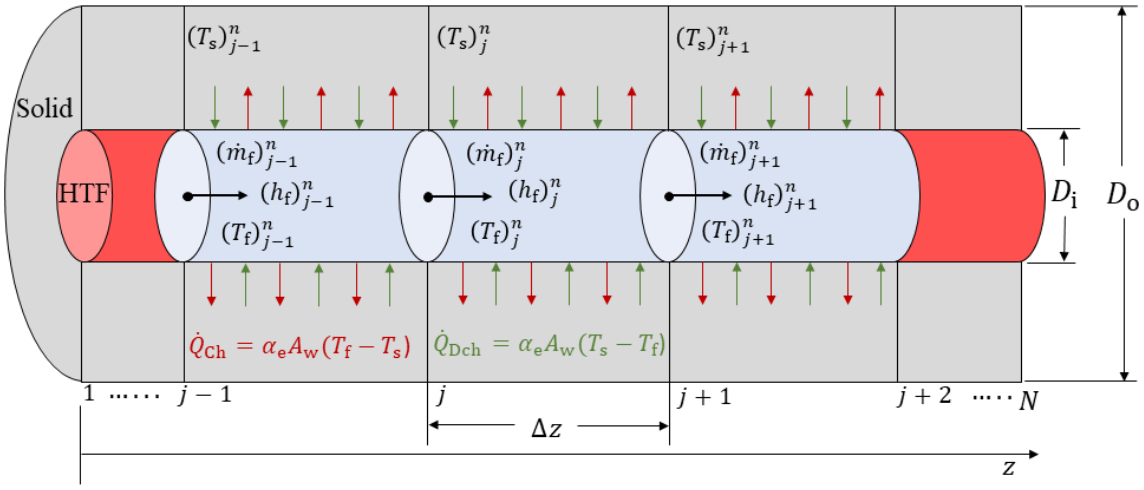

Figure 3.4. Schematic diagram of the cell energy and mass balance analysis as well as the heat flow directions during charging and discharging modes.

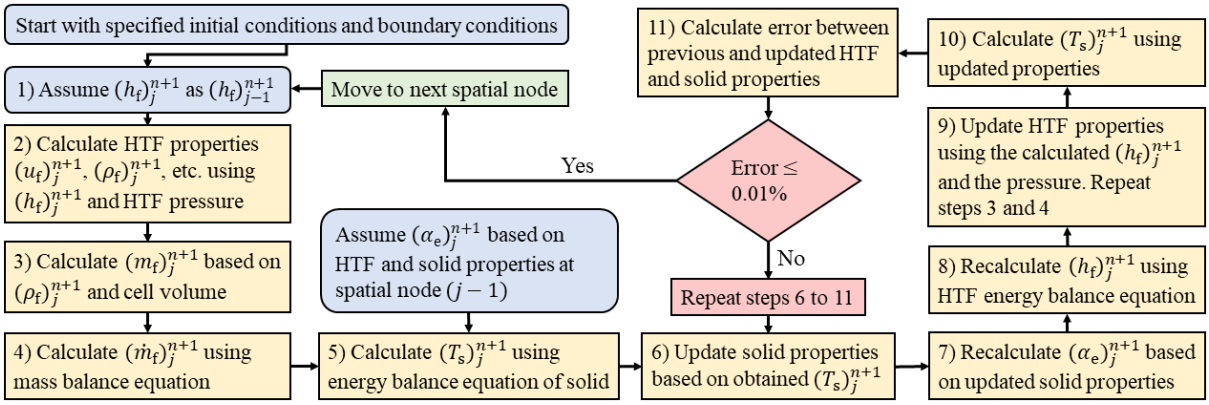

Figure 3.5. Flow diagram of the calculation steps of solving the energy and mass balance resolution algorithm for the concrete model. The steps are repeated for each spatial node ($j = 2$ to $j = N$) and for each time step Δt.

The time step size was determined by comparing the RMSEs of the solid and fluid temperature profiles for a range of time step sizes, with an example shown in Figure 3.6(a). The RMSEs were calculated relative to the data obtained using the highest number of time steps (i.e., based on a step size of 0.1 s and 36000 time steps). Based on data presented in Figure 3.6(a), a time step size of 1 s (i.e., number of time steps in 1 h is 3600) was selected as the calculated RMSE falls below 0.5%. The computation time of running the model with a 1-s time step was 15 min, whereas it was 2.5 h when running the model at a time step of 0.1 s.

Furthermore, the spatial node size was also selected after comparing the RMSEs for different numbers of spatial nodes (i.e., N_{sn}= 800, 400, 200, 80, 40, 20 and 8) for an 8-m long block size, with a time step of 1 s, as shown in Figure 3.6(b). The RMSEs were calculated relative to the data obtained using the highest number of spatial nodes (i.e., 800 spatial nodes which corresponds to Δz = 0.01 m). It can be seen in Figure 3.6(b) that the RMSE decreases when increasing the number of spatial nodes, but such increase also leads to increasing the computational time, which can reach to 4 h when N_{sn}= 800 . Based on the presented data in Figure 3.6(b), the selected number of spatial nodes is 80 (i.e., Δz = 0.1 m) since it gives an acceptable amount of uncertainty (RMSE <1) and reasonable computational time (15 min).

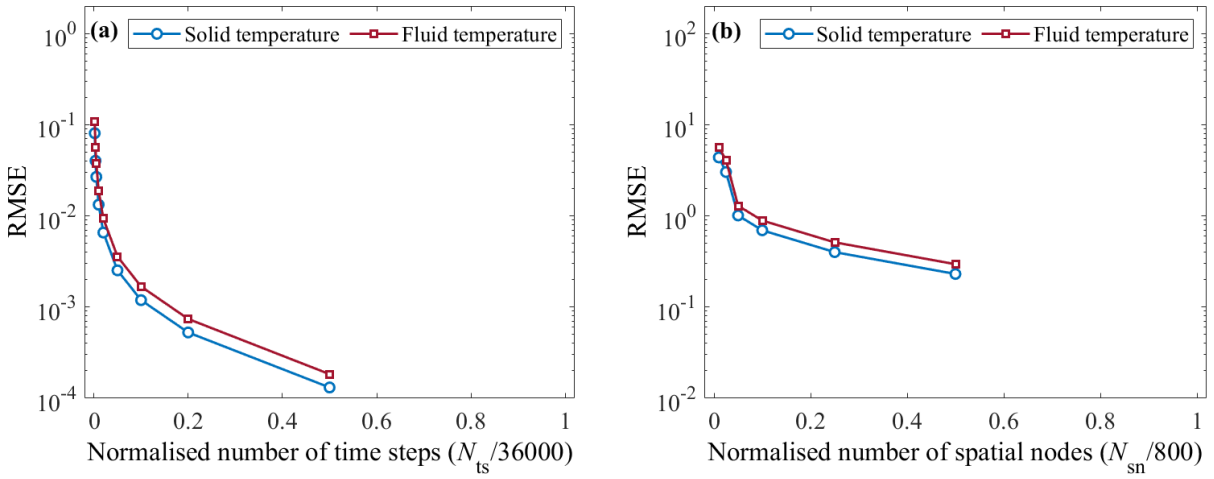

Figure 3.6. Comparison of the calculated RMSEs of the solid and the fluid temperatures for: (a) a range of time step sizes, and (b) different number of spatial nodes for the solid TES model. In (a), the total time is 3600 s, and the maximum number of time steps is 36000, which corresponds to a time step size of 0.1 s. The RMSEs were calculated relative to the temperature profiles obtained using the maximum number of time steps and with $\Delta z = 0.1$ m. In (b), the total block length is 8 m, and the maximum number of spatial nodes is 800, which corresponds to $\Delta z = 0.01$ m. The RMSEs were calculated relative to the temperature profiles obtained using the maximum number of spatial nodes, with data compared every $\Delta z = 1$ m, and using $\Delta t = 1$ s.

3.3.2.1. Validity of using an effective heat transfer coefficient

The assumption of using the effective (corrected) heat transfer coefficient was made to be able to use the lumped capacitance method in the solid-state TES model. The lumped capacitance method is usually applied when the Biot number is smaller than 0.1 as larger Biot numbers indicate significant temperature gradients in the solid domain. However, Xu et al. [128] and Jian et al. [129] derived a corrected version of the heat transfer coefficient valid for large Biot numbers and for transient heat transfer models as well. The results of their analysis showed that the modified lumped capacitance method can be applied to accurately describe and calculate the thermal behaviour of solid-state TES, up to Biot number of 100.

To assess the validity of applying the lumped capacitance model in the concrete TES system covered in Chapter 4, a brief numerical analysis of the expected Biot numbers in the concrete TES model was performed. The Biot number in the formulated model is defined as:

$$Bi = \frac{\alpha}{k_s}\frac{V_s}{A} \tag{3.48}$$

where α is the convective heat transfer coefficient between the HTF and the solid, k_s the thermal conductivity of the solid, V_s the solid volume and A the heat transfer surface area.

The value of k_s (= 1.4 W/m K) was calculated using a temperature-dependent correlation (i.e., see Table 3.4) at 500 °C, and the temperature and pressure of the HTF (steam) used for the calculation of α were assumed to be 550 °C and 11.5 MPa. Figure 3.7 shows expected Biot numbers for a range of HTF mass flowrates, and for different tube and concrete diameter ratios, $\theta = D_o/D_i$. The range of mass flowrates was selected to cover all expected flowrates in the model (i.e., based on maximum and minimum total mass flowrate flowing from the solar superheater or from the SAs and for different numbers of tubes, check Chapter 4 for more details).

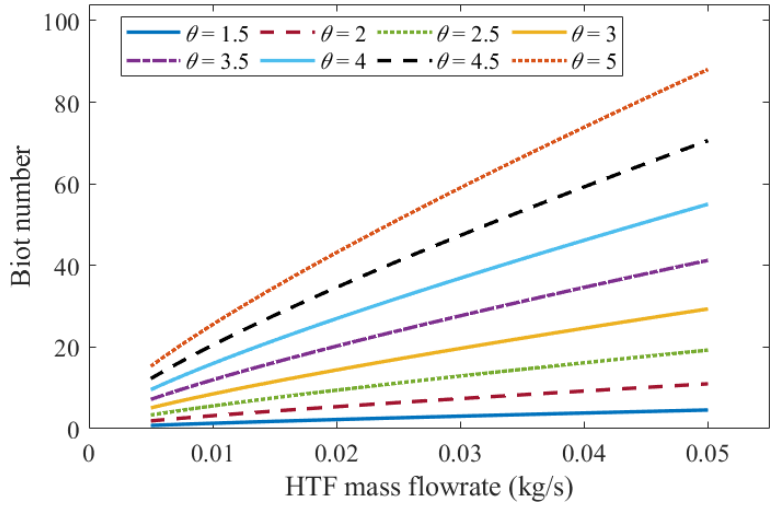

Figure 3.7. Expected Biot numbers ($Bi = \alpha V_s/k_s A$) in the concrete TES model for a range of HTF mass flowrates and different diameter ratios, θ. The diameter ratio is defined as D_o/D_i with an inner diameter, D_i, of 2 cm, and k_s is 1.4 W/m K. The temperature and the pressure of the HTF (steam) for the calculation of the convective heat transfer coefficient, α, is 550 °C and 11.5 MPa.

The expected Biot numbers are between 0.80 and 88. The Biot number increases with the increase of the diameter ratio because of the increase of the solid volume. Moreover, the Biot number also increases with higher HTF mass flowrates due to higher heat transfer coefficients. The results support the validity of using of lumped capacitance method with a corrected heat transfer coefficient for evaluating the thermodynamic performance of the solid TES system in Chapter 4.

3.3.2.2. Solid concrete thermophysical properties

The selected concrete material in Chapter 4 is *HEATCRETE vp1* that was developed by *EnergyNest* and *HeidelbergCement*. *HEATCRETE vp1* is specially made for TES purposes and could withstand heat of up to 550 °C [81,132]. The thermophysical properties of this material are summarised in Table 3.4. The properties are temperature dependent, hence, correlations based on temperature are extracted from the data in Ref. [132]. The density is also temperature dependent but the change in density is less than 1% between 200 °C and 550 °C. Thus, an average density of 2260 kg/m^3 is assumed in the whole temperature range.

Table 3.4. Thermophysical properties of the selected concrete material (*HEATCRETE vp1*). The unit of temperature in the correlations is °C [132].

Thermophysical property	Value/correlation
Density (kg/m^3)	2260
Thermal conductivity (W/m K)	k_s = -0.0027 T + 2.754
Specific heat capacity (J/kg K)	c_s = 1.3192 T + 775

3.3.2.3. Validation of the solid thermal energy storage model

The formulated concrete storage computational model was validated using experimental data from Ref. [129]. The same concrete and tube dimensions, concrete thermophysical properties, initial conditions and boundary conditions, which are reported in Ref. [129], were applied in the model. Two experimental data set that are different in terms of HTF volumetric flowrate and concrete initial temperature profile were examined. Figure 3.8 compares the numerical results with the experimental data reported in Ref. [129]. The HTF and the solid temperatures for a HTF volumetric flowrate of 3 m^3/h are shown in Figure 3.8(a) and Figure 3.8(b), respectively, while for a HTF volumetric flowrate of 4.5 m^3/h are shown in Figure 3.8(c) Figure 3.8(d), respectively. All experimental data are plotted in dots while the numerical results are plotted in lines. The HTF inlet temperature and the initial solid temperature profile (i.e., illustrated in blue in Figure 3.8) for the numerical model are assumed to be the same as the experimental data. The differences of the results were compared using the root mean square error (RMSE), ε_{RMS}:

$$\varepsilon_{\mathrm{RMS}} = \sqrt{\frac{\sum_{i=1}^{N}\left(T_{\mathrm{num}} - T_{\mathrm{exp}}\right)^2}{N}} \tag{3.49}$$

where T_{num} is the temperature from the numerical models, T_{exp} the temperature from the experiments and N the number of data points.

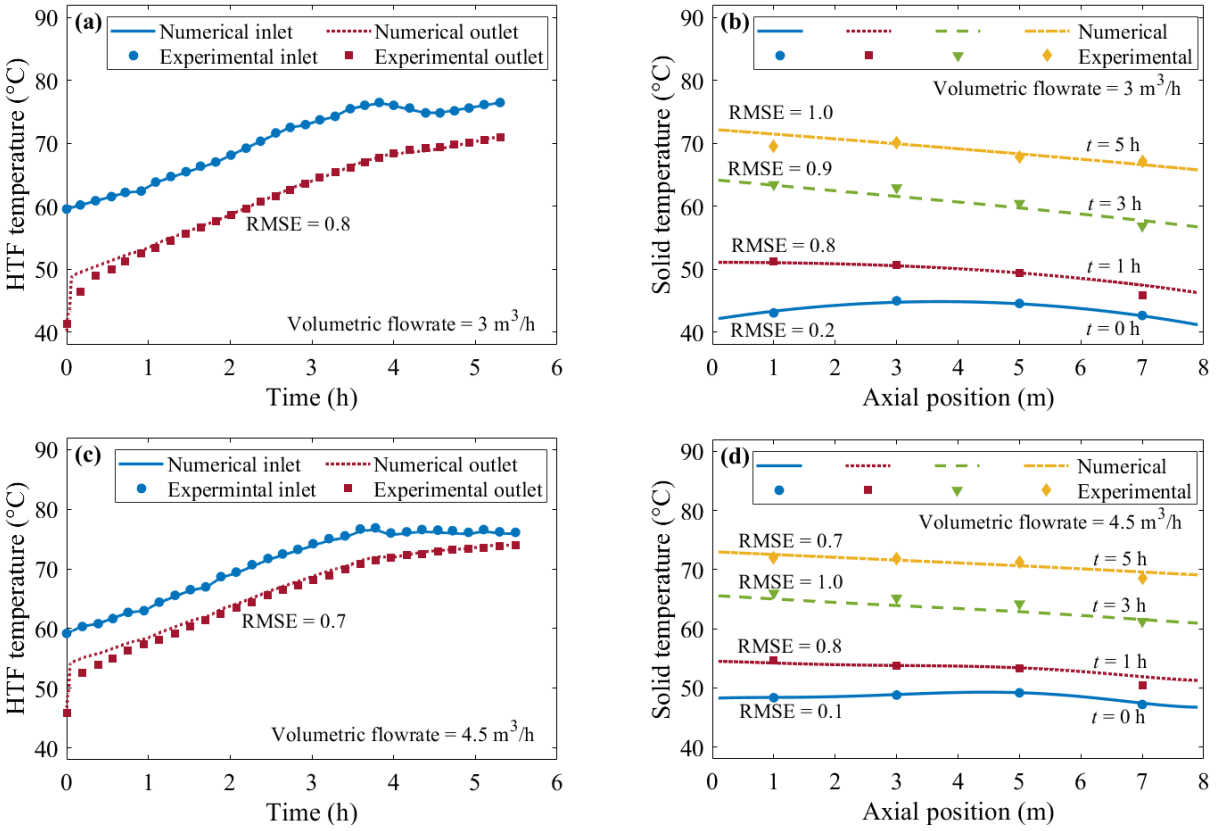

Figure 3.8. Comparison of results obtained from the formulated concrete model and the experimental data published in Ref. [129]. Showing HTF and solid temperatures, respectively, for: (a, b), a HTF volumetric rate of 3 m^3/h, and (c, d) a HTF volumetric rate of 4.5 m^3/h. The HTF temperatures are measured at the inlet and the outlet of the storage unit and the solid temperatures are measured at different axial positions and different charging times.

The RMSEs of all compared data are 1 or less and the behaviour of the numerically calculated HTF and solid temperatures are almost the same as the experimental temperatures. The small difference is acceptable and could be a result of using slightly different thermophysical properties as well as the accuracy of the heat transfer coefficients. It should be noted that the experimental data reported in Ref. [129] and presented in Figure 3.8 covers temperatures in the range of 50-80 °C (i.e., subcooled water at atmospheric pressure), indicating that the formulated model is only validated when the HTF (steam) is fully condensed, and no condensation/boiling process (two-phase flow) is occurring inside the tubes. To the latest

knowledge of the Author, there is no availability of experimental data with steam conditions (i.e., steam with a temperature in the range of 300-550 °C with a condensation process inside the tubes) in the literature that could be used to validate the formulated model during the steam condensation process. Still, the formulated model is partially validated and could be considered as sufficiently accurate in predicting the performance of the solid TES during charging and discharging in the study presented in Chapter 4.

3.3.3. Two-tank molten salt thermal energy storage

The two-tank molten salt TES system that is used in the hybrid nuclear-solar power plant in Chapter 7 was modelled using the general energy and mass balance equations.

In a two-tank molten salt TES system, the HTF (molten salt) is extracted from the cold tank and directed to the solar receiver to absorb heat and then flows to the hot tank. The energy and mass balance equations of the hot tank can be written as [138–140]:

$$m_{\mathrm{MS,HT}} \frac{\mathrm{d}h_{\mathrm{HT}}}{\mathrm{d}t} = \dot{Q}_{\mathrm{SF\rightarrow HT}} - \dot{Q}_{\mathrm{HT,loss}} - \dot{Q}_{\mathrm{HT\rightarrow PGB}} \tag{3.50}$$

$$\dot{Q}_{\mathrm{SF\rightarrow HT}} = \dot{m}_{\mathrm{MS,SF}}\, h_{\mathrm{MS,SF,out}} \tag{3.51}$$

$$\dot{Q}_{\mathrm{HT,loss}} = A_{\mathrm{HT}}\, \alpha_{\mathrm{HT,loss}}\, (T_{\mathrm{HT}} - T_{\mathrm{a}}) \tag{3.52}$$

$$\dot{Q}_{\mathrm{HT\rightarrow PGB}} = \dot{m}_{\mathrm{MS,PGB}}\, (h_{\mathrm{HT,out}} - h_{\mathrm{CT,in}}) \tag{3.53}$$

$$\frac{\mathrm{d}m_{\mathrm{HT}}}{\mathrm{d}t} = \dot{m}_{\mathrm{MS,SF}} - \dot{m}_{\mathrm{MS,PGB}} \tag{3.54}$$

where $m_{\mathrm{MS,HT}}$ is the mass of molten salt in the hot tank, $\dot{Q}_{\mathrm{SF\rightarrow HT}}$ the rate of absorbed heat in the solar receiver, $\dot{Q}_{\mathrm{HT,loss}}$ the rate of heat loss from the hot tank to the environment, $\dot{Q}_{\mathrm{HT\rightarrow PGB}}$ the rate of heat transferred to the power generation block, $\dot{m}_{\mathrm{MS,SF}}$ the mass flowrate of the molten salt that flows into the solar receiver, $\dot{m}_{\mathrm{MS,PGB}}$ the mass flowrate of molten salt directed to the power generation block, $h_{\mathrm{MS,SF,out}}$ the specific enthalpy of molten salt flowing out of the solar receiver, A_{HT} the hot tank surface area, $\alpha_{\mathrm{HT,loss}}$ the heat transfer coefficient between the hot tank and the environment, T_{HT} the temperature of the hot tank, T_{a} the ambient temperature and $h_{\mathrm{HT,out}}$ and $h_{\mathrm{CT,in}}$ are the specific enthalpy of the hot tank and the cold tank, respectively.

The stored heat in the hot tank is then directed to the power generation cycle to heat up the working fluid for power generation, which is then flows back to the cold tank. The energy balance and the mass balance equations of the cold tank are expressed as [138–140]:

$$m_{\mathrm{MS,CT}} \frac{\mathrm{d}h_{\mathrm{CT}}}{\mathrm{d}t} = \dot{Q}_{\mathrm{PGB\rightarrow CT}} - \dot{Q}_{\mathrm{CT,loss}} - \dot{Q}_{\mathrm{CT\rightarrow SF}} \tag{3.55}$$

$$\dot{Q}_{\mathrm{PGB\rightarrow CT}} = \dot{m}_{\mathrm{MS,PGB}}\, h_{\mathrm{CT,in}} \tag{3.56}$$

$$\dot{Q}_{\mathrm{CT,loss}} = A_{\mathrm{CT}}\, \alpha_{\mathrm{CT,loss}}\, (T_{\mathrm{CT}} - T_{\mathrm{a}}) \tag{3.57}$$

$$\dot{Q}_{\mathrm{CT\rightarrow SF}} = \dot{m}_{\mathrm{MS,SF}}\, h_{\mathrm{CT,out}} \tag{3.58}$$

$$\frac{\mathrm{d}m_{\mathrm{MS,CT}}}{\mathrm{d}t} = \dot{m}_{\mathrm{MS,PGB}} - \dot{m}_{\mathrm{MS,SF}} \tag{3.59}$$

where $m_{\mathrm{MS,CT}}$ is the mass of molten salt in the cold tank, $\dot{Q}_{\mathrm{PGB\rightarrow CT}}$ the rate of added heat to the cold tank from the power generation block, $\dot{Q}_{\mathrm{CT,loss}}$ the rate of heat loss from the cold tank to the environment, $\dot{Q}_{\mathrm{CT\rightarrow SF}}$ the energy flow from the hot tank to the solar receiver, A_{CT} the cold tank surface area, $\alpha_{\mathrm{CT,loss}}$ the heat transfer coefficient between the cold tank and the environment and T_{CT} the temperature of the cold tank.

For the designed two-tank molten salt TES system in Chapter 7, the heat loss from the hot and the cold tank to the environment, $\dot{Q}_{\mathrm{HT,loss}}$ and $\dot{Q}_{\mathrm{CT,loss}}$, were assumed to be negligible (fully insulated tanks). However, it was conservatively assumed that there is 5 °C of temperature drop between the solar field and the TES system (hot and cold tanks) and also between the TES system and the power generation block. This temperature drop was assumed to cover any heat loss in the pipes as well as in the tanks. With such temperature drop, the calculated TES charging efficiency, $\eta_{\mathrm{TES,Ch}}$, and discharging efficiency, $\eta_{\mathrm{TES,Dch}}$, were both 96%.

The thermophysical properties of the selected molten salt, solar salt (60% $NaNO_2$ + 40% KNO_3), which is used as HTF and storage material in the study presented in Chapter 7, are listed in Table 3.5. The change of the specific enthalpy of the molten salt was obtained using the specific heat capacity correlation in Table 3.5 and the following equation:

$$\Delta h_{\mathrm{MS}} = \int_{T_{\mathrm{CT}}}^{T_{\mathrm{HT}}} c_{\mathrm{p}}\, \mathrm{d}T \tag{3.60}$$

where Δh_{MS} is the change of the molten salt specific enthalpy from T_{CT} to T_{HT}.

Table 3.5. Thermophysical properties of solar salt (60% $NaNO_2$ + 40% KNO_3) that are used in Chapter 7 [141–145]. *T* is the bulk temperature in °C.

Thermophysical property	Value/correlation
Density (kg/m^3)	$\rho = 1916.3 - 0.636\,T$
Specific heat capacity (J/kg K)	$c_{\mathrm{p}} = 1490 + 0.172\,T$
Thermal conductivity (W/m K)	$k = 0.4949 + (2 \times 10^{-4})\,T$
Dynamic viscosity (Pa s)	$\mu = \dfrac{22.7 - 0.12\,T + (2.28 \times 10^{-4})\,T^2 - (1.47 \times 10^{-7})\,T^3}{1000}$
Melting temperature (°C)	223

3.4. Power generation system model

The generic design and the modelling basis of the considered power generation cycle (steam Rankine cycles and organic Rankine cycles) systems in this thesis are discussed in this section. The modelling procedure and the main equations for full-load (design point) operation are covered in Section 3.4.1, while the off-design (part-load) operation of the designed power generation cycle systems is covered in Section 3.4.2.

3.4.1. Design and modelling of power generation cycles

Most of the designed power generation cycles, either steam Rankine cycle or organic Rankine cycles, in this thesis contains the following key components:

- Heat addition devices (heat exchangers), which could be one or a combination of the following components: nuclear steam generators; solar evaporator; solar superheater; and/or solar reheater.
- One or more of multiple-stages turbines. The turbines were assumed to have side extraction points where the extracted hot stream from the side extraction points is utilised to preheat the working fluid before flowing into the main heat addition device.
- Condensers for heat rejection and brining the working fluid to liquid phase (either subcooled or saturated liquid).
- A series of closed feedwater heaters (CFWH) in steam Rankine cycle systems or regenerators in ORC systems. The CFWHs are treated as heat exchangers.
- Deaerators or open feedwater heater and they are modelled as fluid mixers.
- Pumps to compress the working fluids.
- Electric generators that are driven by the turbines.

The energy and mass balance equations written for each of the above cycle components, and which were solved to predict the thermodynamic performance of the power generation block (i.e., steam Rankine cycle or ORC), are discussed below.

For heat addition devices (heat exchangers), the calculation of the required rate of added heat, the mass flowrates of the working fluid and HTF, the inlet and the outlet enthalpy of both fluids, were determined using the following general energy and mass balance equations:

$$\dot{Q}_{\mathrm{HTF}} = \dot{m}_{\mathrm{HTF}} \left(h_{\mathrm{HTF,out}} - h_{\mathrm{HTF,in}}\right) \tag{3.61}$$

$$\dot{Q}_{\mathrm{wf}} = \dot{m}_{\mathrm{wf}} \left(h_{\mathrm{wf,out}} - h_{\mathrm{wf,in}}\right) \tag{3.62}$$

$$\dot{m}_{\mathrm{HTF,in}} = \dot{m}_{\mathrm{HTF,out}} \tag{3.63}$$

$$\dot{m}_{\mathrm{wf,in}} = \dot{m}_{\mathrm{wf,out}} \tag{3.64}$$

where $\dot{Q}_{\mathrm{HTF}}$ is the rate of heat transferred from the HTF, $\dot{Q}_{\mathrm{wf}}$ the rate of heat been transferred to the working fluid, $\dot{m}_{\mathrm{HTF}}$ the mass flowrate of the HTF, $\dot{m}_{\mathrm{wf}}$ the mass flowrate of the working fluid, h_{HTF} the specific enthalpy of the HTF, h_{wf} the specific enthalpy of the working fluid, and subscripts ‘in’ and ‘out’ stand for inlet and outlet condition, respectively.

In most cases, the rate of heat that is transferred from the HTF, $\dot{Q}_{\mathrm{HTF}}$, is equal to the rate of added heat in the working fluid, $\dot{Q}_{\mathrm{wf}}$. However, in some cases, the use of heat-to-heat efficiency was applied to account for any heat losses taking place in the heat exchanger. The relationship between the two heat rates, $\dot{Q}_{\mathrm{HTF}}$ and $\dot{Q}_{\mathrm{wf}}$, in such cases were expressed as:

$$\dot{Q}_{\mathrm{HTF}} = \frac{\dot{Q}_{\mathrm{wf}}}{\eta_{\mathrm{HX}}} \tag{3.65}$$

where the η_{HX} is the heat-to-heat efficiency of the heat addition device.

In this thesis, the turbines were assumed to consist of several turbine parts (segments). Each part is defined as a group of turbine stages (i.e., each stage consists of a stator and a rotor) that are between the main turbine inlet and the first side extraction point, between two consecutive side extractions, or between the last side extraction point and the main turbine outlet. For example, if a turbine has 3 side extractions, it is divided into 4 parts, Part 1 includes the stages between the turbine inlet and first side extraction, Part 2 represents the stages between the first and second side extractions, Part 3 includes the stages between the second and third side extractions, and Part

4 represents the stages between the third side extraction and main outlet. Therefore, the total amount of generated power by the multi-stage turbines, $\dot{W}_{\mathrm{T}}$, was calculated using:

$$\dot{W}_{\mathrm{T}} = \sum_{i=1}^{n} \dot{W}_{\mathrm{TP},i} \tag{3.66}$$

$$\dot{W}_{\mathrm{TP},i} = \dot{m}_{\mathrm{TP},i}\,(h_{\mathrm{TP,in},i} - h_{\mathrm{TP,out},i}) \tag{3.67}$$

$$\eta_{\mathrm{TP}} = \frac{h_{\mathrm{TP,in}} - h_{\mathrm{TP,out}}}{h_{\mathrm{TP,in}} - h_{\mathrm{TP,out,is}}} \tag{3.68}$$

where $\dot{W}_{\mathrm{TP},i}$ is the amount of generated power by each turbine part, $\dot{m}_{\mathrm{TP},i}$ the working fluid mass flowrate that flows inside each part, η_{TP} the isentropic efficiency of each part, $h_{\mathrm{TP,out}}$ and $h_{\mathrm{TP,in}}$ the inlet and outlet specific enthalpies of the working fluid at each part, n the number of turbine part, and subscript 'is' indicates properties evaluated at equivalent isentropic conditions.

In terms of the working fluid mass flowrate flowing through each turbine part, it was calculated based on the mass balance equation. The mass flowrate of the first turbine part is expressed in Equation (3.69) and while for the other parts are expressed in Equation (3.70):

$$\dot{m}_{\mathrm{TP},1} = \dot{m}_{\mathrm{TP,in},1} = \dot{m}_{\mathrm{TP,out},1} \tag{3.69}$$

$$\dot{m}_{\mathrm{TP},i} = \dot{m}_{\mathrm{TP,out},i-1} - \dot{m}_{\mathrm{SE},j} = \dot{m}_{\mathrm{TP,out},i} \tag{3.70}$$

where $\dot{m}_{\mathrm{TP},1}$is the mass flowrate of the first part, $\dot{m}_{\mathrm{TP},i}$ the mass flowrate for Part $i = 2$ until $i = n$, and $\dot{m}_{\mathrm{SE},j}$ the mass flowrate of side extraction points that ranges from j=1 to $j = n - 1$.

The amount of needed power by each pump to compress the working fluid was calculated by:

$$\dot{W}_{\mathrm{P}} = \dot{m}_{\mathrm{P}}\,(h_{\mathrm{P,out}} - h_{\mathrm{P,in}}) \tag{3.71}$$

$$\eta_{\mathrm{P}} = \frac{(h_{\mathrm{P,out,is}} - h_{\mathrm{P,in}})}{(h_{\mathrm{P,out}} - h_{\mathrm{P,in}})} \tag{3.72}$$

$$\dot{m}_{\mathrm{P}} = \dot{m}_{\mathrm{P,in}} = \dot{m}_{\mathrm{P,out}} \tag{3.73}$$

where $\dot{W}_{\mathrm{P}}$ is the pump power, η_{P} the pump isentropic efficiency and $\dot{m}_{\mathrm{P}}$ the mass flowrate of the compressed working fluid.

The rate of rejected heat in the condenser were calculated using:

$$\dot{Q}_{\mathrm{cond}} = \dot{m}_{\mathrm{cond}}\,(h_{\mathrm{cond,out}} - h_{\mathrm{cond,in}}) \tag{3.74}$$

$$\dot{m}_{\mathrm{cond}} = \dot{m}_{\mathrm{cond,in}} = \dot{m}_{\mathrm{cond,out}} \tag{3.75}$$

where $h_{\text{cond,out}}$ is the working fluid specific enthalpy at saturated liquid conditions ($x = 0$) and at the condensing pressure.

The amount of available thermal power added from the hot-leg stream that is directed from the turbine side extraction and the amount of thermal power added to the working fluid (cold-leg stream) in all CFWHs (i.e., regenerators in ORC systems) were calculated by:

$$\dot{Q}_{\text{CFWH,HL}} = \dot{m}_{\text{CFWH,HL}} \left(h_{\text{CFWH,HL,out}} - h_{\text{CFWH,HL,in}}\right) \tag{3.76}$$

$$\dot{Q}_{\text{CFWH,CL}} = \dot{m}_{\text{CFWH,CL}} \left(h_{\text{CFWH,CL,out}} - h_{\text{CFWH,CL,in}}\right) \tag{3.77}$$

$$\dot{m}_{\text{CFWH,HL,in}} = \dot{m}_{\text{CFWH,HL,out}} \tag{3.78}$$

$$\dot{m}_{\text{CFWH,CL,in}} = \dot{m}_{\text{CFWH,CL,out}} \tag{3.79}$$

$$\dot{Q}_{\text{CFWH,HL}} = \frac{\dot{Q}_{\text{CFWH,CL}}}{\eta_{\text{CFWH}}} \tag{3.80}$$

where η_{CFWH} is the heat-to-heat efficiency of the CFWH, less than 1 if any heat loss is assumed, and subscripts 'HL' 'and CL' represents the hot-leg and the cold-leg streams respectively.

The energy and mass balance equations for the deaerator (open feedwater heater) that were implemented in the power generation cycle model were expressed as:

$$h_{\text{DE,out}} = \frac{\sum(\dot{m}h)_{\text{DE,in}}}{\sum \dot{m}_{\text{DE,in}}} \tag{3.81}$$

$$\dot{m}_{\text{DE,out}} = \sum \dot{m}_{\text{DE,in}} \tag{3.82}$$

where $h_{\text{DE,out}}$ is the specific enthalpy of the working fluid outflowing from deaerator, $\sum(\dot{m}h)_{\text{DE,in}}$ the sum of all inlet flow energy and $\sum \dot{m}_{\text{DE,in}}$ the sum of inlet mass flowrates into the deaerator.

The amount of net electrical power from the power generation cycle, $\dot{W}_{\text{net}}$, and the power generation cycle efficiency, η_{Cyc}, were calculated from:

$$\dot{W}_{\text{net}} = (\eta_{\text{gen}} \sum \dot{W}_{\text{T}}) - \sum \dot{W}_{\text{P}} \tag{3.83}$$

$$\eta_{\text{Cyc}} = \frac{\dot{W}_{\text{net}}}{\sum \dot{Q}_{\text{Cyc}}} \tag{3.84}$$

where η_{gen} is the electric generator efficiency and $\sum \dot{Q}_{\text{Cyc}}$ is the sum of 'the rate' of added heat into the power generation cycle.

The main generic assumptions used in the quasi-steady power generation cycle models in this thesis include:

- all pump suction pressures are adjusted and controlled to avoid pump cavitation [146];
- no mass loss across all power generation cycle components; and,
- all feedwater heaters are equipped with steam traps so that saturated liquid is collected through throttling before flowing into the deaerator/condenser units [133,147].

All other assumptions and parameters including component efficiencies, pressure losses, etc., that are implemented for each power generation cycle model are listed in their respective chapters.

3.4.2. Off-design performance

The power generation cycle model takes into consideration the off-design performance of the power cycle components during part-load operations. For steam turbines, the off-design isentropic efficiency was predicted using a correlation developed by Ray [148], expressed in Equation (3.85). The correlation estimates the stage efficiency by the ratio of blade tip velocity to theoretical steam velocity. The function assumes the blade tip velocity to be proportional to the turbine shaft speed, and the steam velocity to the square root isentropic enthalpy drop across the stage:

$$\eta_{\mathrm{TP}}^{\mathrm{OD}} = \eta_{\mathrm{TP}}^{\mathrm{D}} - \lambda \left(\frac{\omega^{\mathrm{OD}} \sqrt{\Delta h_{\mathrm{is}}^{\mathrm{D}}}}{\omega^{\mathrm{D}} \sqrt{\Delta h_{\mathrm{is}}^{\mathrm{OD}}}} - 1 \right)^2 \tag{3.85}$$

where η_{TP} is the turbine part isentropic efficiency, λ a positive constant, ω the shaft rotational speed, Δh_{is} the equivalent isentropic enthalpy change across the turbine and superscripts 'D' and 'OD' indicate design and off-design conditions. It is assumed that the shaft speed is constant for all loads as being connected to a fixed-frequency power grid, typically 50Hz or 60 Hz depending on the country (e.g., the frequency is fixed at 50 Hz in the UK [149]).

The part-load power generation cycle model also considered the change of steam pressure at the inlet and the outlet of each turbine part due to steam mass flowrate and temperature variations inside the turbine during part-load operation. To calculate the turbine inlet, outlet, and side extractions pressure, the following Stodola's ellipse law was applied [150,151]:

$$\frac{\frac{\dot{m}_{\text{in}}^{\text{OD}}\sqrt{T_{\text{in}}^{\text{OD}}}}{P_{\text{in}}^{\text{OD}}}}{\frac{\dot{m}_{\text{in}}^{\text{D}}\sqrt{T_{\text{in}}^{\text{D}}}}{P_{\text{in}}^{\text{D}}}} = \frac{\sqrt{1-\left(\frac{P_{\text{out}}^{\text{OD}}}{P_{\text{in}}^{\text{OD}}}\right)^2}}{\sqrt{1-\left(\frac{P_{\text{out}}^{\text{D}}}{P_{\text{in}}^{\text{D}}}\right)^2}} \tag{3.86}$$

where P_{in} is the inlet steam pressure, P_{out} the outlet steam pressure, T_{in} the inlet steam temperature, and $\dot{m}_{\text{in}}$ the inlet steam mass flowrate of each turbine part.

The heat exchanger (e.g., superheater, reheater, CFWH, condenser, etc.) models included in this thesis are simple and does not include determination of detail design parameters such as tube and shell dimensions, etc. The adapted heat exchanger models include determination of heat exchanging areas using an averaged heat transfer coefficient, the logarithmic-mean temperature difference in the heat exchanger and the amount of transferred heat as the following:

$$\dot{Q}_{\text{tran}} = \alpha\, A\, \Delta T_{\text{LM}} \tag{3.87}$$

where $\dot{Q}_{\text{tran}}$ is the rate of transferred heat in the heat exchanger, α the overall heat transfer coefficient, A the heat exchanging area and ΔT_{LM} the logarithmic-mean temperature difference.

The off-design performance of the power generation cycle heat exchangers was also considered during part-load operations. The off-design pressure drop across the heat exchanger and the off-design heat transfer coefficient for a designed heat exchanger can be estimated using [152,153]:

$$\Delta P^{\text{OD}} = \Delta P^{\text{D}} \left(\frac{\dot{m}_{\text{HL,CL}}^{\text{OD}}}{\dot{m}_{\text{HL,CL}}^{\text{OD}}}\right)^{1.75} \tag{3.88}$$

$$\alpha^{\text{OD}} = \alpha^{\text{D}} \left(\frac{\dot{m}_{\text{CL}}^{\text{OD}}\,\dot{m}_{\text{HL}}^{\text{OD}}}{\dot{m}_{\text{CL}}^{\text{D}}\,\dot{m}_{\text{HL}}^{\text{D}}}\right)^{0.8} \left(\frac{\dot{m}_{\text{CL}}^{\text{D}\,0.8} + \dot{m}_{\text{CL}}^{\text{D}\,0.8}}{\dot{m}_{\text{CL}}^{\text{OD}\,0.8} + \dot{m}_{\text{CL}}^{\text{OD}\,0.8}}\right) \tag{3.89}$$

where ΔP is the pressure drop across the heat exchanger, α the overall heat transfer coefficient, and superscripts/subscripts ‘OD’, ‘D’, ‘HL’ and ‘CL’ stand for off-design, design, hot-leg and cold-leg flow streams, respectively.

3.5. Cost estimation

The thesis includes comprehensive economic analyses for the considered power plant configurations. Thus, the estimation of the total capital and other associated costs for the

considered power plant is vital to obtain valid and reasonable results. This section covers the cost estimation correlations and functions used to estimate the total costs during the lifetime of the power plants in Chapter 4 and Chapter 7.

3.5.1. Overall approach

The costing of power plants, especially power generation block components, is challenging and can involve uncertainties making it difficult to obtain accurate costs. However, in this thesis, all cost estimation methods were slightly conservative to account for any associated uncertainties related to currency exchange rate, inflation, industry type, and other economic conditions. This was achieved by adjusting the obtained costs using cost indexes from data collection time (i.e., base time) to the time of the analysis as in the following expression, proposed by Seider et al. [154]:

$$C_{\mathrm{A}} = C_{\mathrm{B}} \left(\frac{I_{\mathrm{A}}}{I_{\mathrm{B}}}\right) \tag{3.90}$$

where C_{B} is the costs at data collection time, C_{A} the cost at analysis time, I_{B} the cost index at base time and I_{A} the index in the present year.

The cost indices were based on the chemical engineering plant cost index (CEPCI). The list of cost indices for the analysis years and for the applied cost estimation methods (discussed in Section 3.5.2) are listed in Table 3.6. Please note that all costs were calculated in USD ($).

Table 3.6. List of cost indices used for capital cost estimation [155].

Method	Year	CEPC index
Analysis year	2022	817
Analysis year	2021	708
Seider et al. [154]	2013	567
Towler et al. [156]	2010	533
Morandin et al. [157]	2009	522
Couper et al. [158]	2008	575
Ulrich et al. [159]	2004	400
Turton et al. [160]	2001	397

3.5.2. Costing of power block components

The capital cost of each component in the power generation block was estimated using the average costs obtained from cost correlations reported in Seider et al. [154], Towler et al. [156], Morandin

et al. [157], Couper et al. [158], Ulrich et al. [159] and Turton et al. [160]. Once each component cost was determined, the total cost of the power generation block, C_{PGB}, was then calculated by:

$$C_{\mathrm{PGB}} = \sum C_{\mathrm{T}} + \sum C_{\mathrm{cond}} + \sum C_{\mathrm{DE}} + \sum C_{\mathrm{CFWH}} + \sum C_{\mathrm{P}} + \sum C_{\mathrm{gen}} + \sum C_{\mathrm{CT}} \tag{3.91}$$

where C_{T} is the turbine cost, C_{cond} the cost of each condenser, C_{DE} the cost of each deaerator, C_{CFWH} the cost of each CFWH, C_{P} the cost of each pump, C_{gen} the cost of each electric generator and C_{CT} the cost of the cooling tower if installed.

The following sub-sections summarised the main methods and cost functions that were used for estimating the capital cost of the power generation block.

3.5.2.1. Turbines

The methods used in estimating the capital cost of steam turbines are listed in Table 3.7. The purchase cost of the steam turbine is expressed as $C_{\mathrm{p,T}}$ and the final bare module cost, which takes into consideration the type of material, labour, engineering, fabrication, etc. is expressed as $C_{\mathrm{BM,T}}$. The average of the obtained bare module costs from the listed five methods was used to estimate the capital cost of the steam turbines, which is then used as input in Equation (3.91).

Table 3.7. Main correlations and constants used for steam turbine capital cost estimation.

Method	Cost functions	Limits and units
Seider et al. [154]	$C_{\mathrm{p,T}} = \begin{cases} 10660\ \dot{W}_{\mathrm{T}}^{0.41} & \text{non-condensing} \\ 28350\ \dot{W}_{\mathrm{T}}^{0.405} & \text{condensing} \end{cases}$ $F_{\mathrm{BM,T}} = 3.3$ $C_{\mathrm{BM,T}} = F_{\mathrm{BM,S}}\ F_{\mathrm{M,T}}\ C_{\mathrm{p,T}}$	250-10000 Hp [167] is in Hp
Couper et al. [158]	$C_{\mathrm{p,T}} = \begin{cases} 378\ \dot{W}_{\mathrm{T}}^{0.81} & \text{back pressure} \\ 1100\ \dot{W}_{\mathrm{T}}^{0.81} & \text{vacuum pressure} \end{cases}$ $F_{\mathrm{BM,T}} = 1.5$ $C_{\mathrm{BM,T}} = F_{\mathrm{BM,T}}\ C_{\mathrm{p,T}}$	20-5000 Hp 200-8000 Hp $\dot{W}_{\mathrm{T}}$ is in Hp
Turton et al. [160]	$\log C_{\mathrm{P,T}} = 2.6259 + 1.4398(\log \dot{W}_{\mathrm{T}}) - 0.1776\ (\log \dot{W}_{\mathrm{T}})^2$ $F_{\mathrm{BM,T}} = 3.5$ $C_{\mathrm{BM,T}} = F_{\mathrm{BM,T}}\ C_{\mathrm{p,T}}$	70-7500 kW $\dot{W}_{\mathrm{T}}$ is in kW
Towler et al. [156]	$C_{\mathrm{p,T}} = -14000 + 1900\ \dot{W}_{\mathrm{T}}^{0.75}$ $F_{\mathrm{BM,T}} = 3.3$ $C_{\mathrm{BM,T}} = F_{\mathrm{BM,T}}\ F_{\mathrm{M,T}}\ C_{\mathrm{p,T}}$	100-20000 kW $\dot{W}_{\mathrm{T}}$ is in kW
Morandin et al. [157]	$C_{\mathrm{p,T}} = 40000 + 900\ \dot{W}_{\mathrm{T}}^{0.69}$ $F_{\mathrm{BM,T}} = 1.5$ $C_{\mathrm{BM,T}} = F_{\mathrm{BM,T}}\ C_{\mathrm{p,T}}$	$\dot{W}_{\mathrm{T}}$ is in kW

The material factor, $F_{M,T}$, in the cost function of the Seider et al. [100] method can be found in the first raw of Table 3.8 for different turbine materials.

Table 3.8. Material factors used in capital cost estimation of power generation block components.

Material factor (method)	Carbon steel	Stainless steel 304	Stainless steel 304	Nickel	Monel	Titanium
$F_{M,T}$ (Seider et al. [154])	1	2	2.3	2.5	2.7	6
$F_{M,PV}$ (Seider et al. [154])	1	1.7	2.1	5.4	3.6	7.7
$F_{M,Pu}$ (Seider et al. [154] and Couper et al. [158])	1	2	2	3.5	3.3	9.7
$F_{M,Pu}$ (Turton et al. [160])	1.6	2.25	NA	4.4	NA	NA
$F_{M,PV}$ (Turton et al. [160])	1	3.1	3.1	7.1	NA	9.4
F_{M} (Towler et al. [156])	1	1.3	1.3	1.7	1.65	NA

3.5.2.2. Heat exchangers

The cost of the heat exchanging devices (superheater, reheater, CFWHs, condenser, etc.) in the power generation block was estimated using the average of the bare module cost, $C_{BM,HX}$, of the four listed methods in Table 3.9. The costing parameters include the heat exchanging area (A_{HX}), the design pressure (P_{HX}) that is used to calculate the pressure factor ($F_{P,HX}$), the length factor ($F_{L,HX}$) and the material factor ($F_{M,HX}$), which can be obtained using the listed constants in Table 3.10 for different type of materials.

Table 3.9. Main methods and cost functions used for capital cost estimation of shell-and-tube heat exchangers.

Method	Cost functions	Limits and units
Seider et al. [154]	$C_{p,HX} = F_{P,HX}\, F_{M,HX}\, F_{L,HX}\, C_{HX}$ $C_{HX} = \begin{cases} \exp(12.03 - 0.87\,(\ln A_{HX}) + 0.090\,(\ln A_{HX})^2) & \text{floating head} \\ \exp(11.42 - 0.92\,(\ln A_{HX}) + 0.099\,(\ln A_{HX})^2) & \text{fixed head} \\ \exp(11.55 - 0.92\,(\ln A_{HX}) + 0.098\,(\ln A_{HX})^2) & \text{U-tube} \end{cases}$ $F_{P,HX} = 0.9803 + 0.018\left(\frac{P_{HX}}{100}\right) + 0.0017\left(\frac{P_{HX}}{100}\right)^2$ $F_{L,HX} = 1.25$ $F_{M,HX} = a + \left(\frac{A_{HX}}{100}\right)^b$ $F_{BM,HX} = 3.17$ $C_{BM,HX} = F_{BM,HX}\, C_{p,HX}$	150-12000 ft^2 $F_{L,HX}$ is in ft A_{HX} is in ft^2 P_{HX} is in psig

Couper et al. [158]	$C_{p,HX} = 1.218\, F_{P,HX}\, F_{M,HX}\, F_{D,HX}\, C_{HX}$ $C_{HX} = \exp(8.821 - 0.30863\,(\ln A_{HX}) + 0.0681\,(\ln A_{HX})^2)$ $F_{P,HX} = \begin{cases} \exp(0.7771 - 0.04981\,(\ln A_{HX})) & 100-300 \text{ psig} \\ \exp(1.0305 - 0.07140\,(\ln A_{HX})) & 300-600 \text{ psig} \\ \exp(1.1400 - 0.12088\,(\ln A_{HX})) & 600-900 \text{ psig} \end{cases}$ $F_{D,HX} = \begin{cases} 1 & \text{floating head} \\ \exp(-1.1156 + 0.0906\,(\ln A_{HX})) & \text{fixed head} \\ \exp(-0.9816 + 0.0830\,(\ln A_{HX})) & \text{U-tube} \end{cases}$ $F_{M,HX} = a + b\,(\ln A_{HX})$ $F_{BM,HX} = 2.2$ $C_{BM,HX} = F_{BM,HX}\, C_{p,HX}$	150-12000 ft^2 $F_{L,HX}$ is in ft A_{HX} is in ft^2 P_{HX} is in psig
Turton et al. [160]	$\log C_{p,HX} = \begin{cases} 4.83 - 0.85(\log A_{HX}) + 0.32\,(\log A_{HX})^2 & \text{floating head} \\ 4.32 - 0.30(\log A_{HX}) + 0.16\,(\log A_{HX})^2 & \text{fixed head} \\ 4.19 - 0.25(\log A_{HX}) + 0.20\,(\log A_{HX})^2 & \text{U-tube} \end{cases}$ $F_{P,HX} = 0.03881 - 0.11272(\log P_{HX}) + 0.08183\,(\log P_{HX})^2$ $F_{BM,HX} = 1.63 + 1.66\, F_{M,HX}\, F_{P,HX}$ $C_{BM,HX} = F_{BM,HX}\, C_{p,HX}$	10-10000 m^2 5-14 bar gauge A_{HX} is in m^2 P_{HX} is in bar gauge
Towler et al. [156]	$C_{P,HX} = \begin{cases} 32000 + 70\, A_{HX}^{1.2} & \text{floating head} \\ 28000 + 54\, A_{HX}^{1.2} & \text{U-tube} \end{cases}$ $F_{BM,HX} = 3.5$ $C_{BM,HX} = F_{BM,HX}\, F_{M,HX}\, C_{p,HX}$	10-10000 m^2 A_{HX} is in m^2

Table 3.10. List of constants used to calculate the material factors in the heat exchanger cost functions listed in Table 3.9.

Material (shell/tube)	**$F_{M,HX}$ constants (Seider et al. [154])**		**$F_{M,HX}$ constants (Couper et al. [158])**		**$F_{M,HX}$ (Turton et al. [160])**
	a	***b***	***a***	***b***	
Carbon steel	0	0	0	0	1
Carbon steel/stainless steel	1.75	0.13	NA	NA	1.8
Stainless steel 304	2.7	0.07	0.8193	0.15984	2.75
Stainless steel 316	2.7	0.07	0.8603	0.23296	2.75
Stainless steel 347	2.7	0.07	0.6116	0.22186	2.75

3.5.2.3. Pumps

The cost estimation of the pumps (centrifugal) were performed using the five different costing methods listed in Table 3.11, and the material factors listed in Table 3.8. The pump size factor, S_P, in Seider et al. [154] and Couper et al. [158] cost functions was calculated using:

$$S_P = \dot{V}_P (H_P)^{0.5} \tag{3.92}$$

where $\dot{V}_P$ is the volumetric flowrate in gallons per min and H_P the pump head in ft.

Table 3.11. List of methods used to estimate the costs of centrifugal pumps.

Method	Cost functions	Limits and units
Seider et al. [154]	$C_{\mathrm{p,P}} = F_{\mathrm{T,P}}\, F_{\mathrm{M,P}}\, C_{\mathrm{P}}$ $C_{\mathrm{P}} = \exp(12.166 - 1.145\,(\ln S_{\mathrm{P}}) + 0.086\,(\ln S_{\mathrm{P}})^2)$ $F_{\mathrm{T,P}} = 2.7$ $F_{\mathrm{BM,P}} = 3.3$ $C_{\mathrm{BM,P}} = F_{\mathrm{BM,P}}\, C_{\mathrm{p,P}}$	300-100000 gal ft$^{0.5}$/min $S_{\mathrm{P}} = \dot{V}_{\mathrm{P}}(H_{\mathrm{P}})^{0.5}$ $\dot{V}_{\mathrm{P}}$ is volumetric flowrate in gallons per min H_{P} is the pump head in ft S_{P} is the size factor
Couper et al. [158]	$C_{\mathrm{p,P}} = F_{\mathrm{T,P}}\, F_{\mathrm{M,P}}\, C_{\mathrm{P}}$ $C_{\mathrm{P}} = 3\exp(8.84 - 0.602\,(\ln S_{\mathrm{P}}) + 0.052\,(\ln S_{\mathrm{P}})^2)$ $F_{\mathrm{T,P}} = \exp(13.73 - 2.83\,(\ln S_{\mathrm{P}}) + 0.154\,(\ln S_{\mathrm{P}})^2)$ $F_{\mathrm{BM,P}} = \begin{cases} 2.8 & \text{carbon steel} \\ 2.0 & \text{stainless steel} \end{cases}$ $C_{\mathrm{BM,P}} = F_{\mathrm{BM,P}}\, C_{\mathrm{p,P}}$	300-100000 gal ft$^{0.5}$/min $S_{\mathrm{P}} = \dot{V}_{\mathrm{P}}(H_{\mathrm{P}})^{0.5}$ $\dot{V}_{\mathrm{P}}$ is the volumetric flowrate in gallons per min. H_{P} is the pump head in ft. S_{P} is size factor.
Turton et al. [160]	$\log C_{\mathrm{p,P}} = 3.39 + 0.054(\log \dot{W}_{\mathrm{P}}) + 0.154\,(\log \dot{W}_{\mathrm{P}})^2$ $F_{\mathrm{P,P}} = -0.39 + 0.396(\log \Delta P_{\mathrm{P}}) - 0.0023\,(\log \Delta P_{\mathrm{P}})^2$ $F_{\mathrm{BM,P}} = 1.89 + 1.35\, F_{\mathrm{M,P}}\, F_{\mathrm{P,P}}$ $C_{\mathrm{BM,P}} = F_{\mathrm{BM,P}}\, C_{\mathrm{p,P}}$	0-300 kW 10-100 bar gauge $\dot{W}_{\mathrm{P}}$ is in kW
Towler et al. [156]	$C_{\mathrm{p,P}} = 8000 + 240\, \dot{V}_{\mathrm{P}}^{0.9}$ $F_{\mathrm{BM,P}} = 4$ $C_{\mathrm{BM,P}} = F_{\mathrm{BM,P}}\, F_{\mathrm{M,P}}\, C_{\mathrm{p,P}}$	0.2-126 L/s $\dot{V}$ is in L/s
Morandin et al. [157]	$C_{\mathrm{p,P}} = 30900 + 44160\, \dot{V}_{\mathrm{P}}^{0.9}$ $F_{\mathrm{BM,P}} = 3.5$ $C_{\mathrm{BM,P}} = F_{\mathrm{BM,P}}\, C_{\mathrm{p,P}}$	$\dot{V}$ is in m^3/s

3.5.2.4. Pressure vessels

The capital cost of the pressure vessels (e.g., deaerators and steam accumulators) were estimated using the average cost obtained from the cost functions listed in Table 3.12. These methods are for horizontally oriented vessels. The material factors are listed in Table 3.8.

Table 3.12. List of costing methods used to estimate the cost of pressure vessels (e.g., deaerators and steam accumulators).

Method	Cost functions	Limits and units
Seider et al. [154]	$C_{\mathrm{p,PV}} = F_{\mathrm{M,PV}}\, C_{\mathrm{PV}} + C_{\mathrm{PL}}$ $C_{\mathrm{PV}} = \exp(5.6336 + 0.4599\,(\ln m_{\mathrm{PV}}) + 0.00582\,(\ln m_{\mathrm{PV}})^2)$ $C_{\mathrm{PL}} = 2275\, D_{\mathrm{PV,i}}^{0.2094}$ $F_{\mathrm{BM,PV}} = 3.05$ $C_{\mathrm{BM,PV}} = F_{\mathrm{BM,PV}}\, C_{\mathrm{p,PV}}$	1000-920000 Ib m_{PV} is in Ib $D_{\mathrm{PV,i}}$ is in ft

Couper et al. [158]	$C_{\mathrm{p,PV}} = F_{\mathrm{M,PV}}\, C_{\mathrm{PV}} + C_{\mathrm{PL}}$ $C_{\mathrm{PV}} = 1.67 \exp(8.571 - 0.2330\ (\ln m_{\mathrm{PV}}) + 0.04333\ (\ln m_{\mathrm{PV}})^2)$ $C_{\mathrm{PL}} = 2291\ D_{\mathrm{PV,i}}^{0.2029}$ $F_{\mathrm{BM,PV}} = \begin{cases} 1.7 & \text{carbon steel} \\ 2.8 & \text{stainless steel} \end{cases}$ $C_{\mathrm{BM,PV}} = F_{\mathrm{BM,PV}}\, C_{\mathrm{p,PV}}$	800-914000 Ib m_{PV} is in Ib $D_{\mathrm{PV,i}}$ is in ft
Turton et al. [160]	$\log C_{\mathrm{p,PV}} = 3.5565 + 0.3776(\log V_{\mathrm{PV}}) + 0.0905\ (\log V_{\mathrm{PV}})^2$ $F_{\mathrm{P,PV}} = \frac{1}{0.0063}\left(\frac{(P_{\mathrm{PV}}+1)\, D_{\mathrm{PV,i}}}{2\,(850-0.6\,(P_{\mathrm{PV}}+1))} + 0.00315\right)$ $F_{\mathrm{BM,PV}} = 1.49 + 1.52\, F_{\mathrm{M,PV}}\, F_{\mathrm{P,PV}}$ $C_{\mathrm{BM,PV}} = F_{\mathrm{BM,PV}}\, C_{\mathrm{p,PV}}$	0.1-628 m^3 V_{PV} is in m^3 P_{PV} is in bar gauge $D_{\mathrm{PV,i}}$ is in m
Towler et al. [156]	$C_{\mathrm{P,PV}} = \begin{cases} 10200 + 31\ m_{\mathrm{PV}}^{0.85} & \text{carbon steel} \\ 12800 + 73\ m_{\mathrm{PV}}^{0.85} & \text{stainless steel} \end{cases}$ $F_{\mathrm{BM,PV}} = 4$ $C_{\mathrm{BM,PV}} = F_{\mathrm{BM,PV}}\, C_{\mathrm{p,PV}}$	160-50000 kg 120-50000 m_{PV} is in kg
Morandin et al. [157]	$C_{\mathrm{p,PV}} = 10000 + 4500\ V_{\mathrm{PV}}^{0.6}$ $F_{\mathrm{BM,PV}} = \begin{cases} 1.7 & \text{carbon steel} \\ 2.8 & \text{stainless steel} \end{cases}$ $C_{\mathrm{BM,PV}} = F_{\mathrm{BM,PV}}\, C_{\mathrm{p,PV}}$	V_{PV} is in m^3

3.5.2.5. Cooling tower

The cost of cooling tower was only estimated using the average cost obtained from Couper et al. [158] and Towler et al. [156] cost functions, listed in Table 3.13.

Table 3.13. List of cooling tower costing function.

Method	Cost functions	Limits and units
Couper et al. [158]	$C_{\mathrm{p,CT}} = 164000\ \dot{V}_{\mathrm{CT}}^{0.61}$ $F_{\mathrm{BM,CT}} = 1.2$ $C_{\mathrm{BM,CT}} = F_{\mathrm{BM,PV}}\, C_{\mathrm{p,CT}}$	1-60 kgal/min $\dot{V}_{\mathrm{CT}}$ is in kgal/min
Towler et al. [156]	$C_{\mathrm{p,CT}} = 170000 + 1500\ \dot{V}_{\mathrm{CT}}^{0.9}$ $F_{\mathrm{BM,CT}} = 2.5$ $C_{\mathrm{BM,CT}} = F_{\mathrm{BM,CT}}\, C_{\mathrm{p,CT}}$	100-10000 L/s $\dot{V}_{\mathrm{CT}}$ is in L/s

3.5.2.6. Gear box and generators

The costs of the gear box and the generator attached to the turbine were estimated using [161]:

$$C_{\mathrm{gb}} = 212640\ \dot{W}_{\mathrm{out}}^{0.2434} \tag{3.93}$$

$$C_{\mathrm{gen}} = 130680\ \dot{W}_{\mathrm{out}}^{0.5463} \tag{3.94}$$

where $\dot{W}_{\mathrm{out}}$ is the turbine shaft power in $\mathrm{MW_{el}}$.

3.5.3. Nuclear island components

The estimation of nuclear island capital costs is challenging as it varies depending on the type of reactor, the design, the country, the size, etc. For instance, the actual specific capital costs of nuclear reactors ranged from 2157 \$/kW$_{el}$ in South Korea to 6920 \$/kW$_{el}$ in Slovakia as reported by the International Energy Agency (IEA) [162]. This substantial gap is a result of different reactor design and different safety and security requirements. In this thesis, the cost of nuclear island, in Chapter 7, was estimated using:

$$C_{\mathrm{NI}} = 1128\ \dot{Q}_{\mathrm{NR}} \tag{3.95}$$

where C_{NI} is the total capital costs of the nuclear island and $\dot{Q}_{\mathrm{NR}}$ the reactor thermal power output.

The specific capital cost per kW$_{th}$ in Equation (3.95) was obtained using the average of three different estimates that are listed in Table 3.14. As the specific cost in the literature were reported per kW$_{el}$, the costs were converted to be per kW$_{th}$ assuming a cycle efficiency of 33%. These values were obtained excluding: i) power generation block components (turbine, feedwater heater, etc.) costs; ii) land cost; ii) taxes; and iv) contingency fees which is usually around 10% of the total capital costs [163]. Some of eliminated costs were considered in the total capital cost estimation of the entire power plant.

Table 3.14. Nuclear island capital cost estimation.

Cost	Cost 1 [162]	Cost 3 [163]	Cost 2 [164]	Average
Direct capital (\$/kW$_{th}$)	708	1035	716	820
Indirect capital (\$/kW$_{th}$)	304	355	265	308
Total capital (\$/kW$_{th}$)	1012	1390	981	1128

3.5.4. Solar field components

The costing of the solar tower field components (external receiver, solar tower and heliostat field) was performed using SAM cost correlations that are listed in Table 3.15 [121]. These cost correlations accounts for the direct and indirect cost, and they are updated based on the year of 2022. The cost correlation of the heliostats in Table 3.15 includes site improvement costs (16 \$/m^2) and actual costs of the heliostats (127 \$/m^2). Using the provided correlations, the total solar tower field capital cost, C_{SF}, was obtained using:

$$C_{\mathrm{SF}} = C_{\mathrm{hel}} + C_{\mathrm{tow}} + C_{\mathrm{rec}} \tag{3.96}$$

where C_{hel} is the heliostat field cost, C_{tow} the tower cost and C_{rec} the solar receiver cost.

Table 3.15. Cost correlation used to estimate solar tower field capital costs [121].

Component	Costing parameter	Correlation
Heliostat field	Reflective area (m^2)	$C_{\mathrm{hel}} = 143\, A_{\mathrm{hel}}$
Tower	Tower, receiver, and heliostat heights (m)	$C_{\mathrm{tow}} = 3000 \exp\left(0.0113\left(H_{\mathrm{tow}} - \left(\frac{H_{\mathrm{rec}}}{2}\right) + \left(\frac{H_{\mathrm{hel}}}{2}\right)\right)\right)$
Receiver	Receiver area (m^2)	$C_{\mathrm{hel}} = 103000\, \left(\frac{H_{\mathrm{rec}}}{1571}\right)^{0.7}$

3.5.5. Thermal energy storage system components

The costing methods of the considered TES systems in Chapter 4 and Chapter 7 are discussed in Sections 3.5.5.1 and 3.5.5.2, respectively. The cost of the thermal tanks (PCM tanks) used in Chapter 5 and Chapter 6 was calculated based on specific investment costs of PCM tanks that were reported in the literature.

3.5.5.1. Solid storage blocks

There are no costing methods for concrete blocks proposed in the literature. Hence, the capital cost of the concrete blocks in Chapter 4 was estimated using the costs of its constituent materials (concrete mixture, insulation, steel, etc.). The purchase cost of all concrete blocks was calculated using:

$$C_{\mathrm{p,CB,total}} = N_{\mathrm{CB}}\, (C_{\mathrm{CB},1} + C_{\mathrm{CB},2}) \tag{3.97}$$

$$C_{\mathrm{CB},1} = V_{\mathrm{C}}\, U_{\mathrm{C}} + V_{\mathrm{tubes}}\, U_{\mathrm{tubes}} + A_{\mathrm{s,CB}}\, (U_{\mathrm{Ins}} + U_{\mathrm{P\&S}}) + A_{\mathrm{b,CB}}\, U_{\mathrm{F}} \tag{3.98}$$

$$A_{\mathrm{s,CB}} = 2\, L_{\mathrm{CB}}\, W_{\mathrm{CB}} + 2\, L_{\mathrm{CB}}\, H_{\mathrm{CB}} + 2\, H_{\mathrm{CB}}\, W_{\mathrm{CB}} \tag{3.99}$$

$$A_{\mathrm{b,CB}} = 2\, L_{\mathrm{CB}}\, W_{\mathrm{CB}} \tag{3.100}$$

$$V_{\mathrm{C}} = N_{\mathrm{tubes}}\, D_{\mathrm{o}}^2\, L_{\mathrm{CB}} \tag{3.101}$$

$$V_{\mathrm{tubes}} = N_{\mathrm{tubes}}\, L_{\mathrm{CB}}\, \frac{\pi}{4}\, ((D_{\mathrm{i}} + d_{\mathrm{tubes}})^2 - D_{\mathrm{i}}^2) \tag{3.102}$$

$$C_{\mathrm{CB},2} = C_{\mathrm{CB},1}\, (F_{\mathrm{P\&V}} + F_{\mathrm{E}} + F_{\mathrm{I\&C}}) \tag{3.103}$$

where N_{CB} is the number of blocks, V_{C} the concrete volume, V_{tubes} the tube material volume, $A_{\mathrm{s,CB}}$ the concrete block surface area, $A_{\mathrm{b,CB}}$ the concrete block base area, L_{CB}, H_{CB} and W_{CB} the length, height, and width, respectively, of each concrete block and other symbols are defined in Table 3.16.

Table 3.16 lists the costs of the main components of the concrete blocks and the assumed percentages accounting for indirect costs. The concrete mixture price available in the literature ranges from 124 \$/m^3 to 510 \$/m^3 depending on the mixture and additives [165]. Thus, the average value of the concrete prices was assumed. The costs of other materials (i.e., insulation, foundation, platform and steel, etc.) were also taken as the average value from the referenced studies.

Similarly, to account for all indirect capital costs of concrete blocks (i.e., labour, engineering, and contingency), the purchase costs was multiplied by a bare module factor, $F_{\mathrm{BM,CB}}$, of 1.5 as indicated in Table 3.16. Hence, the total capital cost of the concrete blocks was calculated by:

$$C_{\mathrm{BM,CB}} = F_{\mathrm{BM,CB}}\, C_{\mathrm{p,CB,total}} \tag{3.104}$$

The total capital cost of concrete blocks was also corrected for the year of analysis (2021) using Equation (3.104) since most unit costs listed in Table 3.16 were reported in 2010. The I_{B} for the year of 2010 is 551 [155].

Table 3.16. Costing parameters for concrete blocks.

Components	Symbol	Cost	Reference
Direct costs (\$)	$C_{\mathrm{p,CB,total}}$	-	-
Concrete mixture (\$/m^3)	U_{C}	230	[165]
Tube material – carbon steel (\$k/m^3)	U_{tubes}	17	[127]
Insulation (\$/m^2)	U_{Ins}	290	[166–168]
Foundation (\$/m^2)	U_{F}	2200	[166–168]
Platform and steel (\$/m^2)	$U_{\mathrm{P\&S}}$	490	[166,168]
Interconnecting piping and valves (-)	$F_{\mathrm{P\&V}}$	0.1	Assumed
Electrical (-)	F_{E}	0.1	Assumed
Instrumentation and control (-)	$F_{\mathrm{I\&C}}$	0.1	Assumed
Indirect costs (-)	$F_{\mathrm{BM,CB}}$	1.5	[50]

3.5.5.2. Two-tank molten salt TES system

The costing method for the two-tank molten salt TES system that was employed in Chapter 7 is similar to the costing method used for concrete blocks. The capital cost was estimated using the costs of its constituent materials and components (molten salt, steel, tanks, insulation, etc.). The purchase cost of all TES components, $C_{\mathrm{p,MS,total}}$, was calculated using the following equations:

$$C_{\mathrm{p,MS,total}} = C_{\mathrm{MS},1} + C_{\mathrm{MS},2} \tag{3.105}$$

$$C_{\mathrm{MS},1} = m_{\mathrm{MS}}\, U_{\mathrm{MS}} + 2\left(V_{\mathrm{tm}}\, U_{\mathrm{tm}} + A_{\mathrm{s,tank}}\,(U_{\mathrm{Ins}} + U_{\mathrm{P\&S}}) + A_{\mathrm{b,tank}}\, U_{\mathrm{F}}\right) \tag{3.106}$$

$$H_{\mathrm{tank}} = \frac{D_{\mathrm{i,tank}}}{2} \tag{3.107}$$

$$V_{\mathrm{tank}} = 1.1\, V_{\mathrm{MS}} = \pi\left(\frac{D_{\mathrm{i,tank}}}{2}\right)^3 \tag{3.108}$$

$$D_{\mathrm{o,tank}} = D_{\mathrm{i,tank}} + 2\, d_{\mathrm{tank}} \tag{3.109}$$

$$V_{\mathrm{tm}} = \pi\left(\frac{D_{\mathrm{o,tank}}}{2}\right)^3 - \pi\left(\frac{D_{\mathrm{i,tank}}}{2}\right)^3 \tag{3.110}$$

$$A_{\mathrm{s,tank}} = \pi\, D_{\mathrm{o,tank}}\, H_{\mathrm{tank}} + \frac{\pi}{2}\, D_{\mathrm{o,tank}}^2 \tag{3.111}$$

$$A_{\mathrm{b,tank}} = \frac{\pi}{4}\, D_{\mathrm{o,tank}}^2 \tag{3.112}$$

$$C_{\mathrm{MS},2} = C_{\mathrm{MS},1}\,(F_{\mathrm{P\&V}} + F_{\mathrm{E}} + F_{\mathrm{I\&C}}) \tag{3.113}$$

where m_{MS} is the mass of molten salt, V_{tm} the column of the tank material, $A_{\mathrm{s,tank}}$ the surface area of each tank, $A_{\mathrm{b,tank}}$ the base area of each tank, H_{tank} the tank height, $D_{\mathrm{i,tank}}$ the inner diameter of each tank, d_{tank} the tank wall thickness, $D_{\mathrm{o,tank}}$ the tank outer diameter, V_{tank} the volume of a single tank and other parameters are defined in Table 3.16 and Table 3.17.

The mass of the required molten salt, m_{MS}, in Equation (3.106) and the volume of each tank, V_{tank}, in Equation (3.108) were calculated based on:

$$m_{\mathrm{MS}} = 3600\, \dot{m}_{\mathrm{MS}}\, t_{\mathrm{Dch}} \tag{3.114}$$

$$V_{\mathrm{MS}} = \frac{m_{\mathrm{MS}}}{\rho_{\mathrm{MS}}} \tag{3.115}$$

$$V_{\mathrm{tank}} = 1.1\, V_{\mathrm{MS}} \tag{3.116}$$

where t_{Dch} full-load storage capacity in h, $\dot{m}_{\mathrm{MS}}$ the molten salt mass flowrate at full load, V_{MS} the molten salt volume, and ρ_{MS} the density of the molten salt.

Table 3.17. Costing parameters for two-tank molten salt TES system.

Components	**Symbol**	**Cost**	**Reference**
Direct costs ($)	$C_{\mathrm{P,CB,total}}$	-	-
Molten salt – solar salt ($/kg)	U_{MS}	0.86	[49,169,170]
Tank material – stainless steel 316 (k$/m^3)	U_{tm}	36.7	[171–173]
Indirect costs (-)	$F_{\mathrm{BM,MS}}$	1.8	Assumed

It should be noted that the density of molten salt in Equation (3.115) was calculated based on the minimum density of both temperatures (i.e., hot and cold). Moreover, the volumetric unit price of tank material, U_{tm}, was calculated based mass unit price of 4.68 \$/kg and a stainless steel 316 (i.e., tank material) density of 7840 kg/m^3 [174]. Furthermore, the assumed tank thickness in Equation (3.109) is 44.5 mm [175]. All other unit prices defined in Equations (3.106) and (3.113) are the same as the ones listed in Table 3.16. Similar to the costing of concrete blocks, the estimation of the total capital cost of the two-tank molten salt TES system includes consideration of indirect costs (i.e., labour, engineering, and contingency) which was estimated by considering a bare module factor, $F_{\mathrm{BM,MS}}$. Thus, the total capital cost of the two-tank molten salt TES system was calculated by:

$$C_{\mathrm{BM,MS}} = F_{\mathrm{BM,MS}}\, C_{\mathrm{p,MS,total}} \tag{3.117}$$

The bare module factor, $F_{\mathrm{BM,MS}}$, was assumed to be 1.8 which is higher than the one assumed for concrete blocks. It is a result of assuming higher engineering and labour cost (i.e., dealing with molten salt needs extra care due to toxicity) and higher contingency factor (i.e., possible need to install immersion heaters to avoid freezing of molten salt).

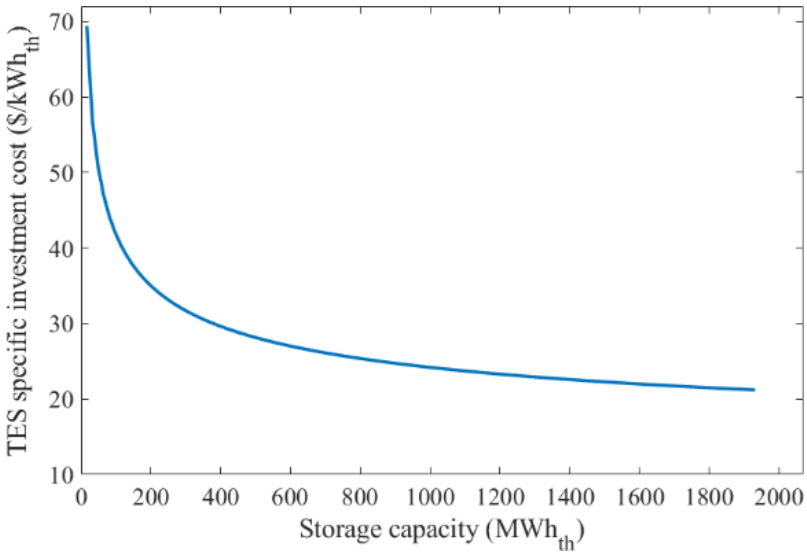

Figure 3.9. The specific cost of the two-tank molten salt TES for a range of TES capacities. The assumed temperature of the hot tank and the cold tank are 570 °C and 320 °C, respectively.

The calculated specific cost of the two-tank molten salt TES system for a range of storage capacity are shown in Figure 3.9. The specific cost decreases (non-linearly) with the increase of storage capacity until reaching specific costs of 20-25 \$/kWh$_{\mathrm{th}}$ for storage capacities above

1000 MWh_{th}. These costs are very comparable to the ones reported in literature [121,176,177]. The decrease in specific cost is nonlinear because, for example, when the tank volume is doubled, the increase of the base and surface areas is less than double. Thus, the associated cost of material (e.g., insulation) is not doubled when the tank size is doubled.

3.5.6. Other costs

The nuclear fuel cost was obtained using an estimated cost of 14 $\$/MWh_{el}$ [178,179]. This cost covers the cost of the entire fuel cycle which are: uranium extraction and conversion; enrichment; fuel fabrication; fuel storage; and waste management.

The operation and maintenance (O&M) cost for the nuclear side were estimated using two separate costs, which are fixed and variable costs. The fixed O&M costs are mandatory and must be paid no matter how much electricity is generated (i.e., usually expressed in $\$/kW_{el}$/year), while the variable O&M costs depend on the amount of generated electricity (i.e., $\$/MWh_{el}$). In this thesis, particularly in Chapter 7, these costs were assumed to be 99.5 $\$/kW_{el}$/year and 3.14 $\$/MWh_{el}$ respectively, based on the U.S. Energy Information Administration (EIA) cost predictions of future SMRs [180].

The O&M cost of the solar tower CSP plants ranges between 12 $\$/MWh_{el}$ and 27 $\$/MWh_{el}$ depending on the location as they have different labour costs and wages [181]. For example, the O&M is 12 $\$/MWh_{el}$ in South Africa, 11 $\$/MWh_{el}$ in Saudi Arabia, and 20 $\$/MWh_{el}$ in United Arab Emirates [181]. Based on these costs, the O&M cost for the case study discussed in Chapter 4 was taken as 12 $\$/MWh_{el}$ since the study was based on South Africa. For Oman, which is taken as a location of the case study presented in Chapter 7, the O&M costs was assumed as 15.5 $\$/MWh_{el}$ (i.e., the average value of the Arabian Gulf countries).

3.6. Performance indicators

In this thesis, the modelled power plants and TES technologies were compared using a set of commonly used thermo-economic performance indicators, which are discussed in this section. The considered definitions of the performance indicators in this section are generic and the specific input parameters and assumptions for each technology are listed in the first sections of Chapters 4,5,6 and 7 as they are different depending on the analysed case study.

3.6.1. Specific investment cost

The specific investment cost (SIC) of power plants gives an indication of the total capital cost per unit of electric power. It is defined as the ratio of the total investment (capital) cost of the entire power plant and the net (maximum) electrical power output from the power plant. This can be expressed as:

$$SIC_{\mathrm{PP}} = \frac{C_{\mathrm{c,PP}}}{\dot{W}_{\mathrm{net}}} \tag{3.118}$$

where $C_{\mathrm{c,PP}}$ is the total capital cost of the power plant and $\dot{W}_{\mathrm{net}}$ the net (maximum) electrical power output from the power plant.

Similarly, the specific investment cost of the power generation block only, SIC_{PGB}, can be calculated by considering the total capital cost of the power generation block as following:

$$SIC_{\mathrm{PGB}} = \frac{C_{\mathrm{c,PGB}}}{\dot{W}_{\mathrm{net}}} \tag{3.119}$$

where $C_{\mathrm{c,PGB}}$ is the total capital cost of the power generation block components only.

3.6.2. Levelised cost of electricity

Most power generation technologies are compared in terms of levelised cost of electricity (LCOE), which is a measure of the net present cost of electricity generation for a power plant over its lifetime. The LCOE is defined as the ratio between the total discounted costs of the power plant for its entire lifetime and the total amount of discounted generated electricity for the same period. The LCOE of the considered power plants in this thesis was calculated using the following generic expression:

$$LCOE = \frac{\sum_{t=1}^{n} \frac{C_{\mathrm{c}_t} + C_{\mathrm{O\&M,F}_t} + C_{\mathrm{O\&M,V}_t} + C_{\mathrm{fuel}_t}}{(1+r)^t}}{\sum_{t=1}^{n} \frac{DE_t}{(1+r)^t}} \tag{3.120}$$

$$DE_t = F_{\mathrm{ava}} \sum_{1}^{365} DE_{\mathrm{day}} \tag{3.121}$$

where C_{c} is the total capital cost per year, $C_{\mathrm{O\&M,F}}$ and $C_{\mathrm{O\&M,V}}$ represent the fixed and variable O&M costs per year, C_{fuel} the fuel cost per year, DE the total amount of generated electricity from the power plant per year, F_{ava} the availability factor of the power plant, n the lifetime of the plant and r the discount rate.

3.6.3. Levelised cost of storage

The levelised cost of storage (LCOS) has a similar definition as the LCOE but it only considers the costs and the amount of discharged electricity using the stored heat in the TES systems. It is a useful indicator to compare the performance of different TES technologies. Using a similar definition of the LCOE but considering the TES system only, the LCOS was calculated by:

$$LCOS = \frac{\sum_{t=1}^{n} \frac{C_{\mathrm{c,TES}_t} + C_{\mathrm{O\&M,TES}_t}}{(1+r)^t}}{\sum_{t=1}^{n} \frac{DE_{\mathrm{TES}_t}}{(1+r)^t}} \tag{3.122}$$

$$DE_{\mathrm{TES}_t} = F_{\mathrm{ava}} \sum_{1}^{365} DE_{\mathrm{TES,day}} \tag{3.123}$$

where $C_{\mathrm{c,TES}}$ is the total capital cost of the TES system per year, $C_{\mathrm{O\&M,TES}}$ the O&M costs of the TES system per year and DE_{TES} the total amount of electricity generated utilising the stored heat in the TES system only.

3.6.4. Net present value

The investment decisions are usually made by evaluating the expected economic performance and the profitability of the power plant for its entire lifetime. One of the economic indicators that gives an indication of the profitability is net present value (NPV), which is defined as the sum of the discounted cashflows for the entire lifetime of the project. NPV gives an indication of the current value of the power plant and helps making decision whether to proceed with the investment or not, especially if the decision is purely made from economic point of view. The NPV can be calculated by:

$$NPV = \sum_{t=1}^{n} \frac{I_t}{(1+r)^t} - \sum_{t=1}^{n} \frac{C_{\mathrm{c}_t} + C_{\mathrm{O\&M,F}_t} + C_{\mathrm{O\&M,V}_t} + C_{\mathrm{fuel}_t}}{(1+r)^t} \tag{3.124}$$

where I_t is the total amount of income per year, usually from selling electricity.

Positive NPVs mean that the project is profitable and can make some profits, while negative NPVs mean that the project will make losses and might not be a good investment, but it all depends on the economic assumptions applied to estimate the projected NPV.

3.6.5. Internal rate of return

Another performance indicator which is used to evaluate the profitability of any investment opportunity is the internal rate of return (IRR). The IRR is defined as the discount rate the makes the NPV equal to zero, and can be calculated by the following expression:

$$0 = NPV = \sum_{t=1}^{n} \frac{I_t}{(1+IRR)^t} - \sum_{t=1}^{n} \frac{C_{\mathrm{c}_t} + C_{\mathrm{O\&M,F}_t} + C_{\mathrm{O\&M,V}_t} + C_{\mathrm{fuel}_t}}{(1+IRR)^t} \quad (3.125)$$

The IRR is usually compared with the discount rate, if the anticipated IRR is higher than the assumed discount rate that is used to calculate the projected NPV, it means that the NPV will be positive, and the power plant will make some profits. However, if the IRR is less than the applied discount rate in the calculation of the NPV, the NPV will be negative, and the project will make losses. Therefore, the IRR can be considered as a cut-off point to whether to proceed with a project or not, especially if the decision is purely made based on economic perspective.

3.6.6. Payback time

Payback time is another economic indicator to consider when it comes to making decision whether to proceed with a project or not. The payback time is defined as the time it takes to fully recover your initial investment (capital) costs. In this thesis, the payback time was estimated by determining the time point where the accumulated and discounted cashflow is equal to zero.

3.7. Whole-electricity system modelling

To adequately quantify the role of flexible solutions in future electricity systems, it is critical to model these systems with sufficient spatial-temporal resolution using a holistic system approach. The approach to system valuation of flexible nuclear configurations used Chapter 6 is based on an extension of the whole-system modelling approach presented in Ref. [182]. This whole-system valuation approach has previously been used to assess battery storage [183], pumped-hydro storage [184] and liquid-air and pumped-heat energy storage [185].

System assessment of flexible nuclear plants in Chapter 6 was carried out by adopting an extended version of the whole-electricity system investment model (WeSIM), presented in Ref. [182], to include specific features of flexible nuclear generation. Capturing the interactions across various time-scales and across various asset types at sufficient temporal and spatial

granularity is critical when analysing future low-carbon electricity systems. WeSIM is a whole-system analysis model that is able to simultaneously optimise long-term investments into generation, network and storage assets, and short-term operation decisions in order to satisfy the demand at least cost while ensuring adequate security of supply, sufficient volumes of ancillary services and meeting system-wide carbon emission targets [182]. WeSIM can quantify trade-offs between using various sources of flexibility, such as demand-side response (DSR) and energy storage, for real-time balancing and for management of network constraints.

A detailed formulation of the model has been previously provided in Ref. [182]; therefore, only the new and additional elements of the model formulation (i.e., new variables, constraints and parameters) that are relevant for flexible nuclear power plant modelling in Chapter 6 are presented here. Extensions to the WeSIM model presented here have been implemented in FICO Xpress Optimisation framework [186]. WeSIM was formulated as a large-scale linear programming problem that was solved using the Newton-barrier optimisation algorithm, which identifies the globally optimal solution over the feasible solution space. Please note that WeSIM model formulation and execution was conducted by Dr. Marko Aunedi from the Department of Electrical and Electronic Engineering at Imperial College London.

3.7.1. Mathematical formulation of the whole-system model

The formulation of the system model presented here assumes a single-node system without considering any distribution, transmission or interconnection assets. A shortened form of the objective function for the mixed-integer linear problem is given in Equation (3.126). The model minimises the total system cost, which is the sum of annualised investment cost associated with power generation (G), flexible nuclear (N), electrolyser (E), hydrogen storage (H) and battery storage (S) assets, and the annual operating cost across all time intervals considered in the study (in this case all 8760 h of a year). Component investment costs are expressed as products of per-unit cost parameters (π) and decision variables for total capacity (μ). The operating cost term (C) is the function of generation output decision variables (p) and reflects the variable operating costs, no-load costs and start-up costs of thermal generators.

$$\min\{z\} = \sum_{i=1}^{G} \pi_i^G \mu_i^G + \sum_{i=1}^{N} \pi_i^N \mu_i^N + \sum_{i=1}^{E} \pi_i^E \mu_i^E + \sum_{i=1}^{H} \pi_i^H \mu_i^H + \sum_{i=1}^{S} \pi_i^S \mu_i^S + \sum_{t=1}^{\tau} \left(\sum_{i=1}^{G} C_{i,t}^G(p_{i,t}^G) + \sum_{i=1}^{N} C_{i,t}^N(p_{i,t}^N) \right) \quad (3.126)$$

A number of further constraints were formulated in the model (detailed mathematical formulation of the main WeSIM model can be found in Ref. [182] and is omitted here for brevity):

- power supply-balance constraints;
- operating reserve constraints for fast and slow reserves;
- generator operating constraints, including minimum and maximum output, ramping constraints and minimum up and down time constraints;
- annual load factor constraints to account for planned maintenance;
- available energy profiles for variable renewables;
- demand-side response constraints that allow demand shifting;
- emission constraints to limit total annual carbon emissions from the electricity system;
- security of supply constraints.

All variables and constraints presented in the remainder of this subsection represent an extension of the WeSIM model, which in its original formulation does not explicitly consider flexible nuclear plant configurations discussed in Chapter 6.

The number of flexible nuclear units in the system is denoted by n_{FN}, which can be either specified as fixed input or optimised by the model. Unit commitment variables, u, are formulated for each time interval, t, and separately for the primary steam Rankine cycle (PSRC) and secondary steam Rankine cycle (SSRC) systems' components of the flexible nuclear units:

$$u_{\mathrm{PSRC},t}, u_{\mathrm{SSRC},t} \leq n_{\mathrm{FN}} \quad (3.127)$$

In all case studies, the PSRC was assumed to operate as a must-run generator, i.e., that all PSRC units were always in synchronised operation (although not necessarily at full output).

The aggregate heat output of flexible nuclear plant steam generators, $\dot{Q}_{\mathrm{SG},t}$, was bounded from below and above by the product of n_{FN} and the lower and upper bound per one unit:

$$n_{\mathrm{FN}}\, \dot{Q}_{\mathrm{SG}}^{\min} \leq \dot{Q}_{\mathrm{SG},t} \leq n_{\mathrm{FN}}\, \dot{Q}_{\mathrm{SG}}^{\max} \quad (3.128)$$

Aggregate power output of PSRC and SSRC components was bounded by the relevant minimum and maximum output levels when these generators are operating:

$$u_{\mathrm{PSRC},t}\,\dot{W}_{\mathrm{PSRC}}^{\min} \le \dot{W}_{\mathrm{PSRC},t} \le u_{\mathrm{PSRC},t}\,\dot{W}_{\mathrm{PSRC}}^{\max} \tag{3.129}$$

$$u_{\mathrm{SSRC},t}\,\dot{W}_{\mathrm{SSRC}}^{\min} \le \dot{W}_{\mathrm{SSRC},t} \le u_{\mathrm{SSRC},t}\,\dot{W}_{\mathrm{SSRC}}^{\max} \tag{3.130}$$

Note that the multiple modules of TES-SSRC units discussed in Chapter 6 (i.e., Section 6.3.2) were treated aggregately in this formulation. The rates of charging and discharging heat into/from the integrated TES systems are given by:

$$\dot{Q}_{\mathrm{TES,Ch},t} \le n_{\mathrm{FN}}\,\dot{Q}_{\mathrm{TES,Ch}}^{\max} \tag{3.131}$$

$$\dot{Q}_{\mathrm{TES,Dch},t} \le n_{\mathrm{FN}}\,\dot{Q}_{\mathrm{TES,Dch}}^{\max} \tag{3.132}$$

The energy content of TES was limited by the aggregate storage size, while the TES balance equation accounts for charging and discharging heat subject to losses:

$$Q_{\mathrm{TES},t} \le n_{\mathrm{FN}}\,Q_{\mathrm{TES}}^{\max} \tag{3.133}$$

$$Q_{\mathrm{TES},t} = Q_{\mathrm{TES},t-1} + \left(\eta_{\mathrm{TES,Ch}}\,\dot{Q}_{\mathrm{TES,Ch},t} - \frac{1}{\eta_{\mathrm{TES,Dch}}}\,\dot{Q}_{\mathrm{TES,Dch},t}\right)\delta \tag{3.134}$$

Heat balance constraints were formulated to ensure that the heat produced by steam generator is used either directly in the PSRC unit or partially stored in TES, while any heat released from TES is used to power the SSRC units:

$$\dot{Q}_{\mathrm{SG},t} - \dot{Q}_{\mathrm{TES,Ch},t} = \dot{Q}_{\mathrm{PSRC},t} = \beta_{\mathrm{PSRC}}\,u_{\mathrm{PSRC},t} + \gamma_{\mathrm{PSRC}}\,\dot{W}_{\mathrm{PSRC},t} \tag{3.135}$$

$$\dot{Q}_{\mathrm{TES,Dch},t} = \dot{Q}_{\mathrm{SSRC},t} = \beta_{\mathrm{SSRC}}\,u_{\mathrm{SSRC},t} + \gamma_{\mathrm{SSRC}}\,\dot{W}_{\mathrm{SSRC},t} \tag{3.136}$$

The link between the input heat and output electricity for PSRC and SSRC units in Equations (3.135) and (3.136) was formulated by assuming a no-load heat rate, β, that is incurred whenever the unit is operating regardless of the output level, and incremental heat rate, γ, that multiplies the generator output level. These heat rate parameters were estimated from the results of thermodynamic modelling presented in Chapter 6. Other operating constraints such as ramping and minimum up/down times were also implemented in the model but were omitted here for brevity.

Finally, the annual availability constraint for the steam generator output was formulated based on the product of the annual availability factor, $F_{\mathrm{ava,FN}}$, and the duration of the year in h, τ,:

$$\sum_{t=1}^{\tau} \dot{Q}_{\mathrm{SG},t} \leq n_{\mathrm{FN}}\, \dot{Q}_{\mathrm{SG}}^{\max}\, \tau\, F_{\mathrm{ava,FN}} \tag{3.137}$$

The total operation cost of flexible nuclear units contributing to total system cost in Equation (3.126) is simply equal to the product of total SG output and the cost of nuclear fuel.

3.8. Summary

In this chapter, the formulation and validation of several thermodynamic and economic computational models were presented and discussed. These models alongside with other specific model inputs and assumption (i.e., discussed at the first sections of Chapters 4 to 7) were utilised to obtain the main results of the case studies investigated in this research. Moreover, several thermo-economic optimisation functions, which are covered in the next chapters, were formulated on the basis of the developed modelling tools. Furthermore, the power generation cycle system models involved the consideration of off-design performance of the cycle components during part-load operations, which is essential to obtain valid results to assess the flexibility of nuclear power plants.

The formulated thermo-economic models will enable to identify the optimum design and operation of several flexible nuclear power plant configurations and also to evaluate the option of extending the conventional steam accumulation TES system in DSG CSP plants. Moreover, this chapter included the formulation of whole-system electricity, which will enable to quantify the system economic benefits that could result from replacing conventional nuclear power plants with extended flexibility ones in future decarbonised electricity grids that have high shares of renewables.

Chapter 4

Thermo-economic analysis of steam accumulation in direct steam generation concentrated solar power plants

4.1. Introduction

Direct steam generation (DSG) concentrated solar power (CSP) is an option that uses water as a heat transfer fluid (HTF) in the solar receivers as well as a working fluid in the thermodynamic power generation cycle [61]. The use of a single fluid offers a number of benefits that are discussed in Section 2.5. Based on the comprehensive literature review that is covered in Chapter 2, Research Gap 1 was identified (i.e., see Section 2.8 for more information), which states that previous research did not compare the thermodynamic performance and the economic returns of operating the two steam-accumulation options (i.e., steam accumulators only and steam accumulator-solid heat storage) in a DSG CSP plant. Therefore, the work presented in this chapter covers Research Gap 1 with the aim of performing a comprehensive thermo-economic analysis and comparison of two steam-accumulation options (i.e., with and without the concrete storage) for an existing DSG CSP plant (Khi Solar One in South Africa) during charging and discharging. The main novel contributions of the work presented in this chapter include:

- Modelling and validation of the power generation cycle of the reference DSG CSP plant in baseload and part-load operating modes, including the analysis of off-design turbine efficiencies.
- Modelling and validation of the charging/discharging modes of SAs, including the performance of parametric thermo-economic analysis for a range of initial water filling ratios.
- Transient modelling and validation of heat transfer between the steam and the concrete, including the consideration of steam condensation process during charging process.
- Parametric analysis of the thermo-economic performance for different sizes of concrete blocks.
- Cost estimation of all TES system components using dedicated costing methods.

- Profitability assessment of the two steam accumulation options for the reference DSG CSP plant at different electricity prices.

The study firstly describes, in Section 4.2, the layout of the selected DSG CSP plant and the compared TES systems. The model inputs and the main assumptions are presented in Section 4.3. The thermodynamic and the economic evaluations of the compared TES system configurations are presented in Sections 4.4 to 4.7. Finally, the key findings and conclusions are summarised in Section 4.8. It should be noted that the presented study in this chapter has been already published as a journal article, which can be found in Ref. [187]

4.2. Description of the reference solar power plant (Khi Solar One)

Khi Solar One, which is a 50-MW_{el} DSG solar tower CSP plant in South Africa, is selected as the reference power plant. The main components of Khi Solar One are: (i) a heliostat field; (ii) a solar tower; (iii) a power generation block; and (iv) a TES system. The solar tower has two solar receivers, an evaporator, and a superheater. The evaporator is designed to collect solar heat and evaporate the feedwater coming from the power generation block to a temperature of 327 °C at 12.3 MPa (i.e., saturated vapour). The evaporated steam is then superheated to 530 °C at 12 MPa in the solar superheater. The main parameters of the two solar receivers and the heliostat field are summarised in Table 4.1. All Khi Solar One design and thermodynamic parameters were provided by the operators of Khi Solar One.

Table 4.1. Khi Solar One solar tower and heliostat field parameters.

Parameter	Symbol	Value
Evaporator efficiency (%)	η_{evp}	92
Evaporator outlet pressure (MPa)	P_{16}	12.3
Evaporator outlet temperature (°C)	T_{16}	330
Superheater efficiency (%)	η_{spr}	85
Superheater outlet pressure (MPa)	P_{1}	12.0
Superheater outlet temperature (°C)	T_{1}	530
Total heliostat reflective area (km^2)	A_{total}	0.57
Heliostat efficiency (%)	η_{hel}	97

The rate of absorbed heat in the evaporator and in the superheater were calculated using direct normal irradiance (DNI) data as the following:

$$\dot{Q}_{\mathrm{evp}} = q_{\mathrm{irr}}\, A_{\mathrm{evp}}\, \eta_{\mathrm{hel}}\, \eta_{\mathrm{evp}} \tag{4.1}$$

$$\dot{Q}_{\mathrm{spr}} = q_{\mathrm{irr}}\, A_{\mathrm{spr}}\, \eta_{\mathrm{hel}}\, \eta_{\mathrm{spr}} \tag{4.2}$$

$$A_{\mathrm{total}} = A_{\mathrm{evp}} + A_{\mathrm{spr}} \tag{4.3}$$

where $\dot{Q}$ is the rate of absorbed heat, q_{irr} the DNI, A the reflective area, η the efficiency and subscripts 'evp', 'spr', and 'hel' stand for the evaporator, superheater, and heliostat.

As indicated in Equations (4.1) and (4.2), the amount of heat depends on the reflective area of the heliostat that is allocated for each receiver. The total heliostat reflective area for both receivers, A_{total}, was assumed to be fixed. However, the fraction of the total area allocated for each receiver (i.e., A_{evp} and A_{spr}) can be varied. This means that if more solar power is required in the evaporator, more reflective area goes to the evaporator, which in turn reduces the reflective area allocated for the superheater as the total reflective area is constant.

The evaporator and the superheater are designed to absorb extra solar thermal power, when available, beside the required amount to generate the 50 MW_{el} of electrical power. The excess heat, which can be absorbed during high solar rays (mid-days), is to be stored in the TES system. The stored heat is then utilised for electricity generation during low or no sun times (i.e., night-time). In this chapter, two TES system configurations are compared. The two configurations are described in detail in Sections 4.2.1 and 4.2.2.

4.2.1. Existing TES configuration with steam accumulators

The schematic diagram of Khi Solar One power plant with its existing TES system is shown in Figure 4.1. The existing TES system configuration consists of two groups of SAs, base SAs and superheating SAs, as well as a storage superheater. During normal operation of the power plant with no TES system operations, feedwater flows into the evaporator (Stream 15) and absorbs solar heat until becoming saturated steam at 12.3 MPa. The saturated steam (Stream 16) is then superheated in the solar superheater to 530 °C at 12 MPa and then flows (Stream 1) to the power generation block for electricity generation.

The charging mode takes place when there is excess solar thermal power in the evaporator. In this case, extra feedwater is fed from the condensate storage tank (Stream 21) to the solar evaporator and then directed to the SAs (Streams 23 and 24). The charging process starts first

with filling the parallelly connected superheating SAs until reaching the maximum allowable pressure and volume levels and then filling the parallelly connected base SAs, which also stops when reaching the maximum pressure and volume levels set for the base SAs. The size and the thermodynamic limits and constraints for all SAs are discussed in Section 4.3.3.

There is the option of charging the superheating SAs with superheated steam from the solar superheater at 530 °C and 12 MPa. However, the temperature of the stored water/steam in the SAs can only reach 324 °C (i.e., saturation temperature at 12 MPa). Reaching this temperature and pressure is expected to have a minor enhancement, relative to the concrete blocks option, on the turbine inlet temperature and the cycle efficiency during discharging mode. Additionally, the intention of this study is to use the same SA limits provided by Khi Solar One operators. Thus, the option of increasing the maximum pressure of the superheating SAs to 12 MPa is not considered in this case study.

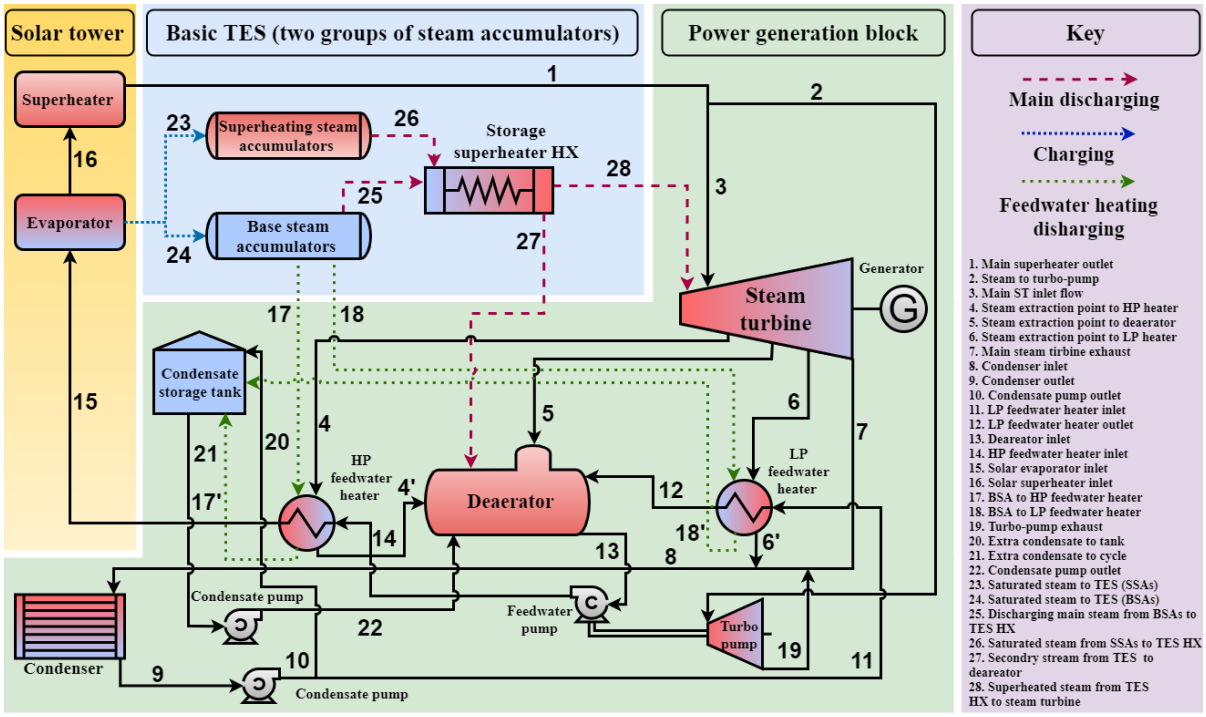

Figure 4.1. Schematic diagram of Khi Solar One with the existing TES system configuration (two groups of steam accumulators).

During main discharging process, the base SAs release saturated steam at the storing pressure. The discharged steam flows into the storage superheater (Stream 25), gets superheated by the higher temperature saturated steam (i.e., higher pressure) from the superheating SAs

(Stream 26), and then flows into the steam turbine for electricity generation (Stream 28). The superheating process of the saturated steam is essential to avoid creation of water droplets in the steam turbine and to increase the cycle thermal efficiency as well. Discharging mode of the base SAs can also be performed for feedwater heating purposes (Streams 17 and 18) during normal operations of the power plant. The direction of the SA feedwater heating stream is indicated by the green dotted lines in Figure 4.1.

4.2.2. Extended TES configuration with solid storage

A schematic diagram of the extended TES system configuration is shown in Figure 4.2. The extended TES system consists of concrete blocks and only one group of SAs. All the other power plant components are the same as in the existing TES system configuration descried in Section 4.2.1.

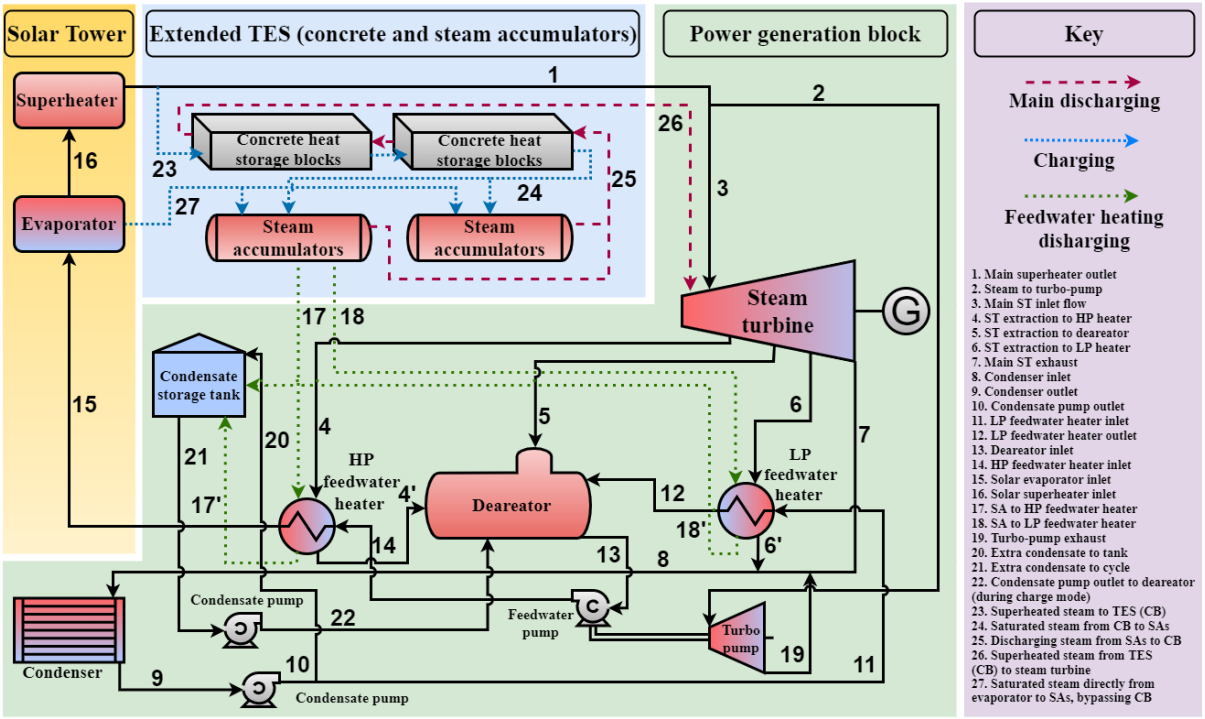

Figure 4.2. Schematic diagram of Khi Solar One with the (proposed) extended TES system configuration (concrete blocks and steam accumulators).

The operation of the power plant with the extended TES system during normal mode is similar to that with the existing TES system. However, the charging process of the extended configuration is different. Excess solar heat in the solar tower is not only utilised to evaporate extra amount of water for storage, but also to superheat the steam to 530 °C, the same temperature of the main

steam flowing into the steam turbine. The superheated steam (i.e., allocated for storage) flows into the concrete blocks (Stream 23), connected in series, first to deposit its high-temperature heat and then fills the parallelly connected SAs (Stream 24). There is also a direct link between the solar evaporator and the SAs (Stream 27), allowing a direct charging of SAs from the evaporator (i.e., as in the existing configuration) in situations when the temperature of steam exiting the last concrete block is higher than the design temperature of the SAs.

The main discharging mode in the extended TES system is performed by releasing the stored saturated steam in the SAs (Stream 25) to the concrete blocks. The saturated steam gets superheated in the higher-temperature concrete blocks and then flows into the steam turbine (Stream 26) for electricity generation. Unlike the existing configuration, there is no need for two groups of SAs and for a storage superheater as steam is superheated while flowing inside the concrete blocks. Similar to the existing TES system, steam can also be released from the SAs for feedwater heating purposes (Streams 17 and 18).

4.3. Model inputs and assumptions

The main power generation cycle, TES system and economic parameters and assumption that are inserted to the generic models discussed in Chapter 3 are listed and presented in this section.

4.3.1. Power cycle model and assumptions

The power generation block of Khi Solar One, illustrated in Figure 4.1 and Figure 4.2, consists of the following:

- a 50-MW_{el} steam turbine driving an electric generator, fitted with three side steam extractions for feedwater heating;
- low-pressure (LP) and high-pressure (HP) closed feedwater heaters, which are supplied by steam from the turbine side extraction points or from the SAs;
- a deaerator that works as an open feedwater heater and maintains the oxygen and other dissolved gases levels below the maximum limits;
- a feedwater pump that is operated by a separate turbo-pump and two condensate pumps;
- a condensate storage tank that stores water at ambient temperature and pressure; and,
- a natural draft condenser to maintain the vacuum at the steam turbine outlet and to condensate the exhaust steam leaving the turbine.

The energy and mass balance equations written for each component (i.e., specifically for Khi Solar One), and which were solved to predict the performance of the power generation block (i.e., steam Rankine cycle), are summarised in Table 4.2.

Table 4.2. Main energy and mass balance equations used in the power generation cycle model.

Component	Part	Energy balance equations	Mass balance equations
Solar evaporator		$\dot{Q}_{\mathrm{evp}} = \dot{m}_{15}\,(h_{16} - h_{15})$	$\dot{m}_{15} = \dot{m}_{16} + \dot{m}_{23} + \dot{m}_{24}$
Solar superheater		$\dot{Q}_{\mathrm{spr}} = \dot{m}_{16}\,(h_{1} - h_{16})$	$\dot{m}_{16} = \dot{m}_{1}$
Steam turbine	Part 1	$\dot{W}_{\mathrm{T,P1}} = \dot{m}_{\mathrm{T,P1}}\,(h_3 - h_4)$ $\eta_{\mathrm{T,P1}} = \frac{h_3 - h_4}{h_3 - h_{\mathrm{is},4}}$	$\dot{m}_{\mathrm{T,P1}} = \dot{m}_3 = \dot{m}_1 - \dot{m}_2$
	Part 2	$\dot{W}_{\mathrm{T,P2}} = \dot{m}_{\mathrm{T,P2}}\,(h_4 - h_5)$ $\eta_{\mathrm{T,P2}} = \frac{h_4 - h_5}{h_4 - h_{\mathrm{is},5}}$	$\dot{m}_{\mathrm{T,P2}} = \dot{m}_{\mathrm{T,P1}} - \dot{m}_4$
	Part 3	$\dot{W}_{\mathrm{T,P3}} = \dot{m}_{\mathrm{T,P3}}\,(h_5 - h_6)$ $\eta_{\mathrm{T,P3}} = \frac{h_5 - h_6}{h_5 - h_{\mathrm{is},6}}$	$\dot{m}_{\mathrm{T,P3}} = \dot{m}_{\mathrm{T,P2}} - \dot{m}_5$
	Part 4	$\dot{W}_{\mathrm{T,P4}} = \dot{m}_{\mathrm{T,P4}}\,(h_6 - h_7)$ $\eta_{\mathrm{T,P4}} = \frac{h_6 - h_7}{h_6 - h_{\mathrm{is},7}}$	$\dot{m}_{\mathrm{T,P4}} = \dot{m}_{\mathrm{T,P3}} - \dot{m}_6 = \dot{m}_7$
	whole	$\dot{W}_{\mathrm{T}} = \dot{W}_{\mathrm{T,P1}} + \dot{W}_{\mathrm{T,P2}} + \dot{W}_{\mathrm{T,P3}} + \dot{W}_{\mathrm{T,P4}}$	
Condenser		$x_9 = 0$	$\dot{m}_8 = \dot{m}_{6'} + \dot{m}_7 + \dot{m}_{19}$ $\dot{m}_9 = \dot{m}_8$
Turbo-pump		$\dot{W}_{\mathrm{TP}} = \dot{m}_2\,(h_2 - h_{19})$ $\eta_{\mathrm{TP,is}} = \frac{h_2 - h_{19}}{h_2 - h_{\mathrm{is},19}}$	$\dot{m}_2 = \dot{m}_{19}$
LP feedwater heater	cold side	$\dot{Q}_{\mathrm{LFWH}} = \dot{m}_{11}\,(h_{12} - h_{11})$	$\dot{m}_{12} = \dot{m}_{11}$
	hot side	$\dot{Q}_{\mathrm{LFWH}} = \dot{m}_6\,(h_6 - h_{6'})$ or $\dot{Q}_{\mathrm{LFWH}} = \dot{m}_{18}\,(h_{18} - h_{18'})$	$\dot{m}_{6'} = \dot{m}_6$ or $\dot{m}_{18'} = \dot{m}_{18}$
HP feedwater heater	cold side	$\dot{Q}_{\mathrm{HFWH}} = \dot{m}_{14}\,(h_{15} - h_{14})$	$\dot{m}_{15} = \dot{m}_{14}$
	hot side	$\dot{Q}_{\mathrm{HFWH}} = \dot{m}_4\,(h_4 - h_{4'})$ or $\dot{Q}_{\mathrm{HFWH}} = \dot{m}_{17}\,(h_{17} - h_{17'})$	$\dot{m}_{4'} = \dot{m}_4$ or $\dot{m}_{17'} = \dot{m}_{17}$
Condensate pump		$\dot{W}_{\mathrm{CP}} = \dot{m}_9\,(h_{10} - h_9)$ $\eta_{\mathrm{CP}} = \frac{h_{\mathrm{is},10} - h_9}{h_{10} - h_9}$	$\dot{m}_9 = \dot{m}_{10}$
Feedwater pump		$\dot{W}_{\mathrm{FP}} = \dot{m}_{13}\,(h_{14} - h_{13})$ $\eta_{\mathrm{FP}} = \frac{h_{\mathrm{is},14} - h_{13}}{h_{14} - h_{13}}$	$\dot{m}_{14} = \dot{m}_{13}$
Deaerator		$\dot{m}_{13}\,h_{13} = \dot{m}_{4'}\,h_{4'} + \dot{m}_5\,h_5 + \dot{m}_{12}\,h_{12} + \dot{m}_{22}\,h_{22}$	$\dot{m}_{13} = \dot{m}_{4'} + \dot{m}_5 + \dot{m}_{12} + \dot{m}_{22}$

Table 4.3. Main cycle parameters and assumptions used in the power generation cycle model at the full rated electrical power of 50 MW_{el}. The data were provided by the operators of Khi Solar One.

Parameter	Symbol	Stream	Value
Turbine inlet temperature (°C)	T_1	1	520
Turbine inlet pressure (MPa)	P_1	1	11.5
Turbine first side extraction pressure (MPa)	P_4	4	2.86
Turbine second side extraction pressure (MPa)	P_5	5	1.27
Turbine third side extraction pressure (MPa)	P_6	6	0.27
Condensing pressure (MPa)	P_7	7	0.018
Condensate pump outlet pressure (MPa)	$P_{10,11}$	10,11	1.34
Feedwater pump outlet pressure (MPa)	P_{14}	14	15.4
LP and HP feedwater heaters pressure loss (MPa)	$\Delta P_{\mathrm{LFWH}}^{\mathrm{loss}}, \Delta P_{\mathrm{HFWH}}^{\mathrm{loss}}$	-	0.70
Deaerator pressure loss (MPa)	$\Delta P_{\mathrm{DE}}^{\mathrm{loss}}$	-	0.57
Solar evaporator pressure loss (MPa)	$\Delta P_{\mathrm{evp}}^{\mathrm{loss}}$	-	3.1
Solar superheater pressure loss (MPa)	$\Delta P_{\mathrm{spr}}^{\mathrm{loss}}$	-	0.3
Turbo-pump isentropic efficiency (%)	$\eta_{\mathrm{TP,is}}$	-	75
Turbo-pump mechanical efficiency (%)	η_{TP}	-	85
Feedwater pump isentropic efficiency (%)	η_{FP}	-	81
Condensate pump isentropic efficiency (%)	η_{CP}	-	78
Generator mechanical efficiency (%)	η_{gen}	-	94
LP and HP feedwater heaters heat-to-heat efficiency (%)	$\eta_{\mathrm{LFWH}}, \eta_{\mathrm{HFWH}}$	-	95
Ambient pressure (MPa)	P_{a}	-	0.1
Ambient temperature (°C)	T_{a}	-	28

The net generated power and net thermal efficiency during nominal operation mode ($\eta_{\mathrm{Cyc,nom}}$), charging mode ($\eta_{\mathrm{Cyc,Ch}}$) and discharging mode ($\eta_{\mathrm{Cyc,Dch}}$) of the plant were calculated from:

$$\dot{W}_{\mathrm{net}} = \eta_{\mathrm{gen}} \sum \dot{W}_{\mathrm{T}} - \sum \dot{W}_{\mathrm{P}} \tag{4.4}$$

$$\dot{Q}_{\mathrm{ST\rightarrow Cyc}} = \dot{m}_{\mathrm{Cyc}} \left(h_1 - h_{15}\right) \tag{4.5}$$

$$\dot{Q}_{\mathrm{ST\rightarrow TES}} = \dot{m}_{\mathrm{TES}} \left(h_{23} - h_{15}\right) \tag{4.6}$$

$$\dot{Q}_{\mathrm{ST}} = \dot{Q}_{\mathrm{eva}} + \dot{Q}_{\mathrm{spr}} \tag{4.7}$$

$$\dot{Q}_{\mathrm{ST}} = \dot{Q}_{\mathrm{ST\rightarrow Cyc}} + \dot{Q}_{\mathrm{ST\rightarrow TES}} \tag{4.8}$$

$$\Delta\dot{Q}_{\mathrm{TES}} = \dot{Q}_{\mathrm{TES\rightarrow Cyc}} - \dot{Q}_{\mathrm{Cyc\rightarrow TES}} \tag{4.9}$$

$$\eta_{\mathrm{Cyc,nom}} = \frac{\dot{W}_{\mathrm{net}}}{\dot{Q}_{\mathrm{ST\rightarrow Cyc}}} \tag{4.10}$$

$$\eta_{\mathrm{Cyc,Ch}} = \frac{\dot{W}_{\mathrm{net}}}{\dot{Q}_{\mathrm{ST\rightarrow Cyc}} + \Delta\dot{Q}_{\mathrm{TES}}} \tag{4.11}$$

$$\eta_{\mathrm{Cyc,Dch}} = \frac{\dot{W}_{\mathrm{net}}}{\dot{Q}_{\mathrm{TES\rightarrow Cyc}}} \tag{4.12}$$

where $\dot{W}_{\mathrm{T}}$ is the turbine power output, $\dot{W}_{\mathrm{p}}$ the power needed by each pump, $\dot{Q}_{\mathrm{ST\rightarrow Cyc}}$ the rate of heat from the solar tower to the cycle, $\dot{Q}_{\mathrm{ST\rightarrow TES}}$ the rate of heat from the solar tower to the TES system, $\dot{Q}_{\mathrm{TES\rightarrow Cyc}}$ the rate of heat from the TES system to the cycle, $\dot{Q}_{\mathrm{Cyc\rightarrow TES}}$ the rate of heat from the cycle to the TES system, $\dot{Q}_{\mathrm{ST}}$ the rate of absorbed heat in the solar tower, $\Delta\dot{Q}_{\mathrm{TES}}$ the net rate of heat added to or extracted from the TES system, η the efficiency and subscripts 'nom', 'gen', 'Cyc', 'Ch', and 'Dch' stand for nominal, generator, cycle, charging and discharging, respectively.

Beside the generic quasi-steady power generation cycle assumptions that are listed in Section 3.4.1 of Chapter 3, the following assumptions were also included in the cycle model:

- 10 °C ≤ ΔT_{LM} in both the LP and HP feedwater heaters;
- 10 °C ≤ ΔT_{pp} of the inlet and the outlet of both HP and LP feedwater heaters;

All other parameters including component efficiencies, pressure losses, etc., are listed in Table 4.3.

4.3.2. Analysis of off-design turbine isentropic efficiency

The assumed turbine isentropic efficiency for each turbine part during nominal (design) and part-load (off-design) operation conditions are listed in Table 4.4.

Table 4.4. Isentropic efficiencies of turbine parts at design and off-design operating conditions.

Turbine part number	Design-point efficiency (%)	Off-design efficiency (%)
1	84	82
2	86	85
3	90	87
4	78	76

The off-design efficiencies in this chapter were assumed after conducting a thorough analysis by comparing the off-design efficiency data (provided by Khi Solar One operators) with correlations for the estimation of off-design turbine efficiencies from Refs. [148,188]. The turbine is divided into 4 parts. Each part is defined as a group of turbine stages and each stage

consists of a stator and a rotor. Turbine Part 1 includes the stages between the turbine inlet and first side extraction, Part 2 represents the stages between the first and second side extractions, Part 3 includes the stages between the second and third side extractions, and Part 4 represents the stages between the third side extraction and main outlet.

The study takes into consideration the effect of the varying steam flow conditions (i.e., pressure, temperature, mass flowrate, etc.) on the turbine isentropic efficiency during part-load operations. The provided data include steam conditions and their corresponding isentropic efficiency during part-load operation. The analysis started by comparing off-design efficiencies at given steam flow conditions (i.e., pressure ratio, mass flowrate, and flow coefficient) to obtain a valid turbine off-design correlation. Figure 4.3 shows the normalised turbine efficiency in off-design conditions versus the corresponding: (a) normalised mass flowrate; (b) pressure ratio across the turbine; and (c) flow coefficient for the four turbine parts. The normalised values were calculated with reference to the design-point efficiencies. The pressure ratio, PR, and the flow coefficient, φ, are defined as:

$$PR = \frac{P_{\text{in}}}{P_{\text{out}}} \tag{4.13}$$

$$\varphi = \frac{\dot{m}_{\text{in}}}{\sqrt{P_{\text{in}}\,\rho_{\text{in}}}} \tag{4.14}$$

The results in Figure 4.3 indicate that there is no observable correlation between all thermodynamic indicators and the normalised off-design efficiencies, except for turbine Part 4 that has a trendline that could be correlated with respect to pressure ratio. Therefore, none of the three off-design turbine efficiency vs. steam condition correlations can be applied to predict the off-design efficiencies.

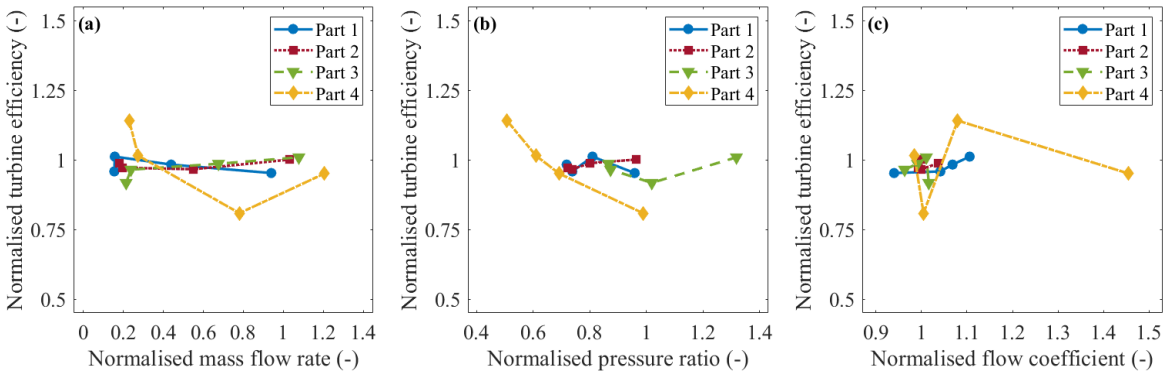

Figure 4.3. Normalised off-design turbine efficiency against (a) normalised mass flowrate; (b) the normalised turbine pressure ratio; and (c) normalised flow coefficient for the four turbine parts. All values are normalised with respect to nominal (design-point) conditions.

The operator provided turbine data were also compared with two main off-design turbine isentropic efficiency correlations from literature. The first was proposed by Van Putten et al. [188] and the second was developed by Ray [148]. The first predicts the off-design turbine stage efficiency based on the 1-D theory of turbomachinery which accounts for blade velocity, steam flow approach angle, etc., as presented in Equations (4.15) to (4.17). All other correlation assumptions and approximations can be found in Ref. [188].

$$\eta_{\mathrm{TS}}^{\mathrm{OD}} = 4\,K_{\mathrm{e0}}\,\frac{v_{\mathrm{b}}}{v_{\mathrm{f}}}\left(\cos\theta - \frac{v_{\mathrm{b}}}{v_{\mathrm{f}}}\right) \tag{4.15}$$

$$v_{\mathrm{f}} = \sqrt{2(h_{\mathrm{in}} - h_{\mathrm{out}}} \tag{4.16}$$

$$v_{\mathrm{b}} = v_{\mathrm{f}}\,\frac{K_{\mathrm{v0}}\,\omega}{\sqrt{\left(h_{\mathrm{in}} - h_{\mathrm{is,out}}\right)}} \tag{4.17}$$

where v_{f} is fluid velocity, v_{b} the blade velocity, K_{e0} the efficiency parameter for an impulse turbine, K_{v0} the velocity parameter, ω the turbine rotational speed and θ the approach angle in rad.

It is not simple to use this correlation as not all parameters are known. Thus, it was assumed that the approach angle is 0.3 rad and the turbine rotational speed fixed at 60 Hz [188]. However, K_{v0} and K_{e0} are different for each individual turbine as well as for each turbine stage, which cannot be assumed and needs to be found either experimentally or by knowing the exact turbine geometry. As geometry information is lacking, both K_{v0} and K_{e0} of each part were obtained by finding the minimum RMSE, indicated in Equation (4.18), using the four operator-provided off-design data:

$$\varepsilon_{\mathrm{RMS}} = \sqrt{\frac{\sum_{i=1}^{N}\left(\eta_{\mathrm{c}} - \eta_{\mathrm{p}}\right)^2}{N}} \tag{4.18}$$

where η_{c} is calculated efficiency, η_{p} the provided efficiency and N the number of conditions.

Figure 4.4 compares, on the left *y*-axes, the off-design turbine efficiencies and best fit efficiencies for turbine: (a) Part 1; (b) Part 2; (c) Part 3; and (d) Part 4. The right *y*-axes of Figure 4.4 shows the relative errors between the operator provided and the best fit efficiency values using the obtained K_{v0} and K_{e0} that gives the least RMSE, shown on the top-left corner, of each turbine part. In Figure 4.4(a), the calculated K_{v0} and K_{e0} are 4.3 and 0.9, respectively. Although the RMSE is the minimum for all values, the relative efficiency error varies for each condition but most of them are lower than 5% for turbine Part 1.

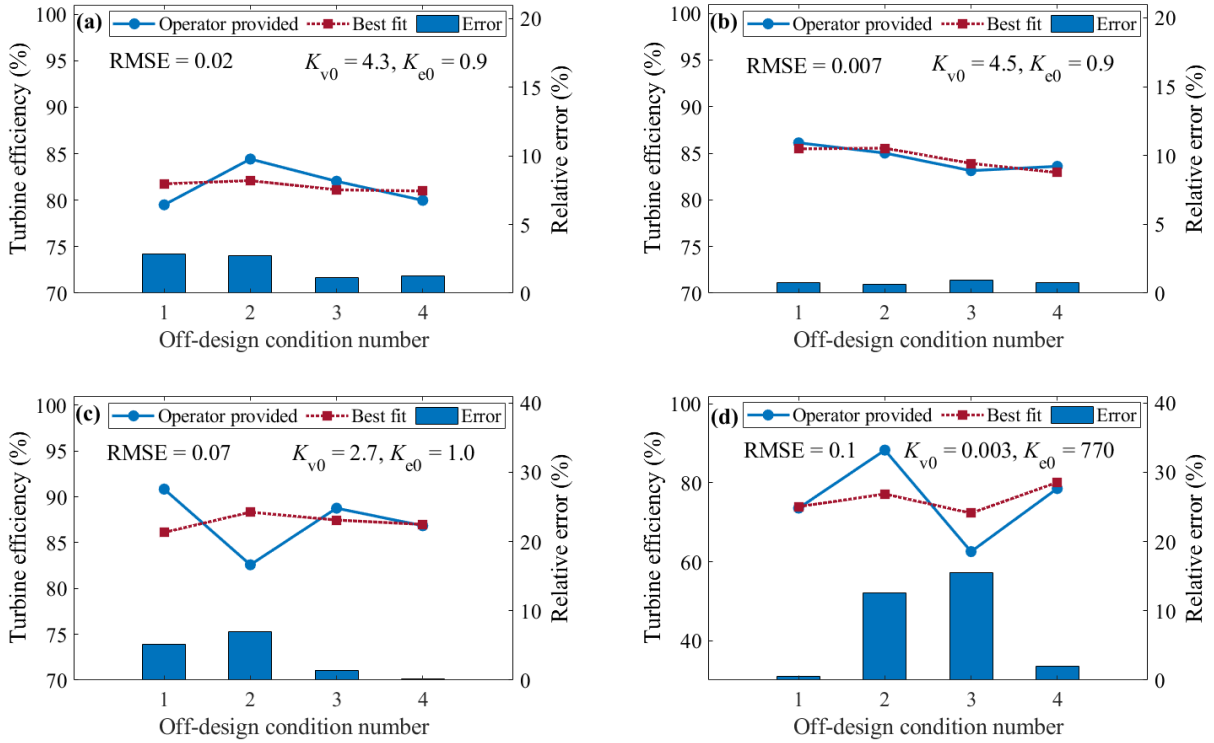

Figure 4.4. Operator provided turbine isentropic efficiencies and best fit efficiencies (i.e., from Van Putten et al. [148] equation), which are determined by finding the K_{v0} and K_{e0} parameters that gives the minimum RMSE of the four given off-design conditions for turbine: (a) Part 1; (b) Part 2; (c) Part 3; and (d) Part 4. The right *y*-axes illustrate the relative error between the two efficiencies.

For turbine Part 2, the obtained correlation efficiencies are similar to the operator provided ones and have relative errors less than 2% as illustrated in Figure 4.4(b). The small error is because of the small variation of turbine efficiency during off-design operation in Part 1 and Part 2. However, it is not the case for Part 3 and Part 4 as the RMSEs and relative errors exceed 15%. This is due to the arbitrary behaviour of turbine efficiency at off-design conditions, which might be higher or lower than the design point efficiency. The large variation in Parts 3 and 4 could be a result of the presence of water droplets in the last stages of the turbine, which largely affects the performance of the turbine. Moreover, the best fit data do not have the same trend as the operator provided data, as it might be higher in some off-design condition and lower in others. Therefore, the obtained best fit data are usually the same for all conditions, which suggests using the average of the off-design efficiency of all provided conditions, especially for Parts 1, 2, and 3.

The operator provided data were also analysed using the second isentropic prediction function developed by Ray [148], that is expressed in Equation (3.85) in Chapter 3. This correlation

estimates the stage efficiency by the ratio of blade tip velocity to theoretical steam velocity. The function assumes the blade tip velocity to be proportional to the turbine shaft speed, and the steam velocity to the square root isentropic enthalpy drop across the stage.

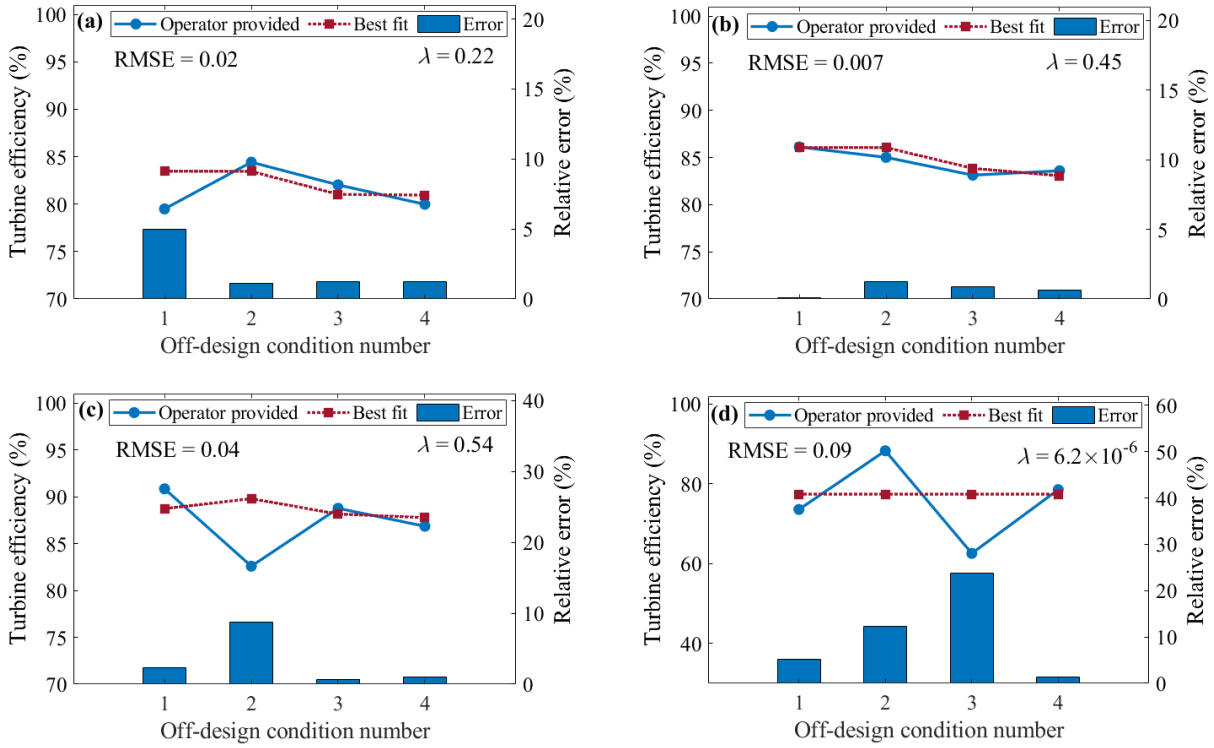

Figure 4.5. Operator provided turbine isentropic efficiencies and the best fit efficiencies (i.e., from Ray's [148] equation), which are determined by finding the positive constant λ that gives the minimum RMSE of the four given off-design conditions for turbine: (a) Part 1; (b) Part 2; (c) Part 3; and (d) Part 4. The right *y*-axes show the relative error between the two efficiencies.

As all variables were known except (λ), which varies depending on the turbine design and geometry, a similar best fit with minimum RMSE approach was performed to determine λ of each turbine part. Figure 4.5 illustrates the difference between the operator provided efficiencies and the obtained best fit efficiencies, on the left *y*-axes, and the corresponding relative error for each off-design condition, on the right *y*-axes, for turbine: (a) Part 1; (b) Part 2; (c) Part 3; and (d) Part 4. The calculated positive constant, λ, is 0.2 for Part 1, 0.45 for Part 2, 0.54 for Part 3 and less than 0.01 for Part 4. The results also suggest that the least error is achieved when the best fit efficiencies are close to the average value, especially for Parts 1 and 4.

The analysis demonstrates that using the average value of the provided off-design efficiencies for each turbine part is a reasonable choice, as it is associated with the lowest discrepancy (RMSE < 0.1) between the provided and correlation-based data for all examined off-design conditions. Although taking the average off-design efficiency introduces some errors in the model, it is still relatively small compared to other error sources associated with other steam cycle model assumptions. Therefore, the average of the off-design efficiencies of each part (i.e., listed in Table 4.4) was used in the turbine model for part-load operations.

The selection of the average part-load efficiency for each turbine part instead of the average part-load efficiency for the whole turbine (82.2%) can be justified by the lower mean absolute error (MAE) for all turbine parts, as clearly illustrated in Figure 4.6.

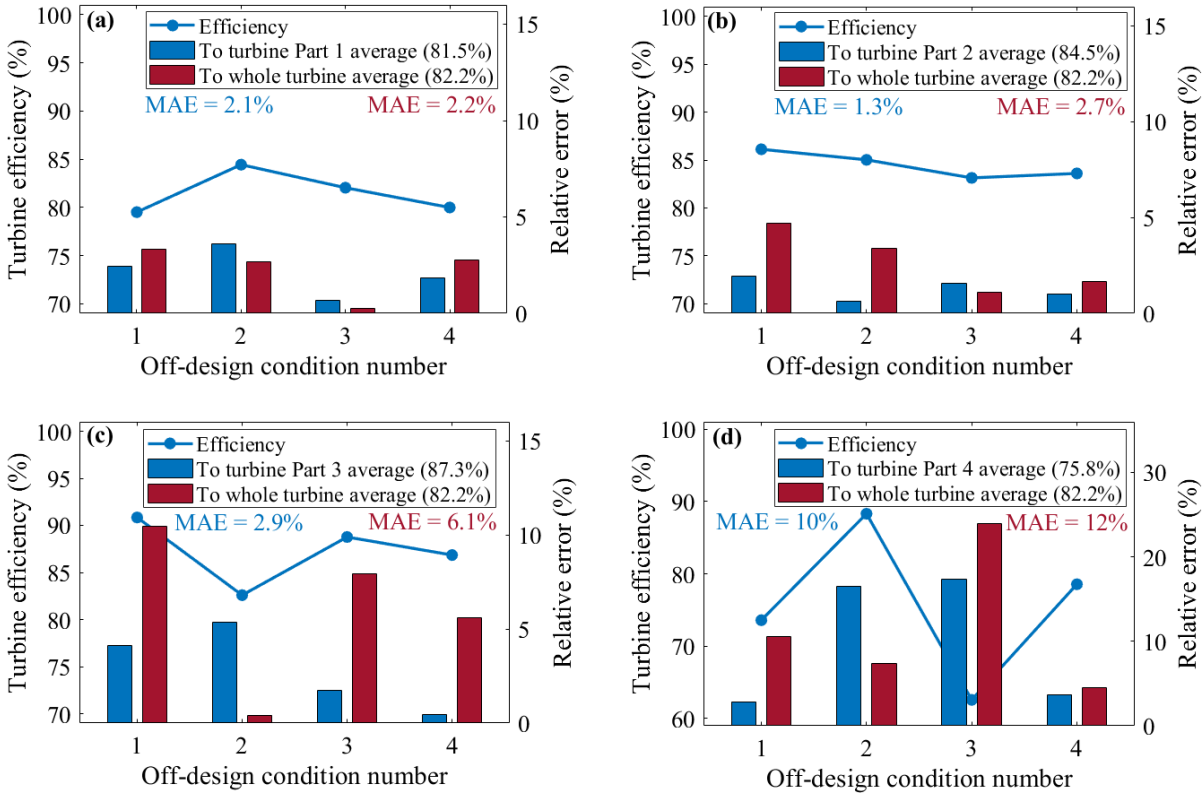

Figure 4.6. Operator provided turbine off-design isentropic efficiencies, on the left *y*-axes, and calculated relative errors, on the right *y*-axes, for turbine: (a) Part 1; (b) Part 2; (c) Part 3; and (d) Part 4. The relative errors are calculated with respect to the average of efficiencies of the turbine part itself (i.e., 4 values) and with respect to the average of all provided efficiencies (i.e., 16 values).

4.3.3. Steam accumulator initial conditions and constraints

The main parameters of the SAs in the compared TES system configurations are summarised in Table 4.5. For the existing TES system, the maximum and the minimum pressures were selected based on operational data provided by the plant operators. The superheating SAs are charged to a higher pressure due to the need of having a higher temperature discharging steam (i.e., higher saturation pressure) for the superheating process during the discharging mode. The minimum pressure of the base SAs is selected based on the lowest pressure the steam turbine can accept. In the extended TES system, the minimum was set by considering a 0.5 MPa pressure loss through the concrete blocks before entering the turbine. The maximum pressure for all SAs is the same since the superheating process undergoes in the concrete blocks. All SAs are also constrained with water filling ratios (WFR) of 0.99. The WFR is defined as:

$$WFR = \frac{V_{\mathrm{L}}}{V_{\mathrm{V}} + V_{\mathrm{L}}} = \frac{V_{\mathrm{L}}}{V_{\mathrm{SA}}} \tag{4.19}$$

where V_{L} is the liquid volume, V_{V} the vapour volume and V_{SA} the volume of the SA.

The maximum inlet (i.e., charging) steam temperature and pressure of all SAs in both TES systems are 327 °C and 12 MPa, respectively, which is set by materials limits. The SA external surfaces are assumed to be perfectly insulated, hence, there is no heat loss to the environment.

Table 4.5. Main SA parameters and constraints in the analysed TES system configurations.

Parameter	Existing		Extended
	Superheating SAs	Base SAs	All SAs
Number of SAs (units)	3	16	19
Useful volume/unit (m^3)	197	197	197
Maximum pressure (MPa)	8.2	4.2	8.2
Minimum pressure (MPa)	3.9	1.4	1.9
Maximum WFR (-)	0.99	0.99	0.99

4.3.4. Economic model inputs

The two TES system configurations were compared using a number of economic performance indicators such as the levelised cost of storage (LCOS) (i.e., cost per kWh of electricity generated utilising stored heat), the levelised cost of electricity (LCOE) and the net present value (NPV),

which were calculated using the listed equations in Section 3.6 of the methodology chapter. The economic assumptions listed in Table 4.6 and the daily mean 24-h DNI profile in Figure 4.7 were considered for the calculation of the key economic performance indicators.

Table 4.6. Economic analysis assumptions [181].

Parameter	Symbol	Value
Operation & maintenance costs ($/MWh$_{el}$)	$C_{\mathrm{O\&M}}$	12
Availability factor (%)	F_{ava}	98
Lifetime of the system (years)	n	25
Discount rate (%)	r	10

Moreover, the internal rate of return (IRR) was also calculated to assess the economic feasibility of investing in the proposed TES configuration. The economic analysis excludes the land, taxation, and financing costs. The electricity generated from Khi Solar One is being sold to the South African Electricity Public Utility (Eskom) under a long-term power purchase agreement (PPA) at a fixed electricity price. However, the price is not declared, perhaps for confidentiality reasons, but it could be around 200 $/MWh$_{el}$ as estimated by the South African Energy Department for CSP plants [189]. As the actual price was not provided, the calculations of the NPVs and the IRRs were performed using a range of historical electricity prices, from 100 $/MWh$_{el}$ to 340 $/MWh$_{el}$.

4.3.5. Analysis of DNI data

In order to assess the hourly performance of Khi Solar One with both TES systems, it is essential to have representative hourly averaged DNI data. Therefore, hourly averaged DNI data for a whole year were generated using Meteonorm in TRNSYS [190], taking Upington in South Africa as the location. Running the power plant simulation model for the whole year (i.e., 8760 h) is time consuming. Thus, the DNI data were analysed to create a valid 24-h DNI profile that captures, to some extent, the anticipated behaviour of a year-long DNI in Upington. The analysis included calculating the mean and the standard deviation of the hourly DNI data for a whole year as shown in Figure 4.7.

Yet, adapting the mean 24-h DNI profile for the comparative study might not capture the performance of the TES systems during a highly fluctuating DNI profile, a lower DNI profile,

or a higher DNI profile. Therefore, the simulation model was also examined for five different 24-h DNI profiles, which are:

- *Profile 1*: mean plus one standard deviation of the DNI data of the whole year;
- *Profile 2*: mean minus one standard deviation of the DNI data of the whole year;
- *Profile 3*: lowest daily DNI of the year;
- *Profile 4*: highest daily DNI of the year; and,
- *Profile 5*: random selected day that has high DNI fluctuation in the same year.

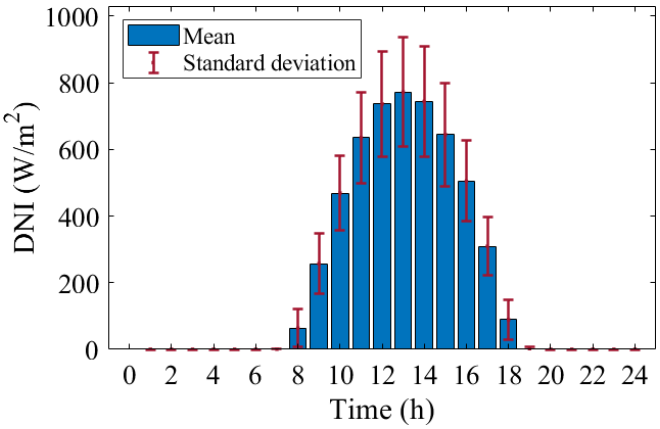

Figure 4.7. Mean and standard deviation of the hourly averaged DNI data for a whole year in Upington, South Africa.

4.3.6. Modes of operation

The power generation cycle system is assumed to operate with a maximum and a minimum electricity generation of 50 MW_{el} and 10 MW_{el}, respectively. In this study, it is assumed that Khi Solar One is operated under the following modes:

- *Mode 1:* electricity is generated at 50 MW_{el} or less by utilising thermal power in the solar tower receivers only and no TES charging/discharging is taking place.
- *Mode 2:* electricity is generated at 50 MW_{el} and charging of TES system is performed when excess solar heat is available for storage.
- *Mode 3:* main thermal power provided by the solar tower receivers and feedwater heating is provided by the SAs in the TES system.
- *Mode 4:* thermal power is discharged from the TES system to generate 50 MW_{el} of electrical power. The TES discharging mode is assumed to start immediately if no thermal power is available in the solar tower.

4.4. Khi Solar One at full rated power

The key results obtained from the formulated Khi Solar One power generation cycle model at full rated (i.e., nominal) power without the operation of the TES system are summarised in Table 4.7. During this mode, the solar-tower receivers supply 150 MW_{th} of thermal power to evaporate and then superheat the subcooled water from 232 °C to 530 °C. About 69% of this thermal power is provided by the solar evaporator while the remaining, 31%, is supplied by the solar superheater.

Table 4.7. List of main results obtained from the formulated Khi Solar One power generation cycle model at full rated power (i.e., no TES system charging/discharging).

Parameter	Symbol	Value
Rate of heat addition in the solar evaporator (MW_{th})	$\dot{Q}_{\mathrm{evp}}$	103
Rate of heat addition in the solar superheater (MW_{th})	$\dot{Q}_{\mathrm{spr}}$	47
Inlet LP feedwater heater pinch-point temperature difference (°C)	$\Delta T^{\mathrm{in}}_{\mathrm{pp,LFWH}}$	13
Outlet LP feedwater heater pinch-point temperature difference (°C)	$\Delta T^{\mathrm{out}}_{\mathrm{pp,LFWH}}$	62
Inlet HP feedwater heater pinch-point temperature difference (°C)	$\Delta T^{\mathrm{in}}_{\mathrm{pp,HFWH}}$	99
Outlet HP feedwater heater pinch-point temperature difference (°C)	$\Delta T^{\mathrm{out}}_{\mathrm{pp,HFWH}}$	66
LP feedwater heater logarithmic mean temperature difference (°C)	$\Delta T_{\mathrm{LM,LFWH}}$	31
HP feedwater heater logarithmic mean temperature difference (°C)	$\Delta T_{\mathrm{LM,HFWH}}$	81
Net electrical power (MW_{el})	$\dot{W}_{\mathrm{net}}$	50
Cycle thermal efficiency (%)	$\eta_{\mathrm{Cyc,nom}}$	33

The temperature-specific entropy (T-s) diagram and the temperature-thermal power (T-$\dot{Q}$) diagram showing the main thermodynamic processes of the steam Rankine cycle and the heat transfer rate at nominal load are respectively shown in Figure 4.8(a) and Figure 4.8(b). The numbered dots in both figures corresponds to the numbered flow streams indicated in Figure 4.1 and Figure 4.2. The heat addition process taking place in the evaporator (i.e., States 15 to 16) and the superheater (i.e., States 16 to 3) are indicated by the blue and the red lines, respectively. Once the superheated steam reaches the turbine, it expands to a condensing pressure of 0.018 MPa. Some amount of steam is extracted from the three turbine side extraction points (States 4, 5 and 6) for feedwater heating (i.e., in LP feedwater heater, deaerator and HP feedwater heater, which is illustrated in Figure 4.8(b)). The slope of lines representing the expansion processes varies as each line is for different turbine part with different isentropic efficiency as listed in Table 4.4. The slope of the last expansion process line (i.e., States 6 to 7) is relatively

less steep as the last turbine part (i.e., Part 4) has the lowest isentropic efficiency (i.e., 78%) among other turbine parts. The steam quality at the main turbine outlet is 0.88, still above the minimum boundary for avoiding erosion and corrosion of the steam turbine blades [87].

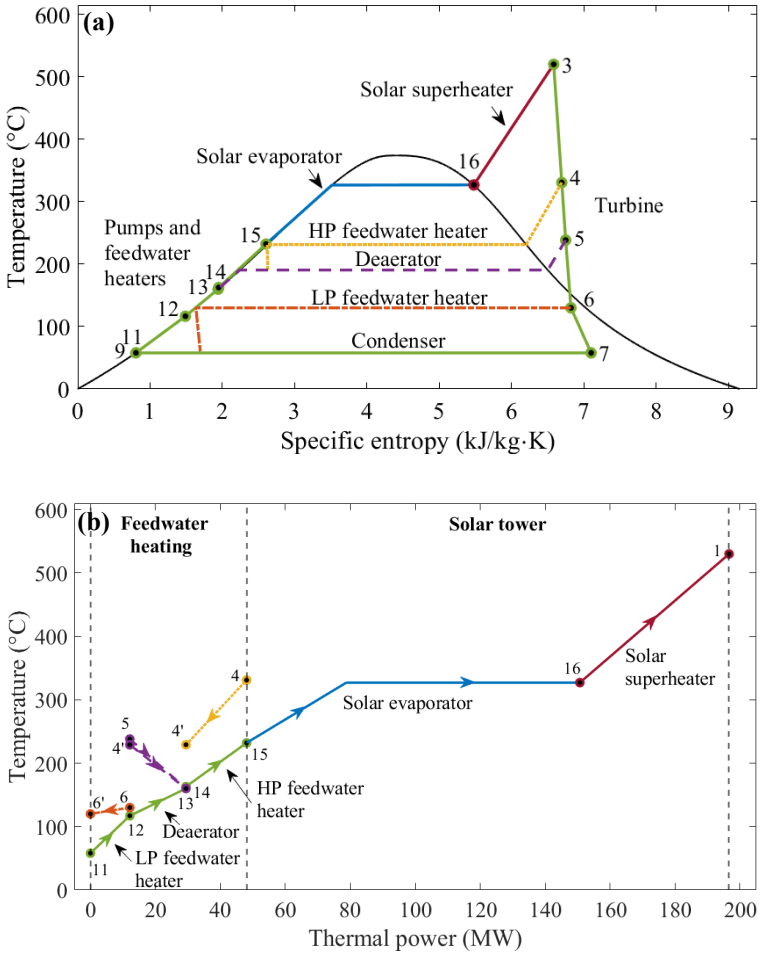

Figure 4.8. (a) Temperature-specific entropy (T-s) diagram and (b) temperature-thermal power (T-$\dot{Q}$) diagram showing the thermodynamic processes and the heat transfer rate in main heat exchangers of Khi Solar One steam Rankine cycle at full rated power. Each numbered dot represents the thermodynamic state of the numbered flow streams in Figure 4.1 and Figure 4.2.

The dashed lines in Figure 4.8(a) and Figure 4.8(b) represent the feedwater heating processes in the HP feedwater heater (yellow), in the deaerator (purple), and in the LP feedwater heater (orange). The steam conditions at the hot-side outlet of the HP and the LP feedwater heaters are assumed to be fully saturated liquid. For the HP feedwater heater, the saturated liquid then flows through a steam trap (i.e., throttle) to reduce its pressure in an isenthalpic process from 2.8 MPa to 1.3 MPa (i.e., pressure of the main flow stream flowing into the deaerator) as steam pressure

of all deaerator inlets should be the same [191]. Similarly, the pressure of steam flowing from the LP feedwater heater is also reduced by a steam trap from 0.2 MPa to 0.018 MPa (i.e., pressure of the main flow stream flowing into the condenser). The steam is fully condensed in the condenser at 0.018 MPa and then pumped by the condensate pump to 1.34 MPa (i.e., States 9 to 11). After that, the subcooled water is preheated from 58 °C to 117 °C in the LP feedwater heater and then to 160 °C in the deaerator as illustrated in Figure 4.8(b). Next, the feedwater is pumped in the feedwater pump to 15.5 MPa before entering the HP feedwater heater. The subcooled water is then heated from 163 °C to 232 °C in the HP feedwater heater with pinch-point temperature differences of 99 °C at the inlet and of 62 °C at the outlet, as shown in Figure 4.8(b). Finally, the feedwater flows back to the solar tower completing a full cycle. The steam thermodynamic properties for each numbered flow stream are listed in Table 4.8.

Table 4.8. Calculated steam thermodynamic properties at full rated power of 50 MW_{el} and without TES charging/discharging. The stream numbers are the same as indicated in Figure 4.1 and Figure 4.2.

Stream number	Mass flowrate (kg/s)	Pressure (MPa)	Temperature (°C)	Quality (-)
1	61.2	12.0	530	superheated
2	1.8	11.5	520	superheated
3	59.5	11.5	520	superheated
4	9.6	2.86	331	superheated
4’	9.6	2.79	229	0
5	2.7	1.27	238	superheated
6	6.0	0.27	130	0.96
6’	6.0	0.20	120	0
7	41.2	0.18	58	0.88
8	48.9	0.18	58	0.79
9	48.9	0.18	58	0
10	48.9	1.34	58	subcooled
11	48.9	1.34	58	subcooled
12	48.9	1.27	117	subcooled
13	61.2	0.70	160	subcooled
14	61.2	15.5	163	subcooled
15	61.2	15.4	232	subcooled
16	61.2	12.3	327	1
19	1.8	0.18	58	0.97

4.5. Performance of Khi Solar One with existing TES system

4.5.1. Analysis of initial base steam accumulators water filling ratio

The analysis of Khi Solar One with the existing TES system starts with determining the initial WFR, defined in Equation (4.19), of the base SAs. The effect of various base SAs initial WFRs on the final pressure and WFR of the base SAs as well as on the amount of stored heat and discharged electricity from the TES system are shown in Figure 4.9. All results are obtained by charging both groups of SAs with saturated steam at 327 °C and 12 MPa. The initial WFR of the superheating SAs for all examined cases is 0.5 as it does not have a significant impact on the overall performance of the TES system. The charging of all SAs stops when either the maximum allowable pressure or the maximum WFR is reached.

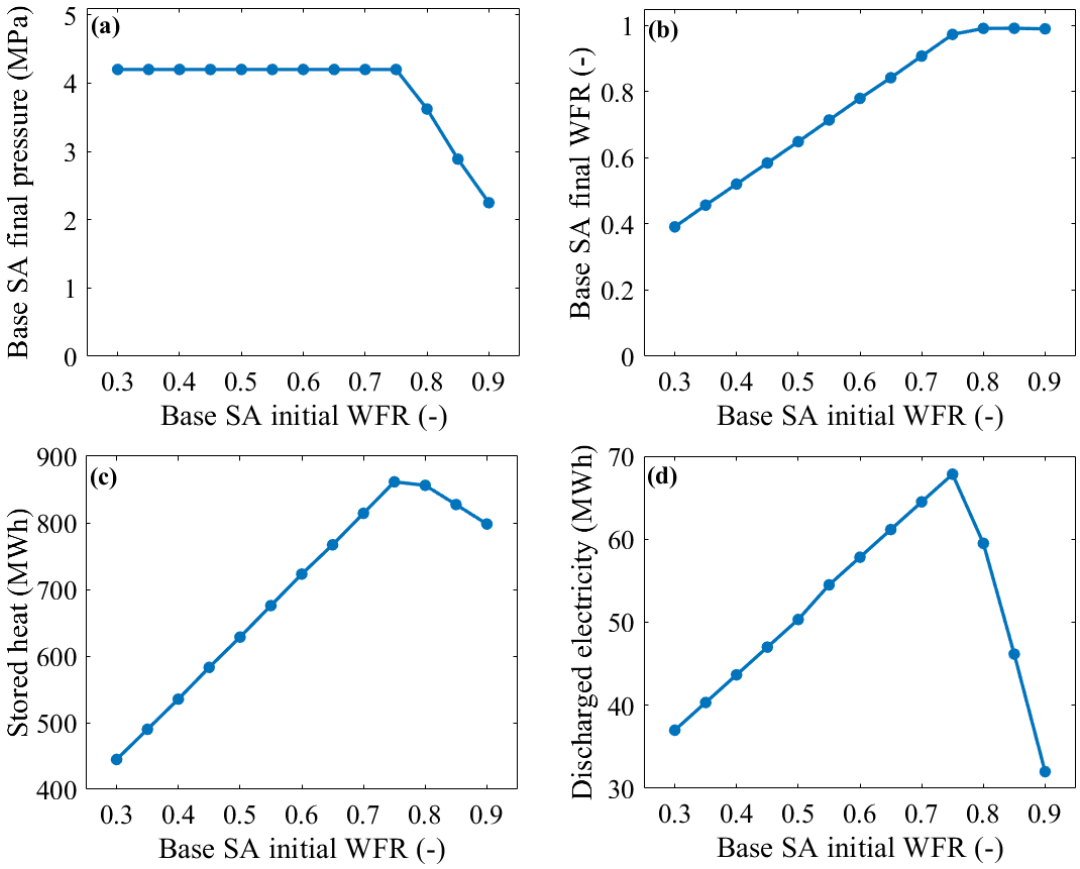

Figure 4.9. Effect of different base SA initial WFR on: (a) final pressure of base SAs, (b) final WFR of base SAs, (c) amount of stored heat in the TES system, and (d) amount of discharged electricity utilising the stored heat in the TES system. The initial WFR of the superheating SA group is fixed at 0.5 for all examined cases.

In Figure 4.9(a), the base SA final pressure reaches the maximum allowable pressure of 4.2 MPa for initial WFRs ranging from 0.3 to 0.75. However, the final WFRs, shown in Figure 4.9(b), for the same initial WFR range have not reached the maximum WFR of 0.99. Moreover, the amount of stored heat in the base SA increases from 440 MWh_{th} for a WFR of 0.3 to about 860 MWh_{th} for a WFR of 0.75. This increase, shown in Figure 4.9(c), is due to having more liquid that absorbs the heat from the charging saturated steam. For initial WFRs greater than 0.75, the final pressure of the base SAs is lower than the maximum pressure since the base SAs are already fully filled with steam to their maximum capacity. This can be clearly seen in Figure 4.9(b) where the final WFRs have reached to 0.99. Although the base SAs are fully charged with steam, the amount of stored heat decreases when the WFR is higher than 0.75 as the final pressure and temperature of the stored steam is lower for these initial WFRs.

The total discharged electricity from the TES system, presented in Figure 4.9(d), has the same behaviour as the amount of the stored heat since more stored heat means higher amount of discharged electricity from the TES system. However, for initial WFRs higher than 0.75, the slope of discharged electricity is much steeper than the slope of the stored heat as not all stored steam is discharged from the same initial pressure (i.e., final pressure after a full charge).

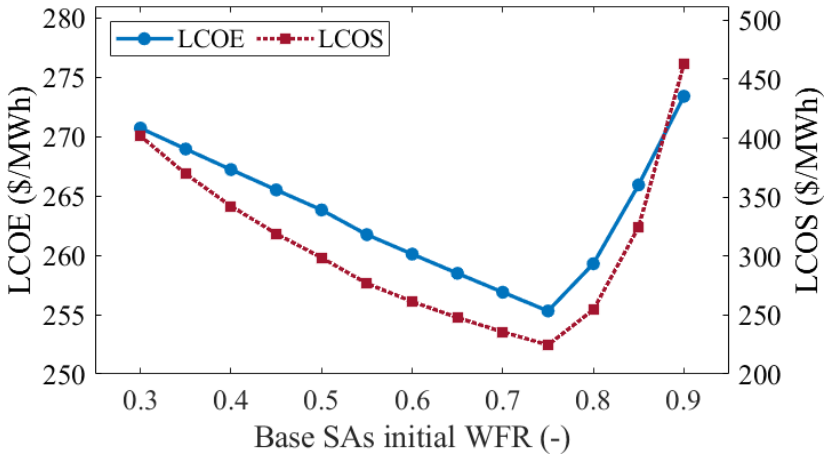

Figure 4.10. LCOE and LCOS of Khi Solar One with the existing TES system for the examined range of initial WFRs of the base SAs.

The calculated LCOE and the LCOS of Khi Solar One for the examined range of the base SAs initial WFRs are presented in Figure 4.10. The lowest LCOE and LCOS are 256 $\$/MWh_{el}$ and 225 $\$/MWh_{el}$, respectively. Both values are observed when the initial WFR is 0.75. It is expected as the behaviour of the LCOE and the LCOS is inversely related to the total amount of discharged

electricity, see Figure 4.9(d). Therefore, a WFR of 0.75 for the base SAs is assumed for evaluating the existing TES system as it gives the lowest LCOE and LCOS.

4.5.2. Performance under the mean 24-h DNI profile

The performance of Khi Solar One with the existing TES system under the mean 24-h DNI profile is shown in Figure 4.11. The operation of the power plant starts after Hour 7 since the amount of solar irradiance is sufficient to provide heat and to operate the plant at 10 MW_{el} of electrical power as shown in Figure 4.11(b). The electrical power output increases to 41 MW_{el} at Hour 9. During the 2 h period from Hour 8 to Hour 9 (inclusive), the plant is assumed to operate exclusively based on the available solar thermal power in the solar tower (i.e., Mode 1 as discussed in Section 4.3.6), which is shown in Figure 4.11(c) by the darkest shaded area. At Hour 10, the thermal power in the solar tower reaches 214 MW_{th}, which is higher than the required amount (150 MW_{th}) to generate the 50 MW_{el} of electrical power. Therefore, Khi Solar One operates on Mode 2, and the excess thermal power (64 MW_{th}) is utilised to evaporate extra steam for storage, i.e., charging phase. The charging phase continues with the increase of the solar power until all SAs are fully charged. The charging phase ends somewhere between Hour 11 and Hour 12 with a total charging time of 152 min. After that, the power plant operates at full rated power until the end of Hour 16.

At Hour 17, though the DNI is only 300 W/m^2, the plant still generates the 50 MW_{el} of electrical power. In this case, it extracts some steam from the base SAs for feedwater heating (i.e., Mode 3). The amount of thermal power provided by the TES system for feedwater heating is illustrated by the light blue shaded area in Figure 4.11(c). The power plant continues operating on Mode 3 at Hour 18 but at a lower electrical power output of 16.3 MW_{el} as there is not enough solar rays at the end of the day. The turbine inlet temperature is constant at 520 °C between Hour 8 and Hour 18 as steam is directly provided by the solar superheater, and the calculated cycle efficiency is 33%. When the sun is down at the end of Hour 18, the main TES system discharging mode starts (i.e., Mode 4). The stored steam is discharged to operate the power plant at a power of 50 MW_{el} for 1 h until the minimum pressure of the base SA is reached. The gradual increase of the TES thermal power during the discharging phase is due to the decrease of pressure and temperature of the discharged steam entering the turbine, which negatively affects the thermal efficiency of the power cycle. Therefore, more heat from the TES system is required to maintain the power level at 50 MW_{el}.

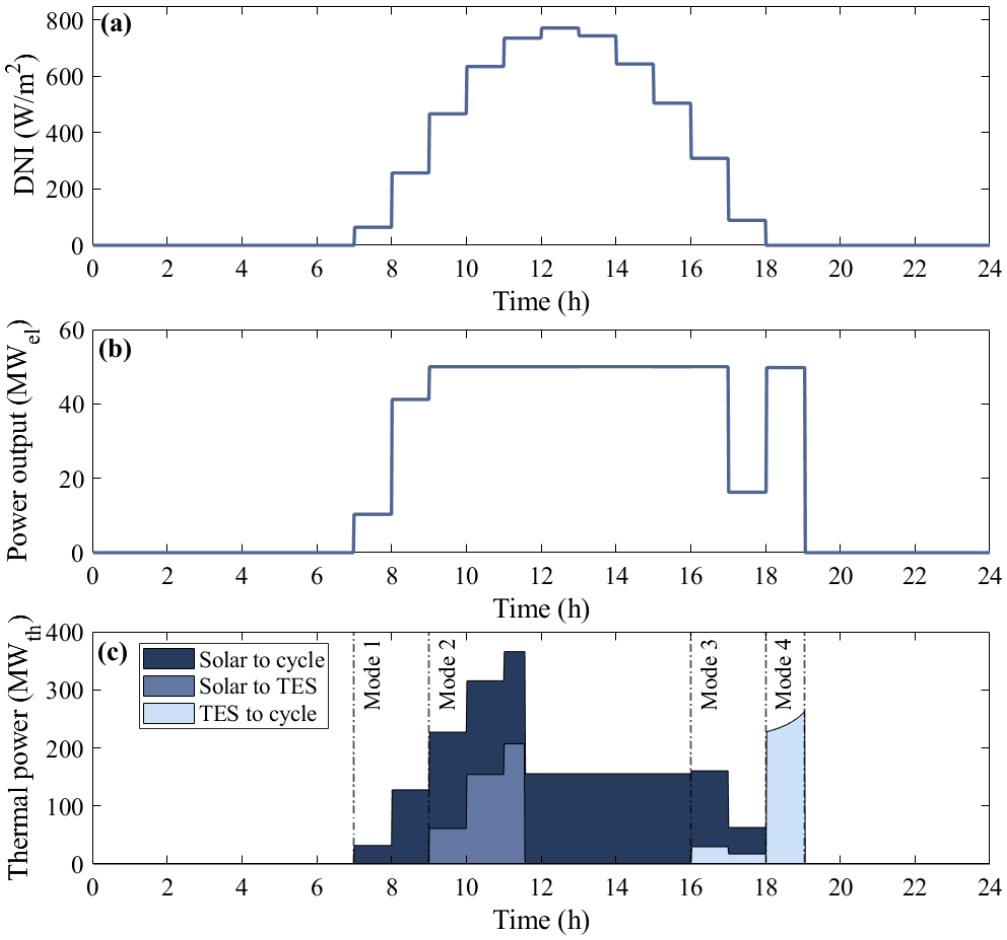

Figure 4.11. Diurnal (24-h) performance of Khi Solar One with the existing TES system configuration: (a) DNI input, (b) corresponding power output, and (c) amount of thermal power either from solar tower to power generation cycle, from solar tower to TES system, or from TES system to power generation cycle.

Figure 4.12 shows that turbine inlet temperature, on the left *y*-axis, and the calculated cycle thermal efficiency, on the right *y*-axis, for the same 24-h DNI profile of Figure 4.11(a). The turbine inlet temperature is constant at 520 °C as steam is directly provided by the solar superheater (i.e., Hour 8 to Hour 18). However, the calculated cycle efficiency fluctuates between 30.5% and 33.5% depending on the net thermal power provided by the TES system during the charging phase as defined in Equation (4.11). Moreover, the cycle efficiency is also affected by the lower turbine isentropic efficiency during part-load operation (i.e., for Hour 8, Hour 9, and Hour 18). During the main discharging mode that starts after Hour 18, the turbine inlet temperature is 286 °C and the cycle efficiency is 24.9%. However, the turbine inlet temperature gradually decreases as the pressure and the temperature of steam exiting both

groups of SAs decreases, which negatively affects the cycle efficiency. The lowest turbine inlet temperature that occurs at the end of the discharging phase is 236 °C with a cycle efficiency of 20.9%. It should be noted that the rate of heat addition term, $\dot{Q}_{\mathrm{TES}\rightarrow\mathrm{Cyc}}$, used for calculating the cycle efficiency (i.e., defined in Equation (4.12)) is obtained using:

$$\dot{Q}_{\mathrm{TES}\rightarrow\mathrm{Cyc}} = \dot{m}_{28}\,(h_{28} - h_{\mathrm{a}}) \tag{4.20}$$

where h_{a} is the specific enthalpy at ambient conditions.

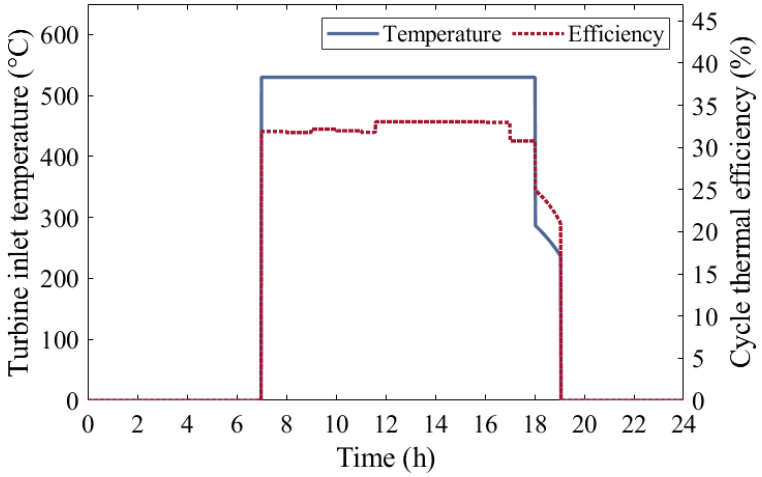

Figure 4.12. Steam turbine inlet temperatures and the calculated cycle thermal efficiencies while operating Khi Solar One with the existing TES system under the mean 24-h DNI profile.

The behaviour of the pressure and the amount of stored heat in both groups of SAs are shown in Figure 4.13(a) and (b), respectively. The initial amount of stored heat is calculated using ambient temperature and pressure as a reference point. The pressure and the amount of stored heat is constant for both groups of SAs until charging phase is started at the beginning of Hour 10. The superheating SAs are initially charged with saturated steam at a mass flowrate of 50 kg/s until reaching the maximum pressure of 8.2 MPa, taking about 16 min. Simultaneously, some steam is extracted from the base SAs to preheat the extra condensate for storage before entering the solar evaporator. This explains the decrease of pressure and stored heat in the base SAs. After filling the superheating SAs, the charging process of the base SAs starts with a net mass flowrate of 20 kg/s as steam is also extracted from the base SAs for feedwater hating. The pressure of the base group continues increasing at a higher slope (i.e., higher mass flowrate of charging steam) in Hour 11 until the middle of Hour 12 when the charging phase is terminated as the maximum pressure is reached.

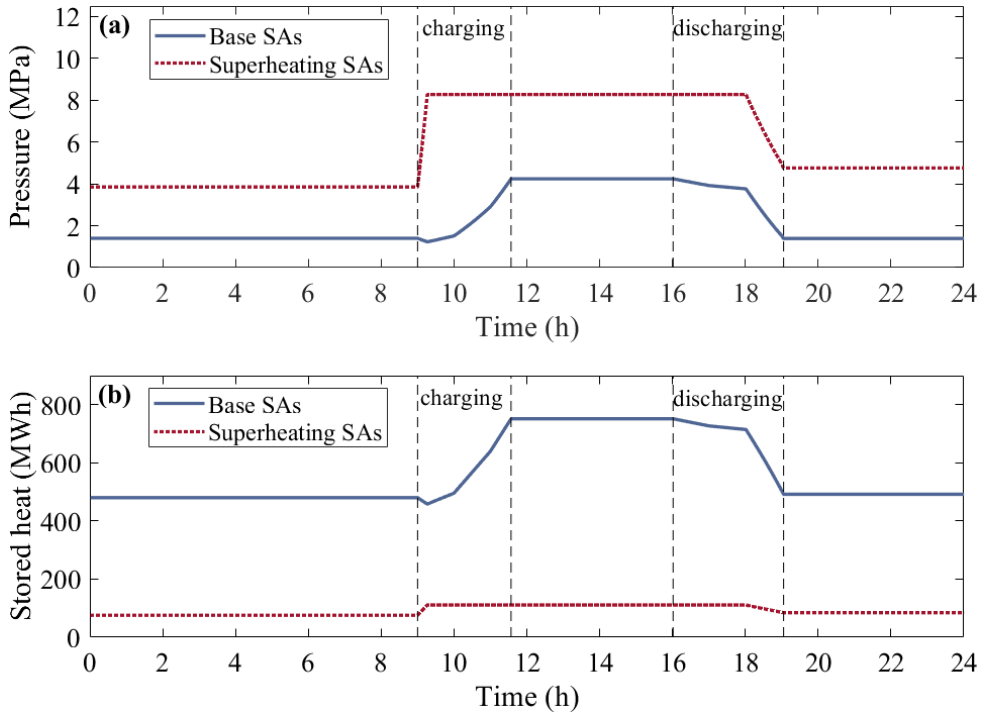

Figure 4.13. (a) Pressure, and (b) stored heat in both groups of SAs for the existing TES system. The data presented here is based on operating Khi Solar One under the mean 24-h DNI input profile as of Figure 4.11.

The discharging phase precisely starts at the beginning of Hour 17, which can be observed by the decrease of pressure and thermal energy stored in the base SAs as indicated in Figure 4.13. However, the discharged steam is only to provide feedwater heating. The main discharging phase (Mode 4) starts at the beginning of Hour 19 and continues for 1 h until terminated when the turbine inlet pressure reached the minimum allowable pressure of 1.4 MPa. The total discharged heat from the TES system is 245 MWh_{th}, that is 89% from the base SAs and 11% from the superheating SAs. The pressure level of the base group goes back to its initial state. However, the pressure and the stored heat in the superheating group is higher than the initial levels. The remaining extra heat can be discharged the following day. If not, the SAs can be calibrated to its initial state by releasing steam and/or injecting condensate.

The mass flowrate of the steam exiting the base SAs and the superheating SAs during the main discharging phase is shown in Figure 4.14(a). At the beginning of the discharge, the steam is released at 71 kg/s. However, the mass flowrate gradually increases to 86 kg/s at the end of the discharge. The increase is to maintain the power level at 50 MW_{el} as steam temperature and pressure is decreasing, see Figure 4.14(b). Moreover, the mass flowrate of the superheated

steam decreases from 10 kg/s at the beginning of the discharge, to 9 kg/s at the end. The decrease is a result of controlling the amount of steam needed to superheat the main flow stream entering the turbine by a maximum of 40 °C. The turbine inlet temperature, i.e., noted as superheater outlet temperature in Figure 4.14(b), is 286 °C at the start of the discharge and a calculated cycle efficiency of 25%. The turbine inlet temperature gradually decreases until it reaches 236 °C (i.e., cycle efficiency is 21%) due to the reduction of steam pressure and temperature during the discharging phase, which negatively affects the cycle efficiency as well.

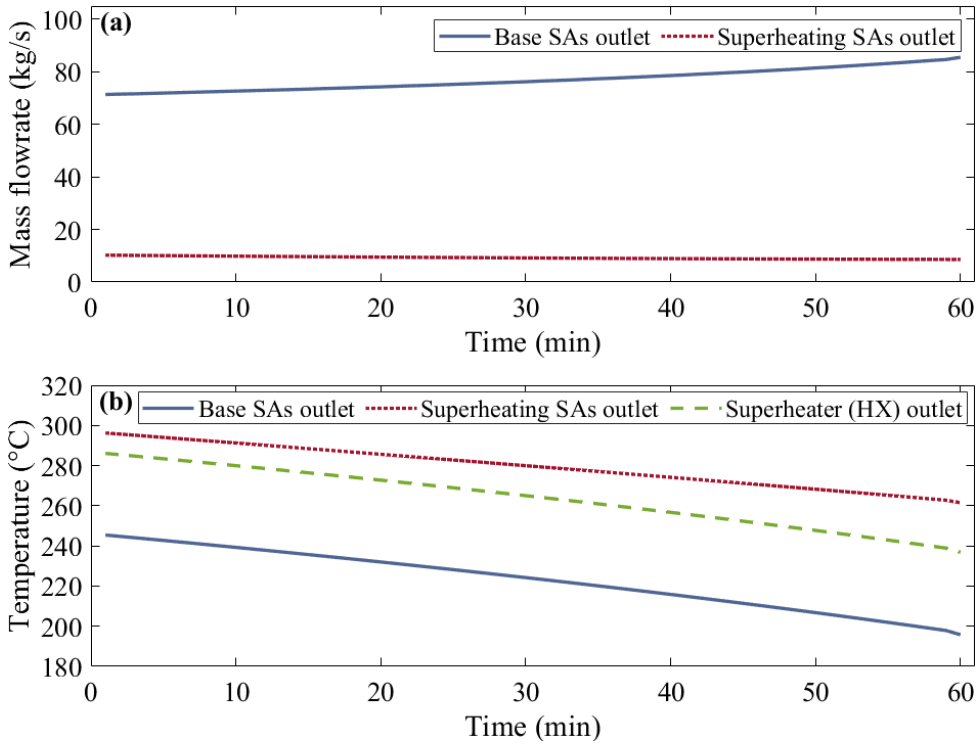

Figure 4.14. (a) Mass flowrate, and (b) temperature of steam outflowing from the base and the superheating SAs as well as in the superheating heat exchanger (i.e., turbine inlet) during the main discharging phase (Mode 4) in the existing TES system.

4.6. Performance of Khi Solar One with extended TES system configuration

4.6.1. Concrete sizing and thermo-economic parametric study

The analysis of the extended TES system starts by assessing the effect of different concrete sizes on the overall performance of Khi Solar One. The total concrete TES size is determined by the number of tubes distributed inside each block and by the number of concrete blocks with a length (L_{CB}) of 10 m. The tubes are assumed to be equally spaced, horizontally and vertically,

in each squared concrete block. The key thermodynamic parameters for a range of concrete TES sizes that have different number of blocks (N_{CB} = 2, 3, 4, 5, 6, and 7), connected in series, and different number of tubes (N_{tubes} = 2025, 2500, 3025, 3600, 4225 and 4900) are compared in Figure 4.15. The parametric study is performed using the same SA initial conditions (i.e., initial pressure is 1.9 MPa and initial WFR is 0.5) and the same 24-h DNI profile. Furthermore, the initial temperature profile of the concrete blocks is determined after running the Khi Solar One with the extended TES system model for two charging/discharging cycles (i.e., two days). The charging of concrete blocks is terminated when steam temperature at the last concrete block outlet is higher than 327 °C (i.e., design temperature of SAs). If this temperature is reached and the SAs are not fully charged yet, the charging of SAs is performed directly from the solar evaporator, see Stream 27 in Figure 4.2.

Figure 4.15(a) shows the relative stored heat in the extended TES system (both SAs and concrete blocks) for the examined range of concrete block sizes. The amount of stored heat in the blocks increases from 427 MWh_{th} for the smallest size (N_{tubes} = 2025 and N_{CB} = 2) to 512 MWh_{th} for the largest size (N_{tubes} = 4900 and N_{CB} = 7), due to the availability of extra TES media (concrete) in the larger sizes.

The amount of discharged electricity from the TES system for the compared sizes is displayed in Figure 4.15(b). The same trend is observed as the amount of discharged electricity depends on the amount of stored heat. Moreover, it can be seen in Figure 4.15(c) that the average steam temperature at the turbine inlet increases by 61%, from 286 °C for the smallest size to 455 °C for the largest size. The increase of temperature is because the larger the concrete blocks size is, the longer the charging time it takes until charging is terminated as more amount of concrete is available. Longer charging time means that concrete reaches higher temperature at the inlet of the first concrete block (i.e., outlet of the last block during discharging mode). Thus, it results in higher steam temperature at the concrete block outlet (i.e., turbine inlet) during the discharging phase. Furthermore, the average cycle efficiency during the discharging mode, shown in Figure 4.15(d), also increases with larger sizes of concrete blocks. The increase is about 7%, from 23.6% for the smallest size to 25% for the largest sizes and it is a result of the increasing steam temperature at the turbine inlet, which agrees with the definition of Carnot thermal efficiency.

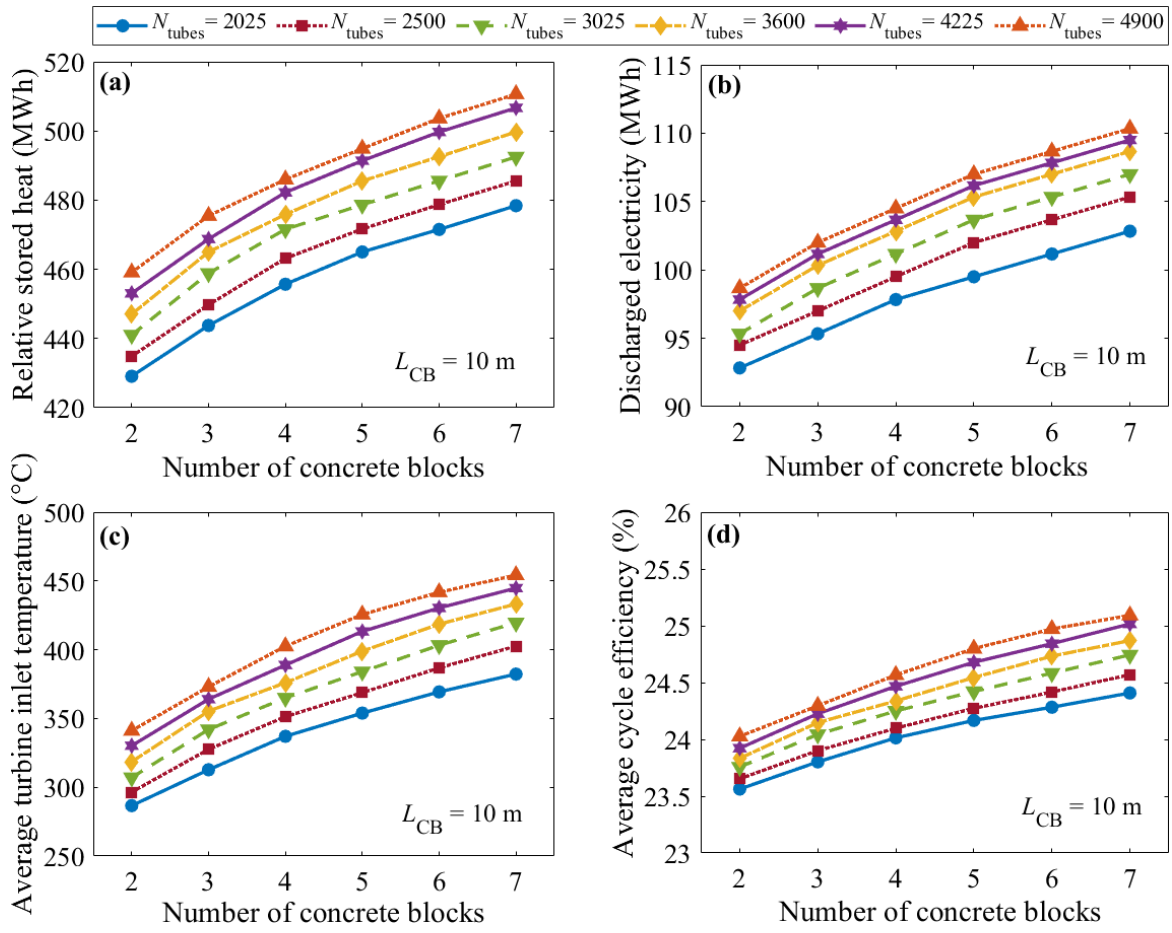

Figure 4.15. (a) Stored heat in the TES system, (b) discharged electricity from the TES system, (c) average turbine inlet temperature, and (d) average cycle thermal efficiency during discharging mode operation, for a range of concrete block sizes that have different number of tubes and concrete blocks.

Although the largest concrete TES size provides the highest amount of discharged electricity from the TES system, it might not be the most cost-effective option. Therefore, a comparison of the projected LCOE and LCOS for all examined concrete block sizes are shown in Figure 4.16(a) and (b), respectively. The LCOE ranges between 241 $/MWh$_{el}$ and 243 $/MWh$_{el}$, with the lowest achieved with 5 concrete blocks, each containing 3600 tubes. The difference of the LCOE between all compared sizes is relatively small as the additional cost of the concrete blocks is insignificant (i.e., $1.2M for the smallest size and $6.9M for the largest size) compared to the total estimated costs of Khi Solar One ($450M). The LCOS ranges from 157 $/MWh$_{el}$ to 168 $/MWh$_{el}$. The investment costs of concrete blocks have a greater impact on the LCOS as it can account between 2% and 12% of the total capital costs of the extended TES system (i.e., estimated capital costs of SAs is $51.3M).

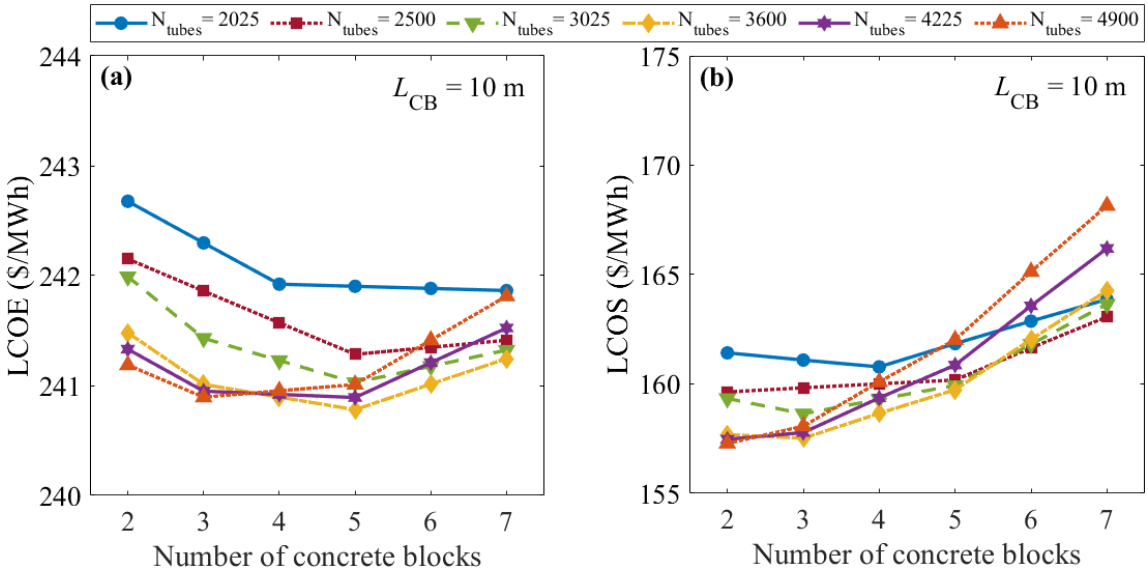

Figure 4.16. (a) LCOE, and (b) LCOS for a range of concrete block sizes that have different number of tubes and concrete blocks.

It is shown in Figure 4.16 that the optimal size based on the minimum LCOS is different from the optimal size based on the minimum LCOE. This is because in the LCOE, a major percentage of electricity, above 80% yearly, is generated without the need of the TES system (i.e., the calculated LCOE without TES system is 268 $/MWh$_{el}$), which results in different behaviour of the LCOE of the power plant. As this study focuses on the performance of Khi Solar One as whole power plant, the concrete TES size with the lowest LCOE (N_{tubes} = 3600, N_{CB} = 5) is selected for further analyses and for the final thermo-economic comparison with the existing TES system. The dimensions of each selected concrete block are L_{CB} = 10 m, W_{CB} = 4.8 m, and H_{CB} = 4.8 m.

4.6.2. Performance under the mean 24-h DNI profile

The performance of the Khi Solar One with the extended TES configuration under the mean 24-h DNI profile is shown in Figure 4.17. For the first hours, i.e., from Hour 1 to Hour 9, the operation behaviour of the Khi Solar One with the extended TES system is the same as in the existing configuration as no heat is stored in the TES system.

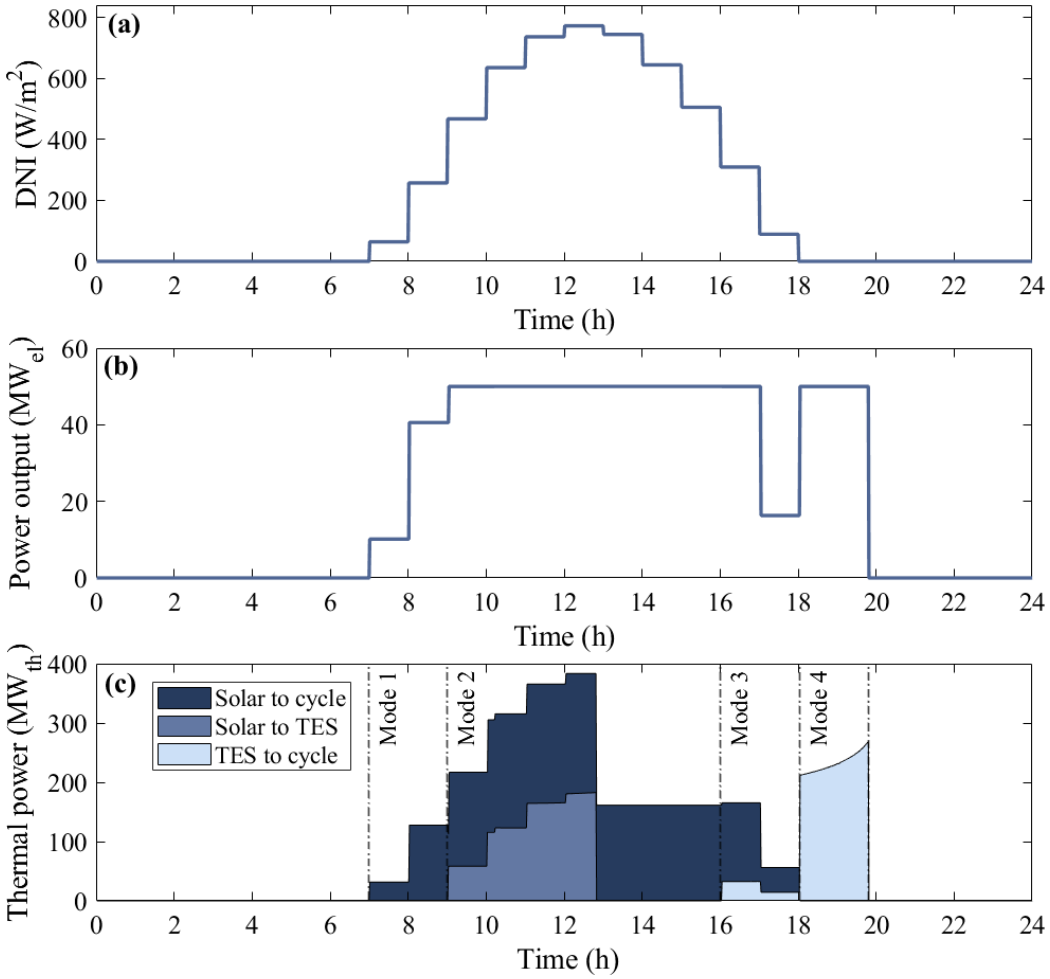

Figure 4.17. Diurnal (24-h) performance of Khi Solar One with the extended TES system configuration: (a) DNI input, (b) corresponding power output, and (c) thermal power either from solar tower to power generation cycle, from solar tower to TES system, or from TES system to power generation cycle.

At the beginning of Hour 10, the available thermal power in the solar tower is 212 MW_{th}. About 71% of this power is utilised to generate the 50 MW_{el} while the remaining 29% is directed to the TES system. The TES charging process can be split into two modes, and each one takes certain amount of time. The first mode is charging the concrete blocks and the SAs using the superheated steam exiting the solar superheater at 520 °C and 11.5 MPa. The superheated steam deposits some of its heat into the concrete blocks before being accumulated in the SAs. However, this charging mode is only valid when the steam outlet temperature from the last concrete block is 327 °C or less. When the steam temperature is above this point, the second charging mode starts, which is charging the SAs directly from the solar evaporator and bypassing the concrete blocks. The charging of SAs continues until reaching a maximum pressure of 8.2 MPa. The calculated total charging time is

227 min, that is 70 min for the first mode and 157 min for the second mode. It is about 45% longer than the total charging time in the existing TES system due to the additional storage capacity provided by concrete and also to the ability to charge the SAs to a higher pressure compared to the base SAs in the existing TES system. There is a slight step increase in the total thermal power after Hour 10, see Figure 4.17(c), which occurs after changing from the first to the second charging mode. This increase is because the solar evaporator has a higher efficiency than the superheater, thus, higher amount of thermal power is available in the evaporators for the same amount of CSP.

After the full charge of the TES system that occurs before the end of Hour 13, Khi Solar One continues operating at 50 MW_{el} of electrical power until the end of Hour 17. During Hour 17, the plant operates on Mode 3 (i.e., defined in Section 4.3.6) where feedwater heating is supplied by the SAs as indicated in the lightest blue shaded area in Figure 4.17(c). At Hour 18, Khi Solar One continues operating on Mode 3 but at 16.3 MW_{el} of power as the available thermal power in the solar tower is not sufficient for maximum power output. Like in the existing configuration, the turbine inlet temperature is 520 °C and the cycle efficiency is 33% between Hour 8 and Hour 18 as steam is directly provided by the solar superheater. The main discharging phase (Mode 4) starts at the beginning of Hour 19 and continues until the turbine inlet pressure reaches the lowest allowable pressure of 1.4 MPa (i.e., SAs pressure is 1.9 MPa considering a 0.5 MPa pressure drop in the concrete blocks). The total discharging time is 106 min and the total generated electricity utilising the stored heat is 88 MWh_{th}. The non-linear increase of TES system thermal power during the discharging phase, shown in Figure 4.17(c), is needed to maintain the power output at 50 MW_{el}. The need of extra power is due to continuous decrease of the discharging cycle efficiency caused by the reduction of steam temperature and pressure at the turbine inlet while steam is discharged from the SAs.

The behaviours of the SAs pressure and the amount of stored heat in TES system for the same 24-h DNI profile are shown in Figure 4.18(a) and (b), respectively. The amount of stored heat is calculated by taking ambient condition as a reference point. The SA pressure is constant at 1.9 MPa until the beginning of Hour 10. During this hour, although SAs are charged with steam, the pressure is slightly decreasing. This is because some amount of steam is simultaneously discharged from the SAs to preheat the condensate that is allocated for storage in the HP feedwater heater, i.e., flow stream number 17 in Figure 4.2. However, the total amount of thermal energy stored in the SAs during the same hour is still increasing because of two main reasons: (i)

the SAs are charged with steam at a higher mass flowrate (35 kg/s) than the mass flowrate of discharged steam (26 kg/s) for condensate preheating; and (ii) the temperature of the charging steam increases from 262 °C at the beginning of the charge to 321 °C at the end as a result of the decreasing heat transfer rate between the steam and the concrete. This can be seen by the gradually decreasing slope of the amount of stored heat in the concrete. The reduction of the heat transfer rate is mainly due to the increasing temperature of the concrete while charging, which decreases the temperature difference between the two media, thus, reducing the heat transfer rate.

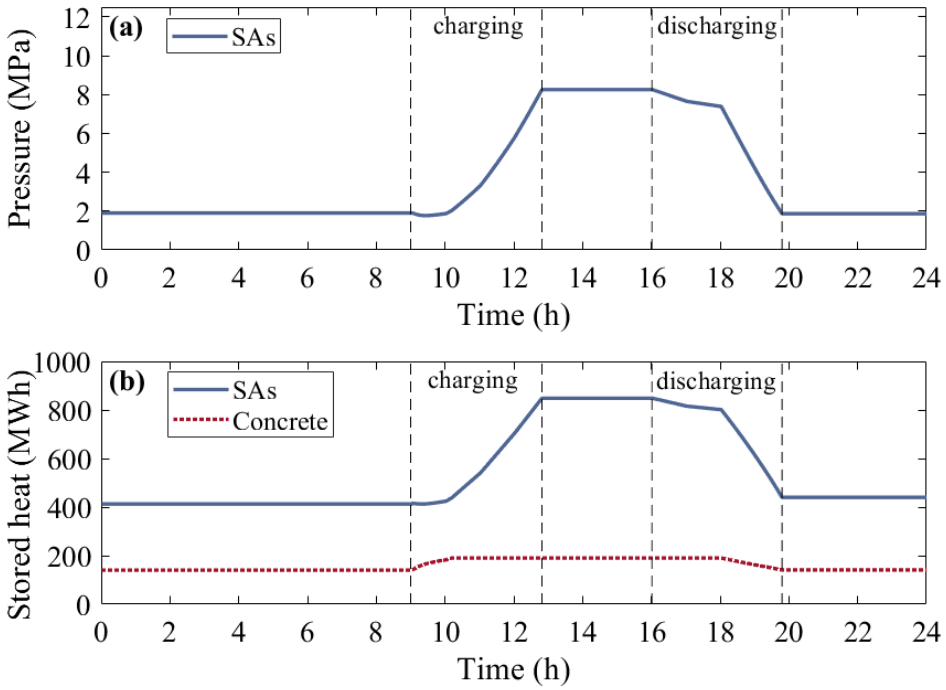

Figure 4.18. (a) Pressure, and (b) stored heat in the SAs and in the concrete blocks of the extended TES system. The data presented here corresponds to the same 24-h DNI input profile as of Figure 4.17.

As the available thermal power for storage increases at the beginning of Hour 11, the steam mass flowrate existing the superheater increases from 35 kg/s to 66 kg/s. The charging continues in the concrete for the first 10 min in Hour 11 but then stops as the steam temperature reaches 327 °C at the last concrete block outlet. It can be seen in Figure 4.18(b) that the rate of heat transfer (i.e., the slope of stored heat) during these 10 min is higher than the heat transfer rate at the end of Hour 10. This is due to the increase of the steam mass flowrate, which increase the effective heat transfer coefficient and thus the rate of heat transfer from steam to concrete. The SAs are not fully charged at this point, therefore, the charging of SAs continues by diverting

steam directly from the solar evaporator until reaching the maximum pressure of 8.2 MPa. At the end of the charging phase, the total stored heat in the extended TES system is 1040 MWh_{th}, that is 850 MWh_{th} in the SAs and 190 MWh_{th} in the concrete blocks.

The discharging phase technically starts at Hour 17 when steam is discharged for feedwater heating as in the existing TES system. However, the main discharging phase (Mode 4) starts at Hour 19 and continues for 107 min until the SA pressure is 1.9 MPa. The total discharged heat is 460 MWh_{th}, that is 410 MWh_{th} from the SAs and 50 MWh_{th} from the concrete blocks. The heat addition in the concrete is entirely utilised to superheat the saturated steam released from the SAs before entering the steam turbine. Although the SAs pressure at the end of the discharge is the same as at the beginning of the day, the amount of the heat is still higher as the post discharge WFR of the SAs is 0.53, which is higher than the initial WFR (0.5). Such difference is a result of the time varying charging temperatures and discharging rates. However, the final WFR can be calibrated to its initial state by releasing steam and/or injecting condensate.

Figure 4.19 shows that turbine inlet temperature, on the left *y*-axis, and the calculated cycle efficiency, on the right *y*-axis, for the same 24-h DNI profile as of Figure 4.17. From Hour 8 to Hour 18, the turbine inlet temperature is constant at 520 °C and the efficiency fluctuates between 30.5% and 33.5% for the same reasons discussed in Section 4.5.2. The turbine inlet temperature at the start of the main discharging phase is 452 °C, which is 58% higher than the maximum inlet temperature (268 °C) in the existing TES system configuration. The calculated cycle efficiency at this point is 28.6%, that is 15% improvement of the highest discharging cycle efficiency (24.9%) calculated in the existing TES system. The turbine inlet temperature gradually decreases as the pressure and the temperature of steam exiting the SAs and then the concrete blocks decrease during the discharge, which negatively affects the cycle efficiency. The lowest turbine inlet temperature that occurs at the end of the discharging phase is 352 °C with a cycle efficiency of 21.8%. These two values are still respectively 49% and 4% higher than those calculated in the existing TES system, see Section 4.5.2 and Figure 4.12.

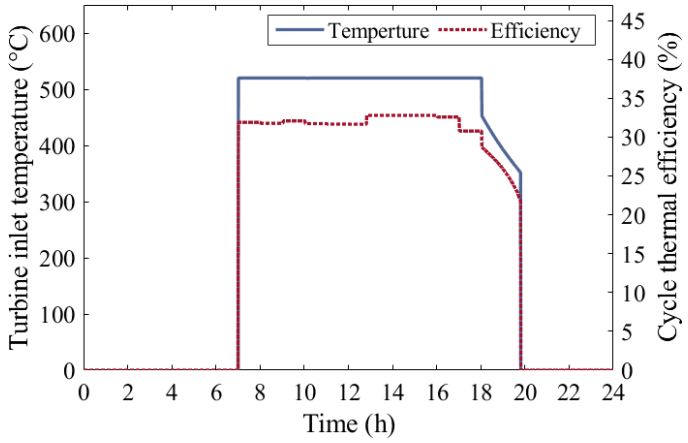

Figure 4.19. Steam turbine inlet temperatures and cycle thermal efficiencies while operating Khi Solar One with the extended TES system under the mean 24-h DNI profile as in Figure 4.17.

Figure 4.20 shows the main steam parameters during the discharging phase of the extended TES system. The steam temperature at the SAs outlet is gradually decreasing from 289 °C (i.e., the saturation temperature of steam at 7.4 MPa) at the start of the main discharging phase to 210 °C (i.e., the saturation temperature of steam at 1.9 MPa) at the end. However, the discharged steam temperature is increased by an average of 154 °C due to heat by the concrete blocks. The turbine inlet temperature at the start of the main discharging phase is 452 °C, which is 58% higher than the maximum inlet temperature (268 °C) in the existing TES system configuration. The calculated cycle efficiency at this point is 29%, that is 16% improvement of the highest discharging cycle efficiency (25%) calculated in the existing TES system. The turbine inlet temperature gradually decreases as the pressure and the temperature of steam exiting the SAs and then the concrete blocks decrease during the discharge, which negatively affects the cycle efficiency. The lowest turbine inlet temperature that occurs at the end of the discharging phase is 352 °C with a cycle efficiency of 22%. These two values are still respectively 50% and 5% higher than those calculated in the existing TES system. The pressure shown on the left *y*-axis of Figure 4.20(b) is the turbine inlet pressure, which is 0.5 MPa lower than the pressure of discharged steam from the SAs to account for the assumed pressure drop. To maintain the power output at 50 MW_{el} with the decreasing steam pressure and temperature, the steam mass flowrate is gradually increased as shown on the right *y*-axis of Figure 4.20(b).

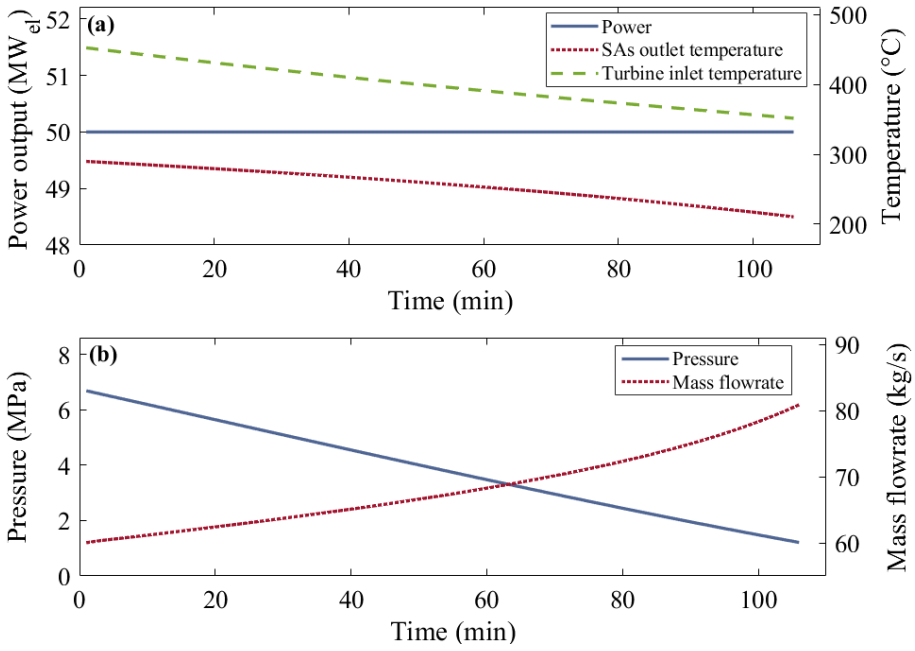

Figure 4.20. (a) Khi Solar One power output, on the left *y*-axis, and steam temperature at the SAs outlet and at the turbine inlet, on the right *y*-axis, and (b) turbine inlet pressure, on the left *y*-axis, and steam mass flowrate, on the right *y*-axis, exiting the SAs during the main discharging mode of the extended TES system.

4.6.3. Temperature profiles of concrete during changing/discharging processes

The temperature progression of the concrete and the steam (in all 5 concrete blocks with a total length L_{total} = 50 m) during the charging phase is shown in Figure 4.21. The steam flow direction is from the left (i.e., from the solar superheater) to the right (i.e., to the SAs). Figure 4.21(a) shows the temperature profile at time zero, just before the start of the charging mode. The initial concrete temperature profile is obtained after running the formulated TES system model for two charging/discharging cycles using the mean 24-h DNI profile. The steam temperature inside the tubes is initially assumed to be the same temperature as of the concrete, and the inlet steam temperature (i.e., boundary condition) is 520 °C.

After a time of 0.2 τ_{Ch} (14 min), the concrete temperature at the inlet has already increased to 412 °C as shown in Figure 4.21(b). At the same time instant, the temperature of steam decreases along the axial length of the concrete blocks until reaching the saturation temperature of 321 °C at 11.5 MPa. At this point, the latent heat of steam is being transferred to the concrete elements. The boundary of the single-phase and the two-phase regions shifts from the left to the right,

shown in Figure 4.21(c), (d) and (e) as charging continues and the concrete temperature is increasing. The temperature difference between the steam in the two-phase region and the concrete decreases as more heat is transferred from the steam to the concrete. The charging phase stops at τ_{Ch} when the steam temperature is 327 °C at the outlet. At this time, the highest concrete temperature is 489 °C (at the inlet of the first concrete block) and the lowest is 322 °C (at the outlet of the last concrete block) as shown in Figure 4.21(f).

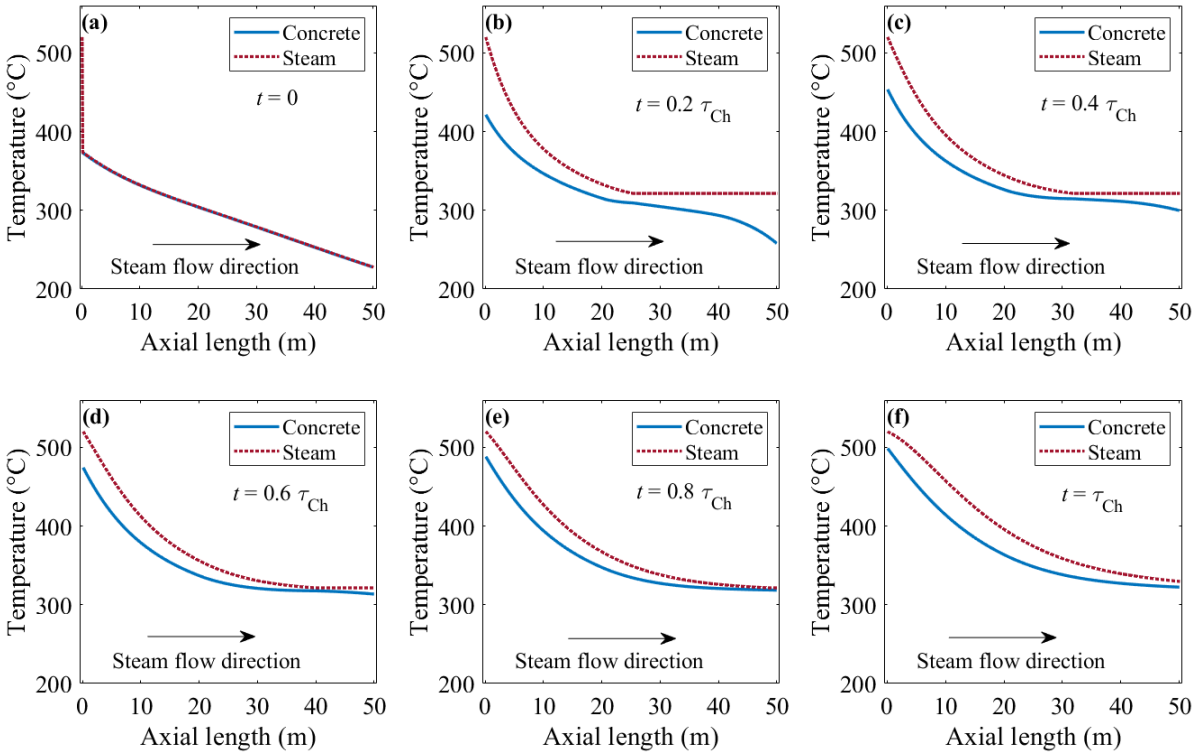

Figure 4.21. Progression of concrete and steam temperature profiles during charging mode at different time instants. The total charging time, τ_{Ch}, is 70 min and the steam flow direction is from the left side (from the solar superheater) to the right side (to the SAs).

The steam and the concrete temperature profiles during the discharging phase are shown in Figure 4.22. The total discharging time (τ_{Dch}) is 106 min and the steam flow direction is from the left (from the SA) to the right (to the turbine). At time zero and before the discharging phase, the steam temperature is assumed to be the same as the concrete temperature, see Figure 4.22(a), since steam has been held inside the tubes for hours after the charging phase. The steam temperature at the first concrete block entrance from the SAs side (i.e., left boundary condition) is 289 °C, which is the temperature of the steam exiting the SAs. During the discharging phase, the concrete and the steam temperature profiles decreases as shown in Figure 4.22(b) to (f).

Moreover, the inlet steam temperature (i.e., on the left side) is also decreasing with time as the pressure and the temperature of all SAs are decreasing during the discharging phase.

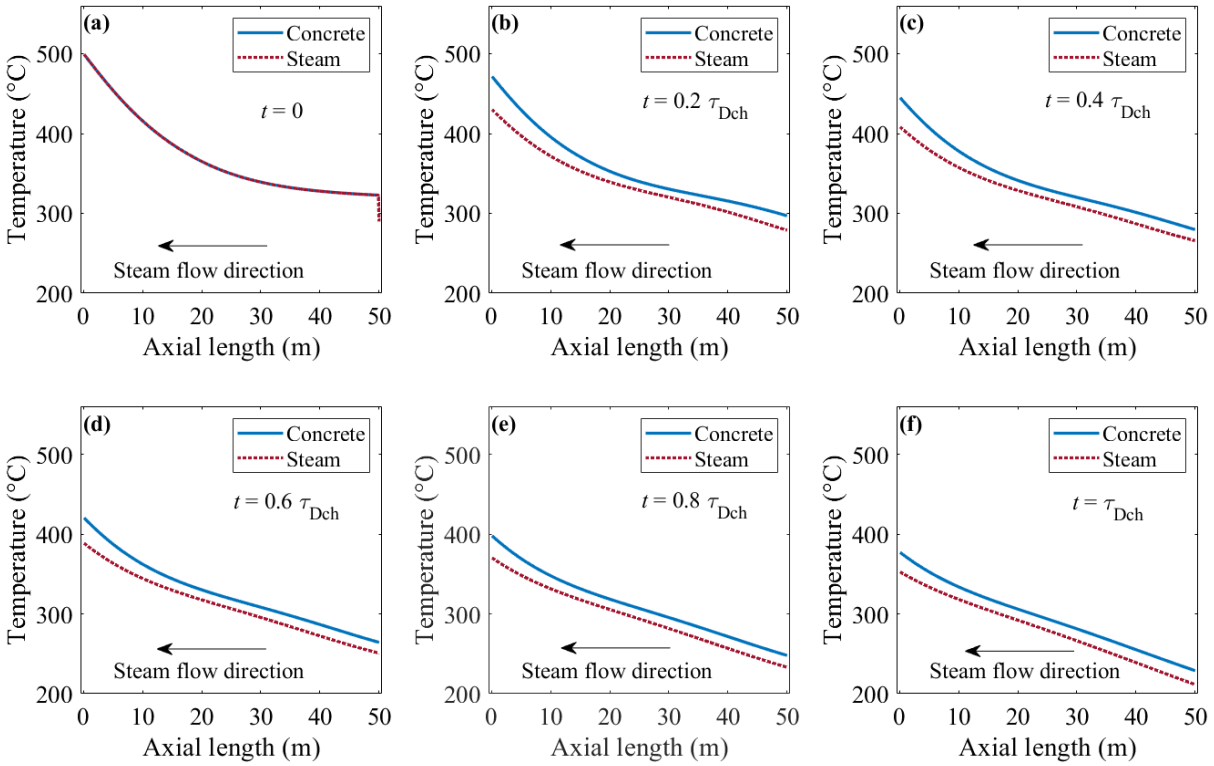

Figure 4.22. Concrete and steam temperature profiles during discharging mode at different time instants. The total discharging time, τ_{Dch}, is 106 min and the steam flow direction is from the right side (from the SAs) to the left side (to the steam turbine).

4.7. Thermo-economic comparison of existing vs. extended TES configuration

4.7.1. Evaluation at different 24-h DNI profiles

The performance of Khi Solar One with the existing and the extended TES for the proposed DNI profiles (i.e., defined in Section 4.3.5) are shown in Figure 4.23 to Figure 4.27. In all figures, (a) shows the DNI input profile, (b) shows the output power, (c) shows the available thermal power, and (d) shows the amount of stored heat in the TES system. For example, Figure 4.22 presents the performance of Khi Solar One using DNI Profile 1, which is the mean plus one standard deviation of the collected DNI data. During the main TES discharging mode that starts at Hour 18, the amount of electricity generated utilising the stored heat in the extended TES system is 97 MWh_{th} while it is only 57 MWh_{th} for the existing TES system, a relative increase of 70%. It

is also shown in Figure 4.23(c) that the extended TES configuration is able to utilise about 60%, that is 2 GWh, of the available heat in the solar receivers (3.36 GWh), whereas only about 46% (1.54 GWh) is employed in the existing TES system. This is mainly due to the ability of the extended TES system configuration to utilise the maximum storage capacity of the existing SAs at maximum pressure, as well as to the addition of the concrete blocks.

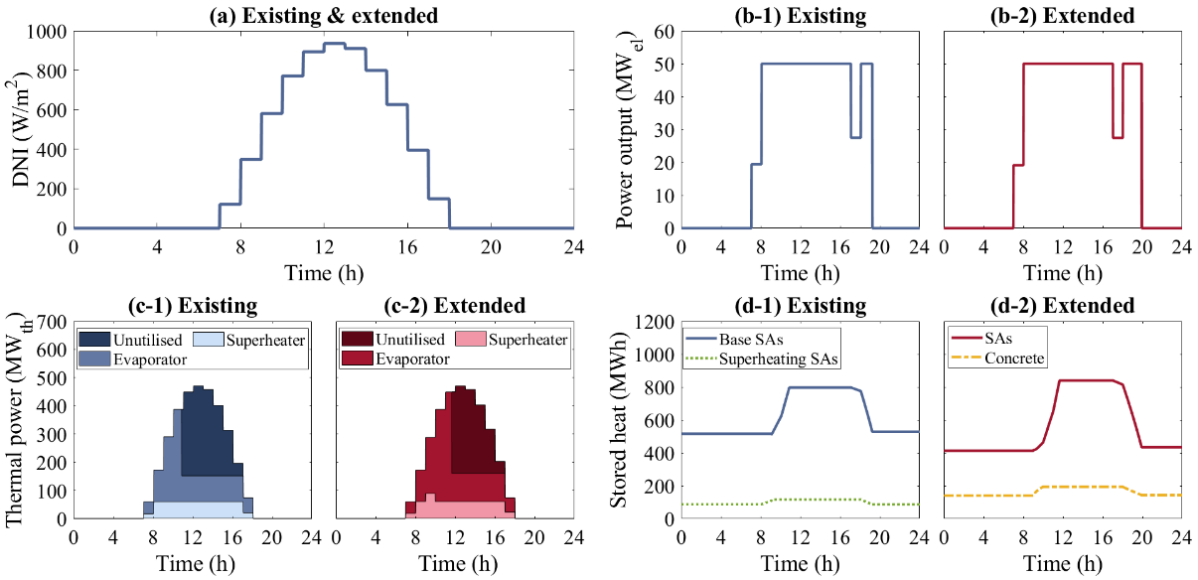

Figure 4.23. Comparison of the thermodynamic performance of the existing and the extended TES systems for DNI Profile 1 as defined in Section 4.3.5, for: (b-1, c-1, d-1) existing TES system, and (b-2, c-2, d-2) extended TES system.

Figure 4.24 compares the performance of Khi Solar One with the two TES system configurations at DNI Profile 2, which is the mean minus one standard deviation of the DNI data. In this DNI profile, the availability of sufficient sunlight is only for 9 h (from Hour 9 to Hour 17), whereas in the mean DNI is 11 h (from Hour 8 to Hour 18). The estimated total heat in the solar receivers is 1.9 GWh_{th}. As shown in Figure 4.24(c), all this heat is utilised for electricity generation in the extended TES system while only 85% of heat is utilised in the existing TES system.

The performance of Khi Solar One with the two TES system configurations is also compared for the lowest daily DNI profile recorded in the year in Figure 4.25. The performance is the same for both TES systems as there is not enough heat to be stored. The total generated electricity during this DNI profile is 69 MWh_{el}.

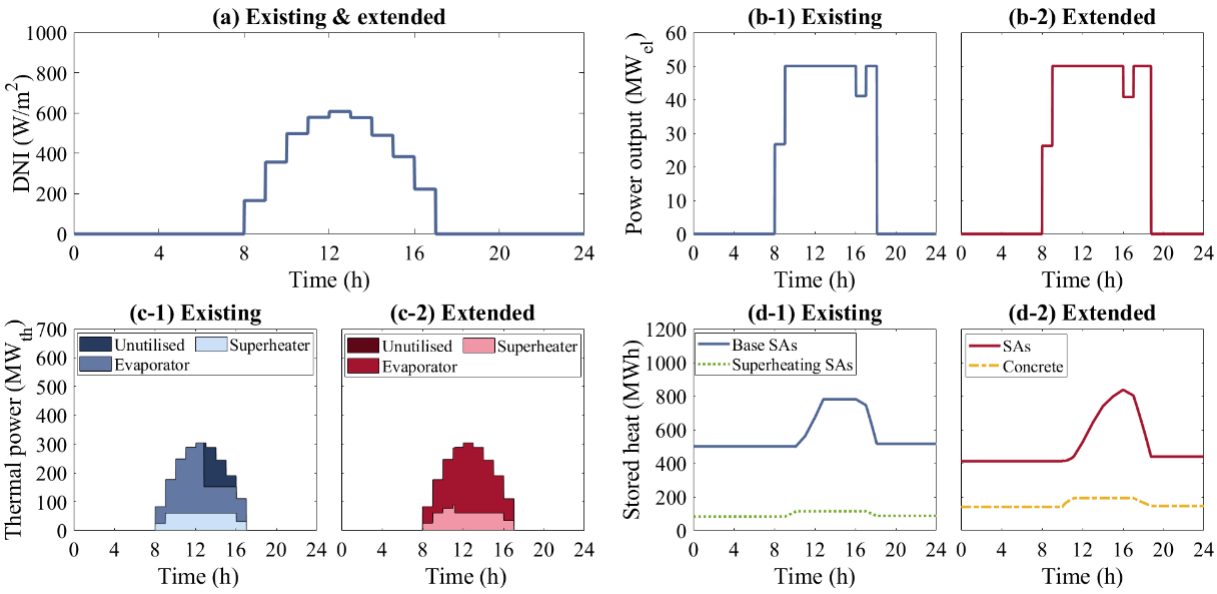

Figure 4.24. Comparison of the thermodynamic performance of the existing and the extended TES systems for DNI Profile 2 as defined in Section 4.3.5, for: (b-1, c-1, d-1) existing TES system, and (b-2, c-2, d-2) extended TES system.

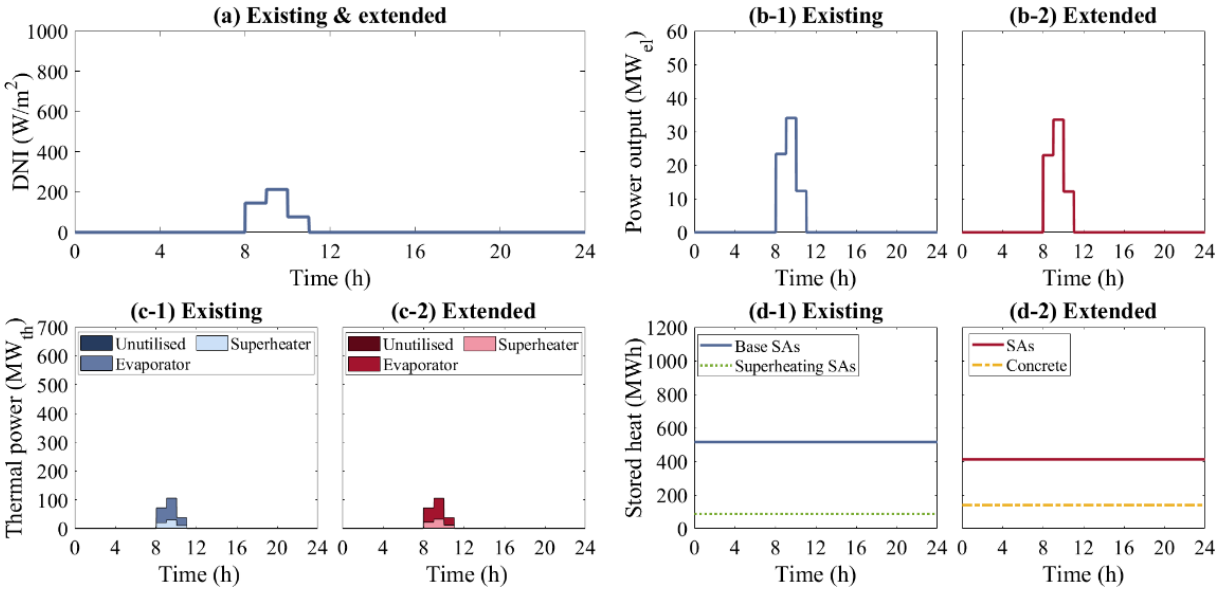

Figure 4.25. Comparison of the thermodynamic performance of the existing and the extended TES system configurations for DNI Profile 3 as defined in Section 4.3.5, for: (b-1, c-1, d-1) existing TES system, and (b-2, c-2, d-2) extended TES system.

The thermodynamic performance of Khi Solar One under DNI Profile 4 (i.e., highest daily DNI recorded in the year) is shown in Figure 4.26. The behaviour under this profile is similar

to the that under DNI Profile 1 as the TES systems are fully charged during the day and then fully discharged after the sunset.

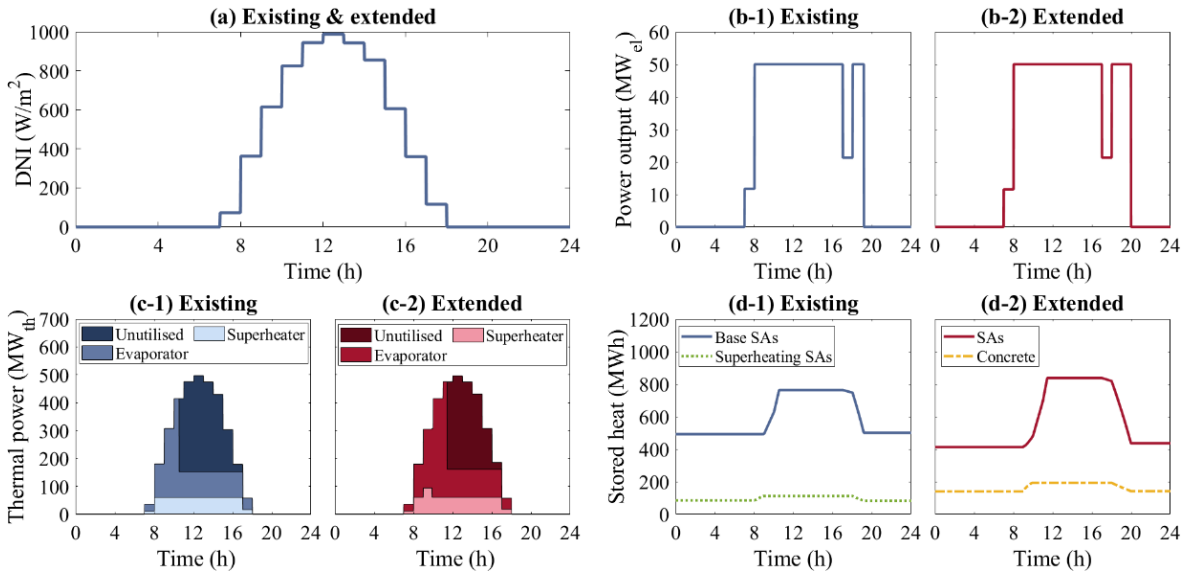

Figure 4.26. Comparison of the thermodynamic performance of the existing and the extended TES system configurations for DNI Profile 4 as defined in Section 4.3.5, for: (b-1, c-1, d-1) existing TES system, and (b-2, c-2, d-2) extended TES system.

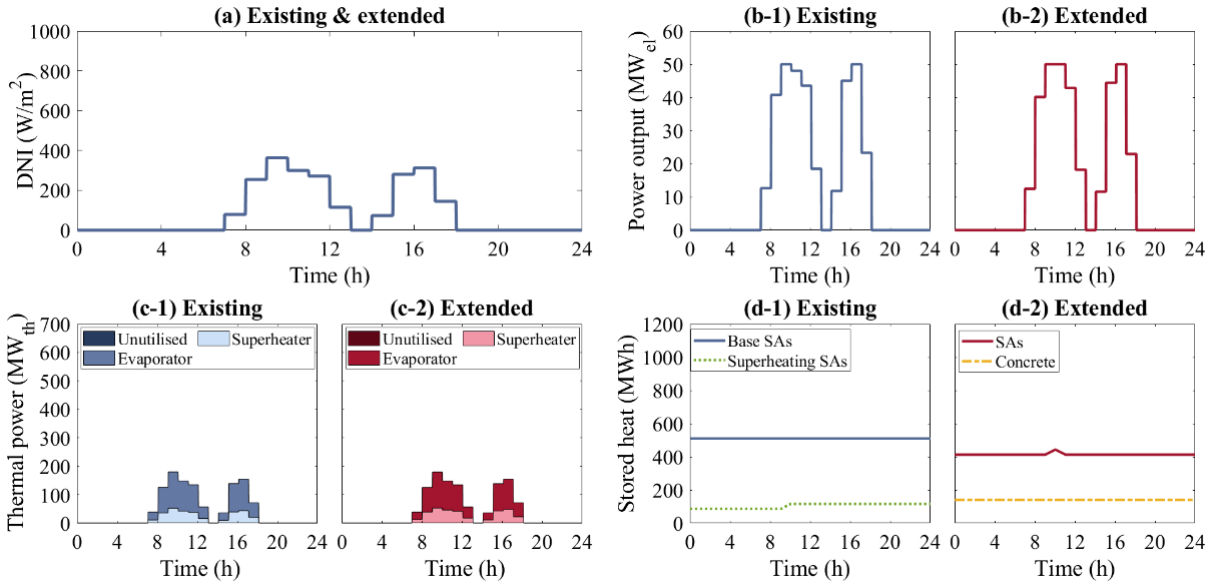

Figure 4.27. Comparison of the thermodynamic performance of the existing and the extended TES system configurations for DNI Profile 5 as defined in Section 4.3.5, for: (b-1, c-1, d-1) existing TES system, and (b-2, c-2, d-2) extended TES system.

Figure 4.27 compares the performance of Khi Solar One for DNI Profile 5, which is the DNI of a randomly selected day that has a high DNI fluctuation. The performance is almost the same for both TES configuration as only small amount of thermal energy (31 MWh_{th}) is available for storage at Hour 10. The existing TES system stores this heat in the superheating SAs. However, this heat is not utilised during Hour 11 for feedwater heating as the superheating SAs are not connected to feedwater heaters. On the other hand, the extended configuration stores the same amount of heat in the SAs and then discharge it during Hour 11 for feedwater heating which increases the power output from 48 MW_{el} to 50 MW_{el} as seen in Figure 4.27(b-2).

4.7.2. Cost and economic performance of both TES configurations

The estimated capital costs of the SAs and of the storage heat exchanger in the existing TES system are listed in Table 4.9. The considered costs in this study were the average value of the obtained costs from the four different methods, which are discussed in Sections 3.5.2.4 and 3.5.5.1 of Chapter 3. The total capital cost of the existing TES system is about \$51.5M, that is \$51.3M for the SAs, and \$230k for the storage heat exchanger. The Turton et al. [160] method predicts SA costs at least eight times higher than other methods (i.e., \$445M). Thus, it is excluded from this study. The maximum and the minimum SA costs are within ±20% of the average cost, which is acceptable when it comes to cost estimation uncertainties. For the heat exchanger costs, the effect of cost variations is minor as it only accounts for 0.2-0.7% of the total capital costs of the existing TES system. Therefore, taking the maximum, the minimum, or the average estimated cost for heat exchanger units does not have a significant effect on the thermo-economic study.

Table 4.9. Estimated capital costs of SAs and storage heat exchanger.

Method	SAs (\$M)	Heat exchanger (\$k)
Seider et al. [154]	41.6	360
Turton et al. [160]	-	320
Couper et al. [158]	53.0	130
Ulrich et al. [159]	59.3	110
Average capital costs	**51.3**	**230**

The estimated costs of the materials and the construction of the 5 concrete blocks (N_{tubes} = 3600, L_{CB} = 10 m, and W_{CB} = H_{CB} = 4.8 m) in the extended TES system are summarised in Table 4.10. The total cost is \$4.2M, that is \$2.8M for the materials (i.e., direct) and \$1.4M for indirect costs.

Table 4.10. Estimated capital costs of the 5 concrete blocks with N_{tubes} = 3600 and L_{CB} = 10 m.

Components	**Cost ($k)**
Concrete mixture	340
Tubes	130
Insulation	370
Foundation	680
Platform and steel	630
Interconnecting piping and valves	210
Electrical	210
Instrumentation and control	210
Contingency	420
Engineering	420
Construction	560
Total costs	**4180**

The estimated capital costs of Khi Solar One with the two TES system configurations are compared in Figure 4.28. The total costs of Khi Solar One with the existing TES system is $450M (11% of this is for the TES system), while is about $454M with the extended TES system (12% of this is for the TES system). The cost difference between the two TES configurations is $4M, less that the total estimated cost of concrete ($4.2M), since the $230k storage superheater is no longer needed in the extended configuration.

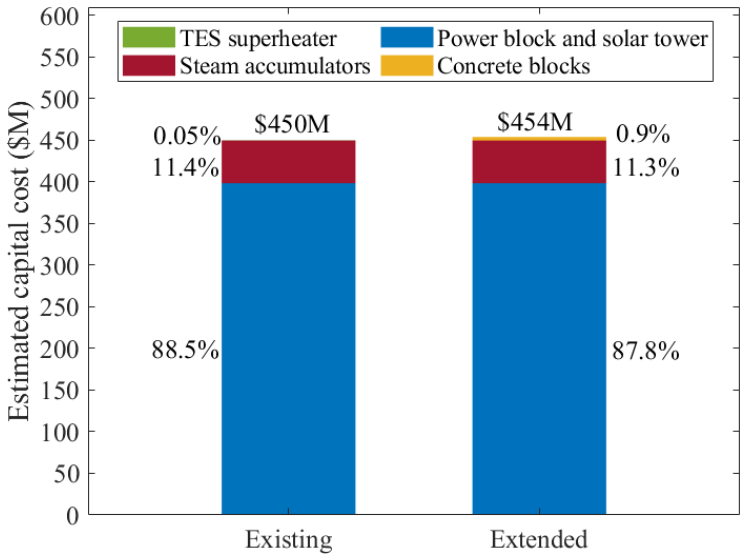

Figure 4.28. Estimated total capital costs of the main components of Khi Solar One with the two analysed TES system configurations (existing and extended).

The economic performance of Khi Solar One with the existing and the extended TES configurations are presented in Figure 4.29. The left *y*-axis of Figure 4.29 compares the projected NPV of Khi Solar One for a range electricity prices, from 100 \$/MWh$_{el}$ to 340 \$/MWh$_{el}$, and the right *y*-axis compares the projected IRR for the same price range. Installation of 5 concrete blocks, connected in series, with N_{tubes} = 3600 and L_{CB} = 10 m is assumed in the extended configuration as they offer the lowest LCOE among the examined size range. The projected NPV of both TES system configurations are negative for electricity prices ranging from 100 \$/MWh$_{el}$ to 240 \$/MWh$_{el}$. In particular, the NPV for the extended case is almost zero at an electricity price of 240 \$/MWh$_{el}$. Khi Solar One could generate positive returns if it operates in electricity markets with prices higher than 260 \$/MWh$_{el}$. In the examined range of electricity prices, the projected NPV of the extended TES system configuration is always higher than the existing TES system configuration. This is due to the ability of storing greater amount of heat, about 177 MWh$_{th}$ of extra heat, with an additional investment of \$4.2M. The addition of concrete blocks allows for extra TES capacity and for storing steam at higher pressure limits in the SAs. The difference between the two NPVs increases with the increasing electricity prices as more income could be generated from selling the extra electricity produced in the extended TES system (i.e., 39 MWh$_{el}$/day). Since the discount rate is 10%, the NPVs are negative for electricity prices that have IRRs lower than 10% and are positive for IRRs higher than 10%.

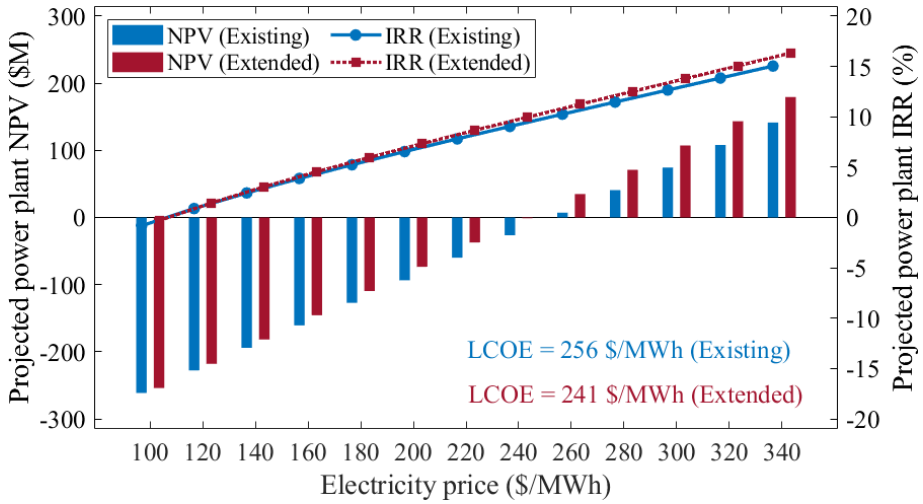

Figure 4.29. Comparison of the projected NPV and the projected IRR of Khi Solar One with the two TES system configurations (existing and extended) for electricity prices from 100 \$/MWh$_{el}$ to 340 \$/MWh$_{el}$.

The breakeven point where the NPV is zero and the IRR is 10% is at an electricity price of 256 $/MWh$_{el}$ for the existing TES system and of 241 $/MWh$_{el}$ for the extended TES system. Thus, based on the analyses and assumptions made in this study, the existing TES configuration could provide positive returns if the generated electricity is sold at a price higher than 256 $/MWh$_{el}$ and the extended TES configuration could be economically positive if the generated electricity is sold at a price higher than 241 $/MWh$_{el}$. The breakeven prices are equal to the calculated LCOE of both TES systems, reported in Figure 4.29.

The key thermodynamic and economic results of Khi Solar One with the existing and the extended TES system configurations are compared in Table 4.11. The results were obtained using the mean 24-h DNI profile for the whole year and an electricity price of 280 $/MWh$_{el}$.

Table 4.11. Main thermodynamic and economic results of Khi Solar One with the existing and the extended TES system configurations. The results are obtained using the mean 24-h DNI profile for the entire year, an electricity price of 280 $/MWh$_{el}$, and the extended TES system has five concrete blocks with N_{tubes} = 3600, L_{CB} = 10 m, W_{CB} = 4.8 m, and H_{CB} = 4.8 m.

Parameter	Existing	Extended	Difference (%)
Generated electricity from Khi Solar One (MWh$_{el}$/day)	517	556	7.5
Generated electricity from the TES system (MWh$_{el}$/day)	67	106	58
Full TES discharge duration (min)	60	107	78
Maximum cycle thermal efficiency at discharging phase (%)	25	29	16
Average cycle thermal efficiency at discharging phase (%)	23	26	13
Maximum turbine inlet temperature at discharge (°C)	286	453	58
Average turbine inlet temperature at discharge (°C)	263	400	52
Total power plant capital cost ($M)	450	454	0.9
Levelised cost of electricity, LCOE ($/MWh$_{el}$)	256	241	-5.9
Levelised cost of storage, LCOS ($/MWh$_{el}$)	225	159	-29
Payback time (years)	18.3	15.6	-15
Net present value, NPV ($M)	41	71	73
Internal rate of return, IRR (%)	11.5	12.5	8.7

Taking the existing configuration as a reference, the extended TES system configuration is able to deliver 58% more electricity than the existing TES system, that is 7.5% extra if considering the power output of Khi Solar One. Moreover, the extended configuration can store heat at a higher temperature than the existing configuration, which increases the average turbine inlet temperature by 52% (i.e., 263 °C for existing and 400 °C for extended) during the TES

discharging mode. The temperature increase enhances the maximum and the average cycle thermal efficiency during the discharging mode by 16% and 13%, respectively.

The improved thermodynamic performance of the extended TES configuration could be achieved with an estimated additional capital cost of $4.2M, i.e., the cost of the concrete blocks. With this additional cost, the calculated LCOS and the LCOE are respectively 29% and 6% lower than those with the existing configuration. At an electricity price of 280 $/MWh$_{el}$, Khi Solar One with the extended configuration could achieve a NPV of $71M whereas it is only $41M for the existing configuration, which is about $30M extra in total revenues for the 25 years (i.e., lifetime of the power plant). The payback time, which is defined as the number of years required until achieving a zero NPV, of Khi Solar One with the extended TES system is 2.7 years shorter than with the existing TES system.

4.8. Summary and conclusions

Two steam accumulating thermal energy storage (TES) options for direct steam generation (DSG) concentrated solar power (CSP) plants were compared taking the Khi Solar One power plant in South Africa as a case study. The compared TES options were: (i) the existing TES system in Khi Solar One, which consists of two groups of steam accumulators (SAs) and a superheater; and (ii) an extended TES system that contains one group of SAs and concrete blocks for higher-temperature storage. The two configurations were thermodynamically and economically analysed using the same existing solar tower and the same power generation cycle components in Khi Solar One.

The thermodynamic analysis of the existing TES system started by determining the initial water filling ratio (WFR) of the base SAs that maximises profitability. It was found that base SAs with initial WFRs of 0.75 gives the lowest levelised cost of electricity (LCOE) of 256 $/MWh$_{el}$. Moreover, different number of concrete blocks with various sizes, in terms of number of tubes, were thermodynamically investigated using a transient heat and mass energy balance computational model, and also economically compared applying the same economic assumptions. It was found that installing five 10-m long concrete blocks, connected in series, with 3600 equally-spaced tubes offers the lowest LCOE of 241 $/MWh$_{el}$.

The performance of Khi Solar One with the existing and with the extended TES systems were compared for the same 24-h hourly DNI input, and the following remarks can be given:

- The extended configuration can store an extra 177 MWh_{th} of heat using the same number of SAs as in the existing configuration and the additional concrete blocks. The TES capacity increase is mainly due to the ability of the extended configuration to utilise the current SAs to store steam at a higher temperature and pressure, as superheating is achieved by the higher-temperature concrete TES unit.
- Maximising the use of the current SAs and the addition of concrete blocks result in an averaged additional electricity of 39 MWh_{el} per day.
- During TES system discharging mode, the average cycle thermal efficiency is 13% higher in the extended configuration as the inlet temperature can reach up to 453 °C while the maximum is 286 °C in the existing TES system configuration.
- With an estimated additional investment cost of $4.2M (i.e., cost of concrete blocks) that only accounts for 1% of the total cost of Khi Solar One, the extended TES system configuration could decrease the LCOE of the DSG CSP plant by 6%, from 256 $/$MWh_{el}$ to 241 $/$MWh_{el}$.
- Extending the existing TES configuration increases the projected net present value of Khi Solar One from $41M to $71M if the generated electricity is sold at 280 $/$MWh_{el}$.

The key results of the presented work in this chapter show that combining concrete blocks with SAs as a TES option have greater economic potential than using SAs only. The main findings from the performed thermo-economic analyses in this chapter provide an adequate answer to Research Question 1 and sufficiently fills the Research Gap 1 that are listed in Section 2.8. Future work recommendations related to the presented study in this chapter are discussed in Section 8.3.

Chapter 5
Nuclear flexibility with current fleet of UK's nuclear power plants

5.1. Introduction

In order to minimise the impact on the grid of high share of variable renewable energy sources, in some countries the intermittent generators are required to aggregate into a virtual power plant (VPP). A VPP is a cluster of dispersed generator units, controllable loads and storages systems, which can operate as a unique power plant, through an energy management system (EMS) which coordinates the power flows coming from the generators, controllable loads and storages [192,193]. Such asset of generation and storage technologies could include flexible generation systems, able to compensate the intermittency of variable renewable energy sources. Moreover, the connection of asynchronous generators to electricity transmission networks due to the high penetration of renewables can result in grid frequency variations, which could exceed given thresholds [194], so that the per unit drop or speed regulation of synchronous generator units can no longer respond adequately, and this can ultimately lead to brownouts or even blackouts. Appropriate energy management actions are thus required in response to such frequency variations, such as curtailment, demand-side management or fast response of conventional generation systems.

In this chapter, a flexible generation-integrated EMS featuring the integration of thermal energy storage (TES) based on phase-change materials (PCMs) and organic Rankine cycle (ORC) units into a nuclear power plant. During off-peak demand, steam can be extracted from such power plants for the charging of an array of PCM-based thermal tanks. At a later time, when this is required and/or economically favourable, the charged TES tanks can discharge heat to secondary ORC power plants in order to generate power in addition to that of the base power plant. ORC plants are of particular relevance in this context as they are suitable for power generation at reduced temperatures and smaller scales [195–198]. The study of this type of solution is of interest as it offers greater flexibility than TES-only solutions that store thermal energy and then release this back to the base power plant, by allowing over-generation during peak demand

whereby the total available power output is higher than the base plant's rated capacity, thanks to the additional power delivered by the secondary power plants. In such an EMS scheme, it is of interest to optimise the derating of the power plants for the charging of the thermal tanks and to control the discharging of the tanks for electricity generation from the secondary plants.

The present work in this chapter goes beyond previous research by: (i) developing and exploring load-following operations via secondary ORC power plants coupled to the TES assets; and (ii) investigating the economic feasibility of such flexible generation solutions integrated to virtual power plant operation, accounting for both investment costs and revenues, all while considering the design of different configurations for integrating TES and ORC plants in a currently operating nuclear power plant, and actual electricity price variations in the UK. In more detail, the work in this chapter include:

- Design a selection of different configurations for integrating TES and secondary ORC plants in a currently operating nuclear power plant in the UK (advance gas-cooled reactor). The overall concept is described in Section 5.2.
- Understand the variations to the performance and operation of baseload power plants from a thermodynamic perspective when integrating different TES strategies (Sections 5.3.1 to 5.3.3), and to quantify the potential variations in generation capacity between peak and off-peak times.
- Identify and discuss the advantages of using PCMs in TES systems, considering the choice of suitable materials and how this affects the performance and operation of the whole EMS.
- Account for the performance and capital cost of the secondary ORC generators that later converts the stored heat to electricity, which is covered in Section 5.3.5.
- By means of an economic analysis (Section 5.5), proceed finally to estimate the potential profits that can result from the operation of the proposed EMS in light of the expected rewards from flexible generation and different TES-ORC sizing criteria.

The main findings and conclusions of the work performed in this chapter are summarised in Section 5.6. It should be noted that the study presented in this chapter has been already published as a journal article, which can be found in Ref. [199]

5.2. Concept description

Figure 5.1 presents an outline of the main components of the power plant under investigation in this chapter, which is an advanced gas-cooled reactor (AGR) nuclear power plant operated by a Electricite de France (EdF) in the UK. The corresponding thermodynamic processes are shown on a temperature-specific entropy (*T*–*s*) diagram in Figure 5.1(b).

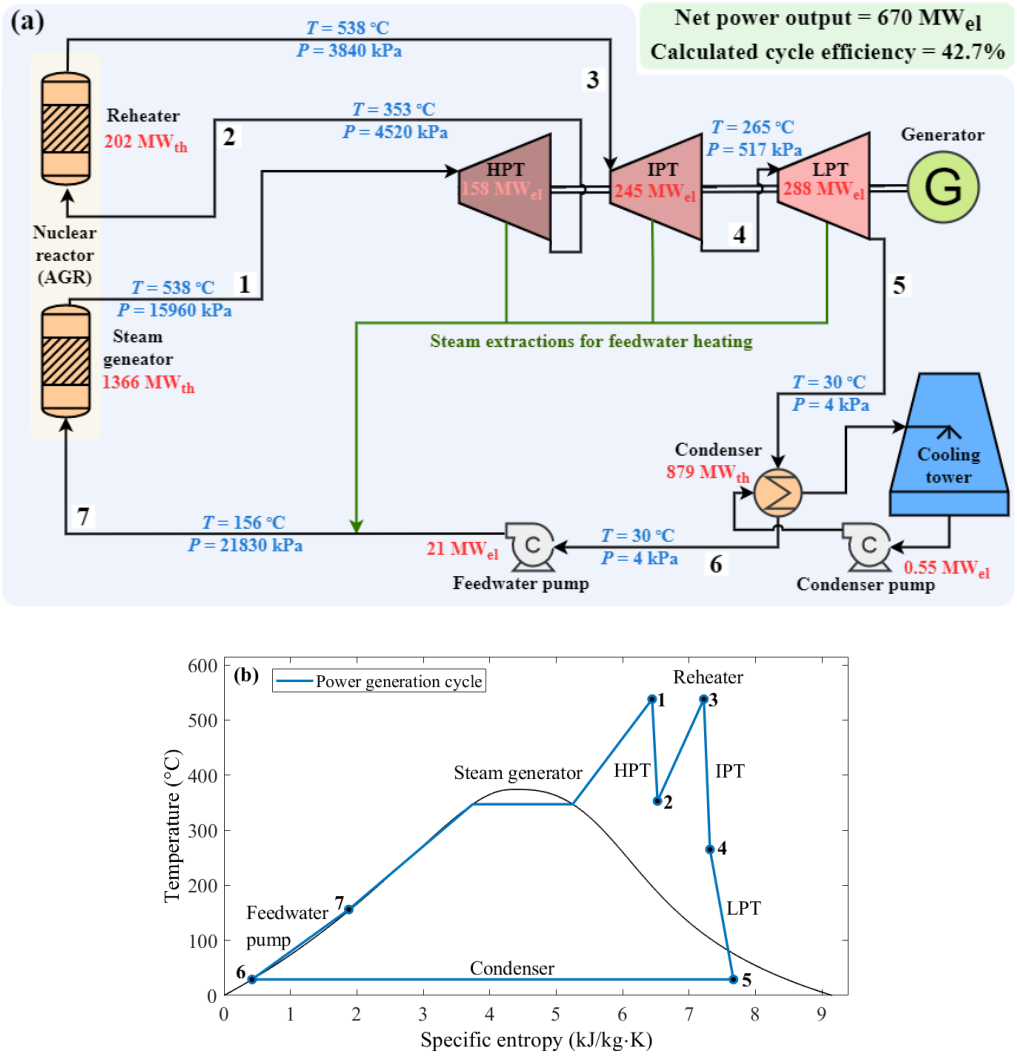

Figure 5.1. (a) Layout of the nuclear power plant considered as a case study in this work, and (b) the corresponding Rankine cycle on a thermodynamic *T*–*s* diagram. For simplicity, multiple bleed points from the turbines for regenerative feed heating are denoted in this figure by a single line connecting the turbines to the output of the feedwater pump.

Referring to Figure 5.1, the working fluid undergoes the following processes [200,201]:

- *Process 1-2*: expansion of the steam through the high-pressure turbine (HPT);

- *Process 2-3*: isobaric heat addition to the steam through the reheater;
- *Process 3-4*: expansion through the intermediate-pressure turbine (IPT);
- *Process 4-5*: expansion through the low-pressure turbine (LPT) to the condenser pressure;
- *Process 5-6*: heat transfer from the steam at constant pressure through the condenser with saturated liquid at State 6;
- *Process 6-7*: pressurisation of the saturated working fluid (liquid) in the feed pump; and
- *Process 7-1*: isobaric heat addition to the working fluid as it flows at constant pressure through the steam generator to complete the cycle.

The thermal input to the power plant is 1570 MW_{th}, the electrical power output is 670 MW_{el} and the electric efficiency at full rated power is 43%. The isentropic efficiencies of the high-, intermediate- and low-pressure turbines are 85%, 92% and 85%, respectively. The electrical power consumption of the feed pump is 21 MW_{el} and its isentropic efficiency is 74%.

The integration of TES system with the aim of modulating the plant's electrical power output, as illustrated in the example in Figure 5.2, is considered in this study. At base conditions, the power output of the plant is constant at the plant's rated power (i.e., at 670 MW_{el}; horizontal line in Figure 5.2). In the proposed EMS, the power plant operator is informed, e.g., one day ahead, of the hourly electricity-exchange prices in the transmission network. An automated EMS then makes decisions for the charging-discharging of the TES stores by solving the unit commitment problem.

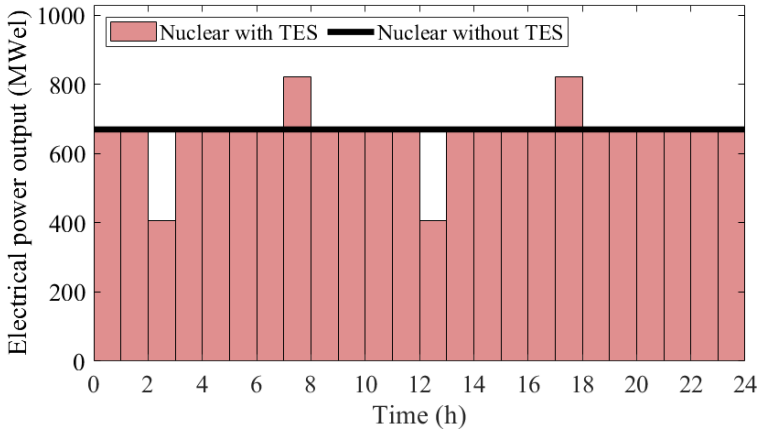

Figure 5.2. Baseline net electrical energy production from the EdF nuclear power plant (670 MW_{el}) and electrical energy production after integration of the TES system. Note derating of power plant and peak capacity exceeding the baseline value due to the contribution of the power generated by the secondary bottoming cycles as part of the TES system in addition to the main power plant.

As an example, Figure 5.2 illustrates a scenario in which the thermal tanks are charged twice per day, at 3 am and 1 pm (signified by dips in the shaded area). The tanks are coupled to and provide thermal energy to secondary ORC power plants, and such plants are shown here indicatively as producing approximately 130 MW_{el} of electrical power during peak demand, which is lower than the stored heat due to the ORC heat-to-electricity conversion losses. The TES tanks are discharged at 8 am and 18 pm (peaks in the shaded area). Such a scenario with flexible operation of power plants, in response to the hourly electricity prices, can play a crucial role in the accelerated penetration of renewable energy sources into the grid. In particular, these TES-ORC systems can be considered autonomous units which could be connected to a virtual power plant providing flexible generation or participating to ancillary services markets.

5.3. Advanced gas-cooled reactors with thermal energy storage

The charging characteristics of thermal energy stores depend strongly on the materials and on the temperature at which steam is extracted from the nuclear power plant. Following consultation with EdF, three technical possible scenarios of steam extraction from the power generation cycle can be considered, which are: (i) before the reheater at 353 °C and 4.52 MPa; and/or (ii) before the LPT at 265 °C and 517 kPa.

The design of the TES tanks is based on shell-and-tube heat exchangers, with the steam condensing as it flows through the tubes and suitable PCMs used in the shells. In both of the above cases, the steam comes into contact with the inner surfaces of the tubes, whose temperatures are below its condensation temperature. Therefore, the design of the TES tanks becomes essentially the design of steam condensers. Several methodologies have been proposed in the literature for designing such condensers [202]. In this study, it was assumed that the conditions (i.e., mass flowrate, diameter) are such that downwards annular flow is established in the tubes [203–205]. This flow regime permits complete wetting of a tube's inner surfaces, such that the steam does not condensate directly on the solid wall but over the surface (interface) of a liquid film [205].

5.3.1. TES integration – Charging with steam extraction before reheater

In this scheme, illustrated in Figure 5.3, the steam undergoes the following processes:

- *Process 2-a*: diversion of part of the working fluid (superheated steam) flow upstream of the reheater followed by isobaric heat rejection and condensation of the steam flow while charging a first PCM thermal-tank (Thermal Tank 1).
- *Process a-b*: isobaric heat rejection of the working fluid (water) while charging a second PCM thermal-tank (Thermal Tank 2).
- *Process b-7*: pressurisation of the subcooled working fluid (water) in a feed pump and return of the diverted flow to the main plant steam generator.

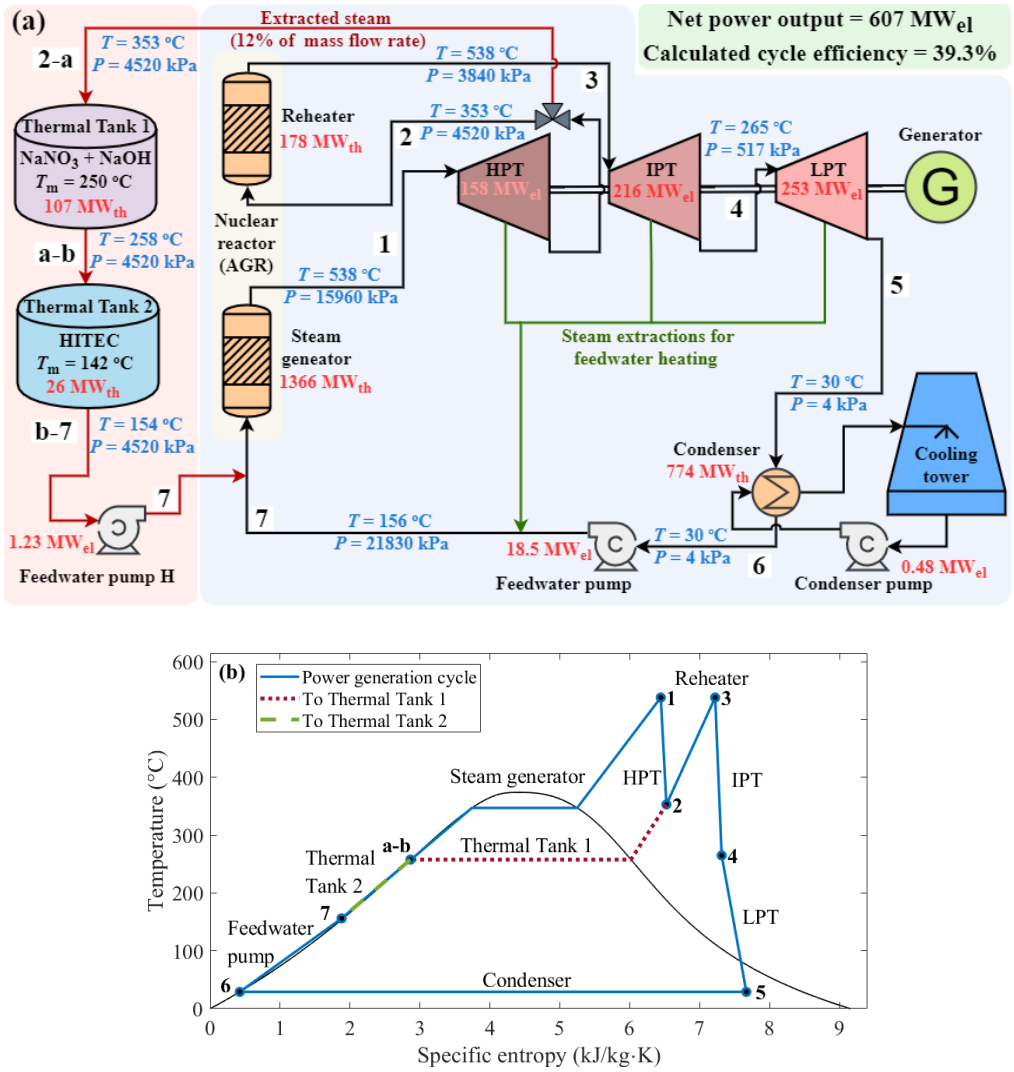

Figure 5.3. (a) Layout of the nuclear power plant integrated with two PCM-based TES tanks that are charged with steam extracted before the reheater, and (b) the corresponding Rankine cycle on a thermodynamic *T*–*s* diagram. For simplicity, multiple bleed points from the turbines for regenerative feed heating are denoted in this figure by a single line connecting the turbines to the output of the feedwater pump.

As a guideline for this particular power plant, EdF had provided with an allowable steam-extraction rate of up to 54 kg/s for diversion from the reheater to Thermal Tank 1 (and also Thermal Tank 2, which is in series with the first tank; see Figure 5.3). This represents 12% of the total steam passing to the reheater under normal conditions. As a result, thermal energy can be stored in Thermal Tank 1 at a maximum heat transfer rate of 107 MW_{th} and in Thermal Tank 2 at a rate of 26 MW_{th} during charging.

Superheated steam at 353 °C (and 4.52 MPa) is extracted before the reheater and condensed isobarically to a stream of saturated liquid water at 258 °C (4.52 MPa). The storage medium in this tank is a PCM mixture of sodium nitrate and sodium hydroxide (86 wt.% $NaNO_3$ + 14 wt.% NaOH) with a melting point of 250 °C [206], which is just below the minimum temperature of the steam in the tank. It is assumed that pure steam enters the pipes of Thermal Tank 1 at a relatively high velocity and that a uniformly thin condensate film forms around the pipe surface. At the output of the tank the steam is separated from the water in a steam drum and recirculated through the condenser [207]. Of great importance in the implementation of such scheme is the space (i.e., volume) required for the installation of the storage tanks that form the core part of this TES system. The procedure used for the design of Thermal Tank 1 is detailed in Appendix A.1 and is based on the methodology described in Ref. [205]. A summary of results relating to the sizing of this heat-exchanger/tank is provided in Table 5.1.

Downstream, and in series with Thermal Tank 1, heat transfer also occurs to Thermal Tank 2 where the condensed, high-pressure (initially saturated) water-stream cools further, again isobarically as it charges this second tank. The inlet temperature of this tank is 258 °C (at 4.52 MPa) and the outlet temperature is 154 °C (at 4.52 MPa). This tank employs a salt mixture referred to as HITEC (composition: 7 wt.% $NaNO_3$ + 53 wt.% KNO_3 + 40 wt.% $NaNO_2$) with a melting point of 142 °C [208,209], which is (as in Thermal Tank 1) just below the minimum temperature in this tank. The approach used for the design of Thermal Tank 2 is based on the single-phase Gnielinski correlation for condensed water flows, assuming a condensing tube surface temperature [210], as summarised in Appendix A.2. Corresponding results are presented in Table 5.1.

Finally, after the two TES tanks, the subcooled liquid (water) is compressed in a feed pump and returned to the steam generator/reactor. The electrical power consumption of the additional feed pump is estimated at 1.23 MW_{el}, by using an isentropic efficiency value of 80% for this component.

The partial diversion of the steam flow to the reheater during the charging of the two cascaded thermal tanks leads to a drop in the thermal input of the power plant from 1570 MW_{th} to 1540 MW_{th}, and the electrical power output of the power plant is derated by 9.4% (from 670 MW_{el} to 607 MW_{el}) and the corresponding thermal efficiency of the plant decreases from 43% to 39%.

5.3.2. TES integration – Charging with steam extraction before LPT

Figure 5.4 depicts the integration of PCM-based TES in an arrangement whereby steam is extracted before the LPT along with its associated *T–s* diagram. In this scheme, the working fluid (steam) undergoes the following processes:

- *Process 4-c*: diversion of part of the working fluid (superheated steam) flow upstream of the LPT followed by isobaric heat rejection and condensation of the steam flow while charging a third PCM thermal-tank (Thermal Tank 3).
- *Process c-7*: pressurisation of the saturated working fluid (water) in a feed pump and return of the diverted flow to the steam generator.

Superheated steam at 265 °C (and 517 kPa) is extracted after the intermediate-pressure turbine and before the LPT, and is condensed isobarically in horizontal tubes in Thermal Tank 3 to a stream of saturated liquid water at 153 °C (and 517 kPa). HITEC is again selected as the storage material for Thermal Tank 3, with a melting temperature of 142 °C. The methodology outlined in Appendix A.1 in relation to the design and sizing of Thermal Tank 1 (see Section 5.3.1) is also adopted for the design of Thermal Tank 3 to know the space requirements for the installation of Thermal Tank 3 as part of this TES scheme. The results are summarised in Table 5.1.

For the case study considered in this work, EdF has provided with a maximum allowable steam extraction rate of 383 kg/s for diversion from (i.e., before) the LPT to Thermal Tank 3, which represents 80% of the total steam flow to the turbine under normal conditions. The corresponding heat transfer rate during charging of the tank is 899 MW_{th}. Furthermore, during the charging of Thermal Tank 3, the thermal input to the power plant is unchanged from the nominal value of 1570 MW_{th}, and its electrical power output is derated by 34% to 443 MW_{el} as its thermal efficiency reduces to 28%. The electrical power consumption of the pump is 13.6 MW_{el}, again based on an isentropic efficiency of 80% as in the scheme in Section 5.3.1.

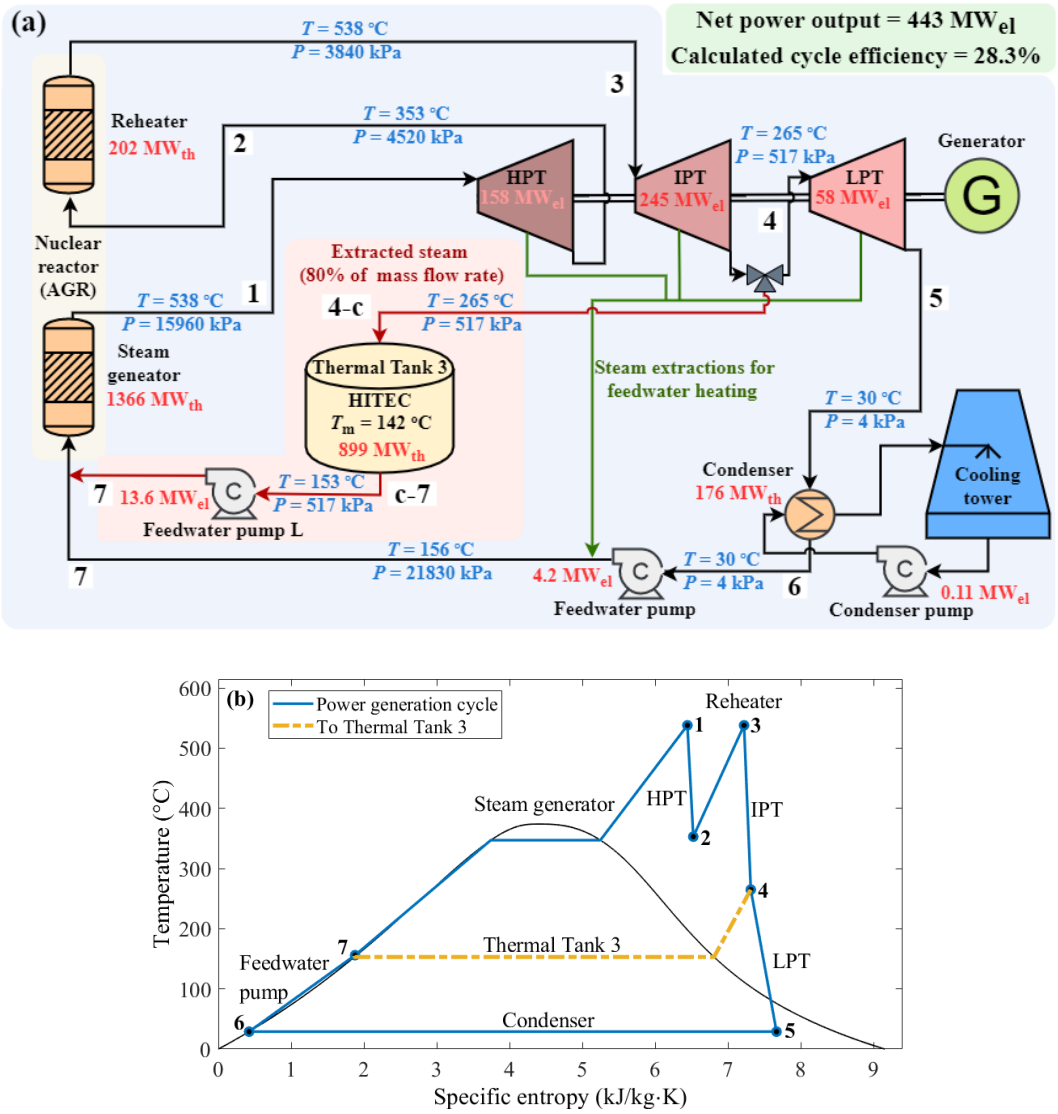

Figure 5.4. (a) Layout of the nuclear power plant integrated with one PCM-based TES tank that is charged with steam extracted before the LPT, and (b) the corresponding Rankine cycle on a thermodynamic *T*–*s* diagram. For simplicity, multiple bleed points from the turbines for regenerative feed heating are denoted in this figure by a single line connecting the turbines to the output of the feedwater pump.

5.3.3. TES integration – Charging with steam extraction before reheater and LPT

In this scheme, the two combined TES systems are considered; steam is extracted before the reheater (as in Section 5.3.1) and before the LPT (as in Section 5.3.2). Due to the steam extraction before the reheater, the minimum allowable steam flowrate through the LPT, which must still be 80% of the remaining steam after the reheater, is now reduced to 337 kg/s, and the heat transfer rate to Thermal Tank 3 is now reduced to 792 MW_{th}. Figure 5.5 shows the combined TES system

and its *T*–*s* diagram. Based on the sizing criteria described in Sections 5.3.1 and 5.3.2 and detailed in Appendix A, the technical details of the three thermal tanks are summarised in Table 5.1.

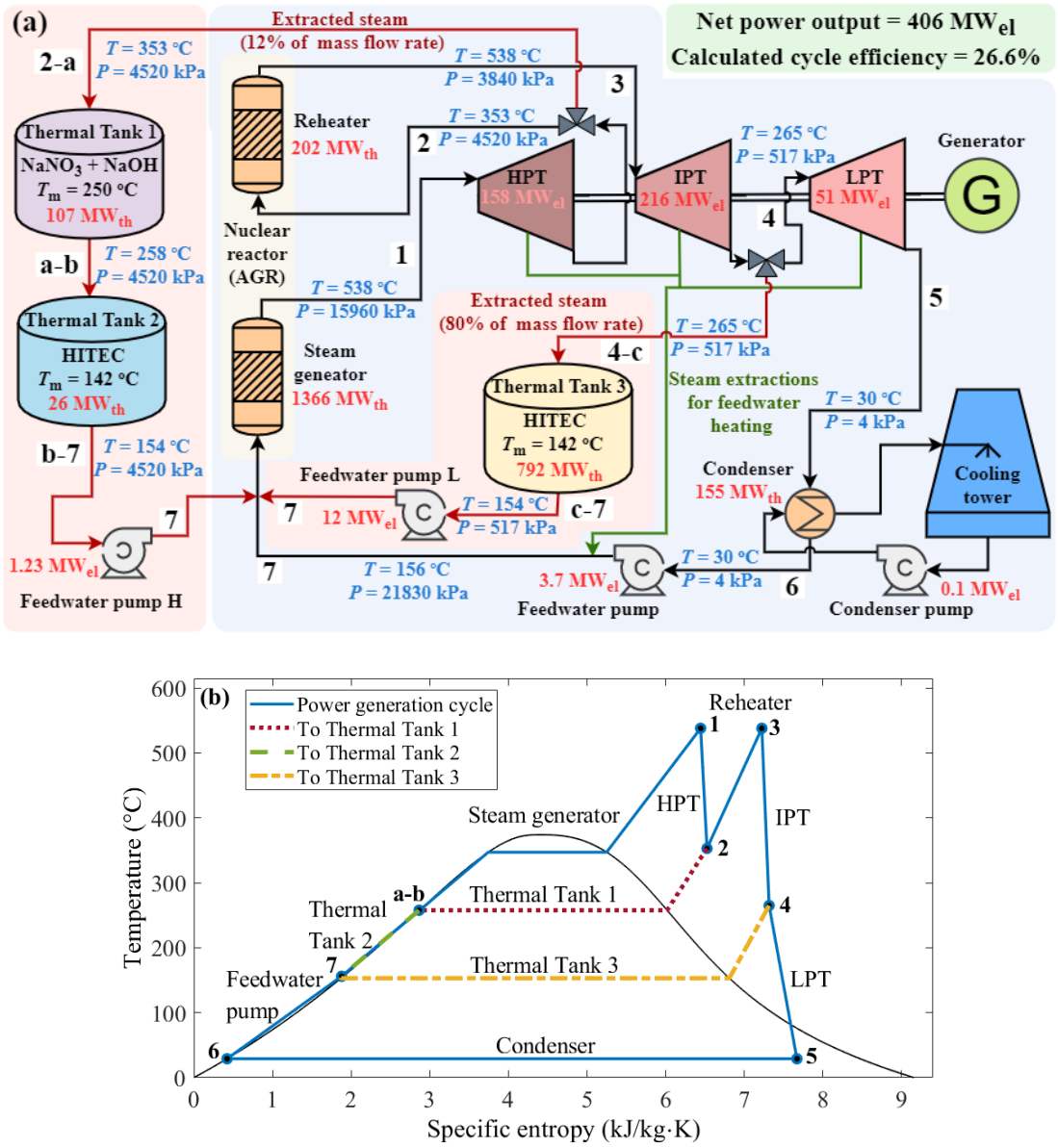

Figure 5.5. (a) Layout of the studied nuclear power plant integrated with three PCM-based TES tanks that are charged with steam extracted before the reheater and before the LPT, and (b) the corresponding Rankine cycle on a thermodynamic *T*–*s* diagram. The dashed lines in the *T*–*s* diagram represent the thermodynamic process of depositing heat into the TES thermal tanks. For simplicity, as in the previous Figure 5.3 and Figure 5.4, multiple bleed points from the turbines for regenerative feed heating are denoted by a single line connecting the turbines to the output of the feed pump.

Table 5.1. Summary of thermal tank designs: dimensions, material properties and other relevant input parameters. Heat storage capacity is referred to thermal storage charging time of 1 h [206,208,209,211].

Thermal tank number (orientation)	**Thermal Tank 1 (horizontal)**	**Thermal Tank 2 (vertical)**	**Thermal Tank 3 (horizontal)**
Phase-change material	$NaNO_3$ + NaOH	$NaNO_3 + KNO_3 + NaNO_2$ (HITEC)	
Melting temperature (°C)	250	142	
Latent heat of fusion (kJ/kg)	160	81.5	
Density (kg/m^3)	2240, 1980*	$\rho = -0.733\theta + 2080^{\dagger}$	
Specific heat capacity (kJ/kg k)	1.19, 1.86*	$c_p = 1.56 - (\theta/1000)^{\dagger}$	
Thermal conductivity (W/m k)	0.66, 0.60*	$k = (2\times10^{-6})\,\theta^2 - (4\times10^{-4})\,\theta + 0.558^{\dagger}$	
Total steam mass flowrate (kg/s)	54	54	337
Heat transfer rate (MW_{th})	107	26	899
Heat storage capacity (GJ)	385	92	3240
Storage density (MJ/m^3)	453	165	165
Volume (m^3)	850	557	19600
Sensible/total heat ratio (%)	20.8	100	10.3
Length (m)	120	–	245
Width (m)	3	–	7
Height (m)	4	17	17
Diameter (m)	–	6.5	–

** First value is for the solid and the second for the liquid phase. $^{\dagger}\theta$ is the PCM bulk temperature in °C.*

5.3.4. TES integration – Charging, discharging and implications for cascaded tank design

Generally, the overall exergy efficiency associated with the charging and discharging of TES tanks is lower when exploiting latent-heat (PCM) storage compared to sensible-heat storage and the heat-source temperature is variable (e.g., when storing the sensible enthalpy of a hot fluid stream in the absence of phase change) [204,205]. However, the generation-integrated energy storage solutions proposed here consider a heat-source temperature that is, to a large extent, constant during the storage-tank charging phase, and furthermore, the stored thermal energy is used later, i.e., during discharge, to drive secondary power plants (ORC systems) by boiling an organic working fluid, again at constant temperature. This makes latent (PCM-based) TES an interesting alternative with trade-offs necessary for achieving the maximum "round-trip" efficiency of the overall system. Furthermore, beyond efficiency considerations, it can be argued that affordability

is an even more desirable performance indicator, e.g., with larger temperature differences between the heat source and the material in the thermal store (up to a point) leading to smaller heat transfer areas (i.e., sizes) and costs, even though the thermodynamic performance is lower.

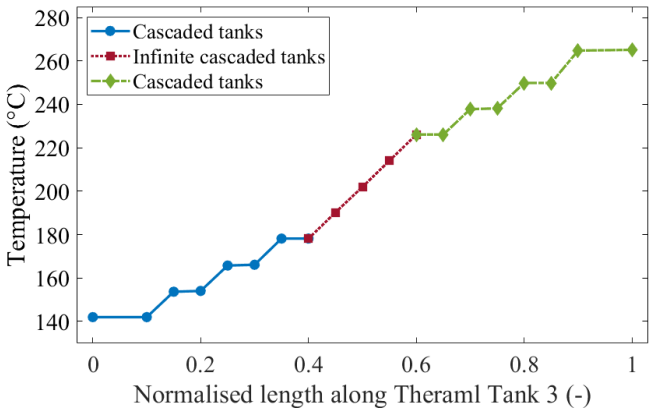

Figure 5.6. Series of (theoretical) varying PCM thermal storage temperatures during charging when a series of cascaded thermal tanks is used in place of the single-PCM (HITEC) Thermal Tank 3. Note that the finite number of stores shown here is for the purposes of illustration.

The appropriateness of using a single PCM-based (latent) thermal store from the point of view of the exergy efficiency of the charging and discharging processes is clear for isothermal heat sources and sinks. The presence of temperature variations can be addressed by increasing the number and respective phase-change temperatures of the thermal storage tanks, in so-called 'cascaded' tanks, which allows one to control the exergy losses in the charging/discharging processes. In the theoretical limit of an infinite number of ideal (zero temperature-difference between the tanks and heat source) cascaded infinitesimal thermal tanks, each featuring a different PCM with a suitable phase-change temperature, this allows an exergetically optimal latent TES solution similar to a perfectly matched sensible thermal-energy store. In this case, the melting points of the PCMs must be chosen to match the temperature variation of the heat transfer fluid (heat source). Figure 5.6 illustrates this concept of cascaded TES tanks. This theoretical case, however, is not a practically feasible or economically viable solution, although it is of interest in setting an upper limit to overall thermodynamic performance. In this work, the case of TES is considered when using a single or a cascade of two PCM tanks in series as one solution in dealing with the aforementioned heat-source temperature variations. In future work, additional cases might be cosnidered, but the present approach suffices in describing our proposed concept for integrating PCM-based TES tanks into power plants along with secondary power generation at a reasonable cost.

Assuming a negligible temperature difference between the heat source and the PCM in a TES tank, the maximum useful stored power $\dot{W}$ during the charging of this tank is the rate change of exergy of the heat-source stream, which can be isothermal or experience temperature variations:

$$\dot{W} = \Delta\dot{H} - T_{\mathrm{d}}\,\Delta\dot{S} = \begin{cases} \dot{Q} - \dot{m}\,T_{\mathrm{d}}\,\Delta s & \text{for isothermal source} \\ \dot{Q} - \dot{m}\,c_{\mathrm{p}}\,T_{\mathrm{a}}\,\ln\left(\dfrac{T_{\mathrm{in}}}{T_{\mathrm{out}}}\right) & \text{for temperature-varying source} \end{cases} \quad (5.1)$$

where $\dot{H}$ and $\dot{S}$ are the enthalpy and entropy of both the heat-source stream and PCM in the tank, $\dot{m}$ and c_{p} are the heat-source stream mass flowrate and specific heat capacity, T_{in} and T_{out} are the inlet and exit temperatures of the stream to/from the tank when its temperature is varying, and $T_{\mathrm{d}} = T_{\mathrm{a}}$ is the dead-state temperature that is taken here to be the ambient temperature (T_{a} = 25 °C).

5.3.5. TES integration – Discharging with secondary power plants

The stored heat is discharged to generate electrical power using secondary power plants, specifically two ORC engines at different temperature levels depending on the temperature of the PCM storage tanks. The main reason of selecting regenerative ORC systems in this study is their capability to operate at low temperature range (less than 250 °C) with higher heat-to-electricity conversion efficiency compared to steam cycles [212].

Figure 5.7 and Figure 5.8 show the schematics of the proposed systems ORC-1 and ORC-2, respectively. System ORC-1 is coupled to Thermal Tank 1 and Thermal Tank 2, while system ORC-2 is coupled to Thermal Tank 3. Both ORC systems contain the following:

- two PCM tanks for heat addition (i.e., Thermal Tank 1 and Thermal Tank 2) for system ORC-1 and one PCM tank (Thermal Tank 3) for system ORC-2;
- an expander (i.e., turbine) with one side extraction for feed heating;
- a water-cooled condenser with a cold stream temperature of 25 °C;
- two pumps (condensate and feed pump); and,
- an internal heat exchanger to preheat the organic working fluid before evaporation.

In system ORC-1, the organic working fluid is evaporated by a constant temperature heat addition (T = 142 °C) from Thermal Tank 1 and then superheated, also at a constant temperature (T = 250 °C) but from Thermal Tank 2. In system ORC-2, the selected organic working fluid is evaporated and superheated at constant temperature (T = 142 °C) from Thermal Tank 3.

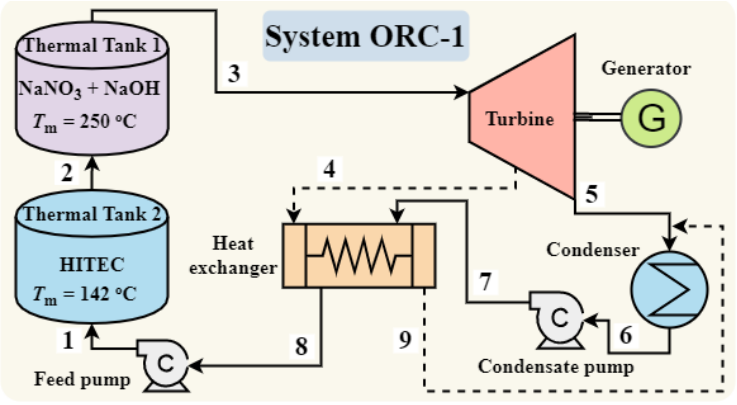

Figure 5.7. Schematic of regenerative system ORC-1 operated by discharging stored heat from Thermal Tank 1 and Thermal Tank 2.

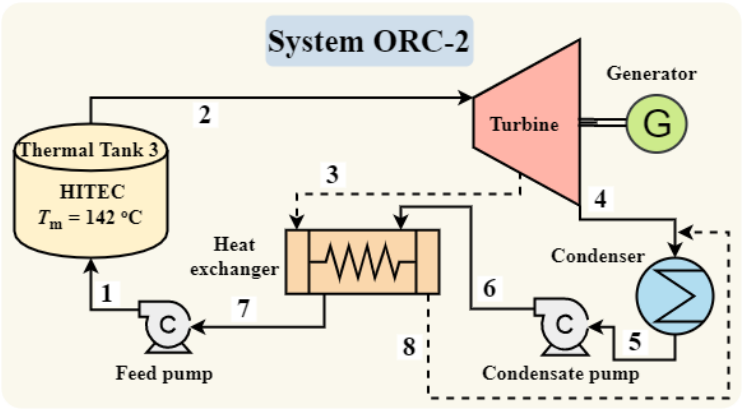

Figure 5.8. Schematic of regenerative system ORC-2 operated by discharging stored heat from Thermal Tank 3.

The thermodynamic parameters of both ORC systems were selected to maximise the heat-to-electricity efficiency of the ORC, giving maximum electrical power output for a fixed amount of heat input. The formulated ORC efficiency optimisation function can be expressed as:

$$\max_{T_{FP}, \dot{m}_{ORC}, \dot{m}_{SE}, P_{evap}, P_{SE}, P_{CP}} \{\eta_{ORC}\} \tag{5.2}$$

where η_{ORC} is the ORC heat-to-electricity efficiency, T_{FP} the feed pump outlet temperature, $\dot{m}_{ORC}$ the cycle mass flowrate, $\dot{m}_{SE}$ the turbine side extraction mass flowrate, P_{evap} the cycle evaporation pressure, P_{SE} the turbine side extraction pressure, and P_{CP} the condensate pump outlet pressure.

The rate of heat addition in all thermal tanks was calculated using:

$$\dot{Q}_{TT} = \eta_{TT}\, \dot{m}_{ORC}\, (h_{out} - h_{in}) \tag{5.3}$$

where $\dot{Q}_{\mathrm{TT}}$ is the rate of added heat from a specified thermal tank, η_{TT} the thermal tank heat-to-heat efficiency, h the enthalpy of the working fluid, and subscripts 'in' and 'out' indicate the conditions at inlet and outlet of the thermal tanks.

The generated power by the turbines, needed power by the pumps and ORC plant's net generated power were calculated based on equations listed in Section 3.4.1. The ORC thermal efficiency in Equation (5.2) was calculated by:

$$\eta_{\mathrm{ORC}} = \frac{\dot{W}_{\mathrm{net}}}{\dot{Q}_{\mathrm{TES}}} \tag{5.4}$$

where $\dot{Q}_{\mathrm{TES}}$ the total heat rate input from thermal tanks.

The optimisation function was solved with the following set of non-linear constraints:

$$P_{\mathrm{cond}} \geq 101.33 \text{ kPa} \tag{5.5}$$

$$T_{\mathrm{cond}} \geq 25 \text{ °C} \tag{5.6}$$

$$P_{\mathrm{evap}} \leq 0.95 P_{\mathrm{crit}} \tag{5.7}$$

$$x_{\mathrm{CP}}^{\mathrm{in}}, x_{\mathrm{FP}}^{\mathrm{in}} \leq 0 \tag{5.8}$$

$$\Delta T_{\mathrm{pp,IHX}}^{\mathrm{in}}, \Delta T_{\mathrm{pp,IHX}}^{\mathrm{out}} \geq 10 \text{ °C} \tag{5.9}$$

$$T_{\mathrm{TT-1}} \leq 142 \text{ °C} \tag{5.10}$$

$$T_{\mathrm{TT-2}} \leq 250 \text{ °C} \tag{5.11}$$

$$T_{\mathrm{TT-3}} \leq 142 \text{ °C} \tag{5.12}$$

where P_{cond} and T_{cond} are the condensation pressure and temperature, P_{evap} the evaporation pressure, P_{crit} the critical pressure of the working fluid, $x_{\mathrm{CP}}^{\mathrm{in}}$ and $x_{\mathrm{CP}}^{\mathrm{in}}$ the working fluid quality at condensate pump and feed pump inlet, respectively, $\Delta T_{\mathrm{pp,IHX}}^{\mathrm{in}}$ and $\Delta T_{\mathrm{pp,IHX}}^{\mathrm{out}}$ the inlet and outlet pinch-point temperature difference of the internal heat exchanger, and $T_{\mathrm{TT-1}}, T_{\mathrm{TT-2}}, T_{\mathrm{TT-3}}$ the working fluid temperature at the outlet of Thermal Tank 1, Tank 2, and Tank 3, respectively.

The evaporation pressure upper bound is set at $0.95 P_{\mathrm{crit}}$ to maintain the cycle in the subcritical region, as well as to reduce the capital costs of the ORC since components that withstand higher pressure are more expensive. All optimisation tasks were solved using MATLAB's non-convex interior point algorithm *fmincon* or genetic algorithm function *ga* within a specified set of upper and lower bounds [108].

The selection of the organic working fluid has a crucial impact on the thermal performance of the ORC. There is a wide range of organic fluids that could be selected but not all of them are considered or analysed in this study. For system ORC-1, the heat source temperature is higher (i.e., up to 250 °C). Therefore, different group of organic working fluids, mostly hydrocarbons, that have higher critical temperature and pressure are suggested to maintain the ORC within the subcritical range [213,214]. For system ORC-2, several refrigerants and short-chained alkanes are suggested and listed in Table 5.2. These fluids are commonly used in commercial ORC power plants with similar heat source temperature range (e.g., geothermal power plants) [213]. The thermodynamic, environmental and safety characteristics of the considered working fluids are reported in Table 5.2.

Table 5.2. Summary of the main thermodynamic, environment and safety properties of the selected organic working fluids for systems ORC-1 and ORC-2 [213–218].

ORC system	Working fluid	Critical *T* (°C)	Critical *P* (kPa)	Boiling point (°C)	GWP	ODP	Flammability
ORC-1	Acetone	235	4690	56.1	Low	0	Flammable
	Benzene	289	4890	80.1	Low	0	Flammable
	Cyclohexane	280	4080	80.7	Low	0	Flammable
	R11	198	4410	23.8	1500	0	Non-flammable
	R141b	204	4210	32.1	725	0.12	Non-flammable
	Toluene	319	4130	111	Low	0	Flammable
ORC-2	Isobutane	135	3630	-11.7	Low	0	Flammable
	Isopentane	187	3380	27.8	Low	0	Flammable
	R123	184	3670	27.6	Low	0.06	Non-flammable
	R1233zd	166	3570	18.3	Low	0	Non-flammable
	R245fa	154	3650	15.1	1030	0	Non-flammable

Table 5.3 summarises the main assumptions of the computational model for both ORC systems. The heat capacity of all thermal tanks is based on the maximum charging scenario, as per Figure 5.5. It is assumed that the heat-to-heat efficiency during discharging is 90%.

Figure 5.9 shows the maximum cycle thermal efficiency, in the left *y*-axis, and the optimal evaporation and condensation pressure, in the right *y*-axis, of the candidate working fluids for: a) system ORC-1, and b) system ORC-2. In system ORC-1, the results show that R11 has the highest cycle efficiency (i.e., 21%) at an optimal evaporation pressure of 4.19 MPa. Toluene has the lowest efficiency since its critical temperature is the highest among the other candidates and also

much higher than the temperature of heat addition. In system ORC-2, the optimised cycle efficiency ranges between 14% and 16% depending on the type and the thermodynamic properties of the working fluid. The results show that isopentane not only gives the highest maximum cycle efficiency (i.e., 16%) at the specified constraints, but also the lowest evaporation pressure (1.73 MPa) which minimises the capital cost of the ORC power plants. Therefore, R11 and isopentane are selected as the working fluids for systems ORC-1 and ORC-2, respectively.

Table 5.3. List of main parameters assumed in both ORC system computational models.

Parameter/assumption	Value
Thermal Tank 1 heat capacity (GJ)	385
Thermal Tank 2 heat capacity (GJ)	92
Thermal Tank 3 heat capacity (GJ)	2850
Thermal tanks heat-to-heat efficiency (%)	90
Turbine isentropic efficiency (%)	80
Turbine mechanical efficiency (%)	96
Pump isentropic efficiency (%)	75
Pump mechanical efficiency (%)	96
Generator electric efficiency (%)	95
Pressure loss in each thermal tank and in the heat exchanger (kPa)	100

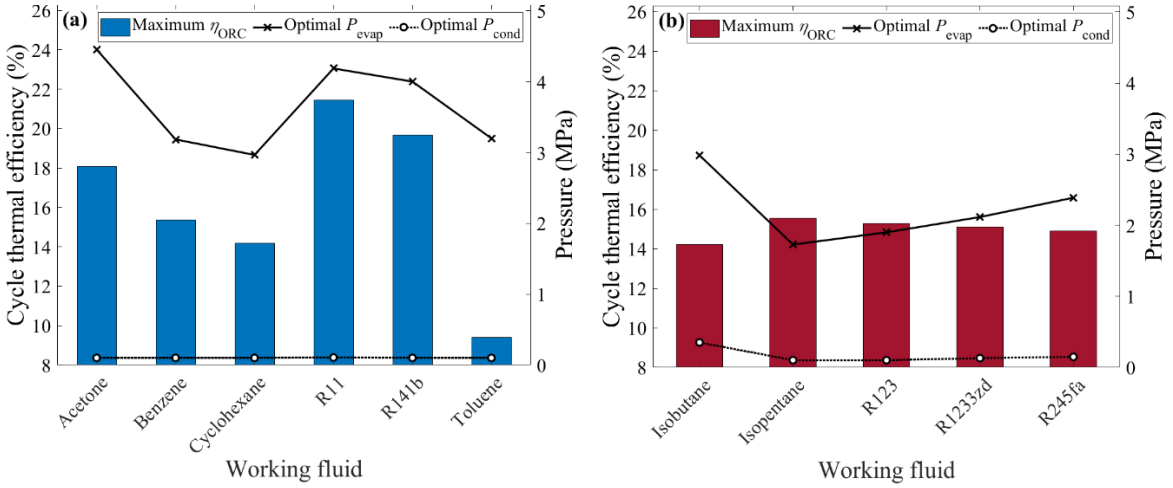

Figure 5.9. Maximum cycle thermal efficiency, on the left *y*-axes, along with corresponding optimal evaporation and condensation pressure, on the right *y*-axes, of the compared organic working fluids for system: (a) ORC-1, and (b) ORC-2.

To obtain the optimal operating conditions of both ORC systems (i.e., mass flowrate, temperature, etc.) for each streamline in the power cycle, the input heat rates of all thermal tanks have to be

determined, which depend on the total discharging duration of heat. For example, if the discharging duration for fixed heat capacity thermal tanks is doubled (from 1 h to 2 h), the discharging heat rate is now halved as the same amount of heat is discharged for longer duration, which corresponds to a reduced electric power from the ORC systems. Therefore, different discharging cases based on the discharging duration and heat rate are introduced and listed in Table 5.4.

Table 5.4. List of the proposed discharging cases.

Case	Full discharging duration (h)	Discharging heat rate (MW_{th})		
		Thermal Tank 1	Thermal Tank 2	Thermal Tank 3
A	1	26	107	792
B	2	13	53.5	396
C	4	6.5	26.8	198
D	8	3.3	13.4	99

Table 5.5. Optimal operating conditions for system ORC-1 using R11 as a working fluid.

Case (thermal tank discharging duration)	A (1 h)	B (2 h)	C (4 h)	D (8 h)
Thermal Tank 1 heat rate (MW_{th})	26	13	6.5	3.3
Thermal Tank 2 heat rate (MW_{th})	107	53.5	26.8	13.4
Turbine inlet mass flowrate (kg/s)	570	285	143	71.3
Turbine inlet temperature (°C)	231	231	231	231
Turbine side extraction pressure (kPa)	261	261	261	261
Turbine side extraction mass flowrate (kg/s)	176	87.8	43.9	21.9
Turbine side extraction temperature (°C)	112	112	112	112
Turbine main exhaust pressure (kPa)	106	106	106	106
Turbine main exhaust mass flowrate (kg/s)	395	197	98.6	49.4
Turbine main exhaust temperature (°C)	84.6	84.6	84.6	84.6
Condenser outlet temperature (°C)	25	25	25	25
Condenser outlet pressure (kPa)	106	106	106	106
Condensate pump outlet pressure (kPa)	4100	4100	4100	4100
Feed pump outlet pressure (kPa)	4190	4190	4190	4190
Feed pump outlet temperature (°C)	102	102	102	102
Net electric power from ORC-1 (MW_{el})	28.4	14.2	7.1	3.6
Gross amount of electricity (MWh)	28.4	28.4	28.4	28.4
Optimised cycle efficiency (%)	21.5	21.5	21.5	21.5
Total nuclear power with system ORC-1 (MW_{el})	698	684	677	674

For each discharging case, the optimal ORC operating parameters that give the maximum thermal efficiency are calculated and reported in Table 5.5 for system ORC-1 and in Table 5.6 for system ORC-2. The main difference between the discharging cases is the ORC mass flowrate as it decreases with the increase of discharging duration, which also affects the ORC installed power. The maximum cumulated power outputs from both the first and the second ORC systems are 152 MW_{el} for Case A, 75.8 MW_{el} for Case B, 37.5 MW_{el} for Case C, and 19 MW_{el} for Case D. Yet, the amount of the total electricity generated for a full discharging phase from the two ORC systems is the same for all cases (152 MWh per full discharge).

Table 5.6. Optimal operating conditions for system ORC-2 using isopentane as a working fluid.

Case (thermal tank discharging duration)	A (1 h)	B (2 h)	C (4 h)	D (8 h)
Thermal Tank 3 heat rate (MW_{th})	792	396	198	99
Turbine inlet mass flowrate (kg/s)	1890	943	471	236
Turbine inlet temperature (°C)	142	142	142	142
Turbine side extraction pressure (kPa)	243	243	243	243
Turbine side extraction mass flowrate (kg/s)	582	291	146	72.7
Turbine side extraction temperature (°C)	93.2	93.2	93.2	93.2
Turbine main exhaust pressure (kPa)	101	101	101	101
Turbine main exhaust mass flowrate (kg/s)	1300	651	326	163
Turbine main exhaust temperature (°C)	76.7	76.7	76.7	76.7
Condenser outlet temperature (°C)	27.8	27.8	27.8	27.8
Condenser outlet pressure (kPa)	101	101	101	101
Condensate pump outlet pressure (kPa)	613	613	678	680
Feed pump outlet pressure (kPa)	1730	1730	1730	1730
Feed pump outlet temperature (°C)	84.1	84.1	84.1	84.1
Net electric power from ORC-2 (MW_{el})	123	61.6	30.8	15.4
Gross amount of electricity (MWh)	123	123	123	123
Optimised cycle efficiency (%)	15.6	15.6	15.6	15.6
Total power from nuclear and ORC systems (MW_{el})	822	746	708	689

Figure 5.10 illustrates the charging and the discharging behaviour of the EMS for the proposed discharging cases for an arbitrary day in the UK, including all thermal tanks and the two ORC generators. The left *y*-axes indicate the power output level, and the right *y*-axes report the wholesale electricity prices during the same hour. The reported electricity price profile in Figure 5.10 are actual prices of a randomly selected day in the UK in 2019 [219]. In all cases, the 1-h charging process is set to take place during the minimum price, which is at 4 am. Thus, the nuclear power

unit generates the minimum rated power (406 MW_{el}) instead of nominal power (670 MW_{el}). The stored heat is then discharged during the maximum electricity prices (i.e., at 8 pm for Case A, from 7-8 pm for Case B, from 6-9 pm for Case C, and from 7-10 am and from 6-9 pm for Case D).

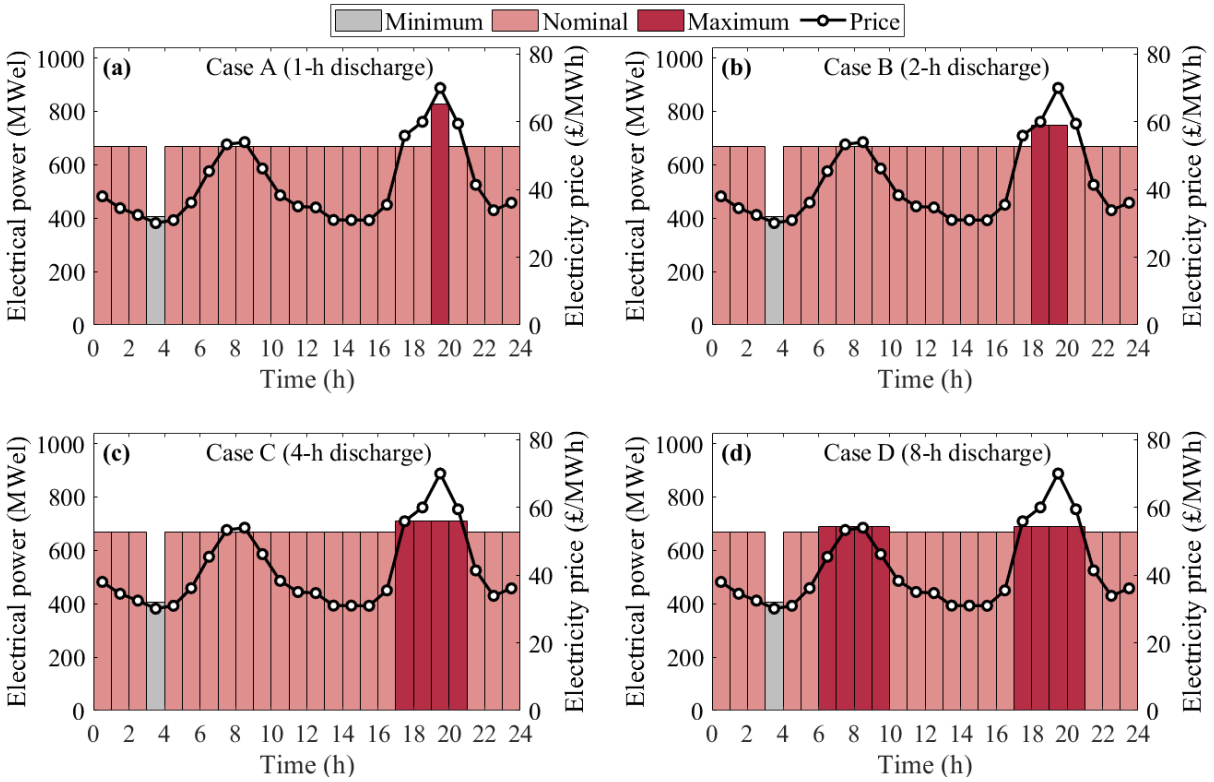

Figure 5.10. EMS electrical power output, on left *y*-axes, and wholesale electricity prices, on the right *y*-axes, for all discharging cases (A, B, C, and D). The minimum output power is when the EMS storing heat and the maximum is when the stored heat is discharged through the proposed ORC systems. The electricity price is the actual prices of a randomly selected day in the UK in 2019.

The EMS behaviour for a two full charging/discharging cycles per day is presented in Figure 5.11. The second 1-h charging phase is assumed to take place after a full discharge of the stored heat. For example, in Case A, the charging process is performed twice during the day at 4 am and 4 pm, where the two minimum prices are observed. However, the second charge phase does not start until all thermal tanks are fully discharged which occurs at 9 am where the electricity price is high. The same concept is applied for all the other cases.

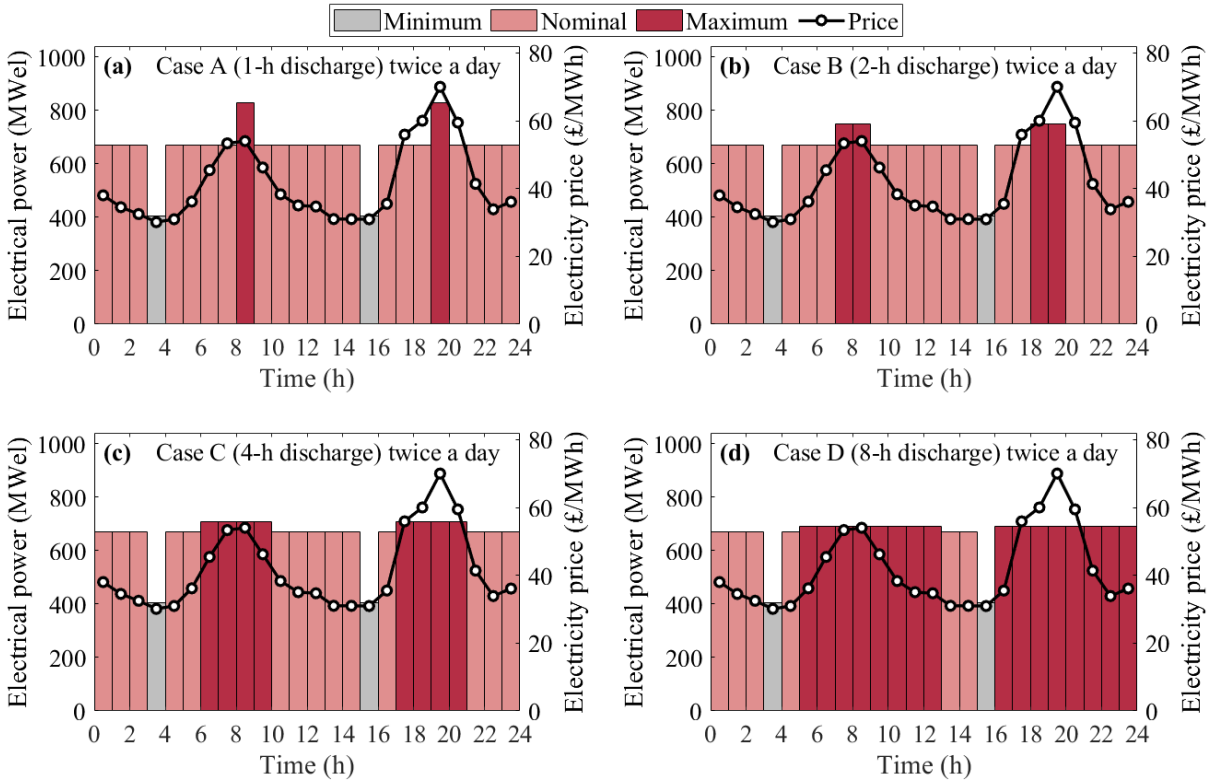

Figure 5.11. EMS electrical power output, in the left *y*-axes, and the wholesale electricity prices, in the right *y*-axes, for all discharging cases (A, B, C, and D) for two charging/discharging cycles per day. The minimum output power is when the EMS storing heat and the maximum is when the stored heat is discharged through the proposed ORC systems. The electricity price is the actual prices of a randomly selected day in the UK in 2019.

5.3.6. Transient operation

Beyond the steady-state design of the thermal tanks considered above, it is necessary to account for the transient thermal performance of these tanks during charging and discharging in order to ascertain whether these processes are fast enough for the purposes of our EMS application. For the PCM in each thermal tank, energy balance equation (Equation (5.13)) is considered in which the change in the internal energy of the PCM is equal to the net amount of energy transferred across the PCM control-volume boundary due to heat transfer over some time interval. This energy exchange can be both latent or sensible. Neglecting the tube walls in the thermal tanks, the temperature of the PCM in a thermal tank is obtained from the following first-order equation:

$$\dot{Q}_{\mathrm{TT}} = \dot{m}\, c_{\mathrm{p}}(T_{\mathrm{in}} - T_{\mathrm{out}}) = \bar{\alpha}\, A_{\mathrm{s}}\, \Delta T_{\mathrm{LM}} = \begin{cases} m_{\mathrm{PCM}}\, c_{\mathrm{PCM}}\, \dfrac{\mathrm{d}T_{\mathrm{PCM}}}{\mathrm{d}t} & \text{for sensible TES} \\ \Delta h_{\mathrm{PCM}}\, \dfrac{\mathrm{d}m_{\mathrm{PCM}}}{\mathrm{d}t} & \text{for latent TES} \end{cases} \tag{5.13}$$

where $\dot{m}$ is the mass flowrate of steam in the tubes, c_{p} the specific heat capacity of the steam, T_{in} and T_{out} the inlet and outlet steam temperatures, $\bar{\alpha}$ the average convection heat transfer coefficient, A_{s} the total tube surface area, ΔT_{LM} the log-mean temperature difference between the steam and the PCM. For sensible TES charging and discharging, m_{PCM} the mass of the PCM in the tank, c_{PCM} the specific heat capacity of the (solid or liquid) PCM, and $\frac{\mathrm{d}T_{\mathrm{PCM}}}{\mathrm{d}t}$ the rate of change of the PCM bulk temperature in the tank. During latent TES charging and discharging, thermal energy is used to induce phase change without a temperature variation for pure substances, and the final term in Equation (5.13) becomes $\Delta h_{\mathrm{PCM}} \frac{\mathrm{d}m_{\mathrm{PCM}}}{\mathrm{d}t}$ where Δh_{PCM} is the PCM specific phase-change enthalpy and $\frac{\mathrm{d}T_{\mathrm{PCM}}}{\mathrm{d}t}$ the rate at which PCM mass changes phase.

Figure 5.12 shows, as an example, the bulk temperature variation of the PCM in Thermal Tank 3 during charging following Equation (5.13). The HITEC is initially in the solid phase at ambient temperature. Steam flows through the tank and the HITEC temperature increases up to its melting point (142 °C) after about 1 h. At this point, isothermal phase change (melting) takes place for about 1 h, after which the PCM becomes a liquid and sensible heat is stored in the tank with a further increase in the liquid PCM temperature.

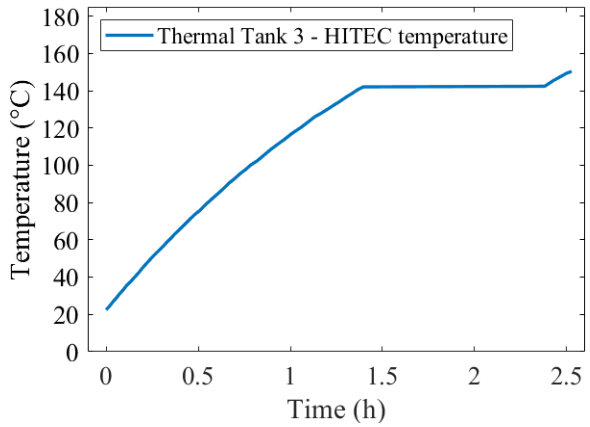

Figure 5.12. PCM (HITEC) temperature in Thermal Tank 3 during charging. In this study, operation with phase change is cosnidered, in the (isothermal) latent heat storage regime.

Similar temporal responses have been obtained for all thermal tanks, which suggests that the tanks are capable of continuously charging and/or discharging over up to 1 h, thereby allowing the EMS concept presented in Figure 5.3, during low and peak demand periods. Therefore, it is only considered in this study the case when using the PCM for latent heat storage, during which time it remains at its phase change temperature. In practice, charging and discharging rates will be different from those evaluated here due to material non-uniformity and unsteady heat transfer effects, however, the rates for charging should remain within 10-20% of these estimates for charging and the double for discharging [210].

5.4. Plant derating during TES charging

Figure 5.13(a) shows the fractional plant derating during TES charging versus the degree of steam extraction when the three TES schemes in Section 5.3 are applied to the EdF nuclear power plant. The fractional derating value is the ratio of the net generator output from the base plant with steam extraction to that without steam extraction, i.e., with a maximum net generator output of 670 MW_{el} from the base power plant. From left-to-right the schemes include: (i) 12% steam extraction before the reheater (for details, see Section 5.3.1); (ii) 80% steam extraction before the LPT (for details, see Section 5.3.2); and (iii) 12% steam extraction before the reheater and 80% extraction of the remaining steam before the LPT (for details, see Section 5.3.3). As a result of these three steam extraction strategies, the electrical power output of the power plant decreases and the amount of stored thermal energy increases, as shown from left to right in Figure 5.13(b).

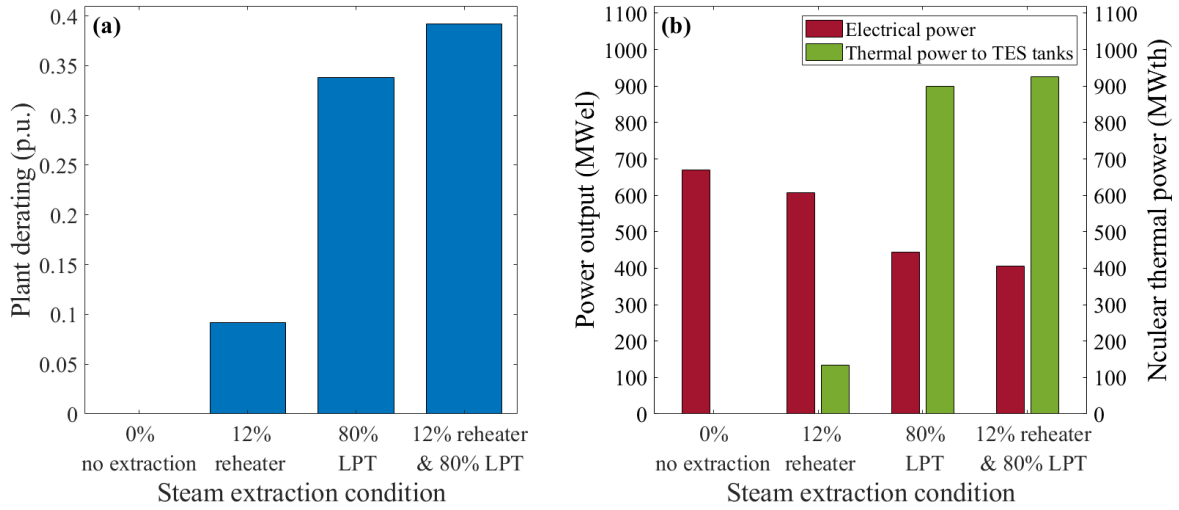

Figure 5.13. (a) Fractional plant derating, and (b) power output of main/base nuclear power plant and stored thermal energy during TES charge, for the three EMS schemes proposed herein.

Figure 5.13 suggests that it is possible to use existing nuclear power plants (Gen. I and II) for flexible generation in load following with a maximum derating of 40%, with minimum loads down to 60% of a plant's rating. The stored thermal energy increases with the amount of steam extraction up to a total of 822 MW_{el} (see Table 5.6), as the net power output reduces by 40%, from 670 MW_{el} to a minimum of 406 MW_{el}. It is interesting to note that the greatest flexibility of the power plant, and therefore the largest potential for load following, is attained for low-temperature TES, when extracting steam before the LPT. Furthermore, Figure 5.14(a) shows the heat input (rate) to the plant and Figure 5.14(b) the plant efficiency during TES charging for the same three steam extraction schemes as in Figure 5.5. The heat input is maximum when steam is not extracted or when it is extracted only before the LPT when heat is stored at the lowest temperature. When steam is extracted before the reheater the total input to the plant drops by 1.5%. As a result of the steam extraction, the thermal efficiency of this particular nuclear plant reduces from 43% (for full-load plant operation) to 26% (for 60% part-load operation).

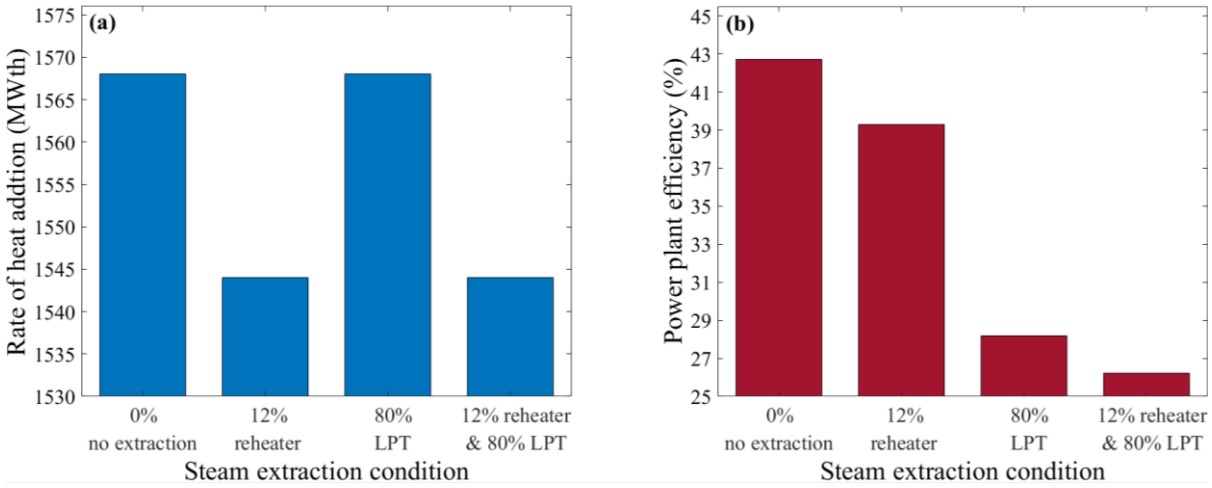

Figure 5.14. (a) Heat input (rate), and (b) efficiency of main/base nuclear power plant during TES charge, corresponding to the same three EMS schemes as in Figure 5.5.

5.5. EMS cost assessment

A simple cost analysis is performed on the proposed EMS (i.e., with three thermal tanks and two ORC plants) to determine at what extent it is an economically viable solution. The cost analysis starts by determining the levelised cost of electricity (LCOE) of the proposed thermal tanks and both ORC systems for each discharging cases (A, B, C, and D of Table 5.4). The LCOE was calculated using the base LCOE expression, Equation (3.120), with the following amendment:

$$LCOE_{\mathrm{EMS}} = \frac{\sum_{t=1}^{n} \frac{C_{\mathrm{c}_1} + C_{\mathrm{O\&M}_t} + C_{\mathrm{Ch}_t}}{(1+r)^t}}{\sum_{t=1}^{n} \frac{DE_t}{(1+r)^t}} \tag{5.14}$$

where C_{c_1} is the capital cost of the thermal tanks and the ORC systems in year 1, $C_{\mathrm{O\&M}}$ is the O&M expenditure in year t, C_{Ch} the charging cost in year t, DE_t the electricity generation from both ORC systems in year t, r the discount rate, and n the life of the system.

The new parameter in the LCOE formula is the charging costs (CH) which accounts for the cost of selling less amount of electricity while charging the thermal tanks. All LCOE calculation parameters and assumptions are presented in Table 5.7. The capital costs of the ORC plants were estimated by taking the average of the investment costs of similar-sized ORC plants from Refs. [213,220,221]. Note that all the costs and prices are presented in GBP (£) since the case study presented in this chapter is based in the UK. The assumed GBP/USD and GBP/EUR exchange rates were 0.80 and 0.85, respectively.

Table 5.7. Cost and LCOE calculation parameters [55,213,220,221].

Cost analysis parameters	**Value**
ORC systems capital costs (£/kW$_{el}$)	1140
TES system capital costs (£/kWh$_{th}$)	25
Operation & maintenance (%)	3% of capital cost
Charging cost per day (£/day)	264 (MWh$_{el}$) × $\overline{EP}_{1,\mathrm{Ch}}$ (£/MWh$_{el}$) for one 1-h charge 528 (MWh$_{el}$) × $\overline{EP}_{2,\mathrm{Ch}}$ (£/MWh$_{el}$) for two 1-h charges
Project lifetime (years)	25
Discount rate (%)	3
Availability factor (%)	90
Projected annual electricity output (GWh$_{el}$)	49.8 for one 1-h charge per day 99.6 for two 1-h charges per day

5.5.1. Electricity prices

In order to evaluate the profitability of the proposed flexible generation system, the wholesale (day-ahead) hourly electricity prices in the UK over the year 2019 were taken as a baseline and a further analysis was performed based on the electricity prices in 2021 (until 15 Nov.) [219]. The calculations were performed assuming that the generated electricity will be entirely sold in the day-ahead or intraday electricity market. However, the electricity generators may consider

the option of selling the generated electricity at different markets such as the balancing market (BM), fast frequency response (FFR), net imbalance volume (NIV) chasing technique, etc., which varies in terms of risk and rewards [222]. Furthermore, it was assumed that the secondary power plants have a rapid ramp rate, meaning that the power plant goes from zero to full rated power or vice versa within a few minutes, so being able to provide the required services to the grid. This means that the ORC plants should operate as a spinning reserve being able to quickly enter into service, incurring in no-load losses that are not explicitly quantified in this study.

Table 5.8 summarises the hourly electricity prices $\overline{EP}$ assumed in the economic analysis, and in particular the prices during charging and discharging periods. The second column of Table 5.8 defines the selection of these prices and the third column summarises the conditions in which these prices were applied in the analysis. As mentioned previously, the prices are yearly averaged and calculated using the minimum or the maximum hourly price during each day:

$$\overline{EP} = \frac{\sum_{i=1}^{365} [\min \text{ or } \max(EP_1, EP_2, \dots, EP_{24})]}{365} \tag{5.15}$$

Table 5.8. Calculated average hourly electricity price for charging and discharging; the average was calculated based on UK electricity market data for years 2019, 2021 and 2022 (until May) [219].

Average hourly price (£/MWh)				Definition and number of hourly prices per day	Charging or discharging duration conditions
Parameter	**2019**	**2021**	**2022**		
$\overline{EP}_{1,\mathrm{Ch}}$	30.2	65.9	126	Minimum price per day (1 h)	One 1-h charge
$\overline{EP}_{2,\mathrm{Ch}}$	30.7	67.2	132	Minimum price per day (2 h)	Two 1-h charges
$\overline{EP}_{1,\mathrm{Dch}}$	63.0	202	271	Maximum price per day (1 h)	One 1-h discharge (Case A)
$\overline{EP}_{2,\mathrm{Dch}}$	60.6	182	262	Maximum price per day (2 h)	One 2-h discharge (Case B) Two 1-h discharges (Case A)
$\overline{EP}_{4,\mathrm{Dch}}$	57.1	159	246	Maximum price per day (4 h)	One 4-h discharge (Case C) Two 2-h discharges (Case B)
$\overline{EP}_{8,\mathrm{Dch}}$	52.8	136	226	Maximum price per day (8 h)	One 8-h discharge (Case D) Two 4-h discharges (Case C)
$\overline{EP}_{16,\mathrm{Dch}}$	47.7	115	203	Maximum price per day (16 h)	Two 8-h discharges (Case D)

5.5.2. Capacity payment

In addition to the revenues from selling electricity in the wholesale electricity market, power generators are entitled to participate in the UK capacity market. The capacity market is

established to ensure security of electricity supply and enhanced capability to match variable demand. This is satisfied by the UK's government providing an incentive (i.e., capacity payment) for power plants that are available to quickly enter into service if needed by the power system during periods of high demand or low unexpected availability of the intermittent renewable sources. The capacity payment encourages new investments in the energy sector as it guarantees a fixed amount of income for generators [223]. In this study, the amount of the capacity payment was assumed as 16.2 £/kW_{el}/year, which is the average of the five years' clearing prices (i.e., from 2015 to 2019) in the four-year ahead delivery capacity auctions [224]. However, energy or electricity storage systems do not get paid the full amount of the clearing price since most of the systems have a limited discharging duration. Therefore, the UK government has provided a derating factor which specifies the payment in percent in the bases of duration, and which penalises plants with a shorter time of operation per day [225]. Table 5.9 summarises the assumed capacity payment for the proposed discharging cases (i.e., A, B, C, and D). The derating factor reported in Table 5.9 was multiplied by the average unitary capacity payment to get the total annual capacity payment for each proposed ORC systems size.

Table 5.9. Assumed capacity payment of all discharging cases [224].

Case (duration)	A (1 h)	B (2 h)	C (4 h)	D (8 h)
Derating factor (%)	36.4	64.4	96.1	96.1
ORC systems power (MW_{el})	152	75.8	37.9	19.0
Annual capacity payment (£k)	896	796	591	296

5.5.3. Economic analysis based on UK wholesale electricity prices in 2019

The economic evaluation was performed by calculating the projected net present value (NPV) of the proposed EMS investment using:

$$NPV_{\mathrm{EMS}} = \sum_{t=1}^{n} \frac{I_t + CP_t}{(1+r)^t} - \sum_{t=1}^{n} \frac{C_{\mathrm{c_1}} + C_{\mathrm{O\&M}_t} + C_{\mathrm{Ch}_t}}{(1+r)^t} \tag{5.16}$$

where I_t is the annual income from selling extra electricity from ORC generators during peak prices, which depends on the number of discharging hours per day, and CP_t the capacity payment.

Figure 5.15 presents the estimated net present value, in the left *y*-axis, alongside with the calculated LCOE, in the right *y*-axis, for the different discharging duration times. It also indicates the average electricity price difference (PD) between charging and discharging modes for the different cases.

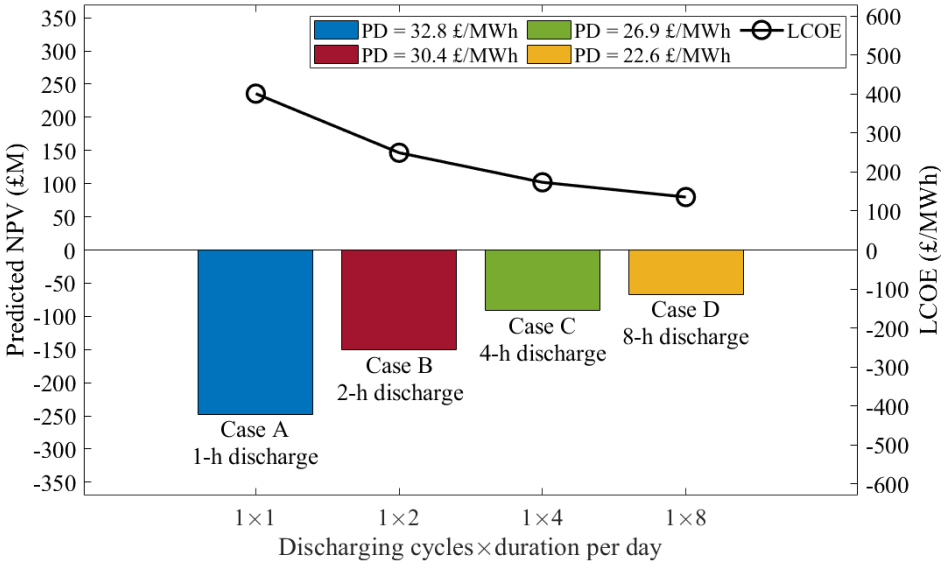

Figure 5.15. Predicted NPV, on the left *y*-axis, and calculated LCOE, on the right *y*-axis, of the proposed EMS with three thermal tanks and two ORC systems for all the four cases of discharging duration (i.e., A, B, C, and D) and one discharge per day. The figure presents results assuming UK wholesale electricity prices in year 2019 and one 1-h charge per day at the minimum electricity price.

Case A has the highest LCOE of 401 £/MWh due to the highest cost of ORC plants (maximum installed size). The LCOE drops to about 136 £/MWh for Case D as a result of the smaller size of the ORC systems, which are designed to generate the same amount of electricity but over longer durations (i.e., 8 h). However, the LCOE is still considered high and not yet comparable to the LCOE of other competitive energy sources, either renewables or fossil fuelled power plants. Moreover, the predicted NPVs of the proposed EMS for all discharging cases are negative due to two main reasons. The first is that the average price difference between off-peak and peak PD is quite low in 2019 UK electricity market. The second reason is the high LCOE which is also influenced by the relatively high average of off-peak electricity price (30.2 £/MWh), i.e., an avoided income when charging the thermal tanks. Therefore, the proposed EMS with one 1-h charge per day is not an economically viable option based on 2019 wholesale electricity prices, even with the proposed smallest size of ORC systems that discharges the same amount of thermal power over 8 h per day.

Results obtained with two charge/discharge cycles per day are presented in Figure 5.16, which shows a 43% relative decrease of the LCOE (i.e., from 401 to 228 £/MWh) in Case A for the option of two cycles a day. This drop is a result of doubling the amount of electricity generated during the assumed investment lifetime. In Case D, the LCOE drops to 95 £/MWh for the same

reasons. However, the NPV is still negative and unprofitable even in for two fully charge/discharge cycles per day. This is due to the lower selling price of electricity when full discharging is performed twice a day for all cases, which is seen in the lower PD reported in Figure 5.16, in comparison to the previous case. The predicted NPV is even more negative for two 8-h discharges (16 h in total) in Case D (-£77.5M) than for a single 8-h discharge (-£66.8M). It is concluded that the EMS profitability greatly depends on the peak and off-peak price difference, which was not sufficiently high in the UK wholesale electricity market in 2019.

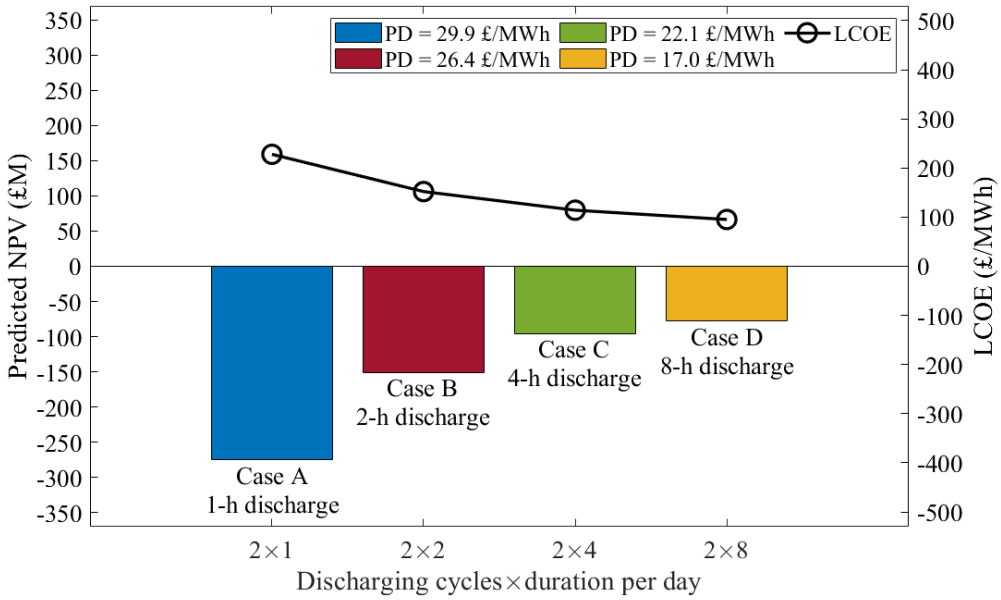

Figure 5.16. Predicted NPV, on the left *y*-axis, and calculated LCOE, on the right *y*-axis, of the proposed EMS with three thermal tanks and two ORC systems for all the four cases of discharging duration (i.e., A, B, C, and D) and two discharges per day. The figure presents results assuming UK wholesale electricity prices in year 2019 and two 1-h charges per day at the minimum electricity price.

A summary of the main economic analysis results of the four examined cases based on 2019 prices, for both one and two discharges per day, are presented in Table 5.10. The total investment costs that consist of the ORC engine costs and the costs of all thermal tanks drops significantly from Case A to Case D as the size of the ORC systems decreases. Specifically, the investment cost drops to around £48M if single daily discharging is performed for longer durations (i.e., 8-h discharge).

Table 5.10. Main economic analysis results of the analysed four cases (UK wholesale electricity prices in 2019).

No. of discharges per day	Case	Total investment costs (£M)	O&M costs (£M/year)	Charging costs (£M/year)	Generated electricity (GWh/year)	Total revenues (£/year)	LCOE (£/MWh)	NPV (£M)
One discharge	A	199	6.0	2.6	49.8	4.0	401	-248
	B	112	3.4	2.6	49.8	3.8	250	-150
	C	69.0	2.1	2.6	49.8	3.4	174	-90.8
	D	47.5	1.4	2.6	49.8	2.9	136	-66.8
Two discharges	A	199	6.0	5.3	99.6	6.9	228	-276
	B	112	3.4	5.3	99.6	6.6	152	-151
	C	69.0	2.1	5.3	99.6	5.8	114	-96.1
	D	47.5	1.4	5.3	99.6	5.0	95.2	-77.5

5.5.4. Economic analysis based on UK wholesale electricity prices in 2021

The same economic analysis used in the previous section is performed here for electricity prices in 2021. During 2021, the electricity prices were much higher and more volatile than in 2019 due to higher natural gas prices, lower wind levels, outages of nuclear plants, and fire damage to electricity interconnectors. The highest and lowest electricity prices recorded in 2021, respectively, were 2500 £/MWh_{el} and -19.4 £/MWh_{el}, which can be compared to the corresponding 2019 prices of 277 £/MWh_{el} and -2.8 £/MWh_{el} [219]. Figure 5.17 shows the predicted NPV and the LCOE for the four cases with two charge/discharge cycles per day and based on 2021 prices.

The peak and off-peak electricity price spread (PD) in 2021 was much higher than those in 2019 (see Figure 5.16), resulting in improved NPVs, however, the NPVs for all examined cases are still negative. For example, the NPV for Case A with two charges/discharges per day improves by 37% relative to the one calculated based on 2019 prices. Moreover, the LCOEs calculated based on 2021 prices are higher than those calculated based on 2019 prices because of the higher averaged off-peak (charging) prices in 2021 (i.e., 67.2 £/MWh_{el} compared to 30.7 £/MWh_{el} in 2019).

Interestingly, it can be seen from Figure 5.17 that Case D has a lower NPV than Case C, which was not the case in the obtained results using 2019 prices (i.e., in Figure 5.15 and Figure 5.16). Although Case D has lower EMS investment and O&M investment costs due to reduced size of the ORC systems, the relative decrease in the total investment costs for Case D relative to Case C is lower than the relative decrease in total revenues gained from selling electricity at a

lower average price, which results in a higher NPV for Case C. This implies that the economics of the EMS has several competing factors, including the EMS investment costs and difference between the peak and off-peak prices. The obtained results support the need for finding the optimum size of the ORC systems, optimum duration of the TES charge/discharge cycles, and the optimum frequency of the cycles that yield the highest NPV for given electricity prices. This optimisation exercise is an interesting area of future work.

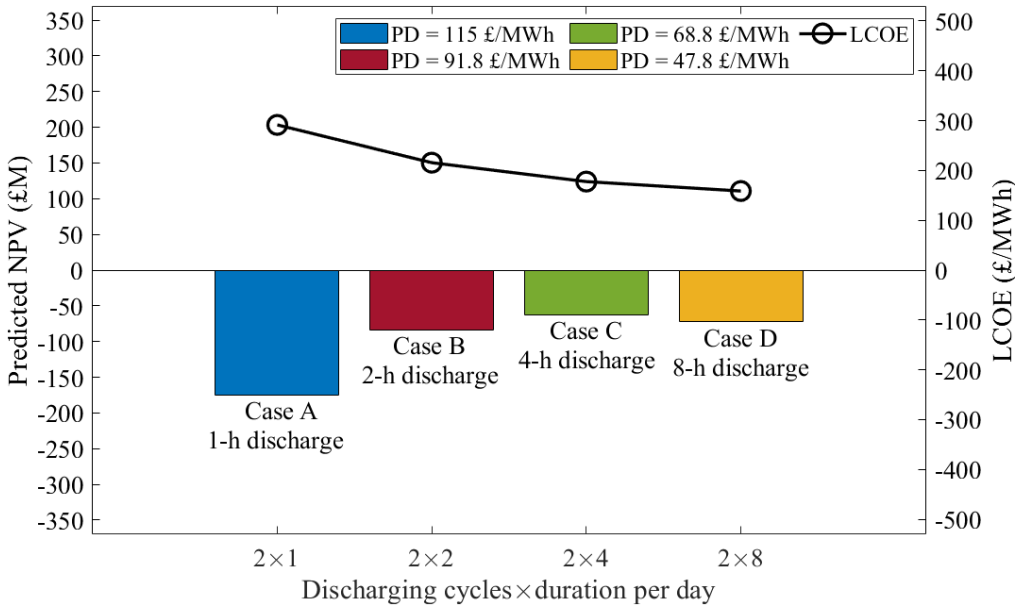

Figure 5.17. Predicted NPV, on the left *y*-axis, and calculated LCOE, on the right *y*-axis, of the proposed EMS with three thermal tanks and two ORC systems for all the four cases of discharging duration (i.e., A, B, C, and D) and two discharges per day. The figure presents results assuming UK wholesale electricity prices in year 2021 and two 1-h charges per day at the minimum electricity price.

The best projected LCOE when considering 2021 decreases to 159 £/MWh when doubling the total amount of generated electricity, i.e., 100 GWh_{el}/year, by having two 1-h charge and 8-h discharge cycles per day (Case D), and the NPV increases to -48.6 £/MWh with one 1-h charge and 8-h discharge cycle per day (Case D).

5.5.5. Assessment of different electricity price scenarios

The electricity market is volatile, and prices can rapidly change on an hourly, daily and longer-term basis (e.g., the trend of the UK wholesale electricity market). Therefore, different electricity price

scenarios are considered here, to evaluate the potential future profitability of the EMS system. The considered pricing scenarios are summarised in Table 5.11. These scenarios can also be applied for different electricity markets in the world that have relatively similar capacity payments to the UK's.

Table 5.11. Considered pricing scenarios for sensitivity analysis of the proposed EMS solutions.

Scenario number	Off-peak price decrease*	Charging prices (£/MWh)		Peak price increase*	Discharging prices (£/MWh)				
		$\overline{EP}_{1,Ch}$	$\overline{EP}_{2,Ch}$		$\overline{EP}_{1,Dch}$	$\overline{EP}_{2,Dch}$	$\overline{EP}_{4,Dch}$	$\overline{EP}_{8,Dch}$	$\overline{EP}_{16,Dch}$
1	10%	27.2	27.7	50%	94.5	90.9	85.6	79.2	71.2
2	25%	22.6	23.1	100%	126	121	114	106	94.9
3	50%	15.1	15.4	150%	158	151	143	117	118
4	75%	7.5	7.7	200%	189	182	171	158	142

** Relative to the prices in 2019 in Table 5.8, and considered in Sections 5.5.1 to 5.5.4.*

Figure 5.18 shows the predicted NPV, on the left *y*-axis and the calculated LCOE, on the right *y*-axis, of the EMS at the four proposed electricity price scenarios. The economic evaluation is performed for all discharging cases (i.e., Cases A, B, C, and D), and for both a single charging/discharging cycle and two charging/discharging cycles per day. Therefore, results relating to 32 combinations of discharging cases and price scenarios are summarised in this figure.

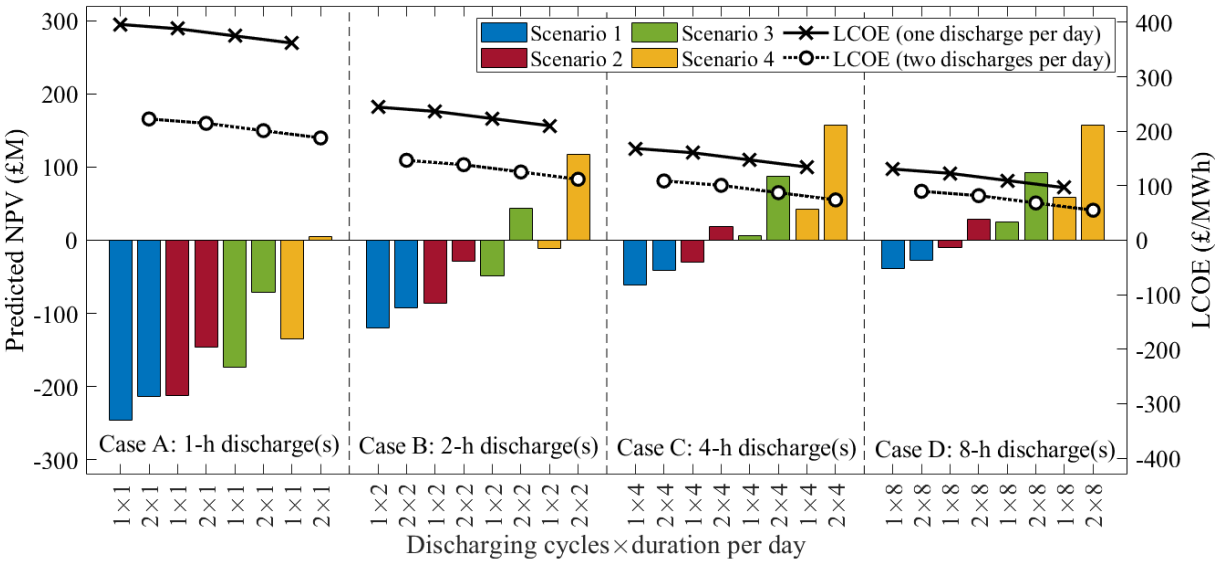

Figure 5.18. Predicted NPV, on the left *y*-axis, and calculated LCOE, on the right *y*-axis, of the EMS for the proposed price increase scenarios. The presented results are obtained considering all four discharging duration cases (i.e., Cases A, B, C, and D) and the two charging options (i.e., one 1-h charge and two 1-h charges) per day.

The LCOE drops significantly when a complete charging/discharging cycle is performed twice per day, as a result of doubling the amount of electricity generated at peak demand periods. Moreover, the LCOE of each case declines slightly from price Scenario 1 to Scenario 4, due to the lower average charging costs (which are the lowest for Scenario 4). The lowest LCOE corresponds to a discharging of 16-h a day (i.e., two 8-h discharge cycles per day) at price Scenario 4. This relatively low LCOE is achieved as the capital costs of the ORC systems and the charging costs are at their lowest amongst the cases considered here. As can be seen, many the combinations are associated with negative NPVs even with the increased selling price at peak demand, but 13 combinations provide positive NPV, at longer discharge durations and with two charge/discharge cycles per day. In general, these results suggest that a positive NPV can result when the average peak and off-peak electricity price variations are at least double those that occurred in the UK market in 2019, and with TES charge/discharge cycles are performed more than once per day with a discharge duration to the ORC plants longer than 2 h. Of importance and with important implications for the future, is the fact that recent electricity price data in the UK are now approaching this limit.

Electricity market price variations during the day are key factors for the profitability of the proposed EMS solutions. Therefore, the breakeven discharging prices, at different TES charging prices, to obtain NPV equal to zero, are presented in Figure 5.19. The minimum average electricity price for all cases and for four different average off-peak prices (AOP) are compared. In every case, the minimum peak price decreases as the AOP declines from 20 to 5 £/MWh. Moreover, the required minimum peak price reduces significantly as the discharging cycle is performed twice a day, especially in Case A and Case B. Taking Case B with two full charges a day and with an AOP of 5 £/MWh, the EMS could be profitable if the averaged peak prices (for 4 h a day) are above 99.2 £/MWh. In conclusion, the flexible nuclear plant configuration with EMS could be a profitable option in a highly fluctuating electricity market with a large difference between off-peak and peak electricity prices.

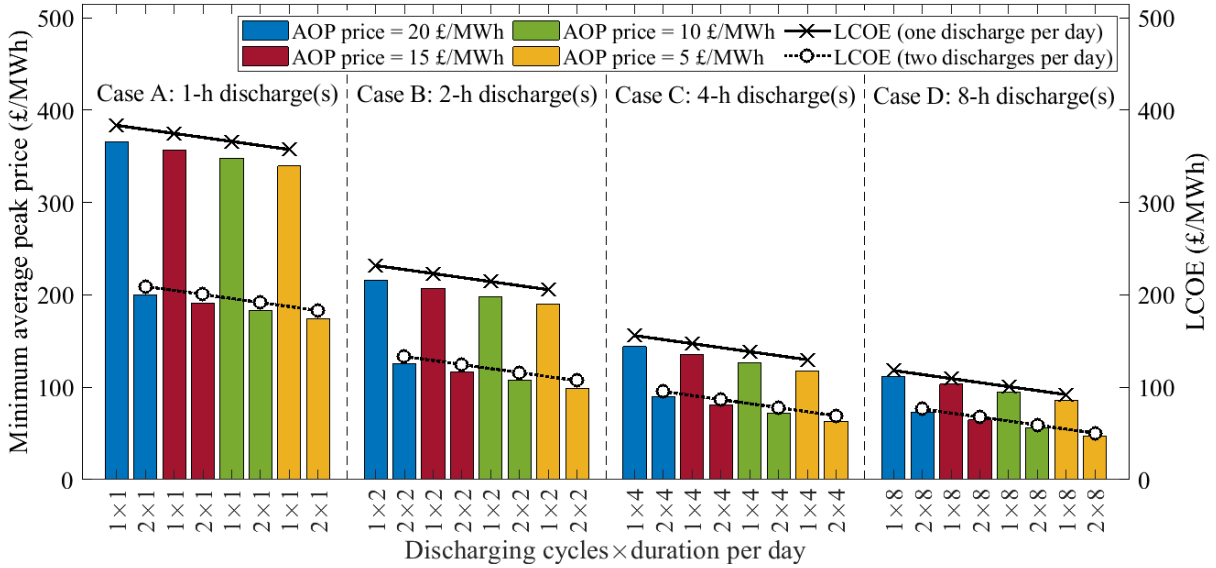

Figure 5.19. Minimum average electricity peak price at discharging, on the left *y*-axis, and resulting LCOE, on the right *y*-axis, for different AOP prices to obtain NPV of the investment equal to 0 for the proposed Cases (A to D) and 1 or 2 full TES charging/discharging per day.

5.5.6. Updated profitability analysis based on 2022 electricity prices

It is concluded from the profitability analysis performed in Sections 5.5.4 and 5.5.5 that the profitability of the EMS is highly dependent on off-peak and peak prices. Therefore, the study was updated based on 2022 (until May 2022) electricity prices which were much higher than 2019 prices (i.e., check Table 5.8 for prices) due to the increase of natural gas prices cause by the Ukraine-Russia conflict. To clearly understand the effect of electricity prices in the profitability of the EMS, profitability curves based on peak and off-peak prices were generated, which are presented in Figure 5.20. Four profitability curves representing the four analysed cases (Case A, B, C, and D) and assuming two charge/discharge cycles per day are illustrated in Figure 5.20

The profitability curves were generated based on the difference between the peak and off-peak prices (peak - off-peak) against the ratio between the off-peak and peak prices (off-peak/peak). The left and top side of each curve means that profits can be made (positive NPV) while the right/bottom side of the curves corresponds to negative NPVs (loss). The dots in Figure 5.20 corresponds to the status of profitability (NPV) based in 2019 prices (squared dots) and 2022 prices (pentagram dots). For both years and all cases, the projected NPVs are in the negative side of the curve meaning that investment in the EMS will not be profitable. Although 2022 electricity prices are much higher than 2019 prices (about 330% higher), the ratio between the

off-peak and peak prices are almost the same. From 2019 to 2022 the peak/off-peak electricity price difference increased by 4.3 times and is now ~100 £/MWh). Such increase is still not sufficient to have a profitable EMS. For example, with an off-peak/peak price ratio of 0.4, Case A can be profitable if the peak/off-peak price difference is higher than 300 £/MWh, where for Cases B, C and D, the price difference has to be higher than 250 £/MWh, 100 £/MWh and 75 £/MWh, respectively. The closes point to the profitability curves is observed for Case C (4-h discharge) with two charge/discharge cycles per day.

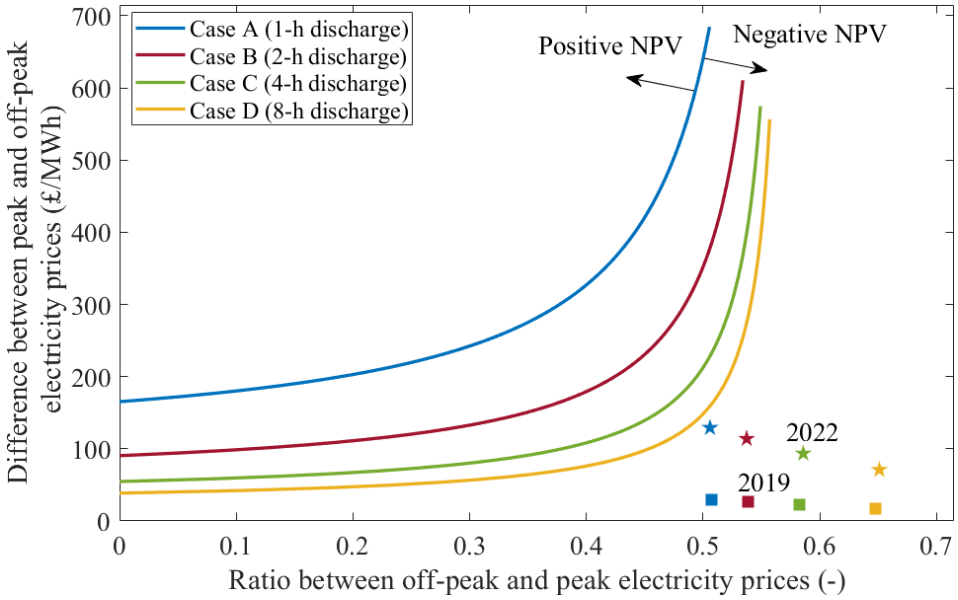

Figure 5.20. Profitability curves of the EMS generated based on the difference between peak and off-peak electricity prices (i.e., peak – off-peak), *y*-axis, and the ratio between off-peak and peak electricity prices (i.e., off-peak / peak), in *x*-axis, of the four discharging duration cases (Cases A, B, C, and D) and for two charge/discharge cycles per day. The squared dots represent calculated price ratios and differences based on 2019 electricity prices while the pentagram dots are for 2022 prices.

5.6. Summary and conclusions

An energy management system (EMS) for the flexible operation of power plants based on generation-integrated thermal energy storage (TES) has been proposed and applied to an existing 670 MW_{el} Rankine-cycle nuclear power plant (advanced gas-cooled reactor) operated by EdF as a case study. The options of steam extraction before the reheater and/or before the low-pressure turbine (LPT) of the power plant during off-peak demand have been investigated.

In this EMS, steam is extracted from the power plant during off-peak demand for the charging of the TES, and at a later time when this is economically favourable these tanks act as the heat sources of secondary thermal power, in particular as evaporators of organic Rankine cycle (ORC) systems that are suitable for extra power generation. As discussed in previous studies in the literature, such as in Ref. [87] and Ref. [88], this type of solution offers greater flexibility than TES-only solutions that store thermal energy and then release this back to the base power plant, in that it allows both derating but also an over-generation compared to the base power plant rating.

In such a scheme, the EMS would be required to optimise the derating of such power plants for the charging of the thermal tanks during off-peak demand periods and to control the discharging of the tanks for electricity generation from the secondary plants during the peak-demand periods. It has been found that when charging the PCM-TES tanks during off-peak demand in a proposed scheme with three TES tanks, a maximum plant derating of 40% can be achieved, i.e., down to 406 MW_{el}. At peak demand, when discharging the PCM-TES tanks, the thermodynamic analysis has suggested that a maximum combined power of 822 MW_{el} can be delivered, which includes the 670 MW_{el} generated by the nuclear power plant and an additional 152 MW_{el} from two secondary generation ORC plants. This is 23% higher than the nuclear plant's full-load rating. The options of lower ORC plant sizes with corresponding longer operating time have been also considered, keeping constant the TES capacity and hence the delivered excess electricity from the ORC systems, but with lower investment costs due to smaller size.

The economic profitability of the proposed integrated storage system has been analysed considering UK hourly prices in the wholesale electricity market during the years 2019 and 2021. It was concluded that profitability of the flexible power plant configuration, defined as a positive net present value (NPV) relative to the business as usual (BAU) operation, can be achieved if: (i) the average peak and off-peak electricity price variations are at least double those that occurred in the UK market in 2019; and (ii) TES discharge duration to the ORC plants is longer than 2 h or the TES charge/discharge cycle is performed more than once a day. Moreover, an investment cost for the case of one 1-h charge and one 1-h discharge per day was estimated at £199M (~$249M) with a total generated electricity of 50 GWh per year, and a LCOE of 401 £/MWh (~501 $/MWh) was obtained based on 2019 electricity prices. However, the investment cost drops to around £48M (~$60M) if discharging is performed for longer durations (i.e., 8-h discharge), which reduces the size of

ORC systems. Furthermore, the projected LCOE also decreases to 95 £/MWh (~119 $/MWh) when doubling the total amount of generated electricity, i.e., 100 GWh/year, by having two charge/discharge cycles per day. When considering the UK electricity prices in 2021, single 1-h charge/discharge cycles per day lead to a LCOE of 463 £/MWh (~579 $/MWh), which decreases to 159 £/MWh (~199 $/MWh) when doubling the total generated electricity (100 GWh/year) by employing two daily 8-h TES charge/discharge cycles.

Finally, it was demonstrated that the economics of the EMS, especially in terms of the NPV, are determined by: (i) the size of the ORC plants (smaller sizes means lower costs but higher discharging duration); (ii) the number of charge/discharge cycles per day; and (iii) the ratio and difference between off-peak and peak electricity prices. It can be also concluded that flexible operation of AGRs can be profitable if the UK's off-peak/peak electricity price ratio decreases slightly, about 15% relative to levels observed over the period 2019-2022, and the peak/off-peak price difference increases to ~200 £/MWh (~250 $/MWh), and these conditions are set for Case C (4-h discharge) with two TES charge/discharge cycles per day. The main conclusion highlights the need to identify the optimum (TES and ORC) system design and sizing, as well as the optimum duration of the TES charge/discharge cycles, and the optimum frequency of the cycles that yield the highest NPV for given electricity prices.

The case study presented in this chapter provides a satisfactory answer to Research Question 2 and adequately fills the Research Gap 2 that are identified and listed in Section 2.8. Future work recommendations related to the presented study in this chapter are discussed in Section 8.3.

Chapter 6
Nuclear flexibility and whole-energy system benefits

6.1. Introduction

Decarbonisation of the electricity system will require a range of technologies to provide flexibility in the context of grid support, balancing, security of supply and integration of variable renewables [226]. These technologies will include various forms of energy storage, demand-side response, expansion of interconnection capacity and more flexible generation technologies, as well as a number of cross-vector flexibility options such as TES and power-to-X. A number of studies have shown that flexibility becomes increasingly important as carbon emissions targets for the electricity sector are reduced and therefore the provision of flexibility will become particularly critical in achieving net-zero carbon or net-negative carbon electricity supply [227]. Nuclear power plants with enhanced flexibility (i.e., combined with thermal energy storage (TES) and secondary power generation cycle systems) could be a valid option of the net-zero carbon or net-negative carbon electricity supply mix, especially with the increasing penetration of renewables.

Energy technologies linking heat and power will play a key role in the integration between the heating/cooling and electricity networks, and therefore recent research has focused on the optimal design and operation of combined heat and power (CHP) systems, centralised heat pumps and TES options for district heating [228]. It has been shown in Ref. [229] that a cost-efficient supply of heat in a local district heating system may require a significantly higher volume of TES to manage local grid constraints and support the integration of high penetration of variable renewables.

To adequately quantify the role of flexible solutions in future low-carbon electricity systems, it is critical to model these systems with sufficient spatial-temporal resolution using a holistic system approach. The approach to system valuation of flexible nuclear configurations used in this chapter is based on an extension of the whole-system modelling approach presented in Ref. [182].

In this chapter, a novel approach to configuring flexible nuclear power plants and quantifying their system value in low-carbon electricity systems is proposed. Specifically, the main novel contributions of the study discussed in this chapter include:

- A technology-rich approach to configuring the design of and operating a selected flexible nuclear power station based on detailed thermodynamic modelling of various individual plant components (secondary Rankine power cycle systems, generators, turbines, PCM-based TES tanks, feed pumps, condensers, feedwater heaters, etc.) and including consideration of part-load operation conditions during the charge of the TES system.
- The design of novel modular units combining PCM-based TES systems and secondary steam Rankine cycle power systems, aiming for a more feasible installation procedure and potentially lower costs of the main components of such an integrated system.
- Optimisation of the thermodynamic performance of the proposed flexible nuclear plant configuration by determining efficient choices for a variety of technical parameters including the choice of suitable PCMs.
- Development of a high-fidelity model of the resulting flexible nuclear power plant within a high-resolution power system model that minimises the total investment and operation cost for generation and storage assets in the system; representation of flexible nuclear includes an explicit consideration of different plant components including TES, steam generator and primary and secondary generation cycles.
- Quantification of the system value offered by the enhanced flexibility of such nuclear plants, considering a range of scenarios characterised by decarbonised electricity supply and a high share of variable renewable generation.

The study covered in this chapter starts with describing the designed flexible nuclear power plant in Section 6.2. The power generation cycle systems model inputs and the design of the conceptual TES as well as the main assumptions used in this study are presented in Section 6.3. The whole energy system model assumption and the proposed scenarios are discussed in Section 6.4. Sections 6.5 to 6.7 present and discuss the thermodynamic performance of the designed flexible nuclear power plant. The performance and the operation of the flexible nuclear power plant, from the whole electricity system perspective, are presented and discussed in Sections 6.8 to 6.10. Finally, the key findings and conclusions are summarised in Section 6.11. It should be noted that the presented study in this chapter has been already

published as a journal article, which can be found in Ref.[230] Note that all the costs and prices are presented in GBP (£) since the case study presented in this chapter is for the UK. The assumed GBP/USD and GBP/EUR exchange rates were 0.80 and 0.85, respectively.

6.2. Description of power plant configuration

The layout of the proposed nuclear power plant, illustrated in Figure 6.1, consists of:

1) A nuclear power island that includes a pressurised water reactor (PWR) and a steam generator (SG), which generates steam utilising nuclear thermal power.
2) A primary steam Rankine cycle (PSRC) system that contains high-pressure turbines (HPT), low-pressure turbines (LPT), a reheater (RH), a condenser, electric generators, six closed feedwater heaters (CFWH), throttling valves, control valves, a condensate pump, a feed pump and a deaerator.
3) TES units, indicated as TES-1 and TES-2 in Figure 6.1. TES-1 unit is proposed to have two PCM tanks (PCM-1 and PCM-2) connected in series. PCM-1 tank is charged using higher temperature steam flowing out from the steam generator, while PCM-2 tank is charged using steam flowing out from PCM-1 tank. Similarly, TES-2 unit has two PCM tanks (PCM-3 and PCM-4), also connected in series. However, TES-2 tanks are charged by lower temperature steam that is extracted after the HPT and before the reheater, as shown in Figure 6.1.
4) Two secondary steam Rankine cycle (SSRC-1 and SSRC-2) systems. System SSRC-1 is operated by discharging the heat stored in TES-1 tanks while system SSRC-2 is operated by utilising the stored heat in TES-2 tanks.

In this study, the reactor is assumed to continuously operate at full rated thermal power whenever it is possible to avoid power disturbance in the reactor and to maximise the economic benefits of investing in such a capital-intensive energy source. In this context, most load following operations are achieved by controlling: (i) the amount of steam flowing from the steam generator to the PSRC system; (ii) the amount of steam directed to both TES units (i.e., charging mode); and (iii) the operation of both SSRC systems (i.e., discharging mode).

During nominal (full-load) operation mode, the generated steam in the SG flows to the PSRC system and no steam is directed to the TES units as the TES system control valves (i.e., located before PCM-1 and PCM-3 tanks) are closed. The TES system charging process is performed at times of low electricity demand (i.e., part-load operation mode) by opening the

TES system valves and allowing some amount of the generated steam to flow into the PCM tanks for heat deposition. The opening of TES valves reduces the mass flowrate of steam flowing to the PSRC system (i.e., to the HPT, reheater and LPT) due to constant steam generation in the SG. This operation method allows operating the PSRC system at reduced power output while running the reactor at full rated thermal power output (i.e., steady steam outlet condition from the SG). The stored heat in the TES system is assumed to be discharged to generate extra electrical power through the operation of the SSRC systems during periods of high demand (i.e., peak electricity prices). The use of SSRC systems is to have the ability to generate extra power during high electricity prices, thus, higher revenues.

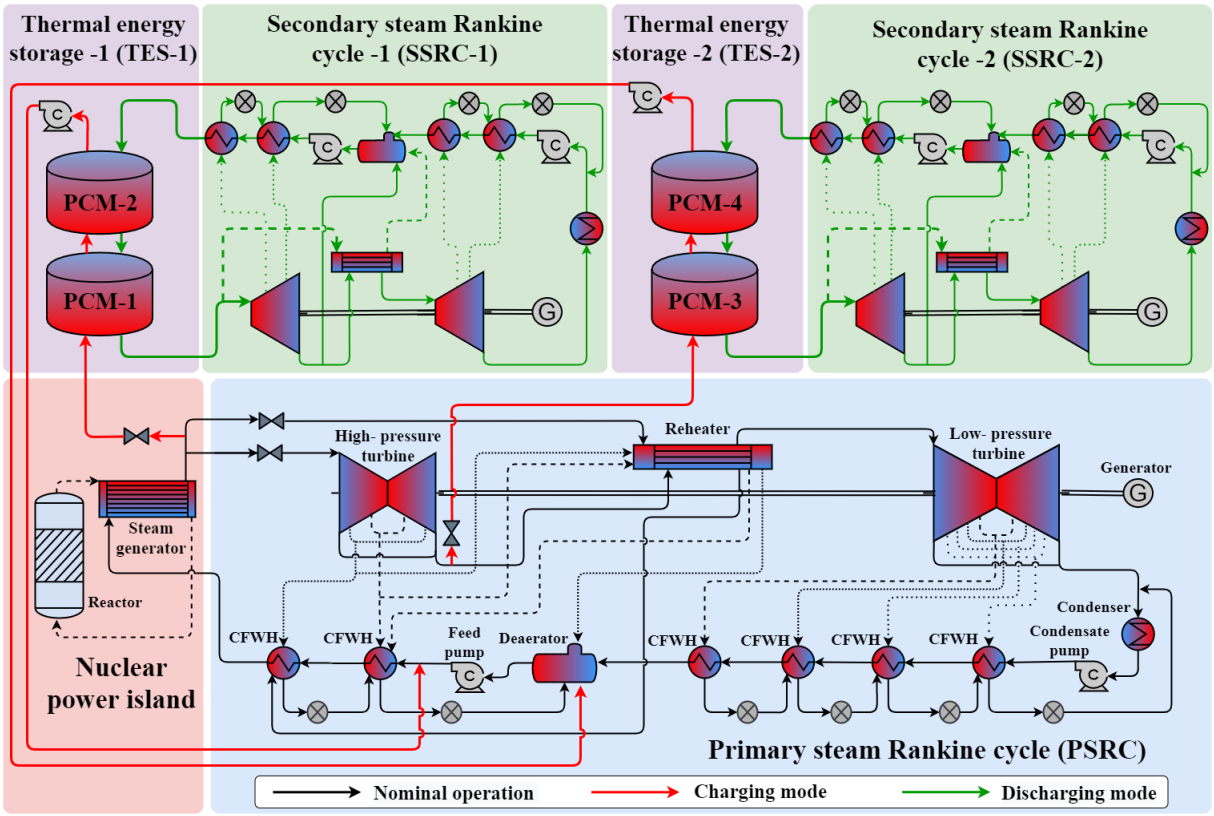

Figure 6.1. Layout of the proposed nuclear power plant coupled with PCM tanks as TES units and secondary power Rankine cycles (SSRCs) systems. Black lines indicate flow streams during nominal operation, red lines indicate thermal energy charging flow streams, and green lines indicate thermal energy discharging flow streams.

6.3. Power generation cycle system and TES system models inputs

6.3.1. Nuclear reactor and primary steam Rankine cycle inputs

The selected nuclear reactor design is the European pressurised reactor (EPR), which is a PWR that generates 4520 MW_{th} of thermal power using nuclear fission [114]. Although there is a wide range of reactor types and designs, the EPR is chosen in this study as it is currently under construction in the UK at Hinkley Point C and is also the choice for the potential future construction of Sizewell C [111]. It is expected that EPR design has a higher potential than other reactor designs to replace the current fleet of AGRs in the UK due to the experience gained from constructing current EPRs. Table 6.1 summarises the main EPR operating parameters that are considered in the PSRC system model, which is explained in detail in the next section.

Table 6.1. Main operation parameters of the EPR.

Parameter	Value	Reference
Reactor thermal power (MW_{th})	4520	[114]
Feedwater temperature (°C)	230	[115]
Feedwater pressure (kPa)	8300	[116]
Steam generator mass flowrate (kg/s)	2553	[115]
Steam generator outlet temperature (°C)	293	[116]
Steam generator outlet pressure (kPa)	7800	[116]

6.3.1.1. Full-load operation

The full-load (nominal load) operation of the PSRC system model was formulated using the operation parameters and assumptions listed in Table 6.2. Full-load operation of the PSRC system means that no steam is directed to the TES units and all nuclear thermal power is utilised for electrical power generation from the PSRC generators. The PSRC parameters at full load such as steam condition at the steam generator outlet, turbine power output, needed pump power, net PSRC system power output, PSRC efficiency, etc. were calculated using the listed set of equations in Sections 3.1 and 3.4.1 in the methodology chapter (Chapter 3).

Table 6.2. Primary steam Rankine cycle assumptions and parameters at nominal power.

Parameter	Value	Reference
Average HPT design isentropic efficiency (%)	87	[231]
Average LPT design isentropic efficiency (%)	87	[231]
Condenser pressure (kPa)	10	[88]
Pump isentropic efficiency (%)	85	[231]
Generator mechanical efficiency (%)	98	[232]
Pressure loss in the reheater (kPa)	300	-
Hot stream outlet steam quality in CFWHs (-)	0	-

One method of obtaining the operating conditions of other PSRC system parameters such as the turbine side extraction pressures and flowrates, steam that flows from the steam generator to the reheater, etc., is to set up an optimisation model with an objective function that maximises the net cycle efficiency as in Equation (6.1). The PSRC system efficiency optimisation tasks were solved using MATLAB's interior point algorithm *fmincon* [108]. This algorithm identifies multiple local minima over a range of initial conditions in order to find the global minimum.

$$\max_{\dot{m}_{\mathrm{RH}(1,2,3)},\, P_{\mathrm{HPT,SE}(1,2)},\, P_{\mathrm{HPT,out}},\, P_{\mathrm{LPT,SE}(1,2,3,4)},\, \dot{m}_{\mathrm{HPT,SE}(1,2)},\, \dot{m}_{\mathrm{LPT,SE}(1,2,3,4)}} \{\eta_{\mathrm{PSRC}}\} \tag{6.1}$$

$$\eta_{\mathrm{PSRC}} = \frac{\dot{W}_{\mathrm{net}}}{\dot{Q}_{\mathrm{SG}}} \tag{6.2}$$

where η_{PSRC} is the PSRC efficiency, $\dot{m}_{\mathrm{RH}\,(1,2,3)}$ the mass flowrates of steam flowing to the reheater, $P_{\mathrm{HPT,SE}(1,2)}$ the HPT side extractions pressures, $P_{\mathrm{HPT,out}}$ the HPT main outlet pressure, $P_{\mathrm{LPT,SE}(1,2,3,4)}$ the LPT side extractions pressures, $\dot{m}_{\mathrm{HPT,SE}(1,2)}$ the steam mass flowrates from the HPT side extractions to high-pressure CFWHs, and $\dot{m}_{\mathrm{LPT,SE}(1,2,3,4)}$ the steam mass flowrates from the LPT side extractions to low-pressure CFWHs.

The optimisation variables, expressed in Equation (6.1), includes determination of the HPT and LPT side extractions (i.e., bleeds) pressures and mass flowrates that give the maximum cycle thermal efficiency at nominal power load. The objective function was formulated to solve the numerical quasi steady PSRC system model while satisfying a set of non-linear constraints listed in Equations (6.3)-(6.8):

$$\Delta T^{\mathrm{in}}_{\mathrm{pp,CFWH}} \geq 5\ ^{\circ}\mathrm{C} \tag{6.3}$$

$$\Delta T^{\mathrm{out}}_{\mathrm{pp,CFWH}} \geq 5\ ^{\circ}\mathrm{C} \tag{6.4}$$

$$x_{\mathrm{HL,CFWH}}^{\mathrm{out}} \leq 0 \tag{6.5}$$

$$P_{\mathrm{TV}}^{\mathrm{out}} = P_{\mathrm{HL,CFWH}}^{\mathrm{in}} \tag{6.6}$$

$$x_{\mathrm{P}}^{\mathrm{in}} \leq 0 \tag{6.7}$$

$$T_{\mathrm{RH}}^{\mathrm{out}} \geq 287\ ^{\circ}\mathrm{C} \tag{6.8}$$

where $\Delta T_{\mathrm{pp,CFWH}}^{\mathrm{in}}$ and $\Delta T_{\mathrm{pp,CFWH}}^{\mathrm{out}}$ are the inlet and outlet pinch-point temperature difference of all CFWHs, $x_{\mathrm{HL,CFWH}}^{\mathrm{out}}$ the CFWH hot-leg outlet steam quality, $P_{\mathrm{TV}}^{\mathrm{out}}$ the throttling valve outlet pressure, $P_{\mathrm{HL,CFWH}}^{\mathrm{in}}$ the CFWH hot-leg inlet steam pressure, $x_{\mathrm{P}}^{\mathrm{in}}$ the inlet steam quality of all pumps, and $T_{\mathrm{RH}}^{\mathrm{out}}$ the reheater outlet temperature.

The constraints related to the pinch-point temperature differences in the CFWHs were set to allow for more effective heat transfer rates between the hot and the cold streams during nominal and part-load operation modes while achieving reasonable sizes (i.e., costs) of heat exchangers. The CFWH hot-leg outlet steam quality constraint, Equation (6.5), was set to maximise the amount of heat transferred from the turbine side extraction steam to the feedwater through a full condensation of steam, leading to higher cycle thermal efficiencies. The pressure equality constraint, Equation (6.6), was to ensure that both CFWH inlets (i.e., from the turbine side extraction and from the throttling valve) have the same pressure. The pump inlet steam quality constraint was necessary to ensure that the steam entering the pumps is either saturated or subcooled liquid to avoid damaging the pumps. Lastly, the reheater steam temperature constraint was implemented to achieve higher cycle thermal efficiencies.

6.3.1.2. Part-load operation (charging mode)

The part-load PSRC system model was constructed by considering the off-design turbine efficiency correlation (Equation (3.85) of Section 3.4.2) for both, the HPT and the LPT. It was assumed that the shaft speed is constant for all loads as the shaft is connected to a power grid with fixed frequency, typically 50 Hz in the UK [149]. In this study, the multiple stages between the turbine inlet and the next side extraction, or between two side extractions or between the last side extraction and the main turbine outlet, are considered as one turbine stage. Therefore, the HPT turbine and the LPT were assumed to consist of 3 and 5 stages, respectively.

The part-load PSRC system model also considered the change of steam pressure at the inlet and the outlet of each stage due to steam mass flowrate and temperature variations inside the turbine during part-load operation. To calculate the turbine inlet, outlet, and side extractions pressure, the following Stodola's ellipse law (Equation (3.86) of Section 3.4.2) was applied.

The part-load cycle efficiency expression and the adjusted optimisation objective function are:

$$\eta_{\mathrm{PSRC}}^{\mathrm{PL}} = \frac{\dot{W}_{\mathrm{net}}}{\dot{Q}_{\mathrm{SG}} - \dot{Q}_{\mathrm{TES}}} \tag{6.9}$$

$$\max_{\dot{m}_{\mathrm{RH}(1,2,3)}, \dot{m}_{\mathrm{HPT,SE}(1,2)}, \dot{m}_{\mathrm{LPT,SE}(1,2,3,4)}, \dot{m}_{\mathrm{TES}-1}, \dot{m}_{\mathrm{TES}-2}} \{\eta_{\mathrm{PSRC}}^{\mathrm{PL}}\} \tag{6.10}$$

where $\dot{Q}_{\mathrm{TES}}$ is the total amount of thermal power available for storage, $\dot{m}_{\mathrm{TES}-1}$ the steam mass flowrate flowing to TES-1, and $\dot{m}_{\mathrm{TES}-2}$ the steam mass flowrate directed to TES-2.

The optimisation variables that are expressed in Equation (6.10) include the HPT and LPT side extractions mass flowrates. This means that these variables are optimised for each power load in order to achieve the maximum possible cycle efficiency at part loads. It is assumed that these side extraction mass flowrates are achieved by the operation of control valves (i.e., usually located between the side extraction points and feedwater heaters) during load following operations.

The optimisation problem was solved using the same optimisation algorithm as in Section 6.3.1.1 and satisfying the constraints listed in Equations (6.3)-(6.8) as well as the following additional constraint that was set to limit the amount of diverted steam from the PSRC system (i.e., before and after the HPT) to the TES system during the charging mode, which reduces the overall impact on the performance of both turbines during off-design conditions:

$$\dot{Q}_{\mathrm{TES}-1} = \dot{Q}_{\mathrm{TES}-2} \tag{6.11}$$

where $\dot{Q}_{\mathrm{TES}-1}$ and $\dot{Q}_{\mathrm{TES}-2}$ are the amount of thermal power available for storage in TES-1 (PCM-1 and PCM-2 tanks) and in TES-2 (PCM-3 and PCM-4 tanks), respectively.

It should be noted that the SG inlet temperature is assumed to be maintained at 230 °C during the charging process of the TES systems. The temperature of steam exiting PCM-2 and PCM-4 tanks is expected to vary during the TES charging process, but these temperature variations are controlled in the feedwater heating system (i.e., the CFWHs and the deaerator). This can be seen in Figure 6.1 where steam outflowing from the TES-1 system is directed to the cold-leg

inlet of the first high-pressure CFWH and steam exiting the TES-2 system is connected to the deaerator, which also operates as an open feedwater heater. The temperature control in the feedwater heating system is achieved by adjusting the amount (i.e., the mass flowrate) of steam flowing from the turbine side extractions. This affects the amount of heat transferred to the feedwater in the CFWHs and thus the feedwater temperature.

6.3.2. Conceptual design of modular TES tanks and secondary steam Rankine cycle units

A conceptual modular TES-SSRC design is proposed in this study. The modular TES-SSRC unit is designed to contain four components attached to the PSRC system. These components are system TES-1 (PCM-1 and PCM-2 tanks), system SSRC-1, system TES-2 (PCM-3 and PCM-4 tanks), and system SSRC-2 as illustrated in the top side of Figure 6.1. The reasons behind proposing modular TES-SSRC units are:

- The potential of capital cost and production time reduction when fabricating the same component for multiple times (i.e., mass production) [233].
- The ability of adding extra modules if larger heat storage capacity is required in the future.
- The capability of placing the modular units in different locations around the nuclear reactor.

The size of the modular TES-SSRC unit was determined by the amount of thermal power available for storage and the TES charging/discharging duration. One modular TES-SSRC unit was sized based on the following assumptions:

- The storage capacities of TES-1 and TES-2 were determined by calculating the amount of heat available for storage when the PSRC power output is reduced by a scale of 10% of the nominal load for 1 h. For example, if the PSRC system is operating at 50% of its nominal power for 1 h, 5 modular TES units can be fully charged at the end of that hour.
- Both systems (SSRC-1 and SSRC-2) were sized to fully discharge TES-1 and TES-2 in 1 h, which was selected based on the assumption of running the whole-electricity system optimisation model with 1-h time resolution.

6.3.3. Thermal energy storage system design and selection of phase change materials

PCMs were selected due to their ability to charge and discharge thermal power at constant temperatures (melting temperature) [62]. The optimal type and design (i.e., shape, dimensions,

etc.) of the PCM tanks in the modular TES-SSRC system is not the focus of the study presented in this chapter. However, the selection of the PCM type was essential to determine the operation temperature range of SSRC-1 and SSRC-2 systems. Table 6.3 summarises the calculated inlet steam conditions and the assumed outlet steam conditions of TES-1 and TES-2 as well as the types of PCM that suit the temperature range of the charging steam (heat-source). Each PCM tank was designed with a specific material, depending on the charging steam temperature and the correspondent PCM melting temperature, to reduce, to some extent, the exergy losses caused by large temperature differences between the PCM and the steam in the charging/discharging processes. It should be emphasised that the size (i.e., volume) of the PCM tanks is expected to between 3000 m^3 and 3500 m^3 for each tank (i.e., calculated based on heat storage density of 46 kWh_{th}/m^3 as in Chapter 5. Thus, sufficient land areas and spaces are required for the installation of these PCM tanks.

Table 6.3. Thermal properties of PCM and steam conditions of the PCM tanks.

Parameters		**TES-SSRC-1**		**TES-SSRC-2**	
		PCM-1 [234–238]	**PCM-2 [206,208,237–241]**	**PCM-3 [206,242,243]**	**PCM-4 [206,208,237–241]**
Material		$NaNO_2$	53% KNO_3+ 40% $NaNO_2$+ 7% $NaNO_3$	87% $LiNO_3$+ 13% NaCl	53% KNO_3+ 40% $NaNO_2$+ 7% $NaNO_3$
Melting temperature (°C)		282	142	208	142
Latent heat of fusion (kJ/kg)		212	81.5	369	81.5
Density (kg/m^3)		2020, 1810*	2000, 1960*	2350, 1890*	2000, 1960*
Specific heat capacity (kJ/kg K)		1.85, 1.60*	1.34, 1.56*	1.54, 1.56*	1.34, 1.56*
Thermal conductivity (W/m K)		1.30, 0.50*	0.57, 0.42*	1.35, 0.63*	0.57, 0.42*
Charging steam inlet condition	Pressure (kPa)	7800	-	2390	-
	Temperature (°C)	293	-	221	-
	Quality (-)	superheated	-	0.88	-
	Mass flowrate (kg/s)	102	102	111	111
Charging steam outlet conditions	Pressure (kPa)	-	7700	-	2290
	Temperature (°C)	-	152	-	152
	Quality (-)	-	subcooled	-	subcooled
	Mass flowrate (kg/s)	102	102	111	111

** First value is for the solid and the second for the liquid phase.*

Selection of the PCM type was based on a minimum of 10 °C temperature difference between the melting temperature of the PCM and the inlet/outlet steam condition in order to ensure

effective heat transfer rates between the flowing steam and the PCM. There are various types of PCMs such as: organic compounds (paraffin and non-paraffin compounds), inorganic compounds (salts, salt hydrate, and metallic), and eutectic which is a mixture of the previous types [244]. For a temperature range from 150 °C to 300 °C, salts and eutectic salts are good candidates because their melting temperature are within the specified range and also because their thermal conductivities (i.e., between 0.4 and 1.5 W/m K) are relatively higher than those of most organic latent-heat storage materials, which could be as low as 0.1 W/m K [234]. Therefore, $NaNO_2$ was selected for PCM-1 tank (melting temperature of 282 °C, which is 11 °C below the steam inlet temperature, 293 °C) [234]. For PCM-2 tank, the selected material was salt mixture referred to as HITEC (composition: 53 wt.% KNO_3 + 40 wt.% $NaNO_2$ + 7 wt.% $NaNO_3$) with a melting point of 142 °C, which is 10 °C below the minimum steam temperature in TES-1 [239]. In TES-2, the selected PCM for tank 3 was an eutectic salt that comprises of 87 wt.% $LiNO_3$ + 13 wt.% NaCl, with a melting temperature of 208 °C, since the maximum steam temperature is 221 °C, which is lower than the maximum steam temperature in TES-2 [206]. For PCM-4 tank, the selected material was the same as in PCM-2 tank (i.e., HITEC).

It was also conservatively assumed a 50 kPa of pressure loss on steam flow across each PCM tank to account for any frictional losses in the tank during charging and discharging process. The mass flowrate listed in Table 6.3 is the average mass flowrate calculated when the PSRC power level is reduced by a step of 10% of nominal power, e.g., from 100% to 90%, from 90% to 80%, etc.

6.3.4. Design and operation of secondary steam Rankine cycle systems (discharging mode)

Discharging of stored heat is performed through system SSRC-1 and system SSRC-2 that are coupled to TES-1 and TES-2, respectively. The temperature range of TES-2 is relatively low for steam Rankine cycles, which might not be a favourable option. However, it is still considered in this study since the size of the SSRC systems is expected to be greater than 45 MW_{el}. Similarly, as in the PSRC efficiency optimisation model, the main steam parameters of the SSRCs were optimised with a set of non-linear constraints to achieve maximum cycle efficiency. The optimisation objective function of each SSRC is as follows:

$$\max_{P_{\mathrm{TES,in}},\, \dot{m}_{\mathrm{RH}},\, P_{\mathrm{HPT,SE(1,2)}},\, P_{\mathrm{HPT,out}},\, P_{\mathrm{LPT,SE(1,2)}},\, \dot{m}_{\mathrm{HPT,SE(1,2)}},\, \dot{m}_{\mathrm{DE}},\, \dot{m}_{\mathrm{LPT,SE(1,2)}}} \{\eta_{\mathrm{SSRC}}\} \tag{6.12}$$

where η_{SSRC} is the SSRC efficiency, $P_{\mathrm{TES,in}}$ the TES inlet pressure, $\dot{m}_{\mathrm{RH}}$ the steam mass flowrate directed to the reheater, $\dot{m}_{\mathrm{DE}}$ the mass flowrate directed to the deaerator, and the other parameters are as defined in Equation (6.1).

In addition to the constraints listed in Equations (6.3)-(6.8), the following constraints were applied in the SSRC optimisation model:

$$T_{\mathrm{TES}}^{\mathrm{in}} \leq T_{\mathrm{m,PCM(2,4)}} - 10\ ^{\circ}\mathrm{C} \tag{6.13}$$

$$T_{\mathrm{TES}}^{\mathrm{out}} \leq T_{\mathrm{m,PCM(1,3)}} \tag{6.14}$$

$$x_{\mathrm{TES}}^{\mathrm{out}} \geq 1 \tag{6.15}$$

where $T_{\mathrm{TES}}^{\mathrm{in}}$ is the steam temperature at the TES inlet, $T_{\mathrm{m,PCM(2,4)}}$ the PCM melting temperature of PCM tank 2 or 4, $T_{\mathrm{TES}}^{\mathrm{out}}$ the steam outlet temperature from systems TES-a and TES-2 during the TES discharging phase, $T_{\mathrm{m,PCM(1,3)}}$ the PCM melting temperature of PCM tank 1 or 3, and $x_{\mathrm{TES}}^{\mathrm{out}}$ the steam quality at the TES outlet.

The constraint in Equation (6.13) is to ensure that the temperature differences between the steam and the PCM in the inlets of PCM-2 and PCM-4 tanks are sufficient for more effective heat transfer rates. The steam outlet temperatures from PCM-1 and PCM-3 tanks are also limited by the melting temperature of the selected materials as indicated in Equation (6.14). The PCM temperature could reach to higher temperatures than the melting temperature of the respective material as PCM tanks are charged with steam (heat-source) of higher temperatures (i.e., at least 10 °C higher than the melting temperature of the selected material). However, the average steam outlet temperature from PCM-1 and PCM-3 tanks during the discharging phase is expected, to a large extent, to be less or equal to the melting temperatures of the selected PCMs. The last constraint, Equation (6.15), was to ensure that the steam condition at the inlet of the turbine is at least saturated vapour to avoid damaging the turbines with very wet steam.

Moreover, the model accounts for TES heat losses to the environment as well as the impact of steam conditions variation (i.e., temperature difference, mass flowrate, pressure, etc.) on the heat transfer rate between the PCM and the steam during charging and discharging modes [245]. Therefore, a charging heat-to-heat efficiency ($\eta_{\mathrm{TES,Ch}}$) of 90% and a discharging heat-to-heat efficiency ($\eta_{\mathrm{TES,Dch}}$) of 90% were assumed (i.e., round-trip efficiency of 81%). Other parameters and steam cycle assumptions are the same as for the PSRC system model, as listed in Table 6.2.

The SSRCs are assumed to operate at full-load conditions most of the time given that the share of each SSRC power output is expected to be only about 2-3% of the total peak power output (i.e., from PSRC and all SSRC systems). Hence, the aggregate SSRC power output can be modulated by switching individual SSRCs on or off when more or less power is required by the electricity grid. Also, the expected decrease in part-load thermal efficiency between SSRCs operating at 100% and at 50% of nominal output is observed to be not greater than 5% (see Section 6.6 for more details). This effect of reduced part-load efficiency was not considered in the study as it is not expected to have a significant impact on the results. Nevertheless, a more accurate modelling of part-load efficiency variations of the SSRC systems should be addressed in future work.

6.4. Whole-energy system modelling assumptions and scenarios

6.4.1. Value of flexible nuclear units in low-carbon electricity systems

System value of flexible nuclear generation in this chapter has been quantified as a whole system benefit from replacing a standard nuclear unit with a flexible alternative that also includes TES and SSRC generation. In the first step, the whole-system model (i.e., see Section 3.7 for model description and formulation) was run to minimise the total system cost and construct a series of counterfactual scenarios in which nuclear generation had no added flexibility features. In the second step, a series of model runs was performed with nuclear units being replaced with flexible nuclear configurations that included TES and SSRC generation. Any resulting reduction in total system cost (but not reflecting the cost of making the nuclear generation more flexible) was then interpreted as whole system benefit of flexible nuclear. Whole system benefit of flexible nuclear is a useful benchmark to compare against the estimated cost of this increased flexibility through TES and a secondary steam cycle. This comparison is provided in the results section (Sections 6.8 to 6.10), with the aim of identifying those electricity system features that result in a positive net benefit of flexible nuclear generation.

As already mentioned in Section 3.7, the formulation and execution of the whole-electricity system investment model (WeSIM) and all system level results were conducted and generated by Dr. Marko Aunedi. The role of the Author of this thesis was to design the flexible nuclear power plant and to investigate the thermodynamics of the designed power plant during load-following modes. The generated results from the thermodynamic analysis (Sections 6.5 to 6.7) such as cycle thermal efficiency at different power loads, SSRC power output and TES system capacity were

used as inputs to the WeSIM, which led to generating results (Sections 6.8 to 6.10) that were analysed to assess the benefits of added nuclear flexibility from a whole-energy system perspective.

6.4.2. Scenarios for flexible nuclear generation value assessment

In order to examine the key drivers for the system value of flexible nuclear, a number of scenarios had been run for different inputs assumptions. Two generic systems had been assumed, North and South, both sized to approximately match the UK electricity system. Although the annual demand volume in both systems was the same, around 400 TWh_{el}, the North system had a higher share of electrified heating demand then South, but a lower share of cooling demand. Also, in the North system it was assumed that onshore and offshore wind were available at relatively higher capacity factors (40% and 54%, respectively), while for solar PV the capacity factor was only 14%. In contrast, in the South the assumed solar PV capacity factor was 24%, while wind capacity factors were lower than in the North (35% and 49% for onshore and offshore, respectively). In all case studies except one it was assumed that there is exactly one nuclear unit in the system, with the PSRC rating of 1610 MW_{el}. This unit was assumed to be either conventional (in the counterfactual studies) or equipped with TES and SSRC units in the flexible studies.

For each of the two systems (North and South) a series of scenarios was investigated, as listed in Table 6.4, by running both counterfactual and flexible nuclear studies. These scenarios (except Scenarios E1, E2 and E3) were proposed by Dr. Marko Aunedi. The purpose of these scenarios was to explore the impact of various assumptions on the system benefit of flexible nuclear, including the level of system carbon emissions, number of nuclear units in the system, variations in SSRC duration (ratio between TES size and maximum SSRC heat intake; default assumption was 1 h), uptake and cost of battery energy storage system (BESS) and demand side response (DSR), and the ability to invest in carbon offsets such as bioenergy with carbon capture and storage (BECCS).

Table 6.4. List of system scenarios used for quantifying system benefits of flexible nuclear.

ID	Scenario description	ID	Scenario description
A	Net zero carbon system	E2	SSRC duration of 2 h
B	Carbon intensity target of 25 gCO_2/kWh	E3	SSRC duration of 4 h
C	Carbon intensity target of 50 gCO_2/kWh	F	Higher cost of BESS (50% higher than baseline)
D	5 nuclear units instead of one	G	Low DSR uptake of 25% (vs. 50% in other cases)
E1	SSRC duration of 0.5 h	H	No investment in carbon offsets (BECCS)

6.4.3. Cost and economic assumptions of the considered technologies

The assumed capital costs (i.e., consists of pre-development and the construction costs) and the fixed and variable operation & maintenance costs of the considered power generation and electricity storage technologies that are implemented in the whole-electricity system investment model (WeSIM) are listed in Table 6.5. These costs were extracted from the electricity generation costs report that was published in 2020 by the UK Department for Business, Energy & Industrial Strategy [246]. Other economic assumptions including pre-development and construction times, lifetimes and discount rates for all considered technologies are also listed in Table 6.5.

Table 6.5. List of cost and economic assumptions of the considered power generation and electricity storage technologies that are implemented in WeSIM [246].

Technology	Lifetime (years)	Const. cost* (£/kW$_{el}$)	Pre-dev. time (years)	Const. time (years)	Var. O&M cost (£/MWh$_{el}$)	Fixed O&M cost (£/kW$_{el}$/year)	Discount rate (%)
Nuclear	60	4340	5	8	5	72.9	9
CCGT	25	610	2	3	4	13.1	8
OCGT	25	430	2	2	4	6.8	7
Gas CCS	25	1310	2	3	5	22.3	7
Biomass	25	3120	3	2	9	69.9	8
BECCS	25	3190	3	4	4	146.2	9
H_2 CCGT	25	610	2	3	4	13.1	8
H_2 OCGT	25	430	2	2	4	6.8	7
Onshore wind	25	1020	4	2	6	23.5	5
Offshore wind	30	1230	5	2	3	24.5	6
Solar PV	35	350	1	1	0	6.0	6
Li-ion batteries (2 hr)	13	287	0	1	0	2.4	5

* *Construction costs comprises of pre-development costs and construction costs.*

6.5. Performance of primary steam Rankine cycle system at nominal load

The main operating parameters of the PSRC system that result in maximum cycle efficiency at nominal power are listed in Table 6.6. The temperature-specific entropy (*T-s*) diagram illustrating the main thermodynamic processes of the PSRC is shown in Figure 6.2. The calculated steam generator outlet temperature is 294 °C at 7800 kPa, which represents a slightly superheated steam. The steam enters the HPT at the same conditions and expands to 2390 kPa, reheated to 289 °C in the reheater, and then continue expanding in the LPT to a condensing pressure of 10 kPa. The

calculated net electrical power is 1610 MW_{el}, which is 1.2% less than the declared design net capacity of 1630 MW_{el} of EPR [114]. Such difference is expected since the actual EPR steam cycle parameters and components might be different to what was assumed in this study. The obtained maximum heat-to-electricity efficiency of the PSRC system is 36%, which is equivalent to a heat rate of 10.1 GJ/MWh_{el}. This efficiency is relatively high compared to other PWRs designs (an average of 33%) but it is achievable with recent improvements in component efficiencies [247].

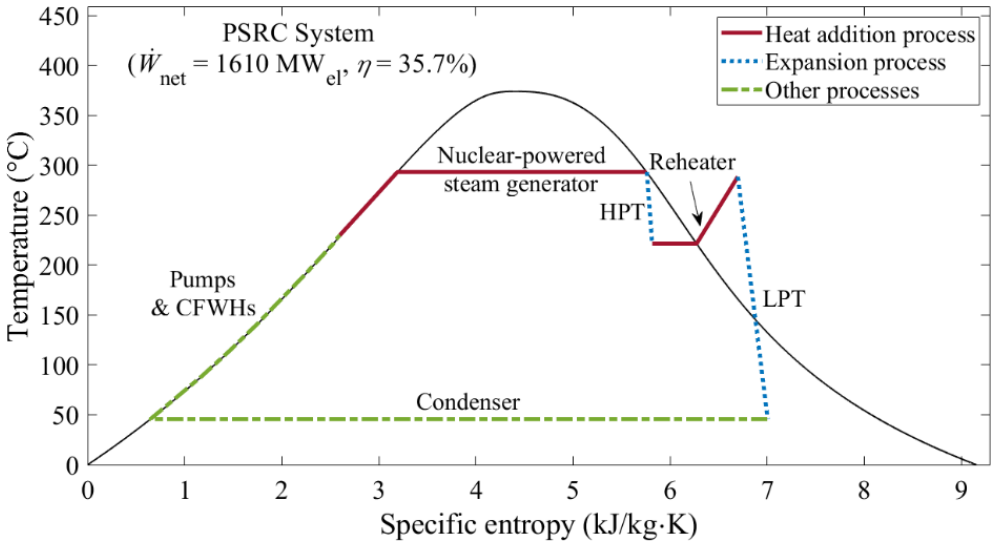

Figure 6.2. Temperature-specific entropy, *T-s*, diagram showing the thermodynamic processes of the efficiency optimised PSRC system during nominal load operation.

Table 6.6. Obtained PSRC steam parameters at nominal power.

Parameter	Value
HPT main outlet pressure (kPa)	2390
HPT main outlet temperature (°C)	221
Reheater main inlet mass flowrate (kg/s)	1880
Reheater outlet temperature (°C)	289
LPT main outlet pressure (kPa)	10
LPT main outlet mass flowrate (kg/s)	1370
Condensate pump outlet pressure (kPa)	2390
Net electrical power (MW_{el})	1610
Cycle efficiency (%)	35.7

6.6. Performance of primary steam Rankine cycle system during part-load operation mode (charging mode)

The nominal operating conditions (i.e., design isentropic efficiencies, mass flowrate, pressure, and temperature of both turbines) of the PSRC system are extracted to run the part-load PSRC system model. Figure 6.3 presents the maximum obtained cycle efficiencies, as defined in Equations (6.2) and (6.9), from 50% to 100% of nominal power (i.e., from 806 to 1610 MW_{el}).

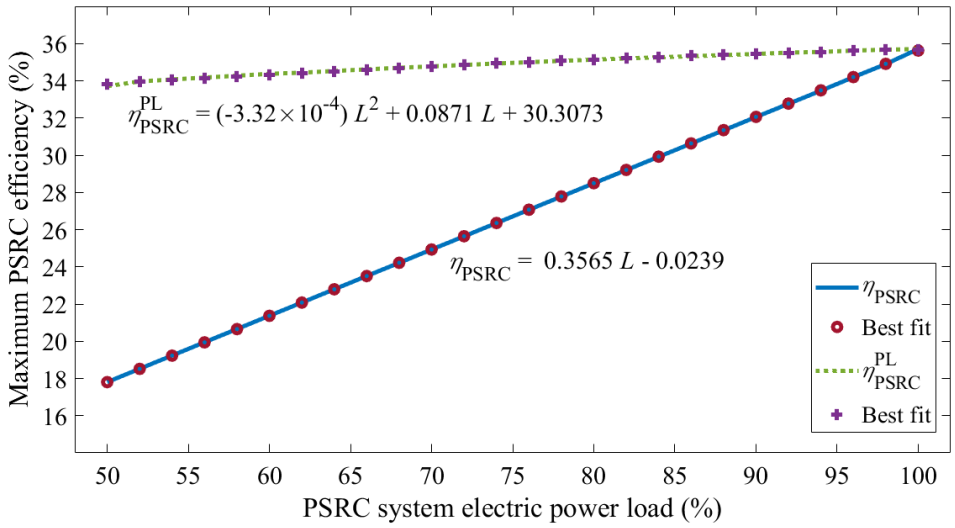

Figure 6.3. Maximum PSRC system efficiency for electric loads from 50% to 100% of nominal power. Parameter (L) in the obtained best fit correlations is the PSRC system power load in %.

The PSRC system efficiency ranges from 18% at 50% power load to 36% at 100% power load. The trend is linear since the rate of heat addition is constant for all power loads (i.e., reactor is operating at maximum thermal power level). However, the part-load PSRC system efficiency is higher for all loads, ranging from 34% at 50% power load to 36% at maximum load. The difference is less than 2% and mainly due to the decrease of turbine isentropic efficiency at part-load operations. Moreover, best fit lines are constructed for both PSRC system efficiency indicators in order to allow estimating the PSRC system efficiency and the incremental heat rate required by the whole-system model.

6.7. Performance of thermal energy storage and secondary steam Rankine cycle systems (discharging mode)

The calculated average amount of stored heat in each TES-SSRC module is 390 MWh_{th} (i.e., in all TES-1 and TES-2 tanks). This was calculated from charging thermal power of 217 MW_{th}

lasting 1 h and the assumed 90% heat-to-heat charging efficiency for TES-1 and for TES-2. In this study, it is assumed that 5 TES-SSRC modules are installed. Therefore, the calculated total amount of stored heat in the 5 modules is 1950 MWh_{th}.

Results obtained from the efficiency optimisation model of systems SSRC-1 and SSRC-2 are summarised in Table 6.7. The temperature-specific entropy (*T-s*) diagrams illustrating the thermodynamic processes of systems SSRC-1 and SSRC-2 are presented in Figure 6.4(a) and Figure 6.4(b), respectively. The steam inlet temperature is 132 °C for both cycles. However, the boiling (i.e., saturation) steam pressure at the TES inlet is higher for system SSRC-1 since steam is boiled at a temperature of 272 °C, which is 10 °C below the melting temperature of PCM-1.

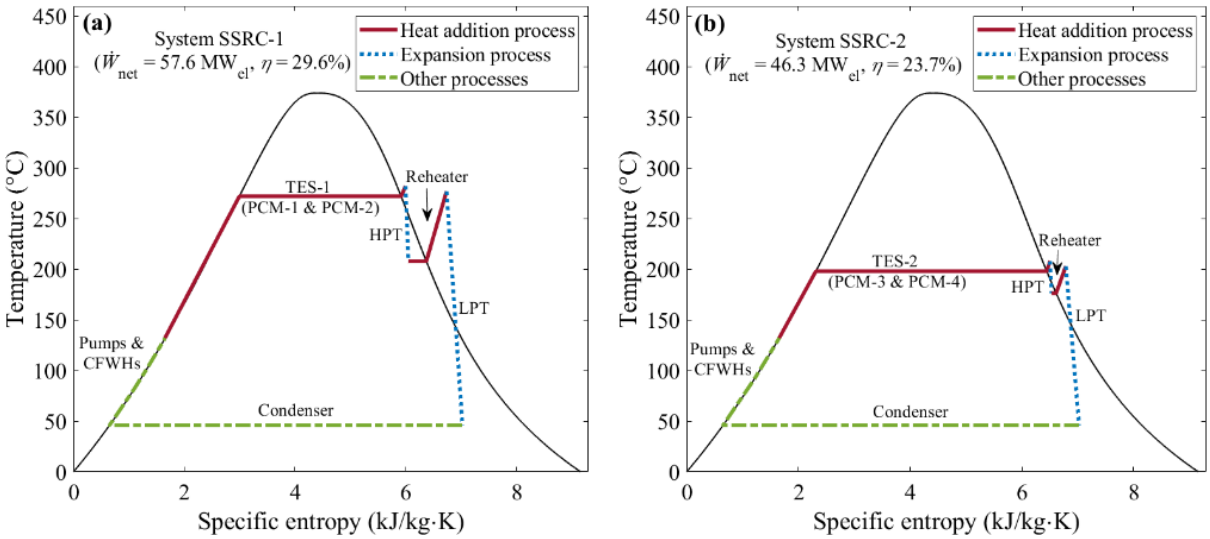

Figure 6.4. Temperature-specific entropy, *T-s*, diagrams indicating the thermodynamic processes of the efficiency optimised SSRC systems. (a) is for system SSRC-1 and (b) is for system SSRC-2.

For system SSRC-2, the maximum temperature is 208 °C and steam is boiled at 198 °C (saturation pressure of 1490 kPa). System SSRC-1 delivers 57.6 MW_{el} of net electric power, resulting in a cycle efficiency of 30%, while system SSRC-2 generates 46.3 MW_{el} of electric power at 24% of cycle efficiency. Although system SSRC-2 efficiency is relatively high, it operates at low pressure and temperature ranges that are not recommended for steam Rankine cycles. Thus, other working fluids such as organic fluid will be considered and compared with steam in future research. The total amount of electrical power from one TES-SSRC module is 104 MW_{el}, which results in 520 MW_{el} output if all 5 installed modules are simultaneously discharging at full rated power capacity. Hence, the maximum power output of the proposed

configuration is 2130 MW_{el} (1610 MW_{el} from the PSRC and 520 MW_{el} from the SSRCs), which is 32% higher than the nominal PSRC system power output. The electricity-to-electricity roundtrip efficiency, which is defined as the amount of electricity generated from all SSRC systems (520 MWh_{el}) divided by the amount of electricity that could be generated from the PSRC system (805 MWh_{el}) during the TES charging phase is 64%.

Table 6.7. Main operating parameters of SSRC systems for 1 h discharging duration.

Parameter	SSRC-1	SSRC-2
TES discharging thermal power (MW_{th})	195	195
TES steam inlet temperature (°C)	132	132
TES steam outlet temperature (°C)	282	208
TES steam mass flowrate (kg/s)	77.2	77.5
TES steam inlet pressure (kPa)	5680	1490
Condensing pressure (kPa)	10	10
Reheater outlet temperature (°C)	277	203
Net electrical power (MW_{el})	57.6	46.3
Cycle efficiency (%)	29.6	23.7

6.8. Benefits of flexible nuclear in low-carbon electricity systems

The results of whole system benefit assessment of flexible nuclear across the two systems considered in this study are shown in Figure 6.5 and Figure 6.6, for the North and South systems, respectively. The two systems are characterised by different shares of wind and solar PV generation and different seasonal demand variations. The system benefits represent annualised system cost savings across different scenarios, based on annualised values for asset investment costs and annual operating costs. For all cases, system benefits are broken down into various cost components, including generation investment, operating cost (OPEX), storage investment, electrolyser investment and hydrogen storage investment. Note that the system benefits are always expressed per one flexible nuclear unit (with a PSRC system size of 1610 MW_{el}), so that in Scenario D with 5 flexible nuclear units the total system benefit was divided by 5 (other scenarios only assumed a single flexible nuclear unit). These benefits can be compared to the costs required to achieve the enhanced flexibility, i.e., the additional investment cost of TES-SSRC modules.

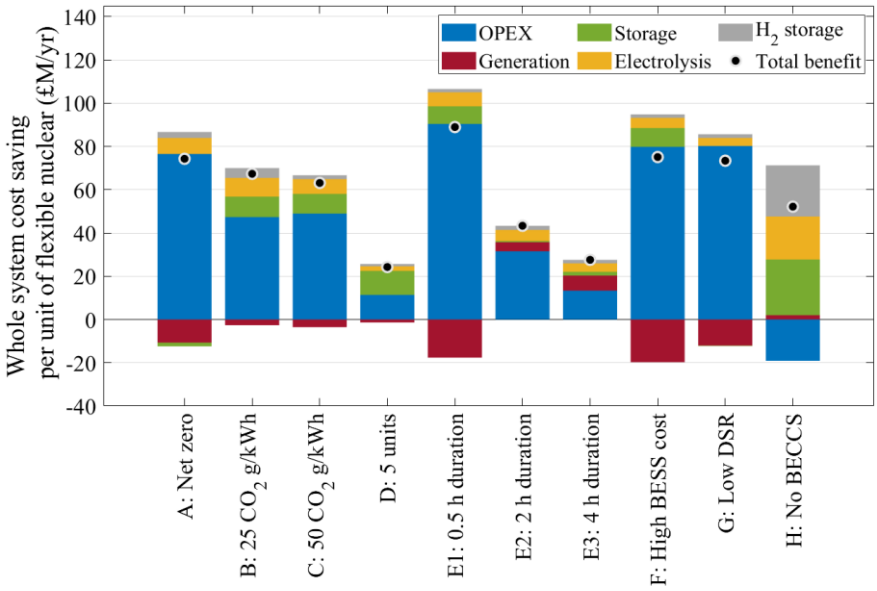

Figure 6.5. Whole system benefit of flexible nuclear across scenarios in the North system. Different components in stacked column charts represent changes in different system cost categories. Black dots represent total system benefits. The scenarios are described in Table 6.4 of Section 6.4.2.

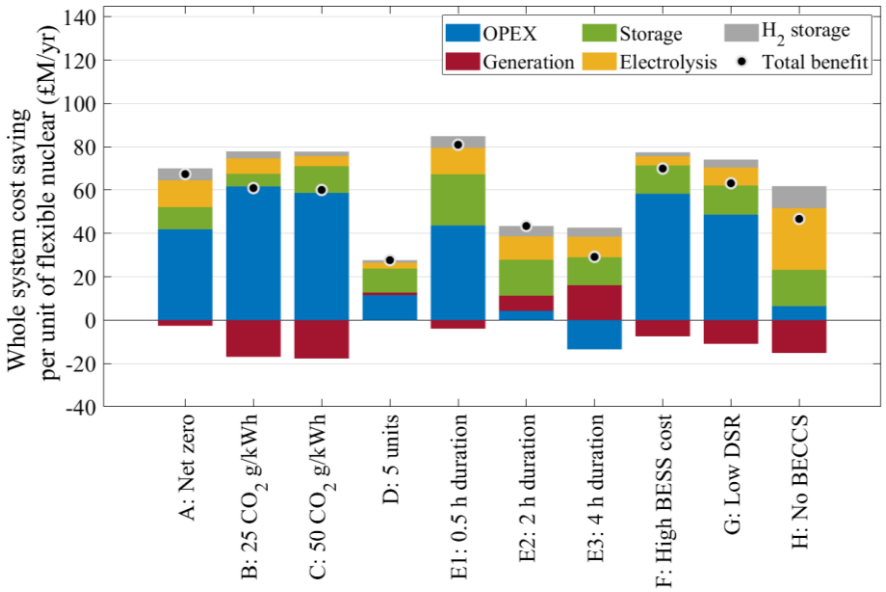

Figure 6.6. Whole system benefit of flexible nuclear across scenarios in the South system. Different components in stacked column charts represent changes in different system cost categories. Black dots represent total system benefits. The scenarios are described in Table 6.4 of Section 6.4.2.

The key conclusions from the system benefit results are as follows:

- System benefit of flexible nuclear generally consists of multiple components, indicating that the enhanced flexibility of nuclear plants can displace alternative flexibility options such as

battery and hydrogen storage with electrolysers, as well as the investment and operating cost of generation capacity. The compound benefit of nuclear flexibility can sometimes have negative components (e.g., the generation component) due to the reconfiguration of the rest of the generation mix and changes in its output, but those are more than offset by positive cost savings in other components.

- The benefit increases with more stringent carbon emission targets, from £60.1-63.1M/yr (~$75.2-78.9M/yr) with 50 gCO_2/kWh to £67.4-74.3M/yr (~$84.3-92.9M/yr) for a net-zero carbon system.
- System values observed in the North system tend to be slightly higher than in the South system if the TES-SSRC duration is 1 h. This can be explained by the higher PV and lower wind penetration in the South, and the need for longer-term flexibility (i.e., over multiple hours) to compensate for the variability of PV generation when compared to wind. For the same reason, a higher system value is observed in the South system with 4-h duration of the TES-SSRC unit.
- System benefits diminish with a larger number of nuclear units, so that with 5 flexible units the benefit per one unit is only about a third of the benefit achieved by a single unit (but still providing higher aggregate benefit for all 5 units of flexible nuclear).
- Increasing the power-to-energy ratio of SSRC generators for the same TES size results in significantly higher system benefits, and *vice versa*, but on the other hand also increases the cost of the flexible nuclear assets.
- Increasing the cost of battery storage (BESS) results in a marginally higher benefit of flexible nuclear (£75.1M/yr (~$93.9M/yr) in the North and £69.9M/yr (~$87.4M/yr) in the South), while reducing the uptake of DSR does not appear to have a material impact on the system value of flexible nuclear.
- Preventing the model to invest into BECCS carbon offsets tends to reduce the system value of flexible nuclear, which now has to compete with biomass and hydrogen generation in the counterfactual case, rather than with CCS and CCGT generation combined with carbon offsets.

Figure 6.7 and Figure 6.8 show the comparison of system net benefits with an estimate of the investment cost of enhanced flexibility for the North and the South systems, respectively. Maroon squared dots in Figure 6.7 and Figure 6.8 represent the estimated cost values (i.e., investment costs of flexible nuclear) for each scenario, while black dots are for the total system benefit. The net system benefits are presented by the blue bars, which is the difference between the total system benefit and the estimated cost of flexibility.

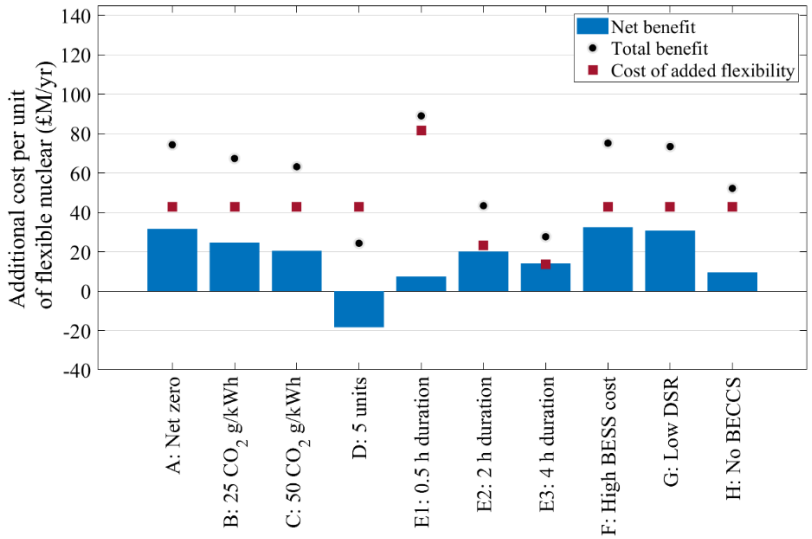

Figure 6.7. Net system benefit of flexible nuclear across scenarios in the North system calculated using total system benefits and cost of added flexibility of nuclear plants (i.e., investment cost of flexible nuclear). The scenarios are described in Table 6.4 of Section 6.4.2.

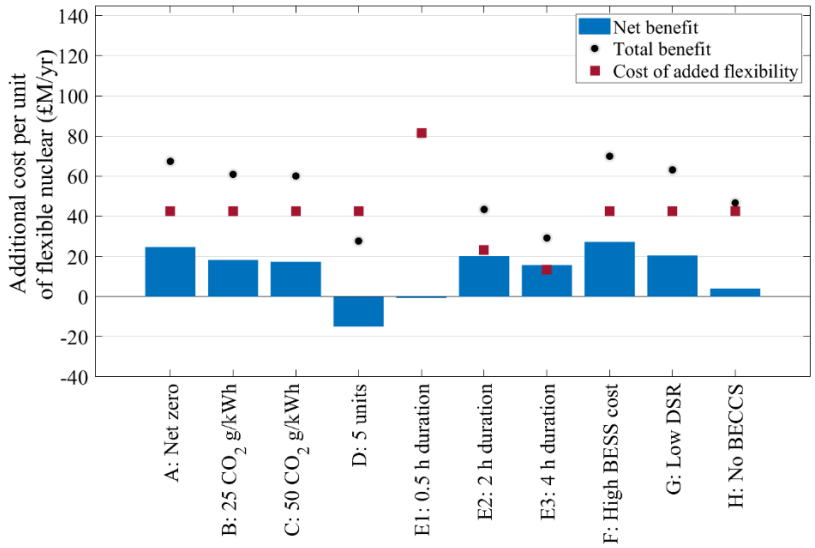

Figure 6.8. Net system benefit of flexible nuclear across scenarios in the South system calculated using total system benefits and cost of added flexibility of nuclear plants (i.e., investment cost of flexible nuclear). The scenarios are described in Table 6.4 of Section 6.4.2.

The estimated cost values are calculated based on the average cost of TES of 25 £/kWh$_{th}$ (~31.3 $/kWh$_{th}$) [55], and the cost of SSRC systems of 965 £/kW$_{el}$ (~1210 $/kW$_{el}$) [121]. With these assumptions the annualised cost of added flexibility is estimated at £42.7M/yr (~$43.4M/yr) per one unit with the default duration assumption for the TES-SSRC component of 1 h. This cost increases to £81.5M/yr (~$101.9M/yr) for 0.5-h duration and drops to

£23.3M/yr (~$29.1M/yr) and £13.5M/yr (~$16.9M/yr) for 2-h and 4-h durations, respectively. At these cost estimates the flexibility upgrade appears to be cost-efficient (i.e., its benefits exceeding the cost) in all cases for both systems (i.e., North and South) except with 5 units added to the system instead of one. The highest net benefit (i.e., the difference between total benefit and cost) is observed in the net zero and high BESS cases, at £31.6-32.4M/yr (~$39.5-40.5M/yr) in the North system and £24.7-27.3M/yr (~$30.9-34.1M/yr) in the South system.

6.9. Impact of flexible nuclear on cost-optimal technology capacity mix

The breakdown of installed power generation capacity by technology obtained from the whole-system model for the North and South systems are shown in Figure 6.9 and Figure 6.10, respectively. In both figures, (a) represents the installed capacities for the baseline case (i.e., without flexible nuclear), while (b) corresponds to the changes of those capacities after replacing the conventional nuclear plant with a flexible one across all scenarios. Each colour in the stacked columns represents different power generation technology as shown in the right-side legends of Figure 6.9 and Figure 6.10.

The capacity mix of the North system (Figure 6.9(a)) is dominated by onshore and offshore wind due to their favourable economics, along with a sizeable volume of solar PV capacity. In the South system (Figure 6.10(a)) the main source of power is solar PV generation because of a higher capacity factor than in the North system. To help with cost-effective integration of variable renewable generation, in both North and South there is a significant volume of battery storage (between 75 and 112 GW_{el} in Scenario A in North and South, respectively). Also, in both systems, with the exception of Scenario H, the generation portfolio includes about 30-35 GW_{el} of gas CCGT generation capacity that is split between conventional CCGT and CCS plant in roughly similar proportions for net zero scenarios (A, D, F and G). In Scenarios B and C, the share of unabated CCGT generation increases due to a less restrictive carbon emission constraint. To meet the net zero carbon target, Scenarios A, D, F and G also include a relatively small amount (0.6-1 GW_{el}) of BECCS capacity that acts as carbon offset and compensates for any emissions from CCGT and gas CCS plants. In Scenario H, where BECCS is not allowed to be built, the model no longer adds any CCGT or gas CCS capacity (as it is not able to offset their carbon emissions), but rather increases the amount of wind, solar PV and battery storage capacity, also accompanied by extra biomass and hydrogen CCGT capacity to provide firm zero-carbon generation.

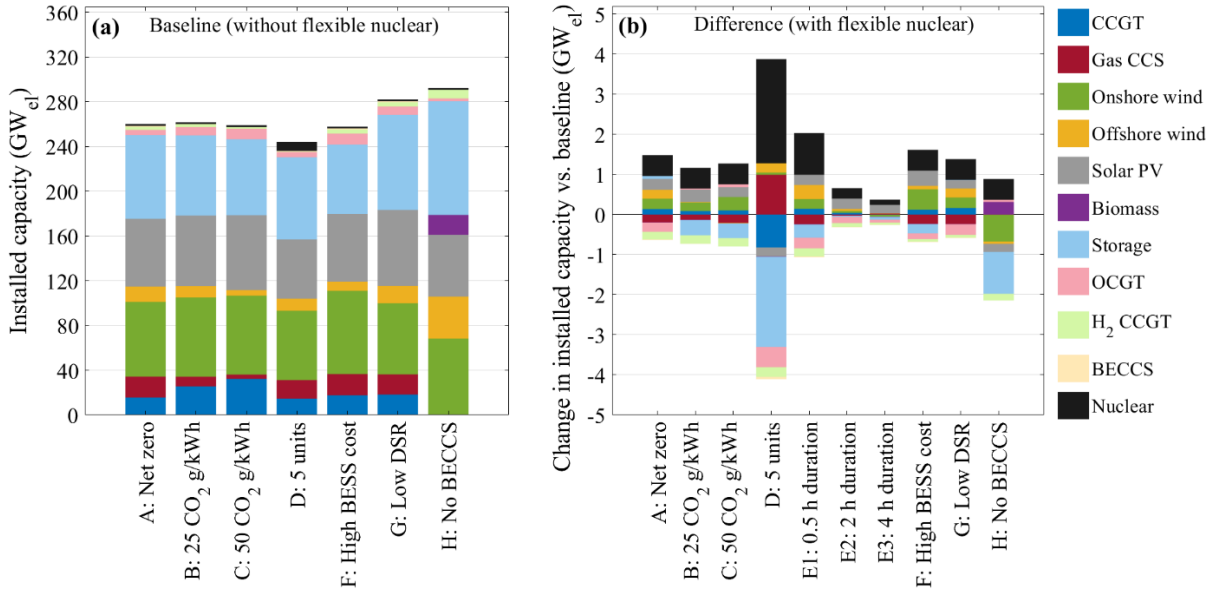

Figure 6.9. (a) Installed power capacity of conventional nuclear power with the other power generation technologies (i.e., baseline), and (b) changes in installed capacity with flexible nuclear in the North system for the considered scenarios that are described in Table 6.4 of Section 6.4.2. The results for Scenarios E1, E2 and E3 were obtained relative to Scenario A.

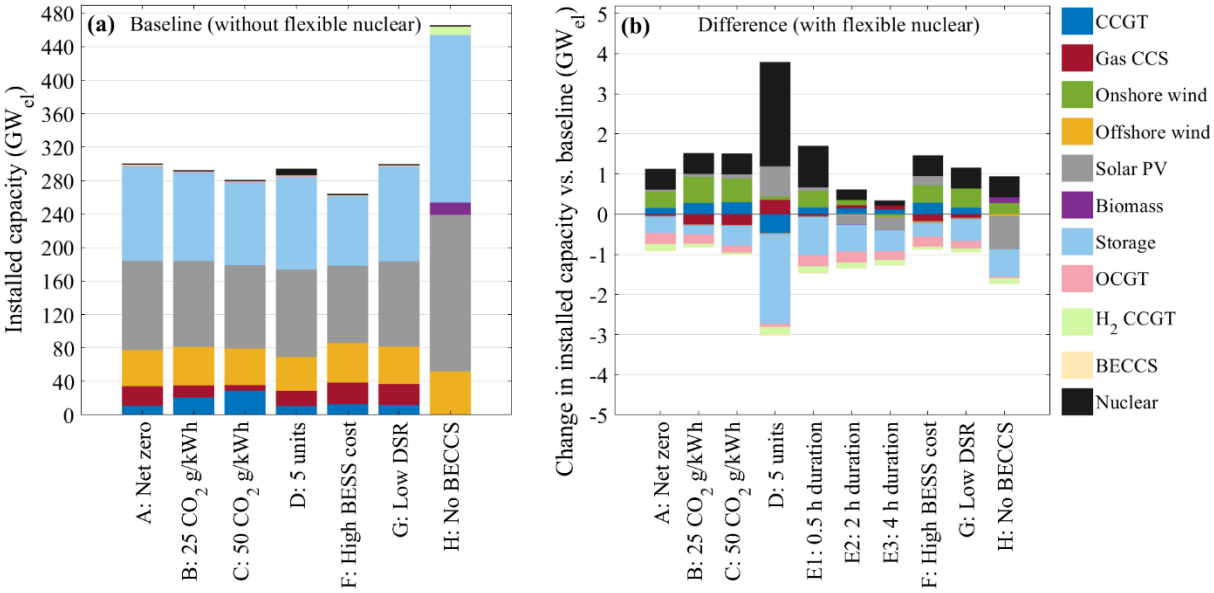

Figure 6.10. (a) Installed power capacity of conventional nuclear power with the other power generation technologies (i.e., baseline), and (b) changes in installed capacity with flexible nuclear in the South system for the considered scenarios that are described in Table 6.4 of Section 6.4.2. The results for Scenarios E1, E2 and E3 were obtained relative to Scenario A.

Figure 6.9(b) and Figure 6.10(b) show how the cost-optimal capacity mix changes when the nuclear units in the system are made more flexible by adding TES and SSRC components. The increase of nuclear capacity (i.e., 520 MW_{el} for most scenarios except for Scenarios D, E1, E2, and E3) in Figure 6.9(b) and Figure 6.10(b) is a result of replacing the conventional nuclear units (1610 MW_{el}) with the added flexibility ones (2130 MW_{el}). This increase is a predetermined choice and not optimised by WeSIM, as the intention of the analysis was to investigate the change of the installed power capacities of other technologies resulting from replacing conventional nuclear units with added flexible ones. The determination of the optimal flexible nuclear capacities is evaluated in a different research study covered in Ref. [248]

Although there are many complex interactions in the impact of flexible nuclear on the technology mix, there is a general trend that making nuclear more flexible increases the capacity of wind and solar PV and to a smaller extent gas CCGT, while reducing the capacity of gas CCS, hydrogen CCGT and battery storage. This is driven by the increased flexibility of nuclear, which both increases the capability of the system to cost-effectively integrate variable renewables, and on the other hand reduces the requirements for other means of flexibility such as battery storage, or dispatchable low-carbon generation such as gas CCS or hydrogen CCGT. Note that the utilisation of flexible nuclear will inevitably lead to some energy losses due to storing and releasing heat from the TES system, which means that at an annual level more electricity needs to be generated, and the least-cost solution suggests this should be mostly done using renewables.

In Scenario H, where BECCS is not allowed as an option, flexible nuclear reduces the need for producing hydrogen from electrolysis and using it in hydrogen CCGT generation. Some of the hydrogen generation is replaced by a slight increase in the capacity of biomass generation. Lower electricity requirements for electrolysis also lead to a net reduction in renewable generation capacity in that scenario as well as lower requirements for battery storage.

6.10. Operation of a flexible nuclear power plant

The utilisation of individual components of a flexible nuclear plant on an hourly basis are illustrated in Figure 6.11 and Figure 6.12. The example shown in Figure 6.11 represents a winter week in the North system, while the one shown in Figure 6.12 represents a summer week in the South system. Both figures include hourly profiles for SG heat output, power output from PSRC and SSRC systems, and net heat output from TES (difference between discharging and

charging). To help identify key drivers for the operating patterns of flexible nuclear, the chart also presents the level of net demand in the system, which is obtained as the difference between total system demand (before any DSR or battery storage actions) and total variable renewable output, which included onshore and offshore wind and solar PV generation.

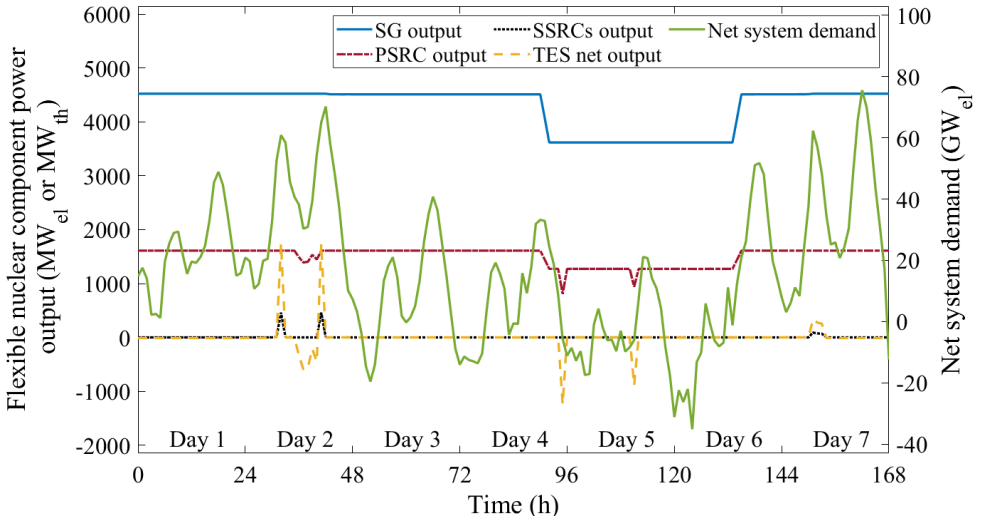

Figure 6.11. Hourly operation of flexible nuclear generation during a winter week in the North system. Net system demand represents the difference between system demand and total wind and solar PV output, and is plotted against the right-hand axis.

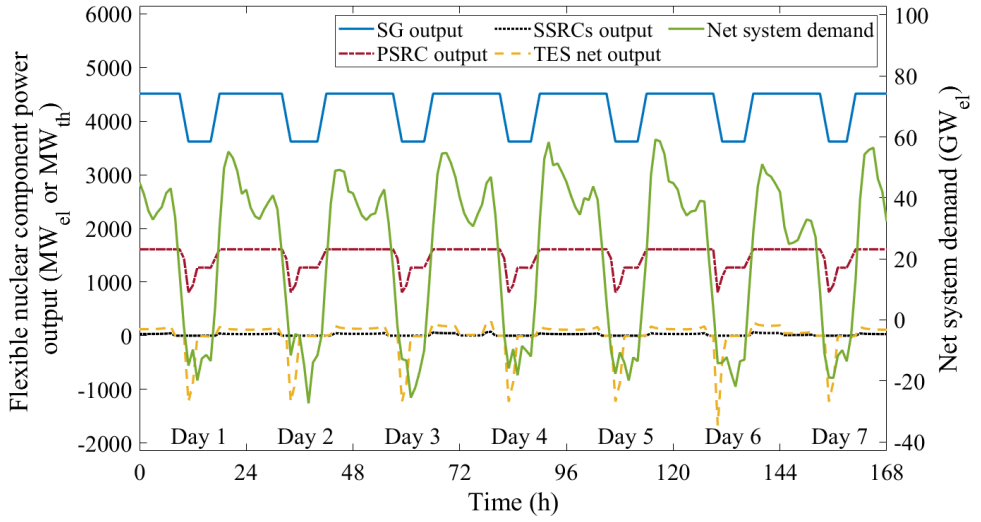

Figure 6.12. Hourly operation of flexible nuclear generation during a summer week in the South system. Net system demand represents the difference between system demand and total wind and solar PV output, and is plotted against the right-hand axis.

As expected, the SSRC generation is activated only during periods of high net demand (i.e., during periods of low renewable output) when energy in the system is scarce, which in the example shown in Figure 6.11 occurs on the second and seventh day of the week. Note that SSRC generator is not always operating during high net demand conditions given that there are other forms of flexibility (DSR and battery storage) with time-varying availability that are also optimised by the model. Heat stored in TES units is replenished during periods of relatively lower net demand, which is observed at midday on Day 2, and around midnight and midday on Day 5. Also note that during Days 5 and 6 the supply of renewable electricity is so abundant that it results in very low or even negative net demand. The SG output on those days is therefore adjusted downwards by 20% (corresponding to the lowest allowed operating point), and so is the PSRC system output, which is further reduced down to 50% of nominal output during those hours when heat is stored into TES units.

In the South system during the summer (i.e., example shown in Figure 6.12), the net demand follows a regular pattern of being during the night and low or even negative during the day, due to high solar PV output in the South. Similar to the North system, the SSRC generators are activated during high demand periods, while the TES charging takes place when the net demand is low and there is excess electricity produced by solar PV generation. It is also observed that the thermal power output from the PSRC system is reduced by 20% during low demand periods around midday and further reduced to 50% of nominal power when charging the TES units.

6.11. Summary and conclusions

A combined thermoeconomic (i.e., thermodynamic and economic) analysis of an upgraded nuclear power plant coupled with thermal energy storage (TES) and secondary power generators was presented. The analysis also included a quantification of the benefits of operating such flexible nuclear power plants in a low-carbon electricity UK system, with results transferable to electricity infrastructure similar to that of the UK. The thermodynamic modelling and optimisation framework presented here allow for the identification of the optimal operating conditions of the primary power generation system during both nominal load and part-load operations, as well as for the determination of the technical design constraints of the proposed modular TES and secondary steam Rankine cycle (SSRC) units. Moreover, the whole-system electricity model enables a quantification of the system value of the enhanced flexibility that such nuclear plants can offer in the context of decarbonising the electricity supply with a high share of variable renewables.

The thermodynamic performance of the primary steam Rankine cycle (PSRC) system of the considered nuclear power plant (European pressurised reactor) was investigated during nominal load and part-load operation modes by taking in consideration the operation of steam turbines at off-design conditions. Results revealed a maximum PSRC thermal efficiency at 100% power load of 36%, which decreased to 34% at 50% power load while the TES charging process was performed, mainly due to the reduced turbine isentropic efficiencies at off-design conditions. Moreover, performance predictions showed that the proposed configuration of adding flexibility through the coupling with PCM-based TES and SSRC systems has the potential to increase overall power output during peak load by 32% (relative to the baseload nuclear plant's nominal rated power) during full TES discharge mode, from 1610 MW_{el} to 2130 MW_{el}, with an overall electricity-to-electricity roundtrip efficiency of 64%, with the 520 MW_{el} of additional peak power being generated by the five installed TES-SSRC modular units. The peak power output can be further increased in cases where additional TES-SSRC modules are installed (i.e., more than five) or when the SSRC generators are sized with a higher power-to-energy ratio utilising the current TES system capacity.

The whole-system economic benefits of a such flexible nuclear plants were quantified by finding the reduction in the total system electrical infrastructure cost resulting from replacing conventional with flexible nuclear plants for several scenarios in the context of the UK's national electricity system. Two generic systems were analysed: North and South (i.e., with different wind and solar PV capacity factors and seasonal demand variations), both sized to approximately match the UK's electricity system with an annual generated electricity of 400 TWh_{el}. Economic benefits of up to about £75M/yr (~$93.4M/yr) were identified in the majority of the analysed scenarios, which equates to almost £1bn (~$1.25bn) in capitalised benefits of flexibility over the lifetime of a single plant. Moreover, the highest net benefit (i.e., the difference between total benefit and the cost of added flexibility of £42.7M/yr (~$53.4M/yr) for 1-h TES discharge duration) was observed in the net zero and high BESS scenarios, at £31.6-32.4M/yr (~$39.5-40.5M/yr) in the North system and £24.7-27.3M/yr (~$30.9-34.1M/yr) in the South system. Nevertheless, the value was found to vary considerably with system characteristics such as the composition of the low-carbon generation mix, carbon target, level of flexibility, and plant parameters such as SSRC duration. This suggests that the value of this technology will be system-dependent, and that system characteristics should be adequately considered when evaluating the benefits of different flexible nuclear plant configurations and choosing the most cost-effective designs and operational characteristics.

The results obtained and the main conclusion drawn from the investigated case study in this chapter provides adequate answers to Research Questions 2 and 3 and adequately fills the identified Research Gaps 2 and 3 that are listed in Section 2.8. Future work recommendations related to the presented study in this chapter are discussed in Section 8.3.

Chapter 7
Design and operation of a hybrid nuclear-solar power plant

7.1. Introduction

Nuclear power plants (NPPs) with load following capabilities are currently required in the energy mix due to the high penetration of renewables that compete with nuclear power in providing baseload demand [249]. However, it is not economically favourable to run nuclear reactors at power levels below the full rated thermal power since it takes longer times to have positive economic returns. Several studies proposed combining NPPs with renewables (i.e., solar thermal power or wind) to create a hybrid system that allows NPPs to operate at constant full rated thermal power. The hybrid systems manage to meet the fluctuating energy demand and utilise the excess thermal energy from the combined resources for other heat applications [21]. Therefore, the hybridisation concept has the potential of delivering flexible power with improved NPPs capital investment return.

Solar energy, in the form of concentrated solar power (CSP), is rapidly growing technology due to its capabilities of providing high temperature thermal power. However, the main disadvantage of CSP plants is their high dependence on weather conditions, which can be tackled by using thermal energy storage (TES) systems that are capable to store excess heat for a period of time and then discharge the stored heat to generate power during low or no sunlight periods. Still, the storage period might not be sufficient to deliver electricity in severe conditions when there are no sun rays for several days (i.e., cloudy days) [22]. Therefore, it is important to investigate the options of increasing the availability and the capacity factors of CSP plants. One option to do that is to hybridise CSP plants with other power plants that have high availability factors such as biomass or nuclear [23,24,250,251].

In this context, the study presented in this chapter evaluates the option of combining nuclear reactor with solar power and integrate them with a TES system to form a hybrid nuclear solar

power plant. The main objectives of the study are: (i) investigating the load following capabilities of a hybrid nuclear-solar power plant while operating the nuclear reactor at full rated thermal power; (ii) assessing the potential of reaching higher power cycle efficiency by the hybridisation concept; and (iii) finding the optimal TES system capacity and solar field size for a specific geographical location. Specifically, the main novel contributions of the study discussed in this chapter include:

- A technology-rich approach and cost-based design optimisation of a hybrid nuclear-solar power plant based on detailed thermodynamic modelling of various individual plant components (solar field, generators, turbines, two-tank molten salt TES tanks, feed pumps, condensers, feedwater heaters, etc.) and including consideration of part-load operation conditions during load following modes.
- Optimisation of the thermodynamic performance of the designed hybrid nuclear-solar power plant configuration at load following modes (part-load conditions).
- Parametric optimisation that determines the most profitable solar field size and the TES system capacity for a selected geographical location.
- Cost estimation of all hybrid nuclear-solar power plant components using dedicated and comprehensive costing methods.
- Comparison of the anticipated thermodynamic and economic performances between a nuclear-only power plant and the designed hybrid nuclear-solar power plant.
- Profitability assessments of nuclear-only and hybrid nuclear-solar power plants for a range of electricity prices and different economic assumptions.

The study presented in this chapter firstly describes in Section 7.2, the layouts of the nuclear-only and the hybrid nuclear-solar power plant. The model inputs, the main assumptions and the design optimisation procedure are presented in Section 7.3. The thermodynamic and the economic evaluations of nuclear-only and the designed hybrid power plants are presented in Sections 7.4 and 7.5, respectively. The sizing of the solar field and TES system capacity are discussed in Section 7.6, while the operation of the designed hybrid power plant is presented in Section 7.7. The thermo-economic comparison and the profitability assessment of for the two power plants are discussed in Sections 7.8 and 7.9. Finally, the key findings and conclusions of the study are summarised in Section 7.10.

7.2. Description of selected power plant configurations

The two selected power plant configurations (nuclear-only and hybrid nuclear-solar) are described in Sections 7.2.1 and 7.2.2, respectively. Both configurations share the same nuclear island (i.e., SMR and steam generator) components. The selected SMR design in this study is NuScale, which is a PWR that generates 250 MW_{th} of thermal power using nuclear fission [114]. Although there is a wide range of SMR types and designs, the NuScale design is chosen in this study as it represents the PWR group that have limits in terms of temperatures and thermal efficiencies, which can be improved by the hybridisation concept. Moreover, the thermal power generation capacity of NuScale is comparable to most CSP plants in terms of output thermal power. Also, NuScale design is already approved and certified by the United States Nuclear Regulatory Commission (NRC) – first SMR approved by the NRC – and it is ready to get commercialised in the next few years [112]. The main operation parameters of NuScale are listed in Table 7.1

Table 7.1. Main operation parameters of NuScale [11,117–119]

Parameter	Symbol	Value
Reactor thermal power (MW_{th})	$\dot{Q}_{SG}$	250
Steam generator inlet temperature (°C)	$T_{SG,in}$	149
Steam generator outlet temperature (°C)	$T_{SG,out}$	306
Steam generator inlet pressure (kPa)	$P_{SG,in}$	3800
Steam generator pressure loss (kPa)	ΔP_{SG}^{loss}	300
Steam generator mass flowrate (kg/s)	$\dot{m}_{SG}$	108

7.2.1. Nuclear-only power plant

The layout of the studied nuclear-only power plant, illustrated in Figure 7.1, consists of typical nuclear power plants components such as:

1) A nuclear power island that includes a PWR and a steam generator, which generates steam utilising nuclear thermal power.
2) A power generation block that contains a steam turbine, a condenser, an electric generator, four closed feedwater heaters (CFWH), a deaerator, throttling valves, control valves, a condensate pump, a feed pump, a circulation pump, and a cooling tower.

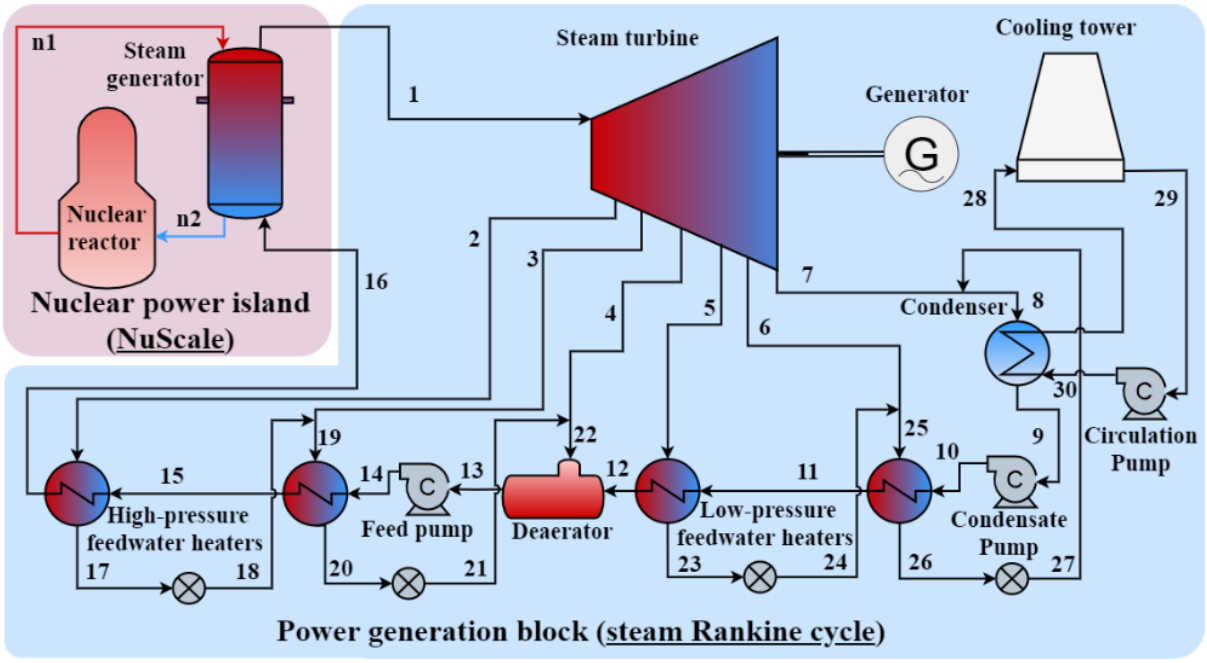

Figure 7.1. Schematic diagram of nuclear-only (NuScale) power plant.

Like in most nuclear power plants, the reactor is assumed to operate at full rated thermal power most of the time (without load following) in order to supply baseload demand and also to maximise the economic benefit of this capital-intensive energy source. The same assumption is applied in the hybrid nuclear-solar power plant in order to have a fair comparison and to investigate the potential of the achieving better thermodynamic and economic benefits during load following operations.

7.2.2. Hybrid nuclear-solar power plant

The layout of the proposed nuclear power plant, presented in Figure 7.2, consists of:

1) A nuclear power island that includes a PWR and a steam generator, which generates steam utilising nuclear thermal power.
2) A power generation block that contains a superheater, a reheater, a high-pressure steam turbine, a low-pressure turbine, a condenser, an electric generator, four CFWHs (two low pressure and two high pressure), a deaerator, throttling valves, control valves, a condensate pump, a feed pump, a circulation pump, and a cooling tower.
3) A concentrated solar power field that contains a solar tower topped with an external receiver and surrounded by a field of heliostats.
4) A two-tank molten salt TES system to store extra heat, which is discharged during low- or no-sun periods.

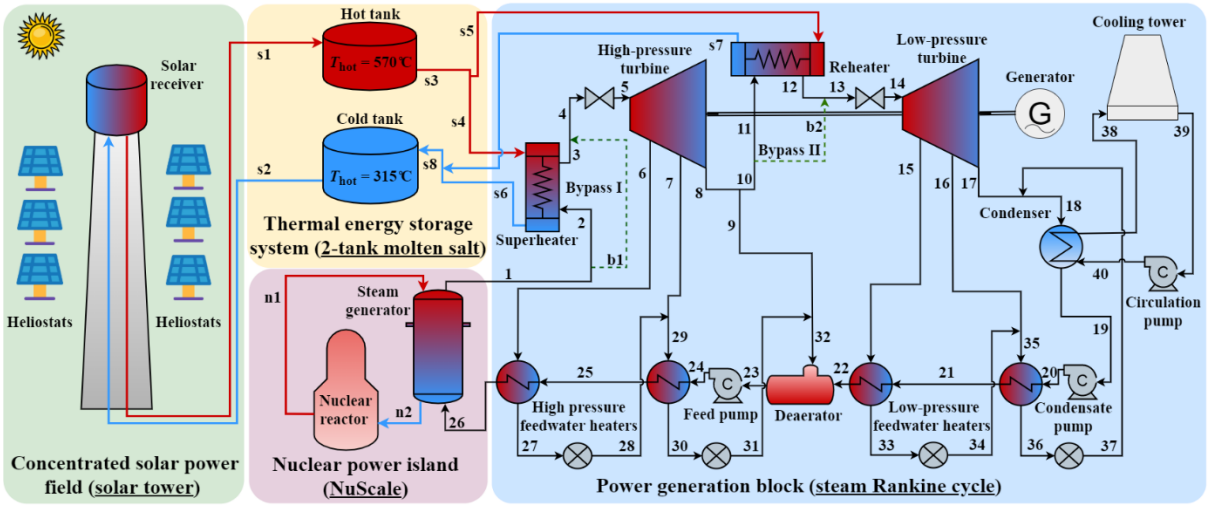

Figure 7.2. Schematic diagram of the proposed hybrid nuclear-solar power plant with two-tank molten salt thermal energy storage system.

In this configuration, the reactor is also assumed to continuously operate at full rated thermal power to avoid power disturbance in the reactor and to maximise the economic benefits. In this context, most load following operations are achieved by controlling: (i) the rate of added heat in the solar superheater; (ii) the rate of added heat in the solar reheater; (iii) the steam mass flowrate bypassing the solar superheater (Stream b1, green dashed line in Figure 7.2); and (iv) the steam mass flowrate bypassing the solar superheater (Stream b2, green dashed line in Figure 7.2). This load following control method can be achieved to about 50-60% of nominal electrical power output, which is still acceptable since such hybridisation concept provides flexibility, to some degree, with continuous operation of the nuclear reactor.

During nominal (full-load) operation mode where there is an adequate sunlight to operate the receiver or enough stored heat in the TES system, the generated steam in the steam generator flows into the superheater, get superheated, then expends in the high-pressure turbine, get reheated in the solar reheater, and then expands again in the low-pressure turbine to the condensing pressure, get condensed in the condenser, and then pumped and preheated in a series of pumps and CFWH until meeting the specified steam generator inlet condition. The TES system charging process is performed when there is extra heat in the solar receiver (Streams s1 and s2), which usually occurs during mid-day hours. The stored heat is then discharged during low/no sunlight periods or during peak demand periods, depending on the chosen operation method and type of electricity market.

7.3. Model inputs and optimisation procedure

This section highlights the design and the optimisation procedure of the nuclear-only and the hybrid nuclear-solar power plants at nominal power output and part-load operating conditions.

7.3.1. Nuclear-only power plant optimisation procedure and key assumptions

The main NuScale operating parameters considered for the design of the power generation block of the nuclear-only power plant are summarised in Table 7.1. Not all the power generation block parameters (e.g., turbine side extraction pressures and mass flowrates) of NuScale are available in the literature as most attached power generation blocks are designed for several NuScale modules. Therefore, the design of power generation block for the nuclear-only power plant in this study was achieved by formulating an optimisation function (i.e., lowest specific investment cost (SIC)) as expressed in Equation (7.1). This optimisation function determines the turbine side extraction steam pressures and flowrates that gives the minimum SIC of the nuclear-only power plant while meeting the main reported parameters of the NuScale power plant such as net electric power output. This method allows to have a fair comparison with the hybrid nuclear-solar power plant (discussed in Section 7.3.2). The nuclear-only power generation block optimisation tasks were solved using MATLAB's interior point algorithm *fmincon* [108]. This algorithm identifies local minima for a given initial point. Therefore, the optimisation task was performed multiple times for different set of initial conditions in order to find the global minimum.

$$\min_{P_{\mathrm{T,SE(1,2,3,4,5)}},\ \dot{m}_{\mathrm{T,SE(1,2,3,4,5)}}} \{SIC_{\mathrm{NO}}\} \tag{7.1}$$

where SIC_{NO} is the specific investment cost of the nuclear-only power plant, $P_{\mathrm{T,SE(1,2,3,4,5)}}$ the pressures of the first, second, third, fourth and fifth turbine side extraction and $\dot{m}_{\mathrm{T,SE(1,2,3,4,5)}}$ the steam mass flowrates of the first, second, third, fourth and fifth turbine side extraction.

The objective function (Equation (7.1)) was formulated to solve the numerical quasi-steady power generation cycle model (i.e., detailed model description is covered in Section 3.4.1) while satisfying a set of non-linear constraints listed in Equations (7.2)-(7.6):

$$\Delta T^{\mathrm{in}}_{\mathrm{pp,CFWH}} \geq 5\ ^{\circ}\mathrm{C} \tag{7.2}$$

$$\Delta T^{\mathrm{out}}_{\mathrm{pp,CFWH}} \geq 5\ ^{\circ}\mathrm{C} \tag{7.3}$$

$$\Delta T_{\mathrm{LM,CFWH}} \geq 5\ ^{\circ}\mathrm{C} \tag{7.4}$$

$$P_{\mathrm{TV}}^{\mathrm{out}} = P_{\mathrm{HL,CFWH}}^{\mathrm{in}} \tag{7.5}$$

$$x_{\mathrm{P}}^{\mathrm{in}} \leq 0 \tag{7.6}$$

where $\Delta T_{\mathrm{pp,CFWH}}^{\mathrm{in}}$ and $\Delta T_{\mathrm{pp,CFWH}}^{\mathrm{out}}$ are the inlet and outlet pinch-point temperature difference of all CFWHs, $\Delta T_{\mathrm{LM,CFWH}}$ the logarithmic-mean temperature difference of all CFWH, $P_{\mathrm{TV}}^{\mathrm{out}}$ the throttling valve outlet pressure, $P_{\mathrm{HL,CFWH}}^{\mathrm{in}}$ hot-leg inlet pressure of all CFWHs and $x_{\mathrm{P}}^{\mathrm{in}}$ the inlet steam quality of all pumps.

The quasi-steady power generation cycle model was formulated based on the generic cycle assumptions that are listed in Section 3.4.1. All other specific parameters including component efficiencies, ambient conditions, etc., for this particular case study are listed in Table 7.2

Table 7.2. Main nuclear-only power plant parameters and assumptions used in the power generation cycle model at the full rated electrical power. The numbers in the symbol subscript represent stream numbers as in Figure 7.1.

Parameter	Symbol	Value	Reference
Turbine full-load isentropic efficiency (%)	η_{T}	87	[231]
Condensing pressure (kPa)	P_7	8.5	[118]
All pumps isentropic efficiency (%)	$\eta_{\mathrm{CP}}, \eta_{\mathrm{FP}}, \eta_{\mathrm{CiP}}$	85	[231]
CFWH heat-to-heat efficiency (%)	η_{CFWH}	95	[252]
Generator mechanical efficiency (%)	η_{gen}	98	[232]
Cooling water inlet temperature (°C)	T_{30}	25	[118]
Cooling water outlet temperature (°C)	T_{28}	38	[118]
Cooling water inlet pressure (kPa)	P_{30}	220	[118]
Ambient pressure (kPa)	P_{a}	101	Assumed
Pressure loss across all CFWHs (% of inlet pressure)	$\Delta P_{\mathrm{CFWH}}^{\mathrm{loss}}$	1	[252]

7.3.2. Hybrid power plant design, optimisation procedure and key assumptions

This section discusses the design and optimisation procedure of the hybrid nuclear-solar power plant at nominal (full-load) and part-load operation mode.

7.3.2.1. Design and sizing of hybrid nuclear-solar power plant

The design procedure of the hybrid nuclear-solar power plant starts by executing an optimisation function that minimises the SIC of the entire hybrid power plant at full-load and without the consideration of the TES system cost. The optimisation function is expressed as:

$$\min_{T_{\mathrm{SH,out}},\, T_{\mathrm{RH,out}},\, P_{\mathrm{HPT,SE(1,2),}}\, \dot{m}_{\mathrm{HPT,SE(1,2)}},\, P_{\mathrm{HPT,out}},\, \dot{m}_{\mathrm{DE}},\, P_{\mathrm{LPT,SE(1,2),}}\, \dot{m}_{\mathrm{LPT,SE(1,2)}}} \{SIC_{\mathrm{HNS}}\} \tag{7.7}$$

where SIC_{HNS} is the specific investment cost of the hybrid nuclear-solar power plant, $T_{\mathrm{SH,out}}$ the superheater cold-leg (i.e., working fluid) outlet temperature, $T_{\mathrm{RH,out}}$ the reheater cold-leg (i.e., working fluid) outlet temperature, $P_{\mathrm{HPT,SE(1,2),}}$ the pressures of the first and the second high-pressure turbine side extraction, $\dot{m}_{\mathrm{HPT,SE(1,2)}}$ the steam mass flowrates of the first and the second high-pressure turbine side extractions, $P_{\mathrm{HPT,out}}$ the outlet high-pressure turbine pressure, $\dot{m}_{\mathrm{DE}}$ the mass flowrate of steam flowing into the deaerator, $P_{\mathrm{LPT,SE(1,2),}}$ the pressures of the first and the second low-pressure turbine side extractions and $\dot{m}_{\mathrm{LPT,SE(1,2)}}$ the steam mass flowrates of the first and the second low-pressure turbine side extractions.

The total cost and the operation conditions of the nuclear island is the same as in the nuclear-only power plant (i.e., see Table 7.1 for NuScale operational parameters). However, the design and the cost of the solar field is variable as it depends on the 'rate of' needed heat in the solar superheater and the solar reheater. The rate of needed heat can be calculated based on the outlet steam temperature from the solar superheater and reheater, which consequently affect the size and the cost of the solar receiver and the heliostat field. Therefore, the cost of the solar field for each solar heat rate was calculated using the optimised solar field design (i.e., minimum investment cost). The cost of the optimised solar field design was performed using SAM software and assuming a solar multiple (SM) of 1.0, a design DNI of 600 W/m^2, an inlet heat transfer fluid (HTF) temperature of 310 °C and an outlet HTF temperature of 575 °C (i.e., see Section 3.2 for more details) [121]. The cost of the TES system was excluded at this stage as the TES system cost depends on the size and capacity of the TES system, which is usually determined by the operation mode and strategy.

The optimisation objective function was formulated to solve the numerical quasi-steady power generation cycle model with the addition of solar superheater and reheater (i.e.., more details about the power generation cycle model can be found in Section 3.4.1) while satisfying the following constraints, in addition to the constraints listed in Equations (7.2)-(7.6):

$$\Delta T_{\mathrm{pp,SH}}^{\mathrm{in}}, \Delta T_{\mathrm{pp,SH}}^{\mathrm{out}} \geq 10\ ^{\circ}\mathrm{C} \tag{7.8}$$

$$\Delta T_{\mathrm{pp,RH}}^{\mathrm{in}}, \Delta T_{\mathrm{pp,RH}}^{\mathrm{out}} \geq 10\ ^{\circ}\mathrm{C} \tag{7.9}$$

$$\Delta T_{\mathrm{LM,SH}} \geq 10\ ^{\circ}\mathrm{C} \tag{7.10}$$

$$\Delta T_{\mathrm{LM,RH}} \geq 10\ ^{\circ}\mathrm{C} \tag{7.11}$$

where $\Delta T_{\mathrm{pp,SH}}^{\mathrm{in}}$ and $\Delta T_{\mathrm{pp,SH}}^{\mathrm{out}}$ are the inlet and outlet pinch-point temperature difference of the solar superheater, $\Delta T_{\mathrm{pp,RH}}^{\mathrm{in}}$ and $\Delta T_{\mathrm{pp,RH}}^{\mathrm{out}}$ are the inlet and outlet pinch-point temperature difference of the solar reheater, $\Delta T_{\mathrm{LM,SH}}$ the logarithmic-mean temperature difference of the solar superheater and $\Delta T_{\mathrm{LM,SH}}$ the logarithmic-mean temperature difference of the solar reheater. These values where assumed to allow sufficient heat transfer rate between the HTF and the working fluid (steam) while maintaining acceptable sizes of superheater and reheater.

Similar to the nuclear-only power generation block, the optimisation tasks and model simulations are formulated and solved using MATLAB's interior point algorithm *fmincon* with different sets of initial conditions in order to find the global minimum [108]. Furthermore, the steam cycle model of the hybrid system adheres to the same main assumptions of the nuclear-only power generation cycle (Section 7.3.1) and mentioned in Section 3.4.1. All other power generation block parameters including component efficiencies, HTF temperature, ambient conditions, etc., for the hybrid system are listed in Table 7.3.

The selected molten salt as HTF and storage medium is solar salt (60% $NaNO_3$ + 40% KNO_3) since it is widely used in many commercial CSP solar tower projects [49], and its thermophysical properties are listed in Table 3.5 in Section 3.3.3. The hot tank and the cold tank temperatures in the two-tank molten salt TES system are assumed to be 570 °C and 315 °C, respectively. It was also assumed that there is 5 °C temperature drop during TES charging and discharging process. This means that the solar receiver inlet and outlet temperatures are respectively 310 °C and 575 °C, and the inlet and outlet temperature of the hot-leg streams in the superheater and the rehears are 565 °C and 320 °C, respectively. The calculated charging and discharging efficiencies ($\eta_{\mathrm{TES,Ch}}$ and $\eta_{\mathrm{TES,Dch}}$) that correspond to the assumed charging and discharging temperature drops were both 96%.

Table 7.3. Main hybrid nuclear-solar only power plant parameters and assumptions used in the power generation cycle model at the full rated electrical power. The numbers in the symbol subscript represent stream numbers in Figure 7.2.

Parameter	Symbol	Value	Reference
High-pressure turbine full-load isentropic efficiency (%)	η_{HPT}	87	[231]
Low-pressure turbine full-load isentropic efficiency (%)	η_{LPT}	87	[231]
Superheater and reheater hot-leg inlet temperature (°C)	$T^{\mathrm{HL}}_{\mathrm{SH,in}}, T^{\mathrm{HL}}_{\mathrm{RH,in}}$	565	Assumed
Superheater and reheater hot-leg outlet temperature (°C)	$T^{\mathrm{HL}}_{\mathrm{SH,out}}, T^{\mathrm{HL}}_{\mathrm{RH,out}}$	320	Assumed
Pressure loss across superheater (% of inlet pressure)	$\Delta P^{\mathrm{loss}}_{\mathrm{SH}}$	1	[252]
Pressure loss across reheater (% of inlet pressure)	$\Delta P^{\mathrm{loss}}_{\mathrm{RH}}$	1	[252]
Condensing pressure (kPa)	P_{17}	8.5	[118]
All pumps isentropic efficiency (%)	$\eta_{\mathrm{CP}}, \eta_{\mathrm{FP}}, \eta_{\mathrm{CiP}}$	85	[231]
CFWH heat-to-heat efficiency (%)	η_{CFWH}	95	[252]
Generator mechanical efficiency (%)	η_{gen}	98	[232]
Cooling water inlet temperature (°C)	T_{40}	25	[118]
Cooling water outlet temperature (°C)	T_{38}	38	[118]
Cooling water inlet pressure (kPa)	P_{40}	220	[118]
Ambient pressure (kPa)	P_{a}	101	Assumed
Pressure loss across all CFWHs (% of inlet pressure)	$\Delta P^{\mathrm{loss}}_{\mathrm{CFWH}}$	1	[252]

7.3.2.2. Optimisation of part-load operations

The optimisation procedure of the part-load (off-design) operation modes was performed by formulating an optimisation function with the objective of maximising the cycle efficiency at each load as the power generation block is already designed at this stage (i.e., see Section 7.3.2.1 for details), the optimisation objective function can be expressed as:

$$\max_{\dot{m}^{\mathrm{HL}}_{\mathrm{SH}}, \dot{m}^{\mathrm{HL}}_{\mathrm{RH}}, \dot{m}_{\mathrm{HPT,SE(1,2)}}, \dot{m}_{\mathrm{DE}}, \dot{m}_{\mathrm{LPT,SE(1,2)}}} \{\eta^{\mathrm{PL}}_{\mathrm{HNS}}\} \tag{7.12}$$

where $\eta^{\mathrm{PL}}_{\mathrm{HNS}}$ is the part-load cycle efficiency, $\dot{m}^{\mathrm{HL}}_{\mathrm{SH}}$ the superheater hot-leg (HTF) mass flowrate and $\dot{m}^{\mathrm{HL}}_{\mathrm{RH}}$ the reheater hot-leg (HTF) mass flowrate.

The superheater and the reheater hot-leg (HTF) mass flowrates were treated as free variables in the optimisation objective function (Equation (7.12)) as this allows controlling the rate of added heat in the superheater and the reheater. The formulated model calculates the available amount of heat to be transferred to the steam in the superheater and in the reheater. Consequently, this

determines the cold-leg (steam) mass flowrates and outlet temperatures while satisfying the designed superheater and reheater (i.e., heat exchanging areas) and the off-design overall heat transfer coefficients. Satisfying such constraints allows the model to calculate the mass flowrates of steam bypassing the superheater and the reheater for each desired power load while operating the nuclear-powered steam generator at fixed conditions. The superheater/reheater heat transfer constraints can be expresses as:

$$\dot{Q}_{\mathrm{hot}} = \dot{Q}_{\mathrm{cold}} = \dot{Q}_{\mathrm{tran}} \tag{7.13}$$

$$\dot{Q}_{\mathrm{tran}} = \alpha^{\mathrm{OD}} A^{\mathrm{D}} \Delta T_{\mathrm{LM}} \tag{7.14}$$

where $\dot{Q}_{\mathrm{hot}}$ is the rate of heat released by the hot stream, $\dot{Q}_{\mathrm{hot}}$ the rate of heat absorbed by the cold stream, $\dot{Q}_{\mathrm{tran}}$ the rate of transferred heat between the hot and the cold streams, α^{OD} the off-design heat transfer coefficient, A^{D} the heat exchanging area of the designed heat exchanger and ΔT_{LM} the logarithmic-mean temperature difference between the two flows.

The same heat transfer area constraints were applied to all CFWHs and also to the steam condenser (i.e., adjustment of cold-leg flow) during part-load operations. The off-design turbine efficiency correlation (Equation (3.85) of Section 3.4.2) for both, the HPT and the LPT, were was considered in the part-load cycle model. Furthermore, the change of steam pressure at the inlet and the outlet of each stage due to steam mass flowrate and temperature variations inside the turbine during part-load operation (i.e., Stodola's ellipse law, Equation (3.86) of Section 3.4.2) were considered in the formulated model.

7.3.3. Location and operation modes

The selected location for the case study discussed in this chapter was Duqm (Latitude: 19.65°, Longitude: 57.66°), which is a city in the Sultanate of Oman, as shown in Figure 7.3. Duqm is a coastal city (i.e., preferred for nuclear reactor for cooling purposes), and it is not very highly populated city. It is mainly an industrial city that have many factories, a dry deck, and refineries. Moreover, Oman is currently investigating the investment opportunities in green and pink hydrogen to be shipped globally from Duqm, and the implementation of the nuclear-only or the hybrid nuclear-solar power plant will help supplying the needed electrical power for hydrogen production.

Figure 7.3. Location of the city of Duqm in the Sultanate of Oman [253].

Additionally, Duqm have an acceptable DNI profile for a coastal city (an average of 630 W/m^2 at mid-day, as illustrated in Figure 7.4) which makes it attractive for solar project. The analysed Duqm DNI data was for the year of 2019 and extracted from the National Solar Radiation Database (NSRDB) supplied by the National Renewable Energy Laboratory (NREL) [254].

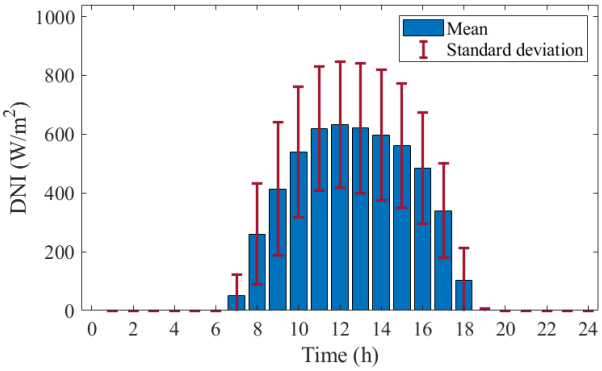

Figure 7.4. Mean and standard deviation of the hourly averaged DNI data for a whole year (year of 2019) in Duqm, Sultanate of Oman [254].

The assumed operation mode of the analysed power plant is continuous operation of the nuclear reactor at full rated power and immediate utilisation of solar power or stored heat in the TES system whenever available. This operation mode is expected to deliver continuous electrical power at nominal power output to supply surrounded end users (factories or hydrogen plants) constant electrical power whenever possible.

7.3.4. Economic model inputs

The main economic assumptions and parameters of the study presented in this chapter are listed in Table 7.4. The listed parameters were used as inputs to calculate the key economic performance indicators (i.e., discussed in Section 3.6) for both, the nuclear-only and the hybrid nuclear-solar power plants. It was also assumed that the costs of the balance of the plant and the piping are respectively 10% and 10% of the total cost of the power generation block components. Moreover, the study assumed a contingency cost that is equal of 10% of the total capital costs of the compared power plants in order to be conservative and to capture any non-considered costs (e.g., taxes, land, interest, etc.).

Table 7.4. Economic analysis assumptions [163,178,179,181].

Parameter	Symbol	Value
Nuclear fuel costs ($/MWh$_{el}$)	C_{fuel}	14
Fixed nuclear island O&M costs ($/kW$_{el}$/year)	$C_{\text{O\&M,F}}$	99.5
Variable nuclear O&M costs ($/MWh$_{el}$)	$C_{\text{O\&M,V,NI}}$	3.2
Variable solar O&M costs ($/MWh$_{el}$)	$C_{\text{O\&M,V,SF}}$	15.5
Balance of plant cost ($)	C_{BOP}	10% of C_{PGB}
Power generation block piping cost ($)	C_{Piping}	10% of C_{PGB}
Contingency ($)	C_{cont}	10% of C_{PP}
Availability factor (%)	F_{ava}	90
Lifetime of the system (years)	n	40
Discount rate (%)	r	7

The determination of the heat exchanger areas, A_{HX}, for capital cost estimation was based on using the average overall heat transfer coefficients, α_{HX}, listed in Table 7.5 and the following equation:

$$A_{\text{HX}} = \frac{\dot{Q}_{\text{tran}}}{\alpha_{\text{HX}}\,\Delta T_{\text{LM}}} \tag{7.15}$$

Table 7.5. Assumed overall heat transfer coefficients for heat exchangers.

Component	Heat exchanger type	α_{HX} (W/m^2 K)	Reference
High-pressure CFWHs	U-tube	3150	[255]
Low-pressure CFWHs	U-tube	2750	[255]
Steam condensers	Fixed head	2800	[256]
Solar superheater	U-tube	1240	[257]
Solar reheater	U-tube	665	[257]

It is also assumed in this chapter that the generated electricity from both power plants will be sold based on power purchase agreement (PPA) as this is a common practice in Oman, especially for renewable projects [258].

7.4. Nuclear only (NuScale) at full rated power

The main nuclear-only power plant thermodynamic and economic analysis results are presented and discussed in the following sections.

7.4.1. Thermodynamic performance at full rated power

The key results obtained for the optimised (lowest SIC) design of the power generation block of the nuclear-only power plant at full rated (i.e., nominal) power are listed in Table 7.6. The calculated net power output is 77.5 MW_{el} and the corresponding cycle efficiency is 31%. These values are within 1% of the officially reported values by NuScale [117]. These errors are expected and acceptable since not all operating parameters were found in the literature.

Table 7.6. Main results of the lowest SIC power generation block for nuclear-only power plant.

Parameter	Symbol	Value
Rate of heat addition in nuclear-powered steam generator (MW_{th})	$\dot{Q}_{\mathrm{SG}}$	250
First inlet LP CFWH pinch-point temperature difference (°C)	$\Delta T^{\mathrm{in}}_{\mathrm{pp,LFWH-1}}$	27
First outlet LP CFWH pinch-point temperature difference (°C)	$\Delta T^{\mathrm{out}}_{\mathrm{pp,LFWH-1}}$	33
Second inlet LP CFWH pinch-point temperature difference (°C)	$\Delta T^{\mathrm{in}}_{\mathrm{pp,LFWH-2}}$	44
Second outlet LP CFWH pinch-point temperature difference (°C)	$\Delta T^{\mathrm{out}}_{\mathrm{pp,LFWH-2}}$	50
First inlet HP CFWH pinch-point temperature difference (°C)	$\Delta T^{\mathrm{in}}_{\mathrm{pp,HFWH-1}}$	42
First outlet HP CFWH pinch-point temperature difference (°C)	$\Delta T^{\mathrm{out}}_{\mathrm{pp,HFWH-1}}$	67
Second inlet HP CFWH pinch-point temperature difference (°C)	$\Delta T^{\mathrm{in}}_{\mathrm{pp,HFWH-2}}$	21
Second outlet HP CFWH pinch-point temperature difference (°C)	$\Delta T^{\mathrm{out}}_{\mathrm{pp,HFWH-2}}$	55
First LP CFWH logarithmic mean temperature difference (°C)	$\Delta T_{\mathrm{LM,LFWH-1}}$	30
Second LP CFWH logarithmic mean temperature difference (°C)	$\Delta T_{\mathrm{LM,LFWH-2}}$	46
First HP CFWH logarithmic mean temperature difference (°C)	$\Delta T_{\mathrm{LM,HFWH-1}}$	54
Second HP CFWH logarithmic mean temperature difference (°C)	$\Delta T_{\mathrm{LM,LFWH-2}}$	36
Condensing pump electrical power input (kW_{el})	$\dot{W}_{\mathrm{CP}}$	220
Feedwater pump electrical power input (kW_{el})	$\dot{W}_{\mathrm{FB}}$	520
Circulation pump electrical power input (kW_{el})	$\dot{W}_{\mathrm{CiP}}$	430
Turbine electrical power output (MW_{el})	$\dot{W}_{\mathrm{T}}$	78.7
Net electrical power (MW_{el})	$\dot{W}_{\mathrm{net}}$	77.5
Cycle thermal efficiency (%)	η_{Cyc}	31

The temperature-specific entropy (*T*-*s*) diagram showing the main thermodynamic processes of the steam Rankine cycle (power generation block) of the nuclear-only power plant at nominal load is shown in Figure 7.5. The heat addition process taking place in the nuclear-powered steam generator is indicated by the red lines, and the steam outflowing from the steam generator is superheated to a temperature of 306 °C. Once the superheated steam reaches the turbine, it expands to a condensing pressure of 8.5 kPa (indicated by the dotted blue line). Some amount of steam is extracted from the five turbine side extraction points for feedwater heating. The steam quality at the turbine outlet is 0.82, which is still above the acceptable minimum to avoid erosion and corrosion of the steam turbine blades [87]. Once the two-phase steam reaches the condenser, it gets fully condensed in the condenser (dashed green line). The condensed steam then flows through a series of pumps and CFWHs (dashed yellow line) and such process increases the pressure of the water/steam to 3.8 MPa and the temperature to 149 °C before entering the steam generator. The calculated steam thermodynamic properties of the optimised power generation block for each numbered flow stream in Figure 7.1 are listed in Table 7.7.

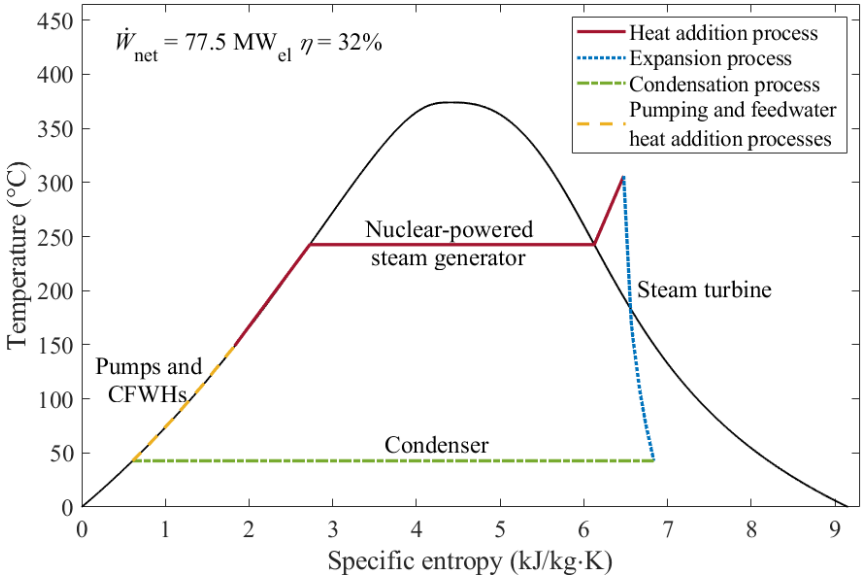

Figure 7.5. Temperature-specific entropy, *T*-*s*, diagram showing the thermodynamic processes of the nuclear-only power plant (NuScale) at full rated power output.

Table 7.7. Calculated steam thermodynamic properties at full rated electrical power of the nuclear-only power plant. The stream numbers are the same as indicated in Figure 7.1.

Stream number	Mass flowrate (kg/s)	Pressure (MPa)	Temperature (°C)	Quality (-)
n1	822	13.8	321	subcooled
n2	822	13.0	265	subcooled
1	106	3.50	306	superheated
2	8.5	0.81	171	0.98
3	6.1	0.56	156	0.96
4	3.1	0.14	109	0.90
5	1.3	0.10	101	0.89
6	1.3	0.04	77	0.86
7	85.5	0.01	43	0.82
8	88.1	0.01	43	0.80
9	88.1	0.01	43	0
10	88.1	0.16	43	subcooled
11	88.1	0.15	50	subcooled
12	88.1	0.14	57	subcooled
13	106	0.13	86	subcooled
14	106	4.22	86	subcooled
15	106	4.00	113	subcooled
16	106	3.80	149	subcooled
17	8.5	0.76	168	0
18	8.5	0.56	155	superheated
19	14.5	0.56	155	superheated
20	14.5	0.53	154	0
21	14.5	0.14	109	superheated
22	17.6	0.14	109	superheated
23	1.3	0.10	99	0
24	1.3	0.04	77	superheated
25	2.6	0.04	77	superheated
26	2.6	0.04	76	0
27	2.6	0.01	43	superheated
28	3100	0.19	38	subcooled
29	3100	0.10	25	subcooled
30	3100	0.22	25	subcooled

7.4.2. Economic performance at full rated power

The total cost breakdown of the nuclear-only power plant and the power generation block are respectively shown in Figure 7.6(a) and (b). The estimated total capital cost of the SIC optimised nuclear-only power plant is \$427M, in which 66% of the total costs is for the nuclear island, 21% for the power generation block and the rest for balance of plant, piping, and project contingency. The minimum SIC of the nuclear-only power plant that is achieved by the optimisation objective function is 5510 \$/kW$_{el}$. This minimum cost is comparable to the capital cost of currently constructed nuclear power plants around the world (2270-6920 \$/kW$_{el}$) [162]. The total cost of the power generation block is \$89M and the corresponding power generation block SIC is 1145 \$/kW$_{el}$. This power generation block SIC is higher than the average of similar sizes power generation blocks (918 \$/kW$_{el}$) as reported in Refs. [121,164,181,259]. This high cost can be considered as conservative, but it was anticipated with the recent high inflation rates (i.e., reaches 10% in the UK in 2022 compared to 2021 prices [260]) that are reflected in the latest CEPC index of 817 for year 2022, where it was only 708 in 2021 [155].

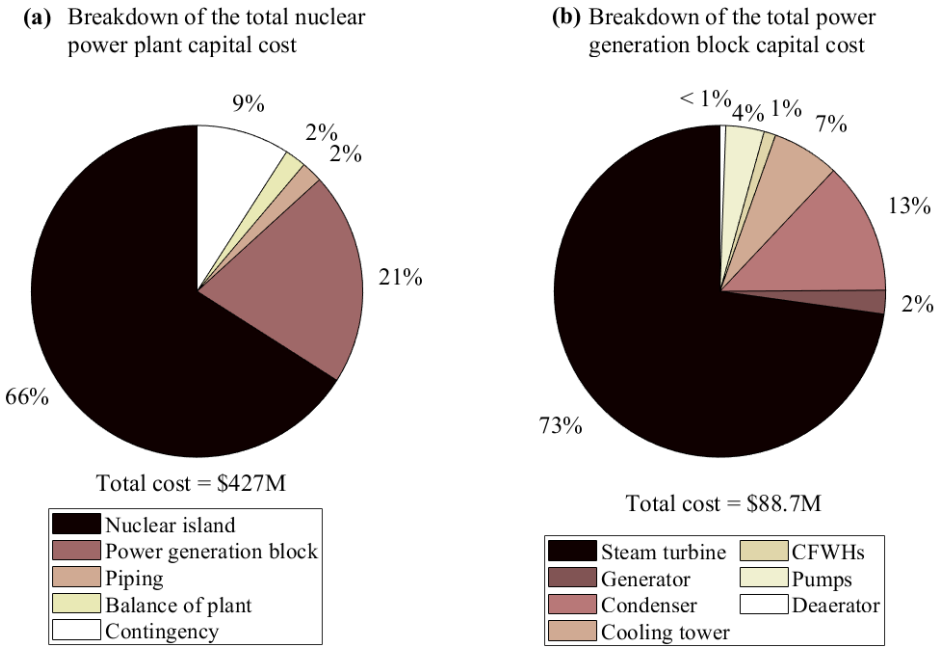

Figure 7.6. Breakdown of capital costs of: (a) nuclear power plant and (b) power generation block.

The key thermo-economic performance indicators of the designed nuclear-only power plant were calculated based on the listed assumptions in Table 7.4 and based on an electricity price (EP) of 100 \$/MWh$_{el}$ throughout the entire lifetime (i.e., under the assumption of singing a

PPA). The expected amount of generated electricity is 611 GWh_{el} which is achieved by running the reactor for 90% of the year at 100% (77.5 MW_{el}) power load. The anticipated LCOE that is calculated based on an annual operation and maintenance cost of $9.5M and an annual fuel cost of $8.5M is 79.9 $/$MWh_{el}$. The calculated LCOE is within the high end of the anticipated range (55-95 $/$MWh_{el}$) for nuclear-only power plants that is reported in the most recent cost report issued by the Nuclear Energy Agency (NEA) [162]. Moreover, the calculated NPV is $160M, payback time is 19 years, and the expected IRR is 10%. These values represent a good investment opportunity when compared to similar size power generation projects. However, such economic indicators are very dependent on the assumed discount rate and average electricity prices. Therefore, these economic indicators are also analysed for different economic assumptions, which are discussed in detail in Section 7.9.

7.5. Hybrid nuclear-solar power plant performance

The thermodynamic and economic performance of the hybrid nuclear-solar power plant are discussed in the following sections.

7.5.1. Performance at full rated power

The key thermodynamic results obtained for the optimised (lowest SIC) design of the power generation block of the hybrid nuclear-solar power plant at full rated power output are summarised in Table 7.8. The calculated net power output resulted from hybridisation concept is 131.1 MW_{el}, which corresponds to an increase of 69% of power capacity relative to the nuclear-only power plant. Such power capacity increase is achieved by the increase of the amount of heat addition in the solar superheater and the reheater. The total amount of heat addition in these two solar-powered components is 101 MW_{th}, that is 57 MW_{th} in the superheater and 44 MW_{th} in the reheater. The calculated cycle efficiency of the hybrid power plant is 37.3%, which is 20% higher than the cycle efficiency of the nuclear-only power plant. This efficiency enhancement is due to the increase of the heat addition temperature and due to the reheating process. Moreover, the solar heat-to-electricity efficiency (i.e., ratio between the extra power generation due to the hybridisation and the rate of solar heat addition) is 53.5%, which is very competitive to the current cycle thermal efficiencies of operating CCGT power plants (45-60%).

Table 7.8. Main results of the lowest SIC power generation block of the hybrid power plant.

Parameter	Symbol	Value
Rate of heat addition in nuclear-powered steam generator (MW_{th})	$\dot{Q}_{\mathrm{SG}}$	250
Rate of heat addition in solar superheater (MW_{th})	$\dot{Q}_{\mathrm{SH}}$	57
Rate of heat addition in solar reheater (MW_{th})	$\dot{Q}_{\mathrm{RE}}$	44
Solar superheater inlet pinch-point temperature difference (°C)	$\Delta T_{\mathrm{pp,SH}}^{\mathrm{in}}$	27
Solar superheater outlet pinch-point temperature difference (°C)	$\Delta T_{\mathrm{pp,SH}}^{\mathrm{out}}$	14
Solar reheater inlet pinch-point temperature difference (°C)	$\Delta T_{\mathrm{pp,RE}}^{\mathrm{in}}$	63
Solar reheater outlet pinch-point temperature difference (°C)	$\Delta T_{\mathrm{pp,RE}}^{\mathrm{out}}$	20
Solar superheater logarithmic mean temperature difference (°C)	$\Delta T_{\mathrm{LM,SH}}$	14
Solar reheater logarithmic mean temperature difference (°C)	$\Delta T_{\mathrm{LM,RE}}$	37
First LP CFWH inlet pinch-point temperature difference (°C)	$\Delta T_{\mathrm{pp,LFWH-1}}^{\mathrm{in}}$	5
First LP CFWH outlet pinch-point temperature difference (°C)	$\Delta T_{\mathrm{pp,LFWH-1}}^{\mathrm{out}}$	34
Second LP CFWH inlet pinch-point temperature difference (°C)	$\Delta T_{\mathrm{pp,LFWH-2}}^{\mathrm{in}}$	123
Second LP CFWH outlet pinch-point temperature difference (°C)	$\Delta T_{\mathrm{pp,LFWH-2}}^{\mathrm{out}}$	21
First HP CFWH inlet pinch-point temperature difference (°C)	$\Delta T_{\mathrm{pp,HFWH-1}}^{\mathrm{in}}$	33
First HP CFWH outlet pinch-point temperature difference (°C)	$\Delta T_{\mathrm{pp,HFWH-1}}^{\mathrm{out}}$	38
Second HP CFWH inlet pinch-point temperature difference (°C)	$\Delta T_{\mathrm{pp,HFWH-2}}^{\mathrm{in}}$	265
Second HP CFWH outlet pinch-point temperature difference (°C)	$\Delta T_{\mathrm{pp,HFWH-2}}^{\mathrm{out}}$	54
First LP CFWH logarithmic mean temperature difference (°C)	$\Delta T_{\mathrm{LM,LFWH-1}}$	15
Second LP CFWH logarithmic mean temperature difference (°C)	$\Delta T_{\mathrm{LM,LFWH-2}}$	58
First HP CFWH logarithmic mean temperature difference (°C)	$\Delta T_{\mathrm{LM,HFWH-1}}$	35
Second HP CFWH logarithmic mean temperature difference (°C)	$\Delta T_{\mathrm{LM,LFWH-2}}$	133
Condensing pump electrical power input (kW_{el})	$\dot{W}_{\mathrm{CP}}$	260
Feedwater pump electrical power input (kW_{el})	$\dot{W}_{\mathrm{FB}}$	437
Circulation pump electrical power input (kW_{el})	$\dot{W}_{\mathrm{CiP}}$	550
High-pressure turbine electrical power output (MW_{el})	$\dot{W}_{\mathrm{HPT}}$	49
Low-pressure turbine electrical power output (MW_{el})	$\dot{W}_{\mathrm{LPT}}$	83
Net electrical power (MW_{el})	$\dot{W}_{\mathrm{net}}$	131
Cycle thermal efficiency (%)	$\eta_{\mathrm{Cyc,nom}}$	37.3

The temperature-specific entropy (*T*-*s*) diagram illustrating the main thermodynamic processes of the power generation cycle of the hybrid nuclear-solar power plant at nominal load is presented in Figure 7.7. Similar to the nuclear-only power plant, the steam evaporation process is taking place in the nuclear-powered steam generator (i.e., illustrated by the red line in Figure 7.7), and the outlet steam condition is slightly superheated to a temperature of 306 °C.

This superheated steam is then flows through the superheater and gets superheated (i.e., dashed purple lines in Figure 7.7) to 538 °C using solar thermal power that is stored in the TES system. Afterwards, the steam expands in the high-pressure turbine to a pressure of 0.61 MPa as indicated by the dotted blue lines in Figure 7.7. Some amount of steam is extracted during the first expansion process to be directed to the high-pressure CFWH for feedwater heating purposes. Then, the steam gets reheated from 300 °C to 502 °C in the solar reheater (dashed purple lines) before entering the low-pressure steam turbine to get expanding to a condensing pressure of 8.5 kPa (dotted blue lines) to generate electrical power. The steam condition at the main outlet of the steam turbine is still in superheated condition (i.e., not in the two-phase region as in the nuclear-only power plant) due to the addition of the superheating and the reheating processes in the hybrid power plant. Some amount of steam also gets extracted from the low-pressure turbine for feedwater heating purposes. The superheated steam then gets fully condensed in the condenser (dashed green line) before flowing through a series of pumps and CFWHs (dashed yellow line). The pumping and the feedwater heating processes increase the feedwater pressure and temperature to 3.8 MPa and 149 °C, respectively, before entering the steam generator. The calculated steam thermodynamic properties of the designed power generation block of the hybrid nuclear-solar power plant at nominal power are listed in Table 7.9. The stream numbers in Table 7.9 correspond to the same stream numbers that are illustrated in Figure 7.2.

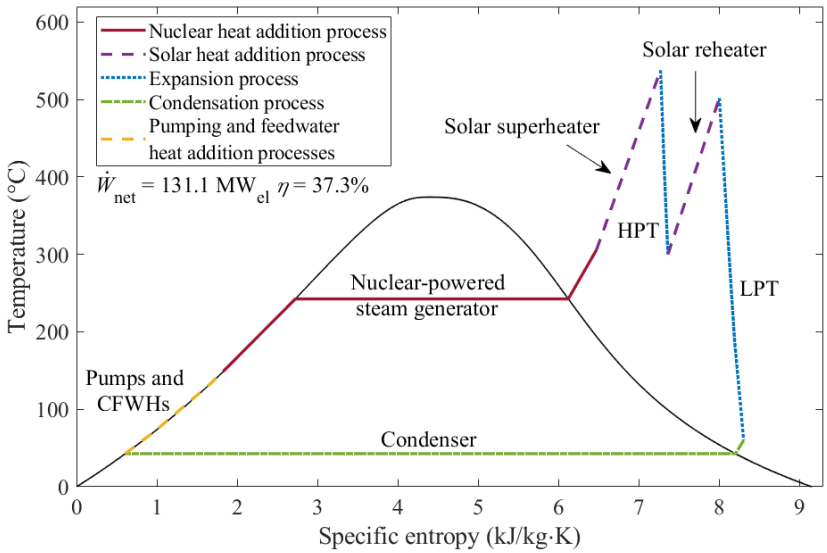

Figure 7.7. Temperature-specific entropy, *T-s*, diagram showing the thermodynamic processes of the designed power generation block (steam Rankine cycle) of the hybrid nuclear -solar power plant that corresponds to the minimum specific investment cost that satisfied the specified constraints.

Table 7.9. Calculated steam thermodynamic properties at full rated electrical power of the hybrid nuclear-solar power plant. The stream numbers are the same as indicated in Figure 7.2.

Stream number	Mass flowrate (kg/s)	Pressure (MPa)	Temperature (°C)	Quality (-)
n1	822	13.8	321	subcooled
n2	822	13.0	265	subcooled
1	106	3.50	306	superheated
2	106	3.50	306	superheated
3	106	3.47	538	superheated
4	106	3.47	538	superheated
5	106	3.47	538	superheated
6	1.1	1.49	414	superheated
7	1.1	0.92	350	superheated
8	104	0.61	300	superheated
9	1.1	0.61	300	superheated
10	103	0.61	300	superheated
11	103	0.61	300	superheated
12	103	0.60	502	superheated
13	103	0.60	502	superheated
14	103	0.60	502	superheated
15	10.3	0.08	254	superheated
16	4.9	0.04	189	superheated
17	88	0.01	60	superheated
18	103	0.01	43	superheated
19	103	0.01	43	0
20	103	0.62	43	subcooled
21	103	0.62	72	subcooled
22	103	0.61	130	subcooled
23	106	0.60	137	subcooled
24	106	3.88	138	subcooled
25	106	3.84	143	subcooled
26	106	3.80	149	subcooled
27	1.1	1.47	197	0
28	1.1	0.92	176	0.05
29	2.2	0.92	176	0.06
30	2.2	0.91	175	0
31	2.2	0.61	160	0.03
32	3.2	0.61	160	0.4
33	10.3	0.08	93	0
34	10.3	0.04	77	0.03
35	15.3	0.04	77	0.04
36	15.3	0.04	77	0
37	15.3	0.01	43	0.06
38	3950	0.19	38	subcooled
39	3950	0.10	25	subcooled
40	3950	0.22	25	subcooled

7.5.2. Thermodynamic performance at different power loads

The optimised (maximum) efficiencies for the 50% to 100% power loads (relative to nominal power load) of the hybrid nuclear solar power plants are shown on the left *y*-axis of Figure 7.8. The right y-axis of Figure 7.8 shows the thermal power input (i.e., purple area is for nuclear thermal power input and green area represents solar thermal power input) and the net power output from the hybrid power plant for 50% to 100% power loads. The maximum power load is the nominal power load that is discussed in detail in Section 7.5.1. The minimum power load is calculated when no steam is directed to the solar superheater and the reheater (all steam is bypassing the superheater and the reheater, Bypasses I and II in Figure 7.2), which represents no solar but only nuclear heat addition in the power generation cycle.

The behaviour of the maximum cycle efficiency (blue line in Figure 7.8) is nonlinearly decreasing from 37.3% at 100% power load to 26.2% at 50% power load. The decrease in the cycle efficiency is because of two main reasons. The first reason is because at part-load operation, some steam is bypassing the superheater and/or the reheater, and this results in lower turbine inlet temperatures (i.e., lower heat addition temperature) compared to nominal load. The second reason is that most cycle components (e.g., steam turbines) are operating at off-design conditions with lower efficiency and effectiveness compared to the design condition, thus, lower power output and lower cycle thermal efficiency. The effect of operating the turbines and other cycle components at off-design conditions can be clearly seen by the difference in efficiency and net power output of operating the hybrid nuclear-solar power plant using nuclear thermal power input only and of nuclear-only power plant (i.e.., discussed in Section 7.4.1). Although both power generation blocks have the same thermal power input (250 MW_{th}), the nuclear-only power plant can deliver 77.5 MW_{el} with a cycle efficiency of 31%, while the hybrid power plant can only generate 65.6 MW_{el} with a cycle efficiency of 26.2% as a result of operating the cycle components at off-design conditions. Moreover, best fit correlation is obtained for part-load efficiency in order to estimate the amount of solar heat required for each power load during the operation analysis of the hybrid power plant.

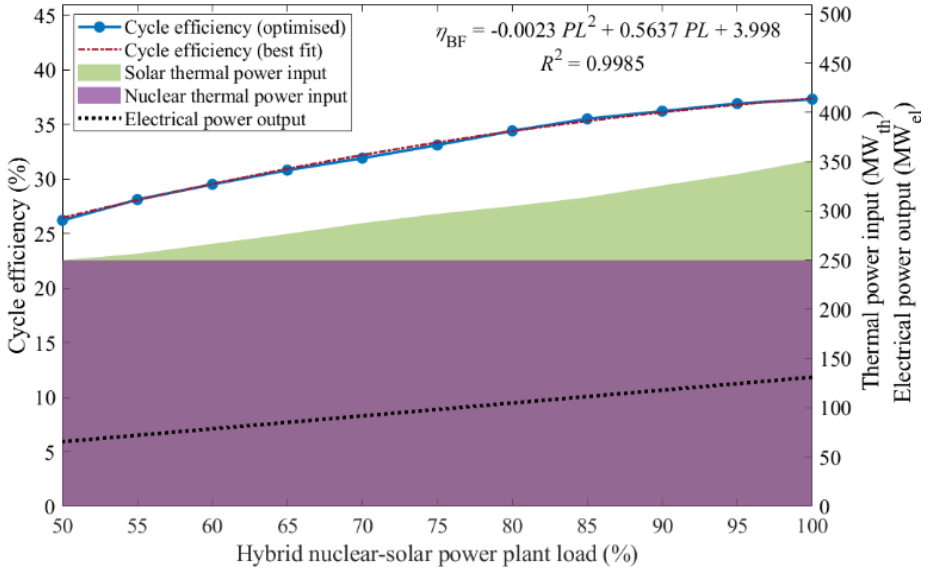

Figure 7.8. Maximum and the best fit efficiencies (left *y*-axis) for electric loads from 50% to 100% of the nominal load of the designed hybrid nuclear-solar power plant. Parameter (PL) in the obtained best fit correlation (η_{BF}) is the hybrid system electric power load in %. The corresponding thermal power input (shaded purple area represent nuclear and shaded green area represents solar) and the corresponding electrical power output for each power load are illustrated on the right *y*-axis.

The main optimised operation parameters of the hybrid power plant for different part loads are listed in Table 7.10. The listed results cover 100%, 90%, 80%, 70%, 60%, and 50% power outputs of the maximum power achieved by the hybrid power plant.

Table 7.10. Main thermodynamic parameters of the efficiency optimised part-load operations (50% -100% of maximum power output) of the hybrid nuclear-solar power plant.

Electric power load (%)	**100 (max)**	**90**	**80**	**70**	**60**	**50 (min)**
Net electrical power output (MW_{el})	131.1	118.1	105	91.9	78.7	65.6
Nuclear thermal power input (MW_{th})	250	250	250	250	250	250
Solar thermal power input (MW_{th})	101	75.9	54.9	37.7	16.7	0
Superheater molten salt mass flowrate (kg/s)	150	150	134	104	48	0
Reheater molten salt mass flowrate (kg/s)	114	48	0	0	0	0
Superheater bypass mass flowrate (kg/s)	0	0	11.8	33.4	73	106
Reheater bypass mass flowrate (kg/s)	0	61	95.2	92	94	92
Superheater steam outlet temperature (°C)	538	538	539	541	546	NA
Reheater steam outlet temperature (°C)	502	516	NA	NA	NA	NA
High-pressure turbine inlet temperature (°C)	538	538	512	463	377	306
Low-pressure turbine inlet temperature (°C)	502	384	274	216	155	144
Optimised cycle efficiency (%)	37.3	36.2	34.8	31.9	29.5	26.2

The obtained results indicate as the power load decreases from 100%, it is more thermodynamically efficient to bypass the reheater (i.e., Bypass II in Figure 7.2) first and then bypass the superheater (i.e., Bypass I in Figure 7.2) until reaching the minimum load (50%). This behaviour can also be seen in the temperature-specific entropy (*T-s*) diagrams of 90%, 80%, 70%, 60% and 50% power loads illustrated in Figure 7.9. Such behaviour can be explained as the optimised efficiency is obtained by shifting the steam expansion line of the low-pressure turbine to the left (i.e., see LPT expansion line in Figure 7.7 for nominal load and LPT expansion lines in Figure 7.9 for lower power loads). The shift is a result of decreasing the amount of added heat in the reheater, leading to the main low-pressure turbine outlet steam to be at a lower superheating temperature compared to nominal or in the two-phase region. Reaching such conditions minimises the amount of wasted heat in the condenser. Thus, achieving higher cycle thermal efficiency with the desired power load.

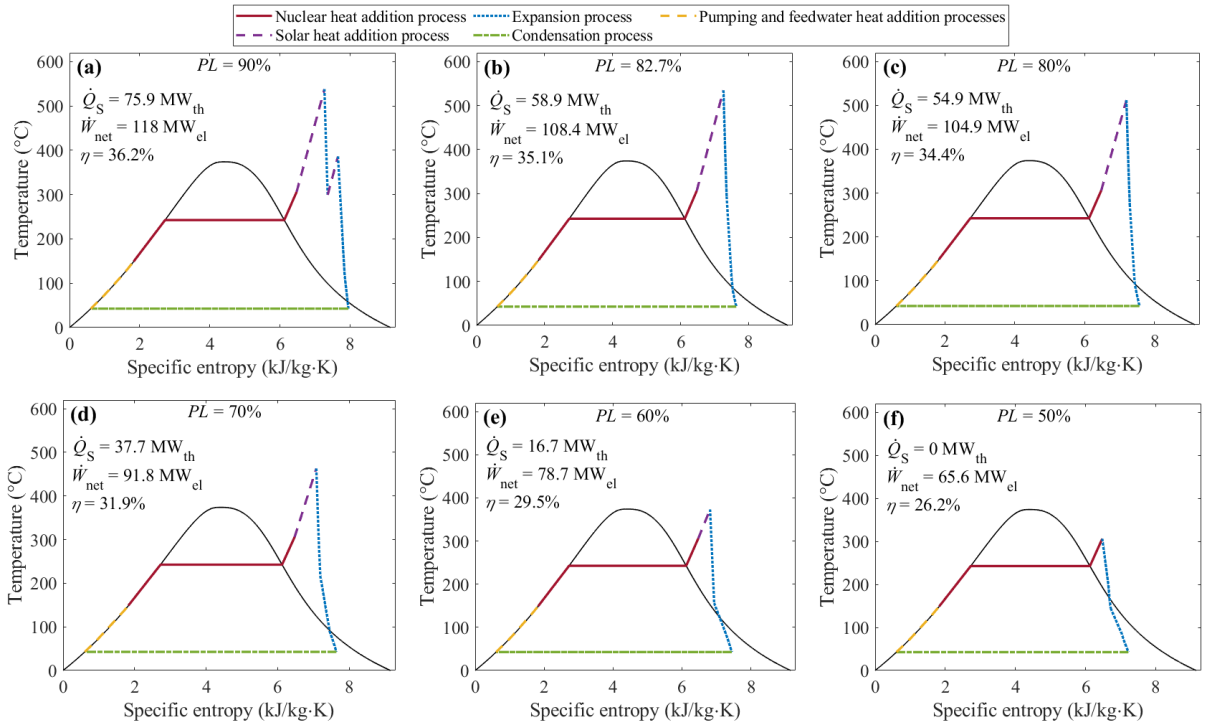

Figure 7.9. Temperature-specific entropy, *T-s*, diagrams showing the thermodynamic processes of the efficiency optimised power generation block of the designed hybrid nuclear-solar power plant at: (a) 90%, (b) 82.7%, (c) 80%, (d) 70%, (e) 60% and (f) 50% power load. The 82.7% power load is achieved when all steam is flowing through the superheater and no steam is flowing through the reheater (i.e., no reheating process).

The shifting of the low-pressure expansion line can only be performed until all steam is bypassing the reheater (i.e., no reheating process is taking place), which corresponds to 82.7% power load, illustrated in Figure 7.9(b). After this point, the efficiency is maximised for each load by decreasing the amount of added heat in the superheater. This process is performed until reaching the minimum load corresponding to all the steam bypassing the superheater (i.e., no superheating process is performed). This control process can be seen by the decrease of the superheating temperature from 538 °C for the 82.7% power load, illustrated in Figure 7.9(b), to 306 °C at 50% power load, illustrated in Figure 7.9(f).

It can be also seen in Figure 7.9 that the slope of lines representing the expansion processes varies for the different power loads. The slope becomes less steep with lower power loads because of lower off-design turbine isentropic efficiencies, which could be as low as 62% for some turbine stages at 50% power load.

7.6. Sizing of solar field and TES capacity

The selection of the optimum size of the solar field (i.e., solar receiver, tower, and heliostat field) and the optimum TES capacity was achieved by conducting a thermo-economic parametric optimisation study. The parametric optimisation analysis was performed for the designed hybrid power plant for a range of solar multiple (SM) and for different TES capacities. The SM is defined as the ratio of the solar power output of the installed solar field to the thermal power input required by the power generation block. This means if the solar multiple is higher than 1, there will be extra heat collected in the receiver than needed in the power generation block, and this extra collected heat can be stored in the installed TES system. In the parametric optimisation analysis, SMs of 1.0, 1.5, 2.0, 2.5 and 3.0 were considered, and the corresponding optimised solar field sizes that were obtained from SAM are summarised in Table 7.11 [121].

The considered TES storage capacities in this analysis are from 0 to 20 of full-load hours. The amount of TES capacity required for full-load operation hour is 105.2 MW_{th}, which was calculated after considering a TES discharging efficiency of 96%. Like the nuclear-only power plant economic analysis, the parametric optimisation analysis was performed using the listed assumptions in Table 7.4 and an electricity price (EP) of 100 \$/MWh_{el}. Furthermore, the considered operation strategy of the hybrid power plant is the one that is discussed in Section 7.3.3.

Table 7.11. List of SAM optimised solar field and receiver parameters for different solar multiples.

Solar multiple	**1.0**	**1.5**	**2.0**	**2.5**	**3.5**
Receiver height (m)	10.64	12.32	13.67	15.67	17.53
Receiver diameter (m)	8.72	10.70	12.09	13.45	15.08
Tower height (m)	106.3	123.9	135.1	160.2	175.3
Number of heliostats (-)	2409	3678	5024	6187	7409
Single heliostat area (m^2)	144	144	144	144	144
Heliostat height (m)	12.2	12.2	12.2	12.2	12.2
Reflective area (km^2)	0.348	0.531	0.725	0.893	1.069
Receiver area (m^2)	291.3	413.9	519.1	661.8	830.4

The amount of the total solar heat that is available from the solar field for the considered SMs and for a range of TES capacities are indicated by the coloured bars (left *y*-axes) in Figure 7.10(a), (b), (c), (d) and (e). The total amount of generated electricity from the hybrid system per year that corresponds to the same SMs and TES capacities are presented on the right *y*-axes of the same figures. Each bar of the total available solar heat is divided into three different categories, the unutilised (lost) heat is shown in red, the heat that goes from the solar receiver to the power generation cycle (through TES tanks but not stored) are presented in blue, and the stored amount of heat in the TES system that is discharged to the power generation cycle during night-time or low-sun periods is shown in green. The available solar heat increases with higher SMs due to ability to collect more solar heat in larger solar fields and receivers. For no storage (TES capacity of 0 h), the amount of unutilised heat is the maximum for all SMs as the extra collected heat cannot be stored. For SMs of 1.0, 1.5, and 2.0 (i.e., shown in Figure 7.10(a), (b), (c), respectively), the amount of unutilised heat diminishes as the size of the TES is increased. Moreover, the higher the SM, the higher the TES capacity that is required to utilise the total amount of the available solar heat. From the discussed figures, it can be said that the needed TES capacity are: 2 h for a SM of 1.0, 9 h for a SM of 1.5, and 14 h for a SM of 2.0. Furthermore, the annual generated electricity becomes almost flat (constant) after reaching the required storage capacities as a result of utilising all of the available solar heat and no further electricity can be generated from the hybrid power plant.

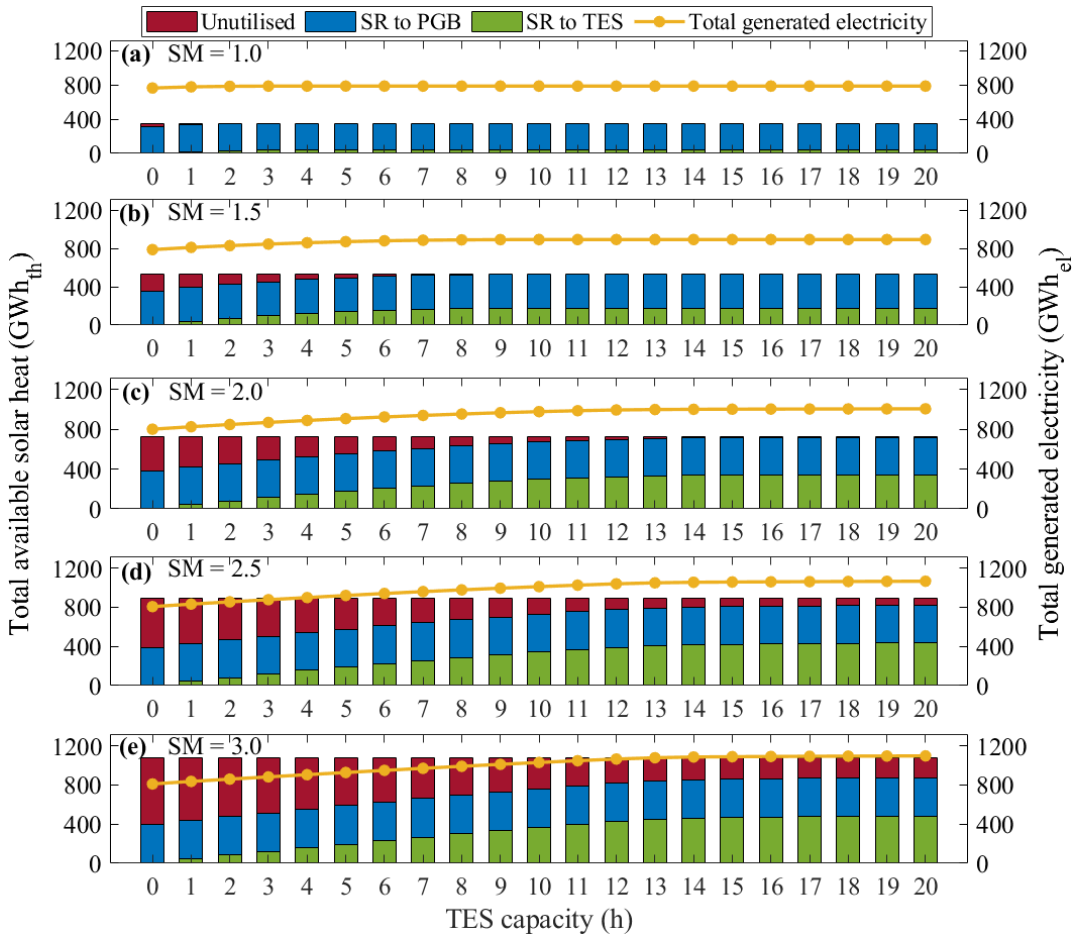

Figure 7.10. Total available solar heat from the solar field, left *y*-axes, and the total generated electricity from the hybrid nuclear-solar power plant, right *y*-axes, across a range of TES capacities and for solar multiples (SMs) of (a) 1.0, (b) 1.5, (c) 2.0, (d) 2.5 and (e) 3.0.

For SMs of 2.5 and 3.0, the amount of unutilised heat is higher, with respect of smaller SMs, for all TES capacities but it also reduces with the increase of the installed TES capacity. Similar to lower SMs, the amount of stored heat for SMs of 2.5 and 3.0 increase with the increase of TES capacity until reaching TES capacities of 13 h or 14 h. The increase of stored heat beyond these points are very minimal as the amount of stored heat during the daytime are sufficient to continuously operate the hybrid power plant at full power capacity during night-time for most of days. The amount of unutilised heat for a SM of 3.0 (Figure 7.10(e)) is much higher than for a SM of 2.5 (Figure 7.10(d)) for all TES capacities, indicating that the solar field is over sized for the designed power generation block and for the considered geographical location. Although the presented results in Figure 7.10 indicate few reasonable solar field and TES sizes, the selection of the optimum size is yet to be determined based on other thermo-economic indicators.

The average power generation cycle efficiency (i.e., average of hourly data for the entire year) and the hybrid power plant capacity factor for the same range of SMs and TES capacities are shown in Figure 7.11 (a) and (b), respectively. The power plant capacity factor is defined as the ratio between the actual generated electricity and the total amount of electricity that could be generated if the power plant is operated at full load for the same period of time. The average cycle efficiency for most of the data are higher than that of the nuclear-only power plant. It is because the larger the sizes of the solar field and the TES system, the higher the amount of collected heat to be stored in the TES system. This results in operating the power plant at full load (higher cycle efficiencies) for longer times each day, which corresponds to higher capacity factors as well. The average cycle efficiency of the hybrid power plant for the smallest solar field (SM =1) and for all TES capacities are below the nuclear-only power plant baseline, meaning that the hybridisation concept with such sizes achieve no thermodynamic gains over the nuclear-only power plant. The presented results show that a hybrid power plant with the biggest solar field (a SM of 3.0) and with a TES capacity of 20 h have the highest average cycle efficiency and maximum capacity power among the considered sizes. Nevertheless, a hybrid power plant with such large solar field and TES capacity might not be the optimum option in terms of economics.

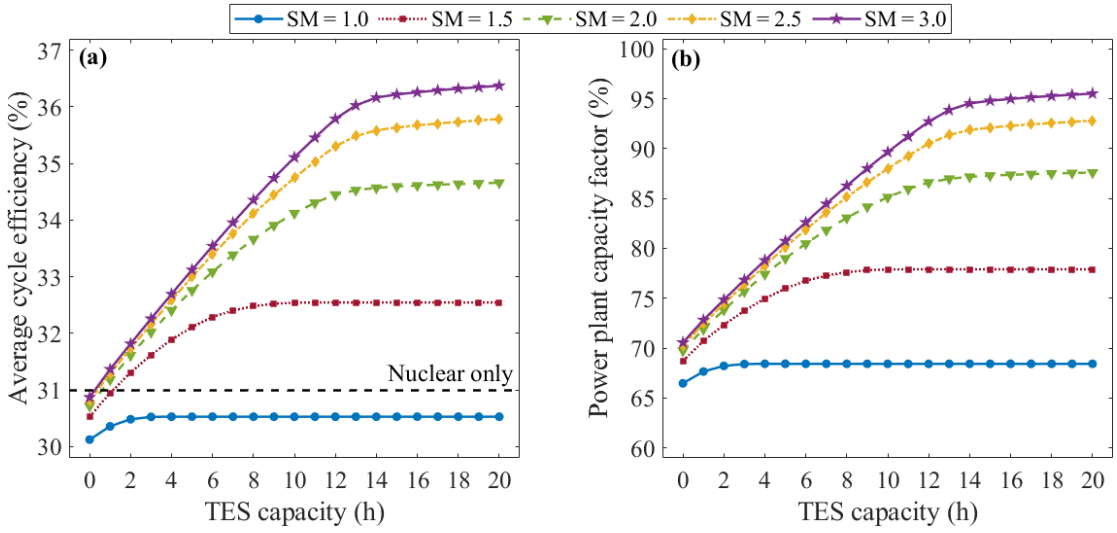

Figure 7.11. (a) Average cycle efficiency and (b) power plant capacity factor of the of the hybrid nuclear-solar power plant for a range of TES capacities and different solar multiples (SM).

The estimated total capital cost and the corresponding SIC of the hybrid nuclear-solar power plant for the examined solar field sizes and TES capacities are shown in Figure 7.12(a) and (b), respectively. The total capital cost ranges from $555M for the smallest solar field size with no TES

system to \$754M for the largest solar field and with 20 h of TES capacity. This is expected as the cost increases with increasing the size of the solar field and the TES tanks. The SIC follows the same trend as of the total capital cost and most of the calculated SICs are below the nuclear-only baseline (5510 \$/kW$_{el}$). Yet, the optimum size cannot be determined based on such economic indicators as selecting a hybrid power plant with the minimum capital cost and SIC does not mean that it has the highest economic returns or the lowest LCOE among the examined sizes.

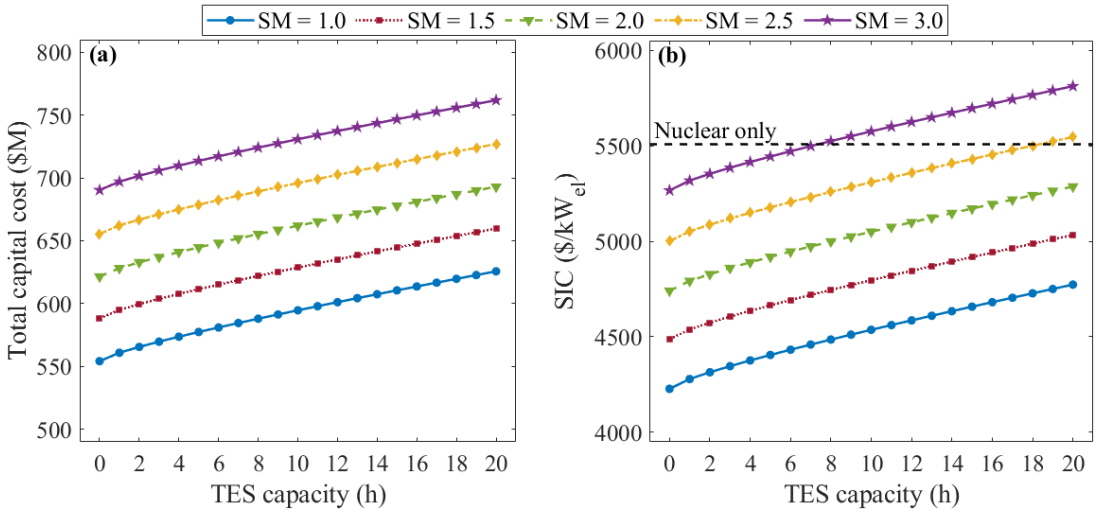

Figure 7.12. (a) Calculated capital costs and (b) calculated specific investment costs (SIC) of the of the hybrid nuclear-solar power plant for a range of TES capacities and solar multiples (SM).

The determination of the optimum solar field size and the optimum TES capacity is based on the obtained results that are shown in Figure 7.13. The calculated LCOEs, NPVs, IRRs and payback times of the hybrid nuclear-solar power plant for the examined range of solar field sizes and TES capacities are shown in Figure 7.13(a), (b), (c) and (d), respectively. Each coloured curve in Figure 7.13 represents different size of solar field (i.e., different SM). The calculation of these economic indicators was performed using the same discount rate, power plant lifetime electricity price and availability factor (i.e., listed in Table 7.4) that were used in the economic analysis of the nuclear-only power plant. It can be seen in Figure 7.13(a) that the LCOE decreases with the increase of TES capacity until reaching a minimum point and then starts increasing again. These lowest LCOE represent the optimum TES capacity for each solar field size and implies that installing larger TES system increase the total costs of the power plant with little extra gains in terms of income and discharged electricity. Moreover, the results show that a hybrid power plant with SMs of 2.0, 2.5 or 3.0 and with TES capacities between

11 h and 20 h have lower LCOE compared to nuclear-only power plant. The lowest LCOE is 76.9 $/MWh$_{el}$ which corresponds to a SM of 2.5 and a TES capacity of 14 h. This minimum LCOE is about 4% lower than the projected LCOE of the nuclear-only power plant.

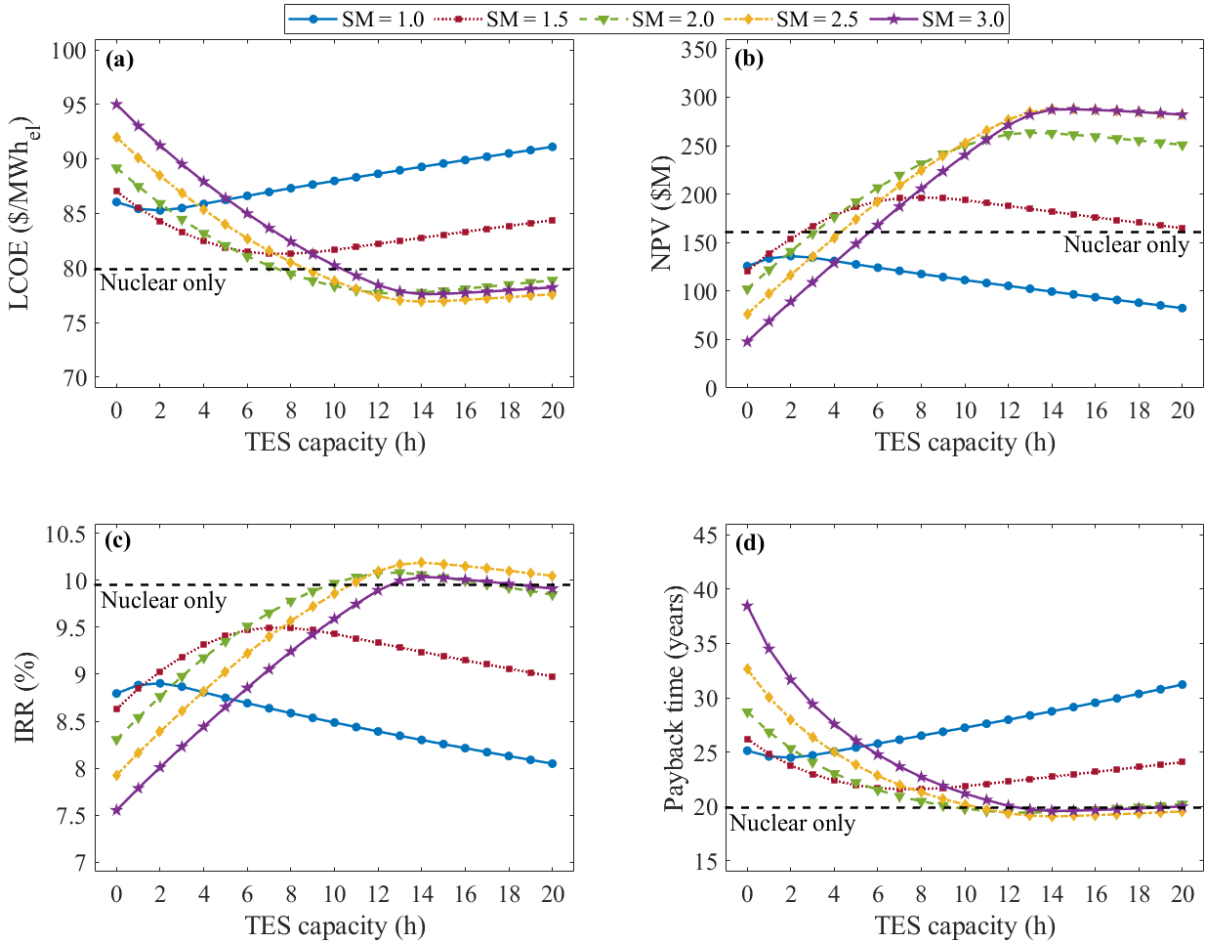

Figure 7.13. (a) Calculated levelised cost of electricity (LCOE), (b) calculated net present value (NPV), (c) calculated internal rate of return (IRR), and payback time of the of the hybrid nuclear-solar power plant for a range of TES capacities and different solar multiples (SM).

In terms of the predicted NPVs that are shown in Figure 7.13(b), the highest NPV is achieved when the LCOE is the lowest. However, this is not always the case as the calculation of the NPV depends on the assumed electricity prices, and the optimum solar field size and TES capacity that have the highest NPV could be different for higher or lower electricity prices. The calculated NPV that corresponds to the lowest LCOE is $287M. This NPV is 79% higher than the one anticipated for the nuclear-only power plant. Such big increase is due to the ability to receive more income for selling extra amount of electricity at a given price. Furthermore, the

IRR and the payback time prediction curves (Figure 7.13(c) and (d)) indicate that the optimum solar field and the optimum TES capacity are the same as the ones that have the lowest LCOE, which are 10.2% and 19.1 years. These values are respectively 2% higher and 4% shorter relative to the ones obtained for the nuclear-only power plant.

In this thermo-economic analysis, the optimum size of the solar field and the TES system is selected based on the lowest LCOE as it is independent on electricity prices and cashflows like the other economic indicators (i.e., NPV, IRR and payback time). Therefore, the optimum design of the hybrid nuclear-solar power plant is when the solar field is designed based on a SM of 2.5 and integrated with a TES system that have a storage capacity of 14 h. The economic performance of the chosen hybrid nuclear-solar power plant design and the nuclear-only power plant will be compared for a range of electricity prices and different discount rates in Section 7.9.

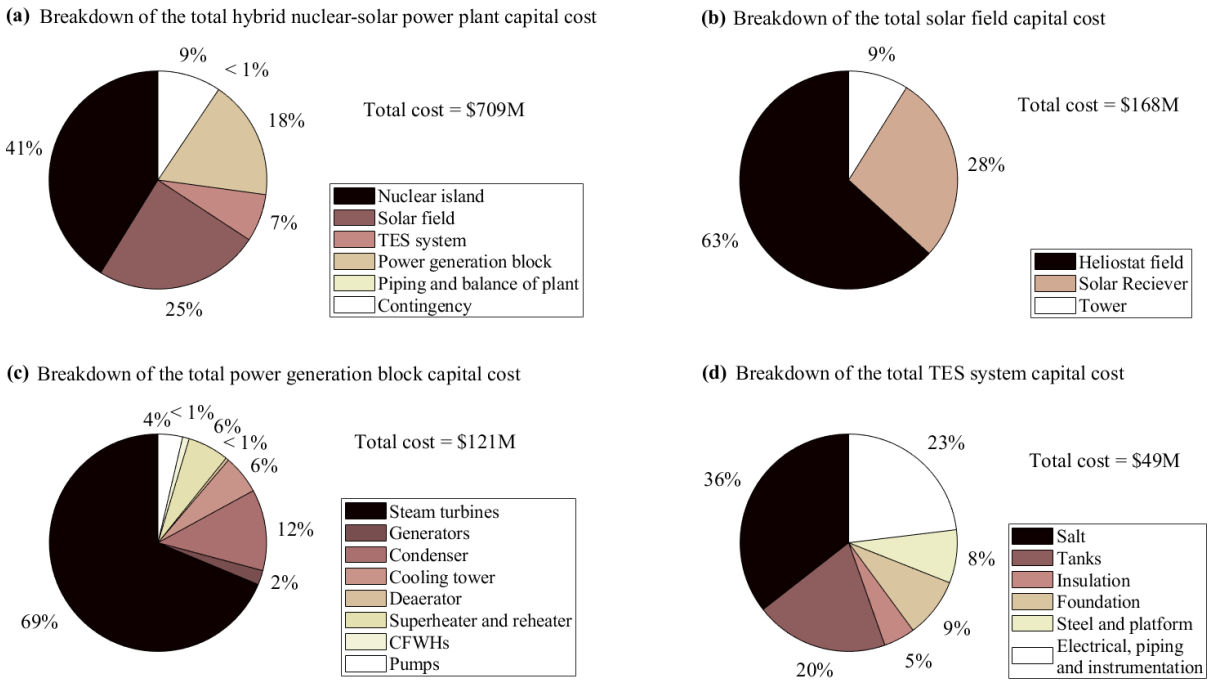

Figure 7.14. Breakdown of capital costs of: (a) hybrid nuclear-solar power plant, (b) designed power generation block, (c) designed solar field at a SM of 2.5, and (d) designed TES system with a storage capacity of 14 h.

The total capital cost breakdown of the selected design of the entire hybrid nuclear-solar power plant, the solar field, the power generation block, and the TES system are respectively shown in Figure 7.14(a), (b), (c) and (d). The estimated total capital cost of the hybrid power plant with the designed power generation block and the optimum solar field and TES system sizes is

$709M, in which 41% of the total costs is for the nuclear island, 25% for the solar field, 7% for the 14-h TES system, 18% for the power generation block and the rest for balance of plant, piping, and project contingency. The calculated SIC of the hybrid power plant is 5410 $/kW$_{el}$, which is about $100 lower than the one calculated for the nuclear-only power plant.

7.7. Hybrid power plant operation

The utilisation of individual components of the designed hybrid nuclear-solar power plant for selected DNI profiles on an hourly basis and for two separate weeks are illustrated in Figure 7.15 and Figure 7.16. The example shown in Figure 7.15 represents a randomly selected week that have continuous and high DNI profile (high DNI-profile week), while the one shown in Figure 7.16 represents a randomly selected week that have low and highly fluctuating DNI profile (low DNI-profile week). In both figures, the DNI profile inputs are shown in (a), the available nuclear and solar thermal power are illustrated in the left *y*-axes of (b), the amount of stored heat in the TES system are presented in the right *y*-axes of (b), the power plant electrical power output profiles are shown in left *y*-axes of (c), while the corresponding cycle thermal efficiencies are illustrated in the right *y*-axes of (c).

For the high DNI-profile week example that is shown in Figure 7.15, the daily DNI profile is high enough to provide the required thermal power to operate the power generation block (i.e., blue bars in Figure 7.15(b)) and to fill in the installed TES tanks (i.e., green bars in Figure 7.15(b)) during the daytime of each day. The stored heat is then discharged to the power generation cycle (i.e., yellow bars in Figure 7.15(b)) once the sun goes down or when there is insufficient thermal power in the solar receiver. It can be seen in Figure 7.15(c) that installing a TES system with a storage capacity of 14 h guarantees that the hybrid power plant is continuously operating at maximum power output with maximum cycle efficiency throughout the entire week, providing that the daily DNI profile is high and consistent.

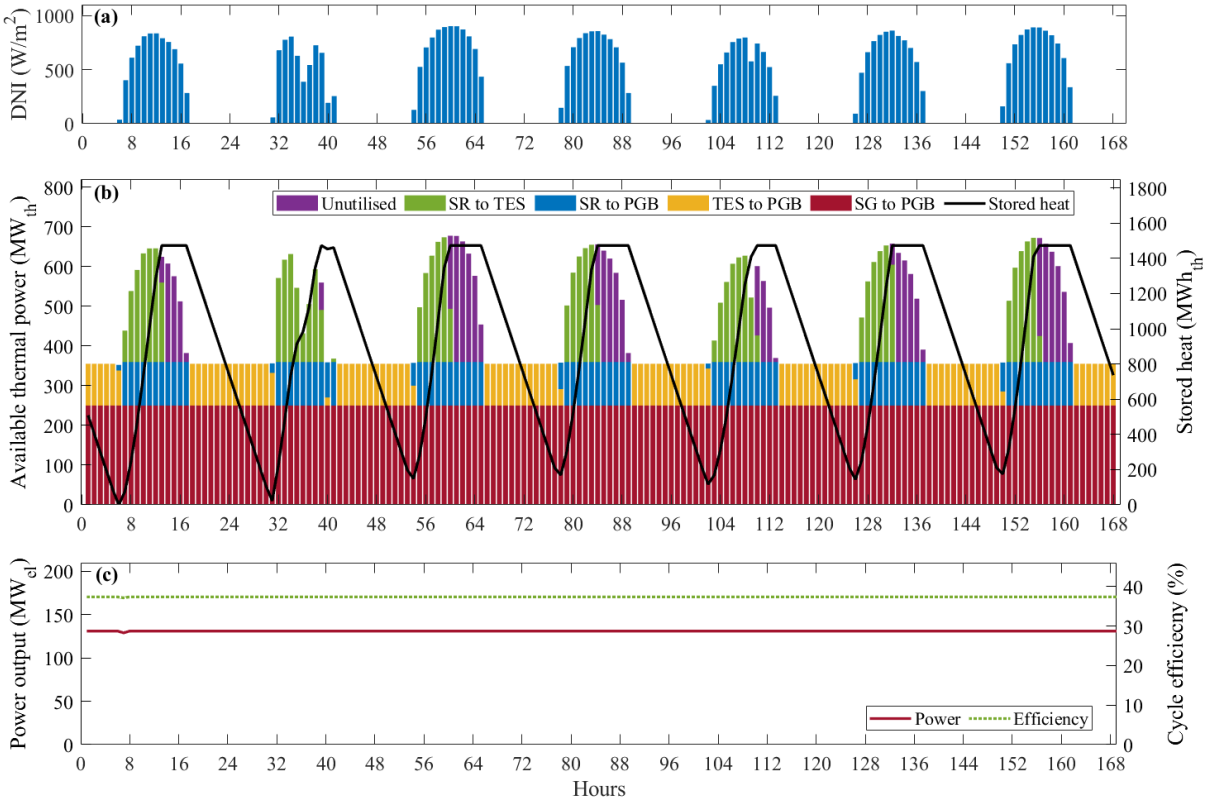

Figure 7.15. (a) DNI profile inputs, (b) available nuclear and solar thermal power, left *y*-axis, and amount of stored heat in the TES system, right *y*-axis, and (c) electrical power output, left *y*-axis, and corresponding cycle efficiency, right *y*-axis, of the hybrid nuclear-solar power plant for an arbitrary selected week that represent a day-continuous and high DNI profile in Duqm.

For the low DNI-profile week example shown in Figure 7.16 that have low and highly fluctuating DNI profile, the performance of the hybrid power plant is very different compared to the example shown in Figure 7.15. In the first day (Hours 1 to 24), some amount of heat is stored in the TES tanks, but it is not even sufficient to run the hybrid power plant at maximum power output until the early morning hours of the next day (i.e., minimum power generation between Hours 27 and 32). For the middle five days (Hour 25 to Hour 144), the performance of the hybrid power plant is almost dependent on the available solar power in the solar receiver, and very small amount of heat is stored in the TES tanks. The stored heat during these five days is barely sufficient to run the power generation block at maximum power output for about 8 h, whereas it was almost 60 h in the high DNI-profile week example illustrated in Figure 7.15.

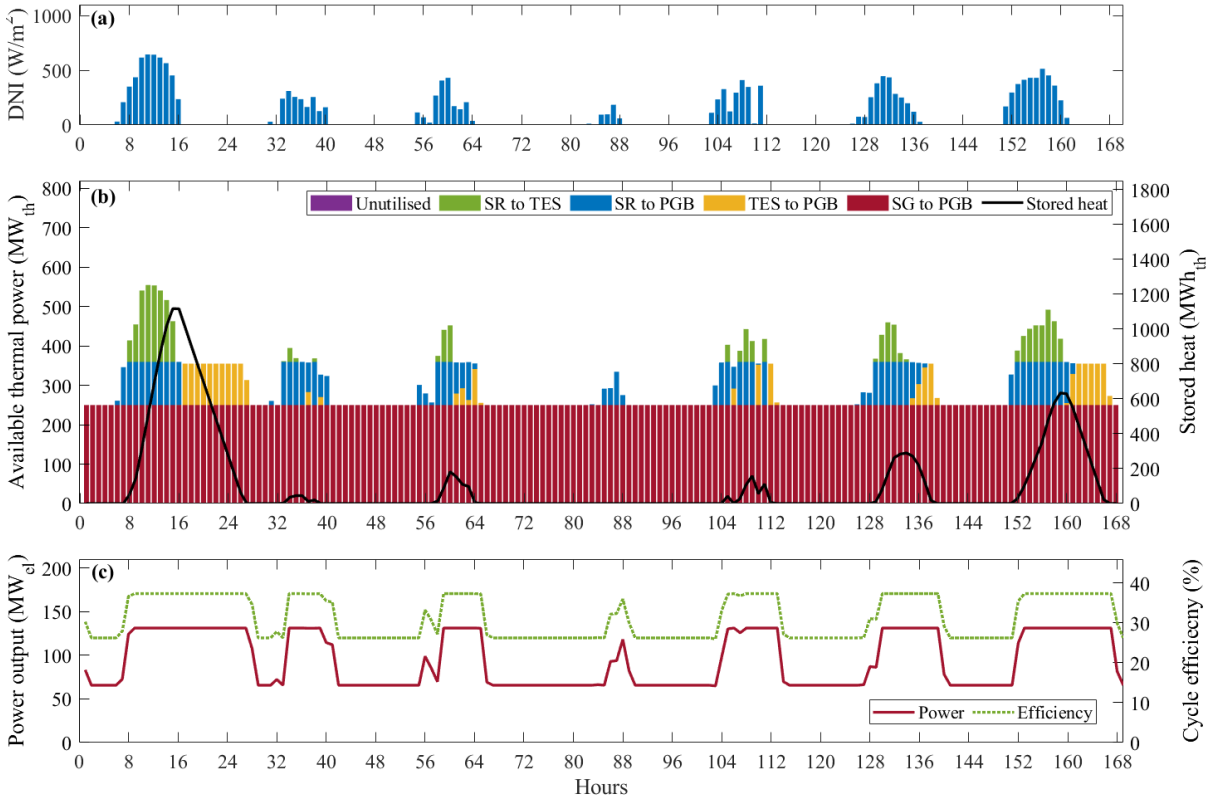

Figure 7.16. (a) DNI profile inputs, (b) available nuclear and solar thermal power, left *y*-axis, and amount of stored heat in the TES system, right *y*-axis, and (c) electrical power output, left *y*-axis, and corresponding cycle efficiency, right *y*-axis, of the hybrid nuclear-solar power plant for a randomly selected week that represent a highly fluctuating and low DNI profile in Duqm.

7.8. Nuclear-only vs. hybrid nuclear-solar power plants

The key thermodynamic and economic indicators of the nuclear-only and the hybrid nuclear-sola power plant are summarised in Table 7.12. The listed economic performance indicators were calculated assuming a project lifetime (n) of 40 years, a discount rate (r) of 7%, an availability factor (F_a) of 90% and an electricity price (EP) of 100 \$/MWh$_{el}$. The hybrid nuclear-solar power plant has: (i) a solar field that is designed based on a DNI of 600 W/m^2 and a SM of 2.5 and (ii) a TES system that can store up to 14 h of heat that is required to operate the hybrid power plant at maximum electrical power load. The hybridisation of nuclear with solar power increases the maximum power output by 69%, from 77.5 MW$_{el}$ to 131 MW$_{el}$, and enhances the power generation cycle efficiency by 15%, compared to nuclear-only power plant. This efficiency improvement is due to the addition of the superheating and the reheating processes in the power generation cycle performed by the solar superheater and reheat.

Table 7.12. Key thermodynamic and economic indicators of the considered nuclear-only power plant and the designed hybrid nuclear-solar power plant. All listed results are obtained assuming a project lifetime (n) of 40 years, a discount rate (r) of 7%, an availability factor (F_a) of 90% and an electricity price (EP) of 100 \$/MWh$_{el}$ throughout entire lifetime.

Parameter	Nuclear-only	Hybrid	Difference (%)
Net power output (MW$_{el}$)	77.5	131.1	69.2
Average cycle efficiency (%)	31	35.6	14.8
Total cost of power generation block (\$M)	88.7	121	36.4
Total cost of nuclear island (\$M)	282	282	0
Total cost of solar field (\$M)	NA	168.3	NA
Total cost of TES system (\$M)	NA	48.4	NA
Estimated cost of piping (\$M)	8.9	12.1	36
Estimated cost of balance of plant (\$M)	8.9	12.1	36
Contingency (\$M)	38.8	64.4	66
Total power plant cost (\$M)	427	709	66
Total generated electricity per year (GWh$_{el}$)	611	950	55.5
Specific investment cost (\$/kW$_{el}$)	5510	5410	-1.8
Specific investment cost of the power block (\$/kW$_{el}$)	1145	926	-19.1
Annual operation and maintenance cost (\$M/year)	9.6	14	45.8
Annual fuel cost (\$M/year)	8.5	8.5	0
Levelised cost of energy (\$/MWh$_{el}$)	79.9	76.9	-3.8
Net present value (\$M)	160	287	79.4
Internal rate of return (%)	10	10.2	2.0
Payback time (years)	19.9	19.1	-4.0

In terms of economics, the total capital cost of the hybrid power plant is 66% higher than the nuclear-only power plant, which is expected due to the increased size of the power plant. However, the SIC of the hybrid power plant and the SIC of the designed power generation block for the hybrid plant are respectively 1.8% and 19% lower than those of the nuclear-only power plant. Additionally, the calculated LCOE of the hybrid plant is 3.8% lower than that of the nuclear-only power plant. Assuming an electricity price of 100 \$/MWh$_{el}$, the anticipated NPV, and the payback time for the hybrid power plant are respectively 79% higher and 4% shorter relative to the those estimated for the nuclear-only power plant.

In conclusion, besides the capability of the hybrid power plant to provide flexible power output (i.e., 50-100% of maximum power output) with continuous operation of the nuclear reactor at

full rated thermal power, the hybrid power plant can achieve enhanced cycle efficiencies and higher economic returns relative to the nuclear-only power plant.

7.9. Economic performance of both plants for different electricity prices

The economic performances of the nuclear-only and the hybrid nuclear-solar power plants for a range of reasonable electricity prices, from 50 \$/MWh$_{el}$ to 120 \$/MWh$_{el}$, and for different discount rates (3%, 5%, 7% and 10%) are presented in Figure 7.17(a), (b), (c) and (d), respectively. The left *y*-axes of all figures compare the projected NPVs, while the right *y*-axes compare the projected IRRs for the same range of electricity prices. The curve of the calculated IRRs at different electricity prices are similar for all considered discounted rates as the IRR is independent of the discount rate. Taking Figure 7.17(a) as an example to compare the IRRs, the higher the electricity price, the higher the IRR is. Such increase is due to the ability to receive more income (revenues) from selling the same amount of electricity at higher prices (i.e., positive impact on the undiscounted cashflows). Moreover, the anticipated IRRs of the hybrid power plant are always higher than those of the for the examined range of electricity prices.

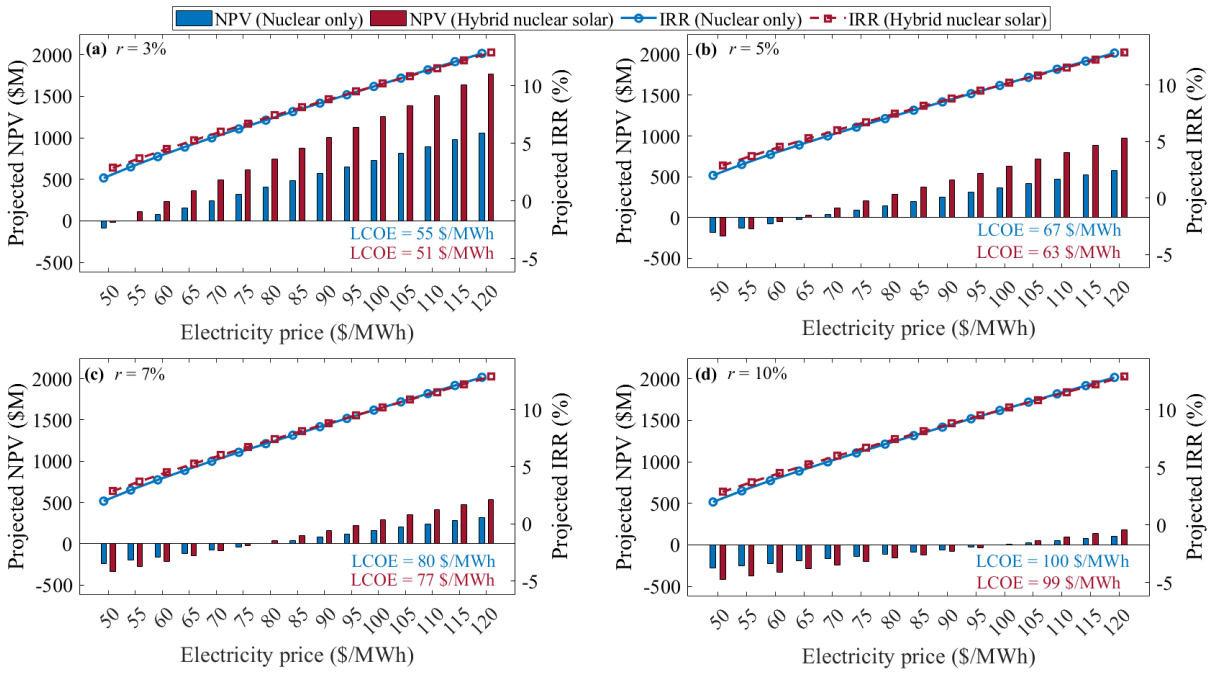

Figure 7.17. Comparison of the projected NPV and the projected IRR of the nuclear-only and the hybrid nuclear-solar power plants for electricity prices from 50 \$/MWh to 120 \$/MWh$_{el}$ and for discount rates (r) of: (a) 3%, (b) 5%, (c) 7% and (d) 10%.

Furthermore, the calculated LCOEs (i.e., written inside the figures) of the hybrid power plant are always lower than those calculated for the nuclear-only power plant for the examined discount rates. In terms of anticipated NPVs, the hybrid power plant can achieve higher positive NPVs relative to those of the nuclear-only power plant, notably when the electricity prices are higher than the calculated LCOE for all examined discount rates. However, for electricity prices lower than LCOE, the anticipated NPVs of the hybrid power plant are more negative (i.e., higher losses) than those of the nuclear-only one as a result of higher capital costs and higher operation and maintenance costs for the hybrid power plant. Either way, the investment decision of both compared power plants should not be made unless the anticipated NPVs are positive, and the hybrid power plant has an economic advantage on that. In conclusion, the hybrid power plant seems to have extra economic benefits over the nuclear-only power plant for the examined range of electricity prices and discount rates.

7.10. Summary and conclusions

The option of combining a small modular nuclear reactor (NuScale) with concentrated solar power (solar tower) integrated with two-tank molten salt thermal energy storage (TES) system to form a hybrid nuclear-solar power plant was explored and investigated in this chapter. The aim of the study was to assess the degree of added flexibility offered by the hybridisation concept and to perform comprehensive thermodynamic and economic analyses on the nuclear-only and the hybrid nuclear-solar power plant configurations. The study involved cost-based design optimisation of the power generation blocks for both configurations. The off-design performance of the power generation block components during part-load operations was also considered in the analysis. Furthermore, parametric optimisation and sizing of solar field and TES system were performed taking the city of Duqm in the Sultanate of Oman as a location for case study.

The power generation block of the nuclear-only power plant was designed based on minimum specific investment cost (SIC) that satisfied a list of technical constraints. The estimated SIC and total capital cost of the designed nuclear power plant are 5510 $/kW$_{el}$ and $427M, respectively. Moreover, the designed power plant has a net power capacity of 77.5 MW$_{el}$ with a cycle thermal efficiency of 31%, and both values are within 1% of the officially declared numbers by NuScale.

The design of the power generation block of the hybrid power plant was executed using the same procedure as in the design of the nuclear-only power plant. The designed hybrid power plant is

able to deliver a net electrical power of 131 MW_{el} and attain a cycle thermal efficiency of 37.3%. For part-load operations, the determination of the power generation cycle operation parameters (i.e., steam pressure, turbine side extraction mass flowrate, etc.) was based on maximising the efficiency at each part load until no heat is added in the solar superheater and the reheater (i.e., operation of the hybrid power plant is solely based on nuclear thermal power input). The obtained results revealed that the hybrid system can be flexible between 50% and 100% of its maximum power output, with a constant operation of the nuclear reactor at full rated thermal power. However, the thermodynamic price of such flexible operation was the diminishing cycle efficiency caused by the operation of power generation block components at off-design conditions. The cycle thermal efficiency could reach as low as 26.2%, which occurs when the hybrid power plant is operated at 50% power load with no heat addition from the solar field or the integrated TES system.

The sizing of the solar field (i.e., size of solar receiver, tower, and heliostat field) and the attached TES system was conducted by considering a range of solar multiples (SMs) and different full-load storage capacities (0 h to 20 h). From 105 of different combinations of solar field and TES system sizes, the optimum sizes that give the lowest levelised cost of electricity (LCOE) of the hybrid nuclear-solar power plant (76.9 $\$/MWh_{el}$) correspond to a SM of 2.5 and a TES capacity of 14 h.

The thermodynamic and the economic performances of the nuclear-only and the designed hybrid power plants were compared, and the comparisons revealed the following remarks:

- The maximum turbine inlet temperature reaches 538 °C in the hybrid power plant while the maximum is 306 °C for the nuclear-only power plant due to the addition of the solar superheater and reheater in the hybrid configuration. This increase in temperature and heat addition resulted in enhancing the cycle efficiency by 15% and increasing the net power output by 69% relative to those of the nuclear-only power plant.
- The calculated SIC and LCOE for the designed hybrid power plant were respectively 2% and 4% lower than those anticipated for the nuclear-only power plant.
- With a capital cost difference of $282M (i.e., cost of solar field, TES system and power generation block modification), the designed hybrid power plant is expected to achieve better economic returns than the nuclear-only power plant. For example, using the same economic assumptions, the projected net present value (NPV) increased from $160M to $287M, the internal rate of return (IRR) increased from 10% to 10.2%, and the payback time decreases from 19.9 years to 19.1 years as a result of the hybridisation concept. These

economic return improvements are mainly due to the ability of generating extra amount of electricity (i.e., extra income) at enhanced thermodynamic performance.

- The designed hybrid power plant is also expected to achieve higher positive NPVs and higher IRRs for discount rates between 3% and 10% and for electricity prices ranging from 50 \$/MWh_{el} to 120 \$/MWh_{el}.

The key results of this chapter showed that combining nuclear reactor with a solar tower CSP technology and a TES system could offer great amount of flexible power (50% to 100% of maximum power), while maintaining the reactor operation at full rated thermal power output. The hybrid power plant could be treated as a reliable (due to having nuclear power), clean (no carbon emissions), flexible (due to having TES system) and reasonably cost-effective source of energy.

The main conclusions of the investigated case study in this chapter gives a sufficient answer to Research Question 4 and adequately fulfil, to some extent, the identified Research Gap 4, which are listed in Section 2.8. Future work recommendations related to the case study discussed in this chapter are expressed in Section 8.3.

Chapter 8
Conclusions

Achieving low or net-zero greenhouse emissions requires substantial and comprehensive global efforts. The decarbonisation of the electricity generation sector is vital to reach these ambitious targets, especially with the increasing demand of electricity resulting from the increasing global population and the electrification of other sectors (e.g., transportation and domestic heating). Nuclear and solar power, in the form of concentrated solar power (CSP), play a major role in providing carbon-free electricity, but still, both power generation technologies need further research investigations in the effort to increasing their flexibility and thermal efficiency. The aim of the research presented in this thesis was to explore and thermo-economically assess the available options of upgrading the flexibility and enhancing the thermal efficiency of nuclear and concentrated solar power generation as well as the thermal energy storage (TES) technologies. The thesis included development and validation of various thermodynamic and economic models that were utilised to achieve the overall aim of this research.

The formulated modelling tools helped investigating the options of extending the TES system that is used in most conventional direct steam generation (DSG) CSP plants in order to achieve higher thermal efficiency levels. Moreover, the option of upgrading the flexibility of the current and future UK's fleet of nuclear power plants were also thermodynamically and economically investigated and analysed, both from technology and whole-electricity system perspectives. Finally, the developed models were utilised to design a hybrid nuclear-solar power plant with the aim of achieving higher thermal efficiency and flexibility levels at reasonable costs.

8.1. Thesis findings

In the efforts of assessing and investigating the thermo-economic characteristics and the load following operations of large-scale carbon-free thermal power plants (nuclear and CSP) and TES technologies, several thermodynamic and economic computational models were developed. These formulated thermo-economic models enabled to identify the optimum design and operation of several flexible nuclear power plant configurations (i.e., through the integration with TES systems

and secondary generators or/and with CSP technologies) and also to evaluate the option of extending the steam-accumulation TES system in DSG CSP plants. The developed power generation cycle systems models were formulated to capture, to some extent, the off-design performance of the cycle components during part-load operations. Moreover, the research included formulation of a whole-system electricity model that enabled quantification of the system economic benefits that could be gained from replacing conventional nuclear power plants with added flexibility ones in future decarbonised electricity grids that have high shares of variable renewables.

In Chapter 4, two steam-accumulation TES options for DSG CSP plants were compared, taking the Khi Solar One power plant in South Africa as a case study. The compared TES options were: (i) the existing TES system in Khi Solar One, which consists of two groups of steam accumulators (SAs) and a superheater; and (ii) an extended TES system that consists of one group of SAs and concrete blocks for higher-temperature heat storage. The two configurations were thermodynamically and economically analysed using the same existing solar tower field and the same power generation cycle components as deployed in Khi Solar One. The study included the determination of the initial water filling ratio (WFR) of the base SAs that maximises profitability. It was found that base SAs with initial WFRs of 0.75 give the lowest levelised cost of electricity (LCOE) of 256 $/MWh$_{el}$. Moreover, the study involved the sizing of the concrete blocks in the extended configuration. It was found that installing five 10-m long concrete blocks with 3600 equally-spaced tubes offers the lowest LCOE of 241 $/MWh$_{el}$.

The performance of Khi Solar One with the existing and with the extended TES systems were also compared for the same 24-h hourly direct normal irradiance (DNI) input. The obtained results showed that: (i) the extended configuration can store an extra 177 MWh$_{th}$ of heat using the same number of SAs as the existing configuration and the additional concrete blocks. This is due to the ability of the extended configuration to utilise the current SAs to store steam at a higher temperature and pressure, which is then used to superheat the steam to higher temperature during discharging mode. Further, (ii) the extended configuration can achieve a higher average cycle thermal efficiency than the existing TES configuration, 13% higher, as the inlet temperature can reach up to 453 °C while the maximum is 286 °C in the existing TES system configuration. Additionally, (iii) with an estimated additional investment cost of $4.2M (i.e., cost of concrete blocks), the extended TES system configuration could decrease the LCOE of Khi Solar One by 6%, from 256 $/MWh$_{el}$ to 241 $/MWh$_{el}$; and (iv) extending the existing

TES configuration increases the projected net present value (NPV) of Khi Solar One by 73%, from \$41M to \$71M, if the generated electricity is sold at 280 $/MWh_{el}$. The key results of the case study covered in Chapter 4 revealed that combining concrete blocks with SAs as a TES option have greater thermodynamic and economic potential than using SAs only.

In Chapter 5, an energy management system (EMS) with the aim of achieving economically enhanced flexible operations of the current UK's fleet of nuclear power plants (i.e., advanced gas-cooled reactor (AGR) based power plants operated by EdF with an electrical power capacity of 670 MW_{el}) was proposed. The enhanced flexibility of the proposed EMS was achieved through combining the AGR with phase change material (PCM)-based TES tanks and secondary organic Rankine cycle (ORC) power generation systems. In the proposed EMS, steam is extracted from the primary power generation system of the power plant during off-peak demand times to charge the TES tanks. At a later time and when it is economically favourable (i.e., peak demand with high electricity prices), these charged TES tanks act as heat sources to the evaporators of the designed secondary ORC systems. Such integration allowed the proposed EMS to generate extra electrical power (i.e., additional 152 MW_{el} on top of the 670 MW_{el} generated by the primacy system) during peak demand, thus resulting in higher revenues from electricity sales.

Furthermore, the economic profitability of the proposed EMS was analysed considering UK hourly prices in the wholesale electricity market during the years of 2019 to 2022. It was demonstrated that the economics of the EMS, especially in terms of the NPV, are determined by: (i) the size of the ORC systems (i.e., smaller sizes mean lower additional investment costs but higher discharging duration); (ii) the number of charge/discharge cycles per day; and (iii) the ratio and difference between off-peak and peak electricity prices. It can be also concluded, for the best analysed case, that flexible operation of AGRs can be profitable if the UK's off-peak/peak electricity price ratio decreases slightly, by about 15% relative to levels observed over the period from 2019 to 2022 and the peak/off-peak price difference increases to about 200 £/MWh_{el} (~250 $/$MWh_{el}$). The main conclusions of the case study presented in Chapter 5 indicated that profitable flexible operation of AGRs is possible under certain scenarios but there is a need to identify the optimum (TES and ORC) system sizes, the optimum TES discharging duration and the frequency of TES charge/discharge cycles per day.

A combined thermodynamic and economic analysis of upgrading the flexibility of a nuclear power plant, European pressurised reactor (EPR), through the integration with PCM-based TES tanks and secondary power generators was presented in Chapter 6. The performed analysis involved quantification of the cost benefits of operating such flexible nuclear power plants in future low-carbon electricity systems. The thermodynamic modelling and optimisation framework presented in Chapter 6 allowed to identify the optimal operating conditions of the primary steam Rankine cycle (PSRC) during nominal load and part-load operations as well as to determine the technical design constraints of the proposed modular TES and secondary steam Rankine cycle (SSRC) systems. Moreover, the formulated whole-system electricity model enabled a quantification of the system value of the enhanced flexibility that such nuclear plants can offer in the context of decarbonising the electrical power grid that have high shares of variable renewables.

The obtained thermodynamic results revealed a maximum PSRC thermal efficiency of 36% at 100% power load, which decreased to 34% at 50% power load during the TES charging process, mainly due to the reduced turbine isentropic efficiencies at off-design conditions. Moreover, performance predictions showed that the proposed configuration of adding flexibility through the coupling with PCM-based TES and SSRC systems can increase the overall power output during peak load by 32% (from 1610 MW_{el} at nominal load to 2130 MW_{el} at peak load) during full TES discharge mode, with an overall roundtrip efficiency of 64%.

The whole-system economic benefit of such flexible nuclear plants was also quantified by estimating the reduction in total system electrical infrastructure cost resulting from replacing conventional with the proposed flexible nuclear plants for several scenarios in the context of the UK's national electricity system. Two generic systems, North and South, that have different wind and solar PV capacity factors and different seasonal demand variations were considered. Economic benefits of up to about £75M/yr (~$93.4M/yr) were projected in the majority of the analysed scenarios. Furthermore, the highest net benefit, which is defined as the difference between total benefit and total cost of added flexibility, was observed in the net zero and high battery energy storage system (BESS) scenarios, at £31.6-32.4M/yr (~$39.5-40.5M/yr) in the North system and £24.7-27.3M/yr (~$30.9-34.1M/yr) in the South system. Nonetheless, the net system benefit was found to vary significantly with different system characteristics such as the composition of the low-carbon electricity generation mix, carbon target, level of flexibility, and nuclear power plant parameters such as SSRC system discharging duration. This suggests that

the value of added flexibility is system-dependent, and that system characteristics should be adequately considered when evaluating the benefits of different flexible nuclear plant configurations and choosing the most cost-effective designs and operational characteristics.

The concept of hybridising a small modular reactor (NuScale) with solar tower CSP integrated with two-tank molten salt TES system with the aim of achieving economically enhanced flexibility and higher thermal efficiency levels was investigated in Chapter 7. The study involved design (i.e., based on lowest specific investment cost (SIC)) of the power generation blocks of a nuclear-only and a hybrid nuclear-solar power configuration including the consideration of off-design performance of power generation block components during part-load operations. Furthermore, parametric optimisation and sizing of solar tower field and TES system were also performed for the hybrid nuclear-solar power plant taking the city of Duqm in the Sultanate of Oman as a location. The designed power generation block for the nuclear-only configuration (i.e., lowest SIC of 5510 $/kW$_{el}$) has an electrical power capacity of 77.5 MW$_{el}$ with a cycle thermal efficiency of 31%. On the other hand, the designed hybrid power plant with the lowest SCI of 5410 $/kW$_{el}$ was able to deliver 131 MW$_{el}$ of net electrical power with a cycle efficiency of 37.3%. Based on the thermal efficiency-based optimisation of part-load operations, the hybrid configuration can be operated between 50% and 100% of the maximum power output, only by regulating the solar heat input and without disturbing the nuclear reactor.

The sizing of the solar field and the TES system in the hybrid configuration was performed considering a range of solar multiples (SMs) and different TES capacities (i.e., 0 h to 20 h of full-load electrical power output). It was observed that a hybrid nuclear-solar power plant with a solar field designed at a SM of 2.5 and integrated with a 14-h TES system have the lowest LCOE of 76.9 $/MWh$_{el}$. The thermodynamic and the economic performances of the nuclear-only and the designed hybrid power plants were also compared, and the following observations were made: (i) the maximum turbine inlet temperature is 538 °C in the hybrid power plant while the maximum is 306 °C for the nuclear-only power plant due to the addition of the solar superheater and reheater (extra heat) in the hybrid plant. This increase in temperature and heat addition resulted in enhancing the cycle thermal efficiency in the hybrid configuration by 15% and increasing the total power output by 69% relative to the nuclear-only power plant. Further, (ii) the calculated SIC and LCOE for the hybrid power plant were respectively 2% and 4% lower than those of the nuclear-only power plant; and (iii) the hybrid power plant could achieve higher positive NPVs, higher

internal rates of return (IRR) and shorter payback times for different economic assumptions and electricity prices, when compared to nuclear-only power plant. The main conclusions of the study presented in Chapter 7 demonstrated that combining nuclear with CSP and a TES system could offer great amount of flexibility (50% to 100% of maximum power capacity), while maintaining the reactor operation at full rated thermal power output. The hybrid power plant can be considered, to some extent, as a reliable, clean, flexible, and cost-competitive source of energy.

In conclusion, the results obtained in this research provide evidence that efficient and economic load following operations of nuclear power plants can be achieved, from technology and whole-electricity system perspectives, through the integration with CSP and TES technologies and with secondary power generation cycle systems.

8.2. Summary of outcomes

The main outcomes of the conducted research to date are the following:

- Thermodynamic computational models of: (i) power generation cycle systems including the estimation of off-design performance of the cycle components during part-load operations (e.g., turbines and heat exchangers); (ii) TES technologies including steam accumulators, solid heat storage blocks and molten salt tanks; and (iii) solar tower CSP technology.
- A set of detailed component-costing and economic models that can be utilised to estimate the investment costs and analyse the economics of power generation and TES technologies.
- Cost-based and efficiency-based optimisation tools that can be used to identify the optimum design and operation of power generation cycle and TES systems.
- Four journal papers on the subject of flexible nuclear, concentrated solar power, and thermal energy storage.
- Four peer-reviewed conference papers across three global conference series.

8.3. Future work recommendations

Several areas of future work related to this research were identified following the observations made from the obtained results.

The TES options of DSG CSP plants case study presented in Chapter 4 was limited to considering thermodynamic and economic sensitivity analysis of semi-defined concrete block and tube

dimensions with no size optimisation and with a reduced-order concrete TES model. Therefore, future work related to this particular study should include: (i) concrete block size optimisation in terms of concrete block dimensions, tube diameter and thickness, and diameter of the surrounded concrete mixture; (ii) thermodynamic performance evaluation of the transient operation of the DSG CSP plant with the two TES options for the entire year instead of selected days only; (iii) formulation and analysis of a transient 3-D computational model for the concrete blocks for more accurate results; and (iv) economic evaluation of constructing similar size DSG CSP plants in other geographical locations or countries that have different electricity market structures.

For the thermodynamic and economic assessment of upgrading the flexibility of current fleet of UK's nuclear power plants (i.e., covered in Chapter 5), it would be very interesting to investigate additional EMS strategies for the provision of ancillary services in transmission networks of smart electricity grids. Such strategies should be considered along with the investigation of increasing the thermal efficiencies of the secondary power plants during peak demand. The requirements for fast-start operation of power generation plants to provide ancillary services to the grid are becoming more and more important, and the trade-offs between costs of fast response operating modes and revenues from ancillary electricity market sales should be carefully investigated, in order to assist investment and management decisions [261]. Moreover, fast start of secondary power plants with aggressive hot starts (which can be, reportedly, within 10 min, and down to 10 s when the plants are at temperature) should also be investigated. Such improvements can offer significant benefits to utilities in terms of primary and secondary frequency responses, and consequently higher profitability in ancillary markets and value to the overall energy system.

Future work related to the proposed flexible nuclear power plant configuration and the quantification of whole-system economic benefits that are discussed in Chapter 6 should include: (i) investigation of other technically applicable steam extraction points from the PSRC system for charging the TES system; (ii) consideration of different working fluids for the secondary power generation cycles; (iii) detailed modelling and sizing of the PCM tanks including thermodynamic analysis of TES system charge/discharge cycle; (iv) investigation of the feasibility for multiple uses of the stored heat to match heating demand and operate thermally driven processes for hydrogen storage, water splitting or synthetic fuels production; and (v) cost-optimisation of the size of individual components (i.e., TES tanks and SSRC systems) from the system perspective.

The investigated concept of hybridising nuclear and solar power that is presented in Chapter 7 was limited to considering light water reactors, pressurised water reactor to be specific, one technology of CSP, two-tank molten salt TES system, and power generation block that is based on steam Rankine cycle. Therefore, future work related to this study should include: (i) design and analysis of several configurations of hybrid nuclear-solar power plants that have different types of nuclear reactors, CSP technologies, TES systems and power generation cycles (e.g., supercritical CO_2 Brayton cycle); (ii) consideration of several locations that have different DNI profiles and different electricity market structures; and (iii) performance of operation optimisation with the aim of maximising economic returns of the hybrid power plant for different wholesale electricity market structures.

Bibliography

[1] Kern F, Rogge KS. The pace of governed energy transitions: Agency, international dynamics and the global Paris agreement accelerating decarbonisation processes? Energy Research & Social Science 2016;22:13-17.

[2] Department of Business, Energy & Industrial Strategy. Nuclear Industrial Strategy - The UK's Nuclear Future. 2013. https://www.gov.uk/government/publications/nuclear-industrial-strategy-the-uks-nuclear-future [accessed: 13 June 2022]

[3] Department of Business, Energy & Industrial Strategy. Climate Change Act 2008 (2050 Target Amendment) Order. 2019. https://www.legislation.gov.uk/uksi/2019/1056/made [accessed: 13 April 2021]

[4] Department of Business, Energy & Industrial Strategy. UK Energy in Brief 2022. http://www.gov.uk/government/statistics/uk-energy-in-brief-2022 [accessed: 2 March 2023]

[5] International Atomic Energy Agency (IAEA), Climate Change and Nuclear Power. 2020. https://www.iaea.org/publications/14725/climate-change-and-nuclear-power-2020 [accessed: 24 May 2022]

[6] World Nuclear Association (WNA). Nuclear Power in France. https://world-nuclear.org/information-library/country-profiles/countries-a-f/france.aspx. [accessed: 10 January 2023]

[7] Campbell C. As Putin threatens nuclear disaster, Europe learns to embrace nuclear energy again. Time. 2022. https://time.com/6169164/ukraine-nuclear-energy-europe/ [accessed: 13 May 2022]

[8] World Nuclear Association (WNA). Nuclear Power in the United Kingdom. https://world-nuclear.org/information-library/country-profiles/countries-t-z/united-kingdom.aspx [accessed: 24 January 2023]

[9] International Atomic Energy Agency (IAEA). Advances in Small Modular Reactor Technology Developments. 2022. https://nucleus.iaea.org/sites/smr/Shared%20Documents/2022%20IAEA%20SMR%20ARIS%20Booklet_rev11_with%20cover.pdf [accessed: 24 January 2022]

[10] Honorio L, Bartaire JG, Bauerschmidt R, Ohman T, et al. Efficiency in Electricity Generation 2003. Union of the Electricity Industry – EURELECTRIC.

[11] Popov D, Borissova A. Innovative configuration of a hybrid nuclear-solar tower power plant. Energy 2017;125:736-746.

[12] Popov D, Borissova A. Innovative configuration of a hybrid nuclear-parabolic trough solar power plant. International Journal of Sustainable Energy 2018;37:616-639.

[13] Jenkins JD, Zhou Z, Ponciroli R, Vilim RB, et al. The benefits of nuclear flexibility in power system operations with renewable energy. Applied Energy 2018;222:872-884.

[14] Denholm P, King JC, Kutcher CF, Wilson PPH. Decarbonizing the electric sector: Combining renewable and nuclear energy using thermal storage. Energy Policy 2012;44:301-311.

[15] Amuda KF, Field RM. Nuclear heat storage and recovery for the APR1400. Journal of Energy Storage 2020;28:101171.

[16] Kluba A, Field R. Optimization and exergy analysis of nuclear heat storage and recovery. Energies 2019;12:4205.

[17] Alameri SA. A coupled nuclear reactor thermal energy storage system for enhanced load following operation. PhD Dissertation. Colorado School of Mines, Colorado, USA, 2015.

[18] Forsberg CW, Stack DC, Curtis D, Haratyk G, Sepulveda NA. Converting excess low-price electricity into high-temperature stored heat for industry and high-value electricity production. Electricity Journal 2017;30:42-52.

[19] Garcia HE, Mohanty A, Lin WC, Cherry RS. Dynamic analysis of hybrid energy systems under flexible operation and variable renewable generation - Part I: Dynamic performance analysis. Energy 2013;52:1-16.

[20] Garcia HE, Mohanty A, Lin WC, Cherry RS. Dynamic analysis of hybrid energy systems under flexible operation and variable renewable generation - Part II: Dynamic cost analysis. Energy 2013;52:17-26.

[21] Ruth MF, Zinaman OR, Antkowiak M, Boardman RD, et al. Nuclear-renewable hybrid energy systems: Opportunities, interconnections, and needs. Energy Convertion and Managment 2014;78:684-694.

[22] Kuravi S, Goswami Y, Stefanokos EK, Ram M, et al. Thermal energy storage for concentrating solar power plants. Technology and Innovation 2012;14:81-91.

[23] Son IW, Jeong YH, Choi YJ, Lee JI. Feasibility study of solar-nuclear hybrid system for distributed power source. Energy Conversion and Management 2021;230:113808.

[24] Son IW, Jeong Y, Son S, Park JH, Lee JI. Techno-economic evaluation of solar-nuclear hybrid system for isolated grid. Applied Energy 2022;306:118048.

[25] Herrmann U, Kearney DW. Survey of thermal energy storage for parabolic trough power plants. Journal of Solar Energy Engineering 2002;124:145.

[26] International Renewable Energy Agency (IRENA). Innovation Outlook: Thermal Energy Storage. 2020. https://www.irena.org/-/media/Files/IRENA/Agency/Publication/2020/Nov/IRENA_Innovation_Outlook_TES_2020.pdf [accessed: 28 April 2022]

[27] Gils HC, Scholz Y, Pregger T, Luca de Tena D, Heide D. Integrated modelling of variable renewable energy-based power supply in Europe. Energy 2017;123:173-188.

[28] Ma Z, Davenport P, Zhang R. Design analysis of a particle-based thermal energy storage system for concentrating solar power or grid energy storage. Journal of Energy Storage 2020;29:101382.

[29] World Nuclear Association (WNA). Nuclear Power in the World Today. 2019. http://www.world-nuclear.org/information-library/current-and-future-generation/nuclear-power-in-the-world-today.aspx [accessed: 4 June 2021]

[30] World Nuclear Association (WNA). Nuclear Power Reactors. 2018. http://www.world-nuclear.org/information-library/nuclear-fuel-cycle/nuclear-power-reactors/nuclear-power-reactors.aspx [accessed: 4 June 2021]

[31] Gjorgiev B, Čepin M. Nuclear power plant load following: Problem definition and application. 20th International Conference Nuclear Energy for New Europe. 12-15 September 2011. Bovec, Slovenia.

[32] International Atomic Energy Agency (IAEA). Non-baseload Operation in Nuclear Power Plants: Load Following and Frequency Control Modes of Flexible Operation. 2018. https://www.iaea.org/publications/11104/non-baseload-operation-in-nuclear-

power-plants-load-following-and-frequency-control-modes-of-flexible-operation [accessed: 18 December 2020].

[33] World Nuclear Association (WNA). Nuclear Power in the United Kingdom. 2019. http://www.world-nuclear.org/information-library/country-profiles/countries-t-z/united-kingdom.aspx [accessed: 12 February 2021].

[34] International Atomic Energy Agency (IAEA). Deployment Indicators for Small Modular Reactors, Methodology, Analysis of Key Factors and Case Studies. 2018. https://www.iaea.org/publications/13404/deployment-indicators-for-small-modular-reactors [accessed: 16 February 2021].

[35] Nuclear Energy Agency (NEA). Small Modular Reactors: Challenges and Opportunities. Nuclear Technology Development and Economics. 2021. https://www.oecd-nea.org/jcms/pl_57979/small-modular-reactors-challenges-and-opportunities?details=true [accessed: 16 May 2021].

[36] International Atomic Energy Agency (IAEA). Nuclear Energy Series: Technology Roadmap for Small Modular Reactor Deployment. 2021. https://www.iaea.org/publications/14861/technology-roadmap-for-small-modular-reactor-deployment [accessed: 27 February 2022].

[37] International Atomic Energy Agency (IAEA). Evaluation of High Temperature Gas Cooled Reactor Performance: Benchmark Analysis Related to the PBMR-400, PBMM, GT-MHR, HTR-10 and the ASTRA Critical Facility. 2013. https://www.iaea.org/publications/8780/evaluation-of-high-temperature-gas-cooled-reactor-performance-benchmark-analysis-related-to-the-pbmr-400-pbmm-gt-mhr-htr-10-and-the-astra-critical-facility [accessed: 27 February 2022]

[38] Locatelli G, Boarin S, Fiordaliso A, Ricotti ME. Load following of small modular reactors (SMR) by cogeneration of hydrogen: A techno-economic analysis. Energy 2018;148:494-505.

[39] Locatelli G, Boarin S, Pellegrino F, Ricotti ME. Load following with small modular reactors (SMR): A real options analysis. Energy 2015;80:41-54.

[40] Nuclear Energy Agency (NEA). Technical and Economic Aspects of Load Following with Nuclear Power Plants. 2011. https://www.oecd-nea.org/upload/docs/application/pdf/2021-

12/technical_and_economic_aspects_of_load_following_with_nuclear_power_plants.pdf [accessed: 27 January 2019]

[41] Persson J, Andgren K, Engström M., Holm A, et al. Lastfoljning I Karnkraftverk: Möjliga effektregleringar för svenska kärnkraftverk utifrån ett internationellt perspektiv, 12 Elforsk. 2011.

[42] Ludwig H, Salnikova T, Stockman A, Waas U. Load cycling capabilities of German nuclear power plants (NPP). VGB PowerTech 2011;95:38-44.

[43] Pouret L, Nuttall WJ. Can Nuclear Power Be Flexible?. Working Papers EPRG 0710, Energy Policy Research Group, Cambridge Judge Business School, University of Cambridge. 2007.

[44] Frick K, Misenheimer CT, Doster JM, Terry SD, Bragg-Sitton S. Thermal energy storage configurations for small modular reactor load shedding. Nuclear Technology 2018;202:53-70.

[45] Lovegrove K, James G, Leitch D, Ngo A, et al. Comparison of Dispatchable Renewable Electricity Options: Technologies for an Orderly Transition. Australian Renewable Energy Agency. 2018.

[46] International Energy Agency (IEA). Technology Roadmap: Solar Thermal Electricity. 2014. https://www.iea.org/reports/technology-roadmap-solar-thermal-electricity-2014 [accessed: 18 March 2019]

[47] Islam MT, Huda N, Abdullah AB, Saidur R. A comprehensive review of state-of-the-art concentrating solar power (CSP) technologies: Current status and research trends. Renewable and Sustainable Energy Reviews 2018;91:987-1018.

[48] The National Renewable Energy Laboratory (NREL). Concentrating Solar Power Projects. 2019. https://solarpaces.nrel.gov/ [accessed: 18 March 2019]

[49] González-Roubaud E, Pérez-Osorio D, Prieto C. Review of commercial thermal energy storage in concentrated solar power plants: Steam vs. molten salts. Renewable and Sustainable Energy Reviews 2017;80:133-148.

[50] Thirumalai NC, Ramaswamy MA, Srilakshmi G, Venkatesh V, Rao BS. Global review of solar tower technology. Centre for Study of Science, Technology and Policy, Karnataka. 2014. https://www.seriius.org/pdfs/global-review-solar-tower-technology.pdf [accessed: 20 March 2019]

[51] Hoffschmidt B. Receivers for Solar Tower Systems. Institute of Solar Research, Font Romeu. 2014.

[52] Pelay U, Luo L, Fan Y, Stitou D, Rood M. Thermal energy storage systems for concentrated solar power plants. Renewable and Sustainable Energy Reviews 2017;79:82-100.

[53] Ho CK. A review of high-temperature particle receivers for concentrating solar power. Applied Thermal Engineering 2016;109:958-969.

[54] Turchi CS, Ma Z, Neises T, Wagner M. Thermodynamic study of advanced supercritical carbon dioxide power cycles for high performance concentrating solar power systems. ASME 2012 6th International Conference on Energy Sustainability, Parts A and B 2012;135:375.

[55] Sarbu I, Sebarchievici C. A Comprehensive review of thermal energy storage. Sustainability 2018;10:191.

[56] International Renewable energy Agency (IRENA). Thermal Energy Storage, Technology Brief. 2013. https://www.irena.org/publications/2013/Jan/Thermalenergy-storage#:~:text=This%20brief%20deals%20primarily%20with,applications%20or%20for%20power%20generation. [accessed: 24 March 2019]

[57] Cárdenas B, Swinfen-Styles L, Rouse J, Hoskin A, et al. Energy storage capacity vs. renewable penetration: A study for the UK. Renewable Energy 2021;171:849-867.

[58] Cárdenas B, León N. High temperature latent heat thermal energy storage: Phase change materials, design considerations and performance enhancement techniques. Renewable and Sustainable Energy Reviews 2013;27:724-737.

[59] Jerz J, Tobolka P, Michenka V, Dvorák T. Heat storage in future zero-energy buildings. International Journal of Innovative Research in Science, Engineering and Technology 2015;4:6722-6728.

[60] Dunham MT, Iverson B. High-efficiency thermodynamic power cycles for concentrated Solar power systems. Renewable and Sustainable Energy Reviews 2014;30:758-770.

[61] Hirsch T, Feldhoff JF, Hennecke K, Pitz-Paal R. Advancements in the field of direct steam generation in linear solar concentrators-a review. Heat Transfer Engineering 2014;35:258-271.

[62] Dirker J, Juggurnath D, Kaya A, Osowade EA, et al. Thermal energy processes in direct steam generation solar systems: Boiling, condensation and energy storage- A review. Frontiers in Energy Research 2019;6:147.

[63] Birnbaum J, Eck M, Fichtner M, Hirsch T, et al. A direct steam generation solar power plant with integrated thermal storage. Journal of Solar Energy Engineering 2010;132:0310141.

[64] Sun J, Liu Q, Hong H. Numerical study of parabolic-trough direct steam generation loop in recirculation mode: Characteristics, performance and general operation strategy. Energy Conversion and Management 2015;96:287-302.

[65] Steinmann WD, Eck M. Buffer storage for direct steam generation. Solar Energy 2006;80:1277-1282.

[66] Laing D, Bahl C, Fiß M, Hempel M, Bauer T, et al. Combined storage system developments for direct steam generation in solar thermal power plants. ISES Solar World Congress 2011, Kassel, Germany.

[67] Karakurt AS, Güneş Ü, Performance analysis of a steam turbine power plant at part load conditions. Journal of Thermal Engineering 2017;3:1121-1128.

[68] Prieto C, Rodríguez A, Patiño D, Cabeza LF. Thermal energy storage evaluation in direct steam generation solar plants. Solar Energy 2018;159:501-509.

[69] Bai F, Xu C. Performance analysis of a two-stage thermal energy storage system using concrete and steam accumulator. Applied Thermal Engineering 2011;31:2764-2771.

[70] Morisson V, Rady M, Palomo E, Arquis E. Thermal energy storage systems for electricity production using solar energy direct steam generation technology. Chemical Engineering and Processing 2008;47:499-507.

[71] Seitz M, Cetin P, Eck M. Thermal storage concept for solar thermal power plants with direct steam generation. Energy Procedia 2013;49:993-1002.

[72] Valenzuela L. Thermal energy storage concepts for direct steam generation (DSG) solar plants. Advances in Concentrating Solar Thermal Research and Technology 2016:269-289.

[73] Bachelier C, Selig M, Mertins M, Stieglitz R, et al. Systematic analysis of Fresnel CSP plants with wnergy storage. Energy Procedia 2015;69:1201-1210.

[74] Guédez R, Arnaudo M, Topel M, Zanino R, Hassar Z, Laumert B. Techno-economic performance evaluation of direct steam generation solar tower plants with thermal energy storage systems based on high-temperature concrete and encapsulated phase change materials. AIP Conference Proceedings 2016:1734.

[75] Li J, Gao G, Kutlu C, Liu K, et al. A novel approach to thermal storage of direct steam generation solar power systems through two-step heat discharge. Applied Energy 2019;236:81-100.

[76] Tian Y, Zhao CY. A review of solar collectors and thermal energy storage in solar thermal applications. Applied Energy 2013;104:538-553.

[77] Salomoni VA, Majorana CE, Giannuzzi GM, Miliozzi A, et al. Thermal storage of sensible heat using concrete modules in solar power plants. Solar Energy 2014;103:303-315.

[78] Laing D, Bahl C, Bauer T, Fiss M, et al. High-temperature solid-media thermal energy storage for solar thermal power plants. Proceedings of the IEEE 2012;100:516-524.

[79] Laing D, Bauer T, Lehmann D, Bahl C. Development of a thermal energy storage system for parabolic trough power plants with direct steam generation. Journal of Solar Energy Engineering 2010;132:551-559.

[80] Eck M, Eickhoff M, Fontela P, Laing D, et al. Test and demonstration of the direct steam generation (DSG) at 500 °C. SolarPaces Conference 2009, Berlin, Germany.

[81] EnergyNest. Thermal battery technology, https://energy-nest.com/technology/ [accessed: 10 September 2021].

[82] Carlson F, Davidson JH, Tran N, Stein A. Model of the impact of use of thermal energy storage on operation of a nuclear power plant Rankine cycle. Energy Conversion and Management 2019;181:36-47.

[83] Park JH, Heo JY, Lee JI. Techno-economic study of nuclear integrated liquid air energy storage system. Energy Conversion and Management 2022;251:114937.

[84] Forsberg C. Hybrid systems to address seasonal mismatches between electricity production and demand in nuclear renewable electrical grids. Energy Policy 2013;62:333-341.

[85] Forsberg CW. Heat in a bottle. ASME Mechanical Engineering 2019;141:36–41.

[86] Forsberg C, Brick S, Haratyk G. Coupling heat storage to nuclear reactors for variable electricity output with baseload reactor operation. Electricity Journal 2018;31:23-31.

[87] Carlson F, Davidson JH. On the use of thermal energy storage for flexible baseload power plants: Thermodynamic analysis of options for a nuclear Rankine cycle. Journal of Heat Transfer 2020;142:052904.

[88] Carlson F, Davidson JH. Parametric study of thermodynamic and cost performance of thermal energy storage coupled with nuclear power. Energy Conversion and Management 2021;236:114054.

[89] Li Y, Cao H, Wang S, Jin Y, et al. Load shifting of nuclear power plants using cryogenic energy storage technology. Applied Energy 2014;113:1710-1716.

[90] Forsberg CW. Variable and assured peak electricity production from base-load light-water reactors with heat storage and auxiliary combustible fuels. Nuclear Technology 2019;205:377-396.

[91] Green M, Sabharwall P, Mckellar MG, Toon SJ. Nuclear hybrid energy system: Molten salt energy storage. 2013. Idaho International Laboratory. Idaho, USA.

[92] Curtis D, Shifflet N, Forsberg C. Technology options for integrated thermal energy storage in nuclear power plants. Transaction of the American Nuclear Society 2017;116.

[93] Carlson F, Davidson JH. Nuclear power coupled with thermal energy storage: Impact of technical performance on economics in an exemplary electricity grid. ASME Open Journal of Engineering 2022;1:011006.

[94] Borowiec K, Wysocki A, Shaner S, Greenwood MS, Ellis M. Increasing revenue of nuclear power plants with thermal storage. Journal of Energy Resources Technology 2020;142:042006.

[95] Duan L, Petroski R, Wood L, Caldeira K. Stylized least-cost analysis of flexible nuclear power in deeply decarbonized electricity systems considering wind and solar resources worldwide. Nature Energy 2022;7:260-269.

[96] Peterseim JH, White S, Tadros A, Hellwig U. Concentrating solar power hybrid plants - Enabling cost effective synergies. Renewable Energy 2014;67:178-185.

[97] Brakmann G, Mohammad FA, Dolejsi M, Wiemann M. Construction of the ISCC Kuraymat. International SolarPACES Conference 2009.

[98] Behar O, Kellaf A, Mohamedi K, Belhamel M. Instantaneous performance of the first integrated solar combined cycle system in Algeria. Energy Procedia 2011;6:185-193.

[99] Tsikalakis A, Tomtsi T, Hatziargyriou ND, Poillikkas A, et al. Review of best practices of solar electricity resources applications in selected Middle East and North Africa (MENA) countries. Renewable and Sustainable Energy Reviews 2011;15:2838-2849.

[100] Horn M, Führing H, Rheinländer J. Economic analysis of integrated solar combined cycle power plants. Energy 2003;29:935-945.

[101] Suman S. Hybrid nuclear-renewable energy systems: A review. Journal of Cleaner Production 2018;181:166-177.

[102] Papaioannou IT, Purvins A, Shropshire D, Carlsson J. Role of a hybrid energy system comprising a small/medium-sized nuclear reactor and a biomass processing plant in a scenario with a high deployment of onshore wind farms. Journal of Energy Engineering 2013;140:04013005.

[103] Petrovic B. Role of high-temperature reactors in sustainable development and synergy with renewable energy sources. 2014. Nuclear and Radiological Engineering Georgia Tech, Atlanta, USA. https://www.ieee.hr/_download/repository/Petrovic_FER_2014-12-16b%28publ%29.pdf [accessed: 13 April 2020]

[104] Zhao BC, Cheng MS, Liu C, Dai ZM. Conceptual design and preliminary performance analysis of a hybrid nuclear-solar power system with molten-salt packed-bed thermal energy storage for on-demand power supply. Energy Conversion and Management 2018;166:174-186.

[105] Naserbegi A, Aghaie M. Exergy optimization of nuclear-solar dual proposed power plant based on GWO algorithm. Progress in Nuclear Energy 2021;140:103925.

[106] White BT, Wagner MJ, Neises T, Stansbury C, Lindley B. Modeling of combined lead fast reactor and concentrating solar power supercritical carbon dioxide cycles to demonstrate feasibility, efficiency gains, and cost reductions. Sustainability 2021;13:12428.

[107] Wang G, Yin J, Lin J, Chen Z, Hu P. Design and economic analysis of a novel hybrid nuclear-solar complementary power system for power generation and desalination. Applied Thermal Engineering 2021;187:116564.

[108] MATLAB. Version 9.10.0 (R2021a), MathWorks Inc. 2021. Natick, Massachusetts.

[109] Lemmon EW, Bell IH, Huber ML, McLinden MO. NIST Standard Reference Database 23: Reference Fluid Thermodynamic and Transport Properties-REFPROP, Version 10.0, National Institute of Standards and Technology. 2018.

[110] Office for Nuclear Regulation (ONR). Operational reactors. 2022. https://www.onr.org.uk/civil-nuclear-reactors/ [accessed: 19 March 2022]

[111] Electric de France Energy (EDF). Nuclear New Build Projects, 2021. https://www.edfenergy.com/energy/nuclear-new-build-projects [accessed: 27 March 2021]

[112] Office of Nuclear Energy. NRC Certifies First U.S. Small Modular Reactor Design. 2023. https://www.energy.gov/ne/articles/nrc-certifies-first-us-small-modular-reactor-design#:~:text=The%20NRC%20accepted%20NuScale's%20SMR,use%20in%20the%20United%20States. [accessed: 26 January 2023]

[113] Nonbøl E. Description of the advanced gas cooled type of reactor (AGR).1996. Risø National Laboratory, Roskilde, Denmark.

[114] International Atomic Energy Agency (IAEA). Country Statistics, Hinkley Point C-1. 2021. https://pris.iaea.org/PRIS/CountryStatistics/ReactorDetails.aspx?current=1072 [accessed: 27 March 2021]

[115] AREVA Nuclear Power and Electric de France Energy (EDF). UK-EPR, Fundamental Safety Overview, Chapter A: EPR Design Description. 2007.

[116] AREVA. European Pressurised Reactor, 2005. http://www.ftj.agh.edu.pl/~cetnar/epr/EPR-broszura.pdf [accessed: 27 March 2021]

[117] NuScale Power, LLC. NuScale Small Modular Reactor. NuScale Power, LLC. Fact sheet. 2022. https://www.nuscalepower.com/en [accessed: 16 April 2022]

[118] NuScale Power, LLC. NuScale Standard Plant Design Certification Application, Chapter Ten: Steam and Power Conversion System, Part 2 – Tier 2. Revision 2. 2018.

[119] Al Kindi AA, Pantaleo AM, Wang K, Markides CN. Optimal system configuration and operation strategies of flexible hybrid nuclear-solar power plants. The 33rd International conference on Efficiency, Cost, Optimisation, Simulation and Environmental Impact of Energy Systems (ECOS) 2020. 29 June - 3 July, 2020. Osaka, Japan.

[120] Ho CK, Iverson BD. Review of high-temperature central receiver designs for concentrating solar power. Renewable and Sustainable Energy Reviews 2014;29:835-846.

[121] The National Renewable Energy Laboratory (NREL). System Advisor Model (SAM). Version 2022.11.21. https://sam.nrel.gov/ [accessed: 18 November 2022]

[122] Sartori E. Convection coefficient equations for forced air flow over flat surfaces. Solar Energy 2006;80:1063-1071.

[123] Pacheco JE, Bradshaw RW, Dawson DB, De la Rosa W, et al. Final Test and Evaluation Results from the Solar Two Project. 2002. Sandia National Laboratories, New Mexico, USA.

[124] Stevanovic VD, Petrovic MM, Milivojevic S, Maslovaric B. Prediction and control of steam accumulation. Heat Transfer Engineering 2015;36:498-510.

[125] Biglia A, Comba L, Fabrizio E, Gay P, Aimonino DR. Steam batch thermal processes in unsteady state conditions: Modelling and application to a case study in the food industry. Applied Thermal Engineering 2017;118:638-651.

[126] González-Gómez PA, Laporte-Azcué M, Fernández-Torrijos M, Santana D. Hybrid storage solution steam-accumulator combined to concrete-block to save energy during startups of combined cycles. Energy Conversion and Management 2022;253:115168.

[127] Jian Y, Falcoz Q, Neveu P, Bai F, Wang Y, Wang Z. Design and optimization of solid thermal energy storage modules for solar thermal power plant applications. Applied Energy 2015;139:30-42.

[128] Xu B, Li PW, Chan CL. Extending the validity of lumped capacitance method for large Biot number in thermal storage application. Solar Energy 2012;86:1709-1724.

[129] Jian Y, Bai F, Falcoz Q, Xu C, Wang Y, Wang Z. Thermal analysis and design of solid energy storage systems using a modified lumped capacitance method. Applied Thermal Engineering 2015;75:213-223.

[130] Carbon Steel Handbook. Electric Power Research Institute (EPRI). 2007.

[131] The Engineering Toolbox. Thermal conductivities of common metals, metallic elements and alloys. https://www.engineeringtoolbox.com/thermal-conductivity-metals-d_858.html [accessed: 10 August 2022].

[132] Hoivik N, Greiner C, Barragan J, Iniesta AC, et al. Long-term performance results of concrete-based modular thermal energy storage system. Journal of Energy Storage 2019;24:100735.

[133] Çengel YA, Boles MA, Kanoğlu M. Thermodynamics: an engineering approach. Ninth edition, McGraw-Hill Education. 2019.

[134] Gnielinski V. New equations for heat and mass transfer in the turbulent flow in pipes and channels. International Chemical Engineering 1976;16:359-368.

[135] Farshad FF, Rieke HH. Surface-roughness design values for modern pipes. SPE Drill & Completion 2006;24:212-215.

[136] Shah MM. An improved and extended general correlation for heat transfer during condensation in plain tubes. HVAC&R Research 2009;15:889-913.

[137] Shah MM. General correlation for heat transfer during condensation in plain tubes: Further development and verification. ASHRAE Transaction 2013;119:3-11.

[138] Guarracino I, Mellor A, Ekins-Daukes NJ, Markides CN. Dynamic coupled thermal-and-electrical modelling of sheet-and-tube hybrid photovoltaic/thermal (PVT) collectors. Applied Thermal Engineering 2016;101:778-795.

[139] Wang K, Pantaleo AM, Herrando M, Faccia M, et al. Spectral-splitting hybrid PV-thermal (PVT) systems for combined heat and power provision to dairy farms. Renewable Energy 2020;159:1047-1065.

[140] Song J, Wang Y, Wang K, Wang J, Markides CN. Combined supercritical CO_2 (SCO_2) cycle and organic Rankine cycle (ORC) system for hybrid solar and geothermal power generation: Thermoeconomic assessment of various configurations. Renewable Energy 2021;174:1020-1035.

[141] Bonk A, Sau S, Uranga N, Hernaiz M, Bauer T. Advanced heat transfer fluids for direct molten salt line-focusing CSP plants. Progress in Energy Combustion Science 2018;67:69-87.

[142] D'Aguanno B, Karthik M, Grace AN, Floris A. Thermostatic properties of nitrate molten salts and their solar and eutectic mixtures. Scientific Reports 2018;8:10485.

[143] Serrano-ópez R, Fradera J, Cuesta-López S. Molten salts database for energy applications. Chemical Engineering and Processing - Process Intensification 2013;73:87-102.

[144] Wu Y, Li J, Wang M, Wang H, Zhao Y. Preparation and thermophysical properties of high thermal conductive solar salt/MWCNTs composite materials. ChemistrySelect 2019;4:4521-4527.

[145] Gilman P, Blair N, Mehos M, Christensen C, et al. Solar Advisor Model (SAM) user guide for Version 2.0. The National Renewable Energy Laboratory (NREL). 2008.

[146] Pump cavitation and how to avoid it: best practices in pump system design. Xylem Applied Water Systems, Xylem Inc. 2015

[147] Golwalker KR, Kumar R. Practical guidelines for the chemical industry: operation, processes, and sustainability in modern facilities. First edition, Springer. 2022.

[148] Ray A. Dynamic modelling of power plant turbines for controller design. Applied Mathematical Modelling 1980;4:109-112.

[149] Gundogdu B, Nejad S, Gladwin DT, Foster MP, Stone DA. A battery energy management strategy for U.K. enhanced frequency response and triad avoidance. IEEE Transactions on Industrial Electronics 2018;65(12):9509-9517.

[150] Cooke DH. On prediction of off-design multistage turbine pressures by Stodola's ellipse. Journal of Engineering for Gas Turbines and Power 1984;107:596-606.

[151] Fuls WF. Enhancement to the traditional Ellipse Law for more accurate modeling of a turbine with a finite number of stages. Journal of Engineering for Gas Turbines and Power 2017;139:112603.

[152] Thanganadar D, Fornarelli F, Camporeale S, Asfand F, Patchigolla K. Off-design and annual performance analysis of supercritical carbon dioxide cycle with thermal storage for CSP application. Applied Energy 2021;282:116200.

[153] Calise F, Capuozzo C, Carotenuto A, Vanoli L. Thermoeconomic analysis and off-design performance of an organic Rankine cycle powered by medium-temperature heat sources. Solar Energy 2014;103:595-609.

[154] Seider WD, Lewin DR, Seader JD, Widagdo S, et al. Product and Process Design Principles: Synthesis, Analysis and Evaluation. Fourth edition, Wiley. 2017.

[155] Chemical engineering essentials for the chemical professional. Chemical engineering plant cost index. 2021. https://www.chemengonline.com/pci [accessed: 16 January 2022].

[156] Towler G, Sinnott R. Chemical Engineering Design: Principles, Practice and Economics of Plant and Process Design. Third edition. Elsevier Ltd. 2022.

[157] Morandin M, Mercangöz M, Hemrle J, Maréchal F, Favrat D. Thermoeconomic design optimization of a thermo-electric energy storage system based on transcritical CO_2 cycles. Energy 2013;58:571-587.

[158] Couper JR, Penney WR, Fair JR, Walas SM. Chemical Process Equipment, Selection and Design. Third edition, Elsevier. 2012.

[159] Ulrich GD, Vasudevan PL, Chemical Engineering Process Design and Economics: A Practical Guide. Second edition, Process Publishing. 2004.

[160] Turton R, Bailie RC, Whiting WB, Shaeiwitz JA, Bhattacharyya D. Analysis, Synthesis, and Design of Chemical Processes. Fourth edition, Pearson Education. 2012.

[161] Weiland NT, Lance BW. SCO_2 Power cycle component cost correlations from DOE data spinning multiple scales and applications. Proceedings of ASME Turbo Expo 2019: Turbomachinery Technical Conference and Exposition. 17-21 June 2019, Arizona, USA.

[162] International Energy Agency (IEA). Nuclear Energy Agency (NEA). Projected Costs of Generated Electricity. 2020.

[163] U.S Department of Energy. U.S Energy Information Administration. Capital Cost and Performance Characteristic Estimates for Utility Scale Electric Power Generating Technologies. 2020. https://www.eia.gov/analysis/studies/powerplants/capitalcost/pdf/capital_cost_AEO2020.pdf [accessed 19 October 2022].

[164] Black GA, Aydogan F, Koerner CL. Economic viability of light water small modular nuclear reactors: General methodology and vendor data. Renewable and Sustainable Energy Reviews 2019;103:248-258.

[165] John E, Hale M, Selvam P. Concrete as a thermal energy storage medium for thermocline solar energy storage systems. Solar Energy 2013;96:194-204.

[166] Libby C. Solar Thermocline Storage Systems: Preliminary Design Study. Electric Power Research Institute (EPRI) 2010.

[167] Nithyanandam K, Pitchumani R. Cost and performance analysis of concentrating solar power systems with integrated latent thermal energy storage. Energy 2014;64:793-810.

[168] Zhao B, Cheng M, Liu C, Dai Z. Thermal performance and cost analysis of a multi-layered solid-PCM thermocline thermal energy storage for CSP tower plants. Applied Energy 2016;178:784-799.

[169] Liu M, Steven Tay NH, Bell S, Belusko M, et al. Review on concentrating solar power plants and new developments in high temperature thermal energy storage technologies. Renewable and Sustainable Energy Reviews 2016;53:1411-1432.

[170] Turchi CS, Vidal J, Bauer M. Molten salt power towers operating at 600–650 °C: Salt selection and cost benefits. Solar Energy 2018;164:38-46.

[171] Indiamart. 316 Stainless Steel price: 316 Grade. https://dir.indiamart.com/impcat/316-stainless-steel-sheet.html [accessed: 2 October 2022].

[172] MEPS International. World Stainless Steel Prices. https://mepsinternational.com/gb/en/products/world-stainless-steel-prices?#product-unit-measurement-conversion-form [accessed: 02 October 2022].

[173] Stainless steel price rises on the horizon for 2023. https://www.hellenicshippingnews.com/stainless-steel-price-rises-on-the-horizon-for-2023/ [accessed 14 January 2023].

[174] Alloy Wire. Stainless Steel 316. https://www.alloywire.com/alloys/stainless-steel-316/ [accessed: 14 January 2023].

[175] Ladkany S, Culbreth W, Loyd N. Molten salts and applications II: 565 °C molten salt solar energy storage design, corrosion, and insulation. Journal of Energy and Power Engineering 2018;12:517-532.

[176] Herrmann U, Kelly B, Price H. Two-tank molten salt storage for parabolic trough solar power plants. Energy 2004;29:883-893.

[177] Bauer T, Odenthal C, Bonk A. Molten salt storage for power generation. Chemie Ingenieur Technik 2021;93:534-546.

[178] Abdel-Raouf MM. Levelized cost analysis of nuclear fuel cycle for light water reactors. INPRO Dialogue Forum on Cooperative Approaches to the Back end of the Nuclear Fuel Cycle: Drivers and Legal, Institutional and Financial Implements. International Atomic Energy Agency (IAEA). 2015.

[179] Shropshire D. Economic viability of small to medium-sized reactors deployed in future European energy markets. Progress in Nuclear Energy 2011;53:299-307.

[180] U.S Department of Energy. U.S Energy Information Administration. Cost and Performance Characteristics of New Generating Technologies, Annual Energy Outlook. 2022.

[181] International Renewable Energy Agency (IRENA). Renewable Power Generation Costs in 2019. 2020 https://www.irena.org/-/media/Files/IRENA/Agency/Publication/2018/Jan/IRENA_2017_Power_Costs_2018.pdf [accessed: 26 February 2021].

[182] Pudjianto D, Aunedi M, Djapic P, Strbac G. Whole-system assessment of value of energy storage in low-carbon electricity systems. IEEE Transaction on Smart Grids 2014;5:1098-1109.

[183] Strbac G, Aunedi M, Konstantelos I, Moreira R, et al. Opportunities for energy storage: Assessing whole-system economic benefits of energy storage in future electricity systems. IEEE Power & Energy Magazine 2017;15:32-41.

[184] Teng F, Pudjianto D, Aunedi M, Strbac G. Assessment of future whole-system value of large-scale pumped storage plants in Europe. Energies 2018;11:246.

[185] Georgiou S, Aunedi M, Strbac G, Markides CN. On the value of liquid-air and pumped-thermal electricity storage systems in low-carbon electricity systems. Energy 2020;193:116680.

[186] Fico Xpress Optimization, https://www.fico.com/en/products/fico-xpress-optimization [accessed: 14 May 2021]

[187] Al Kindi AA, Sapin P, Pantaleo AM, Wang K, Markides CN. Thermo-economic analysis of steam accumulation and solid thermal energy storage in direct steam generation concentrated solar power plants. Energy Conversion and Management 2022;274:116222.

[188] Van Putten H, Colonna P. Dynamic modeling of steam power cycles: Part II - Simulation of a small simple Rankine cycle system. Applied Thermal Engineering 2007;27:2566-2582.

[189] Department of Energy of the Republic of South Africa. Independent Power Producers Procurement Programme (IPPPP): An Overview. 2018.

[190] Meteonorm. Worldwide irradiation data. 2019. https://meteonorm.com/en/ [accessed: 18 June 2020].

[191] Zhao Y, Liu M, Wang C, Li X, et al. Increasing operational flexibility of supercritical coal-fired power plants by regulating thermal system configuration during transient processes. Applied Energy 2018;228:2375-2386.

[192] Pudjianto D, Ramsay C, Strbac G. Virtual power plant and system integration of distributed energy resources. IET Renewable Power Generation 2007;1:10.

[193] Lombardi P, Styczynski ZA, Buchholz BM. Optimal operation of a distribution power system with renewable generators and desalination plants. GCC Power 2008.

[194] Spagnuolo G, Petrone G, Araujo S, Cecati C, et al. Renewable energy operation and conversion schemes: A summary of discussions during the seminar on renewable energy systems. IEEE Industrial Electronics Magazine 2010;4:38-51.

[195] Markides CN. Low-concentration solar-power systems based on organic Rankine cycles for distributed-scale applications: Overview and further developments. Frontier Energy Research 2015;3:47.

[196] Oyewunmi OA, Taleb AI, Haslam AJ, Markides CN. An Assessment of working-fluid mixtures using SAFT-VR Mie for use in organic Rankine cycle systems for waste-heat recovery. Computational Thermal Sciences: An international Journal 2014;6:301-316.

[197] Oyewunmi OA, Taleb AI, Haslam AJ, Markides CN. On the use of SAFT-VR Mie for assessing large-glide fluorocarbon working-fluid mixtures in organic Rankine cycles. Applied Energy 2016;163:263-282.

[198] Oyewunmi OA, Markides CN. Thermo-economic and heat transfer optimization of working-fluid mixtures in a low-temperature organic Rankine cycle system. Energies 2016;9:448.

[199] Romanos P, Al Kindi AA, Pantaleo AM, Markides CN. Flexible nuclear plants with thermal energy storage and secondary power cycles: Virtual power plant integration in a UK energy system case study. e-Prime - Advances in Electrical Engineering, Electronics and Energy 2022;2:100027.

[200] Moran MJ, Shapiro HN. Vapor power systems, Fundamentals of Engineering Thermodynamics. Fourth edition, John Wiley & Sons, USA. 1999.

[201] Central Electricity Generating Board (CEGB), Feed water heating systems, Modern Power Station Practice. Second edition, Pergamon Press, Oxford, UK. 1971.

[202] Carberry JJ. Media for heat transport. Chemical Engineering 1953;60:225-228.

[203] Kearney D, Herrmann U, Nava P, Kelly P, et al. Assessment of a molten salt heat transfer fluid in a parabolic trough solar field. Journal of Solar Energy Engineering 2003;125:170-176.

[204] McTigue JD, White AJ, Markides CN. Parametric studies and optimisation of pumped thermal electricity storage. Applied Energy 2015;137:800-811.

[205] Crandall DM, Thacher EF. Segmented thermal storage. Solar Energy 2004:77:435-440.

[206] Sarbu I, Dorca A. Review on heat transfer analysis in thermal energy storage using latent heat storage systems and phase change materials. International Journal of Energy Research 2019;43:29-64.

[207] Freeman J, Hellgardt K, Markides CN. An assessment of solar-powered organic Rankine cycle systems for combined heating and power in UK domestic applications. Applied Energy 2015;138:605-620.

[208] HITEC® Heat Transfer Salt, Coastal Chemical Co., L.L.C, Brenntag Company, Houston, Texas, United States. http://stoppingclimatechange.com/MSR%20-%20HITEC%20Heat%20Transfer%20Salt.pdf [accessed :10 November 2020].

[209] Boerema N, Morrison G, Taylor R, Rosengarten G. Liquid sodium versus Hitec as a heat transfer fluid in solar thermal central receiver systems. Solar Energy 2012;86:2293-2305.

[210] Gupta A, Mathie R, Markides CN. An experimental and computational investigation of a thermal storage system based on a phase change material: heat transfer and performance characterization. Computational Thermal Sciences: An international Journal 2014;6:341-359.

[211] Elmaazouzi Z, El Alami M, Agalit H, Bennouna EG. Performance evaluation of latent heat TES system-case study: Dimensions improvements of annular fins exchanger. 6th International Conference on Energy and Environment Research, ICEER 2019, 22–25 July, 2019, University of Aveiro, Portugal.

[212] Zhang X, Wu L, Wang X, Ju G. Comparative study of waste heat steam SRC, ORC and S-ORC power generation systems in medium-low temperature. Applied Thermal Engineering 2016;106:1427-1439.

[213] Song J, Loo P, Teo J, Markides CN. Thermo-economic optimization of organic Rankine cycle (ORC) systems for geothermal power generation: A comparative study of system configurations. Frontier Energy Research 2020;8:6.

[214] Song J, Gu CW. Analysis of ORC (organic Rankine cycle) systems with pure hydrocarbons and mixtures of hydrocarbon and retardant for engine waste heat recovery. Applied Thermal Engineering 2015;89:693-702.

[215] Matuszewska D, Olczak P. Evaluation of using gas turbine to increase efficiency of the organic Rankine cycle (ORC). Energies 2020;13:1499.

[216] Eyerer S, Dawo F, Kaindl J, Wieland C, Spliethoff H. Experimental investigation of modern ORC working fluids R1224yd(Z) and R1233zd(E) as replacements for R245fa. Applied Energy 2019;240:946-963.

[217] Bao J, Zhao L. A review of working fluid and expander selections for organic Rankine cycle. Renewable and Sustainable Energy Reviews 2013;24:325-342.

[218] Zhu J, Bo H, Li T, Hu K, Liu K. A thermodynamics comparison of subcritical and transcritical organic Rankine cycle system for power generation, Journal of Central South University 2015;22:3641-3649.

[219] NORD POOL, Historical market data. www.nordpoolgroup.com/historical-market-data [accessed: 20 November 2022].

[220] Lemmens S. A perspective on costs and cost estimation techniques for organic Rankine cycle systems. 3rd International Seminar on ORC Power Systems. 2015. Brussels, Belgium.

[221] Quoilin S, Van Den Broek M, Declaye S, Dewallef P, Lemort V. Techno-economic survey of organic Rankine cycle (ORC) systems. Renewable and Sustainable Energy Reviews 2013;22:168-186.

[222] Panagiotakopoulou P. Different types of electricity markets modelled using PLEXOS integrated energy model- the UK balancing market example, Energy Exemplar. https://energyexemplar.com/wp-content/uploads/Different-types-of-electricity-

markets-modelled-using-PLEXOS-Integrated-Energy-Model-_The-UK-Balancing-Market-example.pdf [accessed: 25 June 2020].

[223] ENGIE. Understanding the capacity market. Leeds, UK. www.engie.co.uk/wp-content/uploads/2016/07/capacitymarketguide.pdf [accessed: 19 August 2021].

[224] National Grid ESO. Electricity market reform – delivery body, Auction results. https://www.emrdeliverybody.com/CM/Capacity%20Auction%20Information.aspx [accessed: 25 June 2020].

[225] Department for Business, Energy & Industrial Strategy. Capacity market consultation – improving the framework, government response. 2017. Crown, London, UK.

[226] Strbac G, Pudjianto D, Aunedi M, Djapic P, et al. Role and value of flexibility in facilitating cost-effective energy system decarbonisation. Progress in Energy 2020;2:042001.

[227] Aunedi M, Wills K, Green T, Strbac G. Net-zero GB electricity: cost-optimal generation and storage mix. Energy Futures Lab White Paper 2021. https://www.imperial.ac.uk/energy-futures-lab/reports/white-papers/net-zero-gb-electricity/ [accessed: 6 July 2021]

[228] Hast A, Rinne S, Syri S, Kiviluoma J. The role of heat storages in facilitating the adaptation of district heating systems to large amount of variable renewable electricity. Energy 2017;137:775-788.

[229] Aunedi M, Pantaleo AM, Kuriyan K, Strbac G, Shah N. Modelling of national and local interactions between heat and electricity networks in low-carbon energy systems. Applied Energy 2020;276:115522.

[230] Al Kindi AA, Aunedi M, Pantaleo AM, Strbac G, Markides CN. Thermo-economic assessment of flexible nuclear power plants in future low-carbon electricity systems: Role of thermal energy storage. Energy Conversion and Management 2022;258:115484.

[231] Fröhling W, Unger HM, Dong Y. Thermodynamic assessment of plant efficiencies for HTR power conversion systems. International Atomic Energy Agency (IAEA). 2002.

[232] Wibisono AF, Shwageraus E. Thermodynamic performance of pressurized water reactor power conversion cycle combined with fossil-fuel superheater. Energy 2016;117:190-197.

[233] Lloyd CA, Roulstone ARM, Middleton C. The impact of modularisation strategies on small modular reactor cost. Proceedings of the 2018 International Congress on Advances in Nuclear Power Plants (ICAPP) 2018;1042–1049.

[234] Wei G, Wang G, Xu C, Ju X, et al. Selection principles and thermophysical properties of high temperature phase change materials for thermal energy storage: A review. Renewable and Sustainable Energy Reviews 2018;81:1771-1786.

[235] Li Z, Lu Y, Huang R, Chang J, et al. Applications and technological challenges for heat recovery, storage and utilisation with latent thermal energy storage. Applied Energy 2021;283:116277.

[236] Bauer T, Steinmann WD, Laing D, Tamme R. Thermal Energy Storage Materials and Systems. Annual Review of Heat Transfer 2012;15:131-177.

[237] Jankowski NR, McCluskey FP. A review of phase change materials for vehicle component thermal buffering. Applied Energy 2014;113:1525-1561.

[238] Liu F, Gao B, Wang S, Wang Z, Shi Z. Measurement and estimation for density of $NaNO_2$-KNO_3-$NaNO_3$ ternary molten salts. World Non-Grid-Connected Wind Power and Energy Conference (WNWEC) 2009;1-4.

[239] Fernández AG, Galleguillos H, Fuentealba E, Pérez FJ. Thermal characterization of HITEC molten salt for energy storage in solar linear concentrated technology. Journal of Thermal Analysis and Calorimetry 2015;122:3-9.

[240] Niyas H, Rao CRC, Muthukumar P. Performance investigation of a lab-scale latent heat storage prototype – Experimental results. Solar Energy 2017;155:971-984.

[241] Xiao X, Wen D. Investigation on thermo-physical properties of molten salt enhanced with nanoparticle and copper foam. 7th International Conference of Renewable Energy Research and Applications (ICRERA) 2018;1445-1449.

[242] Gasanaliev AM, Gamataeva BY. Heat-accumulation properties of melts. Russuia Chemical Reviews 200;69:179-186.

[243] Kenisarin MM. High-temperature phase change materials for thermal energy storage. Renewable and Sustainable Energy Reviews 2010;14:955-970.

[244] Xu B, Li P, Chan C. Application of phase change materials for thermal energy storage in concentrated solar thermal power plants: A review to recent developments. Applied Energy 2015;160:286-307.

[245] Li P, Van Lew J, Chan C, Karaki W, et al. Similarity and generalized analysis of efficiencies of thermal energy storage systems. Renewable Energy 2012;39:388-402.

[246] Department of Business, Energy & Industrial Strategy. Electricity Generation Costs 2020. 2020. https://assets.publishing.service.gov.uk/government/uploads/system/uploads/attachment_data/file/911817/electricity-generation-cost-report-2020.pdf [accessed: 25 July 2023]

[247] Breeze P. Power Generation Technologies. Second edition, Newnes, London, UK. 2019.

[248] Aunedi M, Al Kindi AA, Pantaleo AM, Markides CN, Strbac G. System-driven design of flexible nuclear power plant configurations with thermal energy storage. Energy Conversion and Management 2023;291:117257.

[249] Masters GM. Renewable and Efficient Electric Power Systems. 2004. John Wiley & Sons Inc., Hoboken, New Jersey, United States.

[250] Pantaleo AM, Camporeale SM, Miliozzi A, Russo V, et al. Thermo-economic assessment of an externally fired hybrid CSP/biomass gas turbine and organic Rankine combined cycle. Energy Procedia 2017;105:174-181.

[251] Pantaleo AM, Camporeale SM, Sorrentino A, Miliozzi A, Shah N, et al. Hybrid solar-biomass combined Brayton/organic Rankine-cycle plants integrated with thermal storage: Techno-economic feasibility in selected Mediterranean areas. Renewable Energy 2020;147:2913-2931.

[252] Thanganadar D, Fornarelli F, Camporeale S, Asfand F, et al. Thermo-economic analysis, optimisation and systematic integration of supercritical carbon dioxide cycle with sensible heat thermal energy storage for CSP application. Energy 2022;238:121755.

[253] Mapsland. Large detailed political map of Oman with roads, cities and airport. https://www.mapsland.com/asia/oman/large-detailed-political-map-of-oman-with-roads-cities-and-airports [accessed: 4 March 2023]

[254] The National Renewable Energy Laboratory (NREL). NSRDB: National Solar Radiation Database. 2019. https://nsrdb.nrel.gov/data-viewer [accessed: 4 December 2022]

[255] Álvarez-Fernández M, Portillo-Valdés L del, Alonso-Tristán C. Thermal analysis of closed feedwater heaters in nuclear power plants. Applied Thermal Engineering 2014;68:45-58.

[256] Saari J, Kaikko J, Vakkilainen E, Savolainen S. Comparison of power plant steam condenser heat transfer models for on-line condition monitoring. Applied Thermal Engineering 2014;62:37-47.

[257] González-Gómez PA, Gómez-Hernández J, Briongos J V., Santana D. Thermo-economic optimization of molten salt steam generators. Energy Conversion and Management 2017;146:228-243.

[258] Garcia MM. Practical cross-border insights into renewable energy law: Renewable Energy 2023. Third edition. International Comparative Legal Guides.

[259] Dersch J, Pauca J, Schuhbauer C, Schweitzer A, Stryk A. Blueprint for Molten Salt CSP Power Plant. Final report of the research project "CSP-Reference Power Plant" No. 0324253. 2021. Cologne, Germany.

[260] Trading Economics. Inflation Rate. https://tradingeconomics.com/country-list/inflation-rate [accessed: 12 February 2023]

[261] Eddington M, Osmundsen M, Jaswal I, Rowell J, Reinhart B. Fast start combined cycles: how fast is fast?. Power Engineering, 2017. www.power-eng.com/articles/print/volume-121/issue-3/features/fast-start-combined-cycles-how-fast-is-fast.html [accessed: 25 June 2020].

Appendix A

Design of thermal tanks

A.1. Thermal Tank 1

For the calculation of the heat exchange area, A, and tube length, L, of Thermal Tank 1, the following set of assumptions are made:

1. The vapour density is much lower than the liquid density as the following:

$$\rho_{\mathrm{L}} \ll \rho_{\mathrm{V}} \, , F_{\mathrm{f}} \approx 1 \, , \delta_{\mathrm{F}} \ll D_{\mathrm{tube}} \tag{A.1}$$

where ρ_{L} and ρ_{V} are the vapour-phase (steam) and condensate/liquid-phase (water) densities, F_{f} is the waviness correction factor of the film flow, δ_{F} is the film thickness, and D_{tube} is the heat exchange tube diameter. Here, we use a number of standard type 316 stainless steel tubes with a diameter D_{tube} = 102 mm and a tube thickness d = 6 mm.

2. The velocity of the liquid phase is negligible compared to the velocity of the vapour phase, and the shear stress throughout the vapour phase is negligible.

3. The desuperheating length/area is negligible compared to the condensation length/area.

Given a variable distance z along the heat-exchanger tube of total length L (i.e., inlet at z = 0 and outlet at $z = L$) inside the tank, we define local dryness (mass) fractions at points: $\dot{x}_1$ = 0.99, $\dot{x}_2$ = 0.90, $\dot{x}_3$ = 0.50, $\dot{x}_4$ = 0.1, $\dot{x}_5$ = 0.01, $\dot{x}_6$ = 0.001, where for example for the local value $\dot{x}_2$:

$$z_2 = 0.1\, L \text{ corresponds to } \dot{x}_2 = 1 - \frac{z_2}{L} = 0.9 \tag{A.2}$$

In this case, the local value of the dryness fraction, e.g., $\dot{x}_2$ = 0.90 here, is linked to the local liquid-phase mass flowrate $\dot{m}_{\mathrm{L,z}}$ and vapour-phase mass flowrate $\dot{m}_{\mathrm{V,z}}$ through its definition:

$$\dot{x}_2 = \frac{\dot{m}_{\mathrm{V,z_2}}}{\left(\dot{m}_{\mathrm{L,z_2}} + \dot{m}_{\mathrm{V,z_2}}\right)} = \frac{\dot{m}_{\mathrm{V,z_2}}}{\dot{m}_{\mathrm{V,z=0}}} \tag{A.3}$$

where conservation of mass was used to replace the local mass flowrates with the vapour mass flowrate of the extracted steam before the reheater at the inlet to Thermal Tank 1, $\dot{m}_{\mathrm{V,z=0}}$, since the inlet liquid mass flowrate is zero, $\dot{m}_{\mathrm{L,z=0}} = 0$.

The local distribution of the vapour and liquid phases in the pipe can be described by the volumetric vapour-phase fraction $\varepsilon = V_{\mathrm{V}}/(V_{\mathrm{V}} + V_{\mathrm{L}})$, with V_{V} and V_{L} the local vapour and liquid volume phase-fractions, which is given as a function of the flow parameter, F, from the relation:

$$\varepsilon = 1 - \frac{1}{1 + \frac{1}{8.48\,F}} \tag{A.4}$$

where F is given by:

$$F = \frac{\max\left\{\left(2\,Re_{\mathrm{L,z}}\right)^{0.5};\ 0.132\,Re_{\mathrm{L,z}}^{0.9}\right\}}{Re_{\mathrm{V,z}}^{0.9}}\,\frac{\mu_{\mathrm{L}}}{\mu_{\mathrm{V}}}\sqrt{\frac{\rho_{\mathrm{V}}}{\rho_{\mathrm{L}}}} \tag{A.5}$$

and where the two Reynolds numbers, one for each fluid phase, are defined as:

$$Re_{\mathrm{L,z}} = \frac{\dot{m}_{\mathrm{L,z}}}{\pi\,d\,\mu_{\mathrm{L}}} \tag{A.6}$$

$$Re_{\mathrm{V,z}} = \frac{\dot{m}_{\mathrm{V,z}}}{\pi\,d\,\mu_{\mathrm{V}}} \tag{A.7}$$

with μ_{L} and μ_{V} are the liquid and vapour dynamic viscosities, respectively.

The local heat transfer coefficient in the condensate liquid-film flow is described by a dimensionless Nusselt number. In the laminar film-flow region near the pipe inlet, this can be found from the correlation:

$$Nu_{\mathrm{L,z,La}} = \frac{\alpha_{\mathrm{L,z}}\,\Lambda}{k_{\mathrm{L}}} = 0.693\left(\frac{1 - \frac{\rho_{\mathrm{V}}}{\rho_{\mathrm{L}}}}{Re_{\mathrm{L,z}}}\right)^{1/3} \tag{A.8}$$

whereas in the turbulent region after the transition/entrance length, it can be found from the correlation:

$$Nu_{\mathrm{L,z,Tu}} = \frac{\alpha_{\mathrm{L,z}}\,\Lambda}{k_{\mathrm{L}}} = \frac{0.0283\,Re_{\mathrm{L,z}}^{7/24}\,Pr_{\mathrm{L}}^{1/3}}{1 + 9.66\,Re_{\mathrm{L,z}}^{-3/8}\,Pr_{\mathrm{L}}^{-1/6}} \tag{A.9}$$

in both cases based on a characteristic (Nusselt film height) length scale of the film flow:

$$\Lambda = \left(\frac{u_{\mathrm{L}}^2}{g}\right)^{1/3} \tag{A.10}$$

Based on the above, a total Nusselt number, $Nu_{\mathrm{L,z}}$, can be evaluated:

$$Nu_{\mathrm{L,z}} = \sqrt{Nu_{\mathrm{L,z,La}}^2 + Nu_{\mathrm{L,z,Tu}}^2} \tag{A.11}$$

The local heat transfer coefficient, $\alpha_{\mathrm{L},z}$, is defined as:

$$\alpha_{\mathrm{L,z}} = \frac{q'_{\mathrm{z}}}{(T_{\mathrm{Ph}} - T_{\mathrm{w,z}})} \tag{A.12}$$

with q'_{z} the local heat flux on the vertical tube wall, T_{Ph} the temperature at the film free-surface and $T_{\mathrm{w,z}}$ the tube wall temperatures, which from the above is given by:

$$\alpha_{\mathrm{L,z}} = \frac{K\, Nu_{\mathrm{L,z}}\, k_{\mathrm{L}}}{\Lambda} \tag{A.13}$$

that uses a correction factor for shear stress:

$$K = \left(\frac{\tau_{\mathrm{V}}}{\rho_{\mathrm{L}}\, g\, \delta_{\mathrm{L}}}\right)^{1/3} \tag{A.14}$$

where g is gravitational acceleration, and ρ_{L} and k_{L} the density and thermal conductivity of water.

The overall heat transfer coefficient α at the local point z_2 is:

$$\frac{1}{\alpha_{\mathrm{z_2}}} = \frac{1}{\alpha_{\mathrm{L,z}}} + \frac{w}{k} \tag{A.15}$$

where k is the thermal conductivity of 316 stainless steel. It is worth noting that the outer surface temperature of the 316 stainless steel tube is assumed to be equal to the PCM melting temperature of 250 °C. Furthermore, the overall heat transfer coefficient between the two local points is:

$$\bar{\alpha}_{\mathrm{z_{1,2}}} = \frac{\alpha_{\mathrm{z_1}} + \alpha_{\mathrm{z_2}}}{2} \tag{A.16}$$

The necessary tube length between these two local points is given by:

$$\Delta L_{1,2} = \frac{\Delta m_{\mathrm{L,z_{1,2}}}\, \Delta h_{\mathrm{v}}}{\pi\, d\, \bar{U}_{\mathrm{z_{1,2}}}\, \Delta T} \tag{A.17}$$

Beyond the transfer of latent heat from the condensing steam, sensible heat is also transferred in a section of the tank. For the calculation of the heat transfer in this section, instead of the phase-change enthalpy, the total difference of the specific enthalpies of steam and saturated water is used:

$$\Delta h = \Delta h_{\mathrm{vap}} + c_{\mathrm{pV}}\,(T_{\mathrm{V}} - T_{\mathrm{sat}}) = \Delta h_{\mathrm{v}} + c_{\mathrm{p,V}}\,\Delta T_{\ddot{\mathrm{U}}} \tag{A.18}$$

The condensation area required is:

$$A_{\ddot{\mathrm{U}}} = A\left(1 + \frac{c_{\mathrm{p,V}}\,\Delta T_{\ddot{\mathrm{U}}}}{\Delta h_{\mathrm{vap}}}\right) \tag{A.19}$$

where $c_{\mathrm{p,V}}$ is the specific heat capacity of the steam and $\Delta T_{\ddot{\mathrm{U}}}$ the superheated temperature difference. Full details and a procedure from solving these equations are given in Ref. [205].

Since we have evaluated the heat exchange area A and the tube length L, we have to check these values against the pressure drop and the number of tubes in the condenser. These calculations are based on an iterative method by setting arbitrarily the number and the length of the tubes until the pressure drop gives satisfactorily results.

For the calculation of the pressure drop, the shear stress, τ_{V}, is given by:

$$\tau_{\mathrm{V}} = \frac{\xi_{\mathrm{r}}}{8}\,\rho_{\mathrm{V}}\,u_{\mathrm{V}}^2 \tag{A.20}$$

where ξ_{r} is a friction factor for rough pipes that can be found from:

$$\xi_{\mathrm{r}} = \xi_{\mathrm{g}}(1 + 850\,F) \tag{A.21}$$

and ξ_{g} is the friction factor for smooth pipes that can be evaluated from the correlation:

$$\xi_{\mathrm{g}} = 0.184\,Re_{\mathrm{V,z}}^{-0.2} \tag{A.22}$$

Furthermore, the velocity, v_{V}, is given by:

$$v_{\mathrm{V}} = \frac{4\,\dot{m}_{\mathrm{V,z}}}{\rho_{\mathrm{V}}\,\pi\,(d - 2\,\delta_{\mathrm{F}})^2} \tag{A.23}$$

where the film thickness δ_{F} is found from:

$$\delta_{\mathrm{F}} = \frac{1 - \varepsilon}{4}\,d \tag{A.24}$$

for $\varepsilon \geq 0.67$.

The pressure drop between these two points is:

$$\Delta P_{1,2} = \frac{\tau_{V_1} + \tau_{V_2}}{2} \frac{4\,\Delta L}{d - \left(\delta_{F_1} + \delta_{F_1}\right)} \tag{A.25}$$

Therefore, the total length of the tubes is given by:

$$\Delta L = \Delta L_{0,1} + \Delta L_{1,2} + \Delta L_{2,3} + \Delta L_{3,4} + \Delta L_{4,5} + \Delta L_{5,6} \tag{A.26}$$

The heat exchange surface area is:

$$A_S = \pi\, d\, \Delta L \tag{A.27}$$

and the total pressure drop is:

$$\Delta P = \Delta P_{0,1} + \Delta P_{1,2} + \Delta P_{2,3} + \Delta P_{3,4} + \Delta P_{4,5} + \Delta P_{5,6} \tag{A.28}$$

Seeking a solution with a pressure drop less than 100 Pa, an acceptable solution is found with a tube length of 120 m and a pressure drop of 67 Pa.

Finally, the required volume of PCM in Thermal Tank 1 for heat transfer to the tank over 1 h, which amounts to a thermal energy storage capacity of 107 MWh, is found from:

$$Q_{TT-1} = \rho_{PCM}\, V_{TT-1}\, \Delta h_{PCM} = \frac{\pi\, D_{TT-1}^2\, L}{4}\, \rho_{PCM}\, h_{PCM} \tag{A.29}$$

where ρ_{PCM} is the density of the PCM, h_{PCM} the phase-change enthalpy of the PCM, Q_{TT-1} the heat storage of 107 MWh, V_{TT-1} the required volume and D_{TT-1} the diameter of the PCM in the tank. The total volume of Thermal Tank 1 is the sum of the volume of the tubes in the tank plus the volume of the PCM in this store and is given by:

$$V_{TT-1} = \frac{\pi}{4}\, D_{TT-1}^2\, L + \frac{\pi}{4}\, d_{o,TT-1}^2\, L \tag{A.30}$$

where $d_{o,TT-1}$ is the outer diameter of the 316 stainless steel tubes, which is 114 mm.

A.2. Thermal Tank 2

The calculation of the dimensionless numbers in the heat transfer equations requires knowledge of the properties of water. These, however, are temperature dependent and therefore the problem of the design of this thermal tank is solved by iteration. The steps of this procedure are as follows:

1. Calculation of the Reynolds number *Re*:

$$Re = \frac{v_{\mathrm{L}}\, d_{\mathrm{i}}}{\nu_{\mathrm{L}}} \tag{A.31}$$

where v_{L} is the bulk water velocity in the tubes, D_{i} the internal diameter of the tubes, and ν_{L} the kinematic viscosity of water. In our design, we have used 316 stainless steel tubes with an internal diameter of 76 mm and a wall thickness of 1 mm. We have also assumed that the flow in the pipes of Thermal Tank 2 is such that the flow is turbulent.

2. Calculation of the mean Nusselt number $\overline{Nu}$ from the Gnielinski correlation for heat transfer in turbulent flows through tubes:

$$\overline{Nu} = \frac{(f/8)\, Re\, Pr}{1 + 12.7\,\sqrt{f/8}\,(Pr^{2/3} - 1)}\left[1 + \left(\frac{d_{\mathrm{i}}}{L}\right)^{2/3}\right] \tag{A.32}$$

where Pr is the Prantdl number and:

$$f = (1.8 \log Re - 1.5)^{-2} \tag{A.33}$$

within the following ranges of validity:

$$10^4 \leq Re \leq 10^6, 0.1 \leq Pr \leq 1000, \frac{D_{\mathrm{i}}}{L} \leq 1 \tag{A.34}$$

3. Calculation of the average convective heat transfer coefficient $\bar{\alpha}$ over a length of a tube based on the mean Nusselt number $\overline{Nu}$ from Equation (A.32):

$$\overline{Nu} = \frac{\bar{\alpha}\, d_{\mathrm{i}}}{k_{\mathrm{L}}} \tag{A.35}$$

where k_{L} is the thermal conductivity of the water.

4. Calculation of the total heat transfer rate to the thermal tank/heat exchanger $Q_{\mathrm{TT-2}}$:

$$Q_{\mathrm{TT-2}} = \bar{\alpha}\, n\, A_{\mathrm{s}}\, \Delta T_{\mathrm{LM}} = 2\, n\, \pi\, d_{\mathrm{i}}\, L\, \bar{\alpha}\, \Delta T_{\mathrm{LM}} \tag{A.36}$$

where n is the number of the tubes, A_{s} the heat-transfer area of a single tube, and ΔT_{LM} is the logarithmic mean temperature difference which is defined as:

$$\Delta T_{\mathrm{LM}} = \frac{(T_{\mathrm{w}} - T_{\mathrm{in}}) - (T_{\mathrm{w}} - T_{\mathrm{out}})}{\ln\left(\frac{T_{\mathrm{w}} - T_{\mathrm{in}}}{T_{\mathrm{w}} - T_{\mathrm{out}}}\right)} \tag{A.37}$$

where T_{in} and T_{out} are the inlet and outlet temperatures of the saturated (inlet) and subcooled (outlet) water respectively, and T_{w} the tube surface temperature which is assumed to be uniform and equal to the PCM melting temperature at 142 °C.

5. Calculation of the pressure drop associated with fully developed flow in each tube [202]:

$$\Delta P = f \, \frac{\rho_{\text{L}} \, u_{\text{L}}^2}{2 \, d_{\text{i}}} \, L \tag{A.38}$$

where ρ_{L} is the density of the liquid water, and ξ the friction factor that is obtained from:

$$f = (0.790 \, \ln Re - 1.64)^{-2} \tag{A.39}$$

valid in the range:

$$3 \times 10^3 \leq Re \leq 5 \times 10^6 \tag{A.40}$$

6. Calculation of the feed pump power associated with this pressure drop:

$$\dot{W} = \frac{n \, \Delta P \, \dot{m}}{\rho_{\text{L}}} \tag{A.41}$$

where $\dot{m}$ is the mass flowrate of water in a single tube.

7. Calculation of physical properties of water at the mean temperature $\bar{T} = T_{\text{in}} + T_{\text{out}}/2$. The iteration above is repeated by increasing or decreasing the length of the tubes L and number of tubes n until the calculated heat transfer to the tank is almost equal to 26 MW_{th}.

8. Calculation of the required volume of PCM for storing 26 MW_{th} in Thermal Tank 2 over 1 h leads to a thermal energy storage capacity of 26 MWh, is performed using:

$$Q_{\text{TT}-2} = \rho_{\text{PCM}} \, V_{\text{TT}-2} \, h_{\text{PCM}} = \frac{\pi \, D_{\text{TT}-2}^2 \, L}{4} \, \rho_{\text{PCM}} \, h_{\text{PCM}} \tag{A.42}$$

where $Q_{\text{TT}-2}$ the thermal energy storage capacity of Thermal Tank 2, i.e., 26 MWh, ρ_{PCM} the density of the PCM, $V_{\text{TT}-2}$ the required volume of the PCM in tank, h_{PCM} the phase-change enthalpy of the PCM, and $D_{\text{TT}-2}$ the diameter of the tank.

9. Finally, the total volume of the thermal tank is the sum of the volume of the tubes in the thermal tank plus the volume of the PCM and is given by:

$$V_{\text{TT}-2} = \frac{\pi}{4} \, D_{\text{TT}-2}^2 \, L + \frac{\pi}{4} \, d_{\text{o,TT}-2}^2 \, L \tag{A.43}$$